UNIVERSITY OF EXETER

DOCTORAL THESIS

Exploring the Space of Electromagnetic Materials, with Applications to Antenna Design

---

Author:
James R. Capers

Supervisors:
Prof. Simon A. R. Horsley
Dr. Steve J. Boyes
Prof. Alastair P. Hibbins

A thesis submitted in fulfillment of the requirements
for the degree of Doctor of Philosophy in Physics

1st June 2023

Declaration of Authorship

Submitted by James Ross Capers, to the University of Exeter as a thesis for the degree of Doctor of Philosophy in Physics, 1st June 2023.

This thesis is available for Library use on the understanding that it is copyright material and that no quotation from the thesis may be published without proper acknowledgement.

I certify that all material in this thesis which is not my own work has been identified and that any material that has previously been submitted and approved for the award of a degree by this or any other University has been acknowledged.

Acknowledgements

There are so many people without whom this thesis would not have been possible.

First and foremost, huge thanks are due to my supervisors: Simon, Alastair and Steve. You each brought something different and essential to my work over the last 4 years.

Simon – I cannot thank you enough. Your patience, generosity with your time and infectious enthusiasm have made the PhD thoroughly enjoyable, even when nothing seemed to be working. I'm so grateful for the opportunities you've given me to learn things for myself and make my research my own. Your guidance, support and friendship have been truly invaluable.

Alastair – sorry I didn't end up doing any experiments! You always provided a fresh perspective and reminded me of the big picture. You also finally taught me when to use "which" and "that"... I might even stop getting it wrong one day.

Steve – your insights into the applications of my work have been a source of both motivation and excitement. You've been so generous with your time, encouragement, and support.

I am also greatly indebted to many kind, smart and passionate friends and colleagues. I would like to thank Dean Patient in particular, for putting up with my ramblings, silly questions and proof-reading many terrible first drafts. Josh Glasbey is also due particular thanks, for his questions that made me doubt everything and his patience for my silly COMSOL questions.

I must also thank my friends and house-mates, Daisy Hall, Will Borrows and Ed Baker for providing so much laughter, joy and friendship these last 4 years. Here's to many more. The waves group and my friends within the

CDT have also been incredibly helpful during the PhD. I'd like to acknowledge Ian Hooper in particular for his meshing wizardry and for asking all the difficult questions I hoped no-one would pick up on.

Finally, I'd like to thank my family for everything else. My parents, for showing an interest in what I'm doing, even if they're not totally sure what it all means. Without their constant encouragement to peruse what I enjoy, I would not be where I am today. My sisters, for making me laugh and always trying to take me down a peg, whether I like it or not. My grandparents, for their wisdom and kind words whenever I needed to hear them. The animals, Alfie, Charlie, Frodo and Sam, for always bringing a smile to my face.

Abstract

The ability to manipulate electromagnetic radiation is key to a huge range of current technologies, from communications and sensing to cooking and energy generation. It is expected that improving our ability to manipulate radiation in new ways will lead to many new technologies, such as invisibility cloaks and optical computing. One way to advance our ability to shape the electromagnetic field is using materials structured at the sub wave–length scale: metamaterials. With exotic properties not found in nature, metamaterials have revolutionised our ability to control fields, including light, sound, vibration, and heat. However, despite intensive research interest for almost two decades, the problem of designing metamaterials for specific applications remains challenging. Typical methods either make limiting assumptions, such as only allowing phase to be controlled, or rely on a large number of full–wave simulations. These are particularly expensive for metamaterials as there is a large length scale separation between the sub–wavelength elements of the metamaterial and the tens to hundreds of wavelength size of the metamaterial. Additionally, there has been much interest in using genetic algorithms or machine learning techniques to design materials, although these can be hard to interpret.

In this thesis, we attempt to address some of these issues. Employing the coupled dipole approximation to model metamaterials as collections of dipolar scatterers, we derive a perturbative method for designing metamaterials for a wide range of applications. After formulating the basic method, we proceed to extend it to design multi–functional metamaterials, allowing functionality to be multiplexed. Simple proof–of–concept experiments outline some of the key challenges to realising the structures we design, indicating where future development efforts could be focused. Switching focus to the elements that make up the metamaterials, we then consider how the resonances of individual meta–atoms can be manipulated. In this context, we derive both analytic and numerical approaches to control the scattering for dielectric slabs, cylinders and spheres.

Contents

List of Figures

Chapter 1

Introduction

> *"It's of no use whatsoever...this is just an experiment that proves Maestro Maxwell was right—we just have these mysterious electromagnetic waves that we cannot see with the naked eye. But they are there."* – Attributed to H. Hertz

1.1 Motivation

One of the greatest unifications in physics came in 1873, when Maxwell published his equations of electromagnetism [1]. These equations combined two phenomena that were previously thought to be unconnected: electricity and magnetism. A surprising consequence of Maxwell's theory is that free space supports electromagnetic waves: oscillating electric and magnetic fields. Strikingly, the speed of these waves is related to quantities that were taken to be proportionality constants in equations linking forces to charges and currents, but turn out to be the material properties called permittivity and permeability.

Shortly after Maxwell's seminal work, Poynting calculated that electromagnetic waves can carry energy [2]. This was verified experimentally by Hertz [3], using a simple dipole emitter made of two metallic spheres and a detector that we would today call a loop antenna. Hertz's original apparatus is shown in Figure 1.1. Although Hertz himself supposedly did not realise it, his experiments lit the way for wireless communication for the

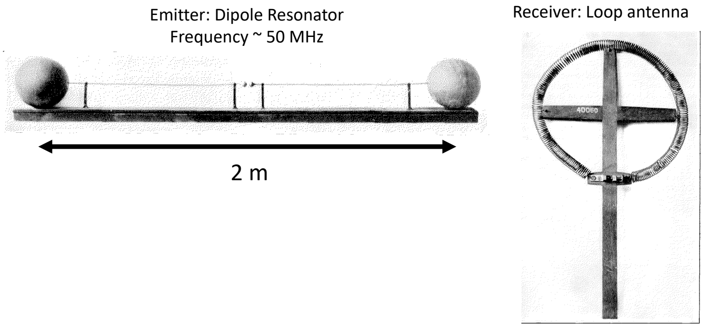

Figure 1.1: Hertz's original emitter (left) and detector (right), used in the first experimental demonstration that electromagnetic waves could transport energy (images public domain).

next two centuries. Marconi and Braun were the fathers of wireless telegraphy, for which they won the Nobel prize in 1909. Together they developed Hertz's ideas to design devices that would bring the ability to transmit information using electromagnetic radiation to the masses. Since the first successful radio transmission from Poldhu in Cornwall to Signal Hill in Newfoundland, wireless technology has been continuously developed and improved for over 100 years.

Moving beyond its initial use for broadcast radio, the true 'wireless revolution' began in the 1990s, with the proliferation of wireless networks connecting computers, as well as the release of hand–held devices like mobile phones. Since then, the number and density of connected devices as well as demand for high data rates has grown significantly meaning that today the electromagnetic spectrum is extremely congested. The current frequency allocations for the United Kingdom are shown in Figure 1.2. All frequencies from 8.3 kHz to 275 GHz are allocated for specific purposes, such as satellite and mobile communications, meteorological surveying or military uses. The lack of gaps for new capabilities presents a significant barrier to the higher data rates or device densities that will need to be achieved in

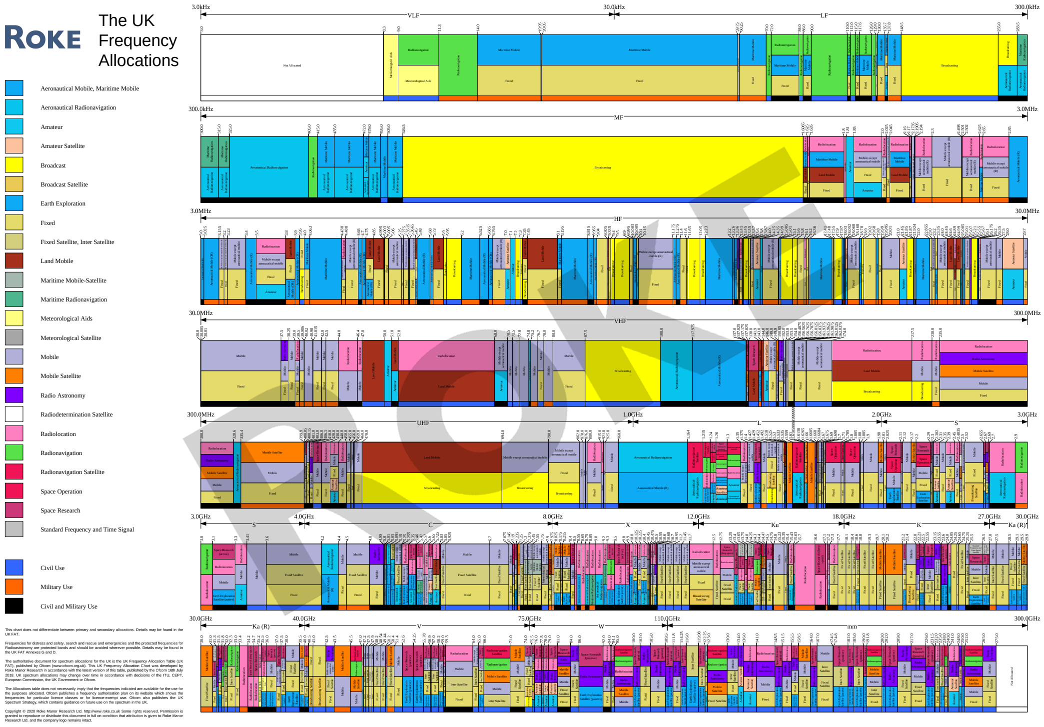

Figure 1.2: The UK's frequency allocations (Credit: Roke Manor Research Ltd). For illustrative purposes only.

future communications systems. There has therefore been a recent drive towards 'smarter' systems, that are more frequency selective, directive or multi–functional, to avoid unnecessary interference or competition for communication frequencies.

In addition to the demands on civilian communication infrastructure, military competition for electromagnetic advantage has never been more intense. A previous Chief of Defence Staff, Air Chief Marshal Sir Stuart Peach, said "...to understand, manage and control the electromagnetic environment is a vital role in warfare at all levels of intensity. The outcome of future operations will be decided by the protagonist who does this to decisive advantage" [4]. Effective communication and sensing is essential for battlefield advantage, however one's opponents will attempt to degrade access to key parts of the spectrum. To mitigate this, and to gain advantage, there is great desire to explore how more effective, resilient and dynamic electromagnetic systems can be designed.

One way to control the properties of electromagnetic emitters is to adjust the geometry of the emitter itself. This approach has led to *many* different antenna designs for a wide range of applications [5, 6]. The disadvantage of this approach is that the emitters can be geometrically complicated, and their functionality cannot be changed easily. One can therefore try to move the complexity into a material layer, that should be straightforward to build as well as thin and light so that it can be changed to re–configure the system for a different purpose. Metamaterials, materials that are structured on the sub–wavelength scale to achieve designer manipulation of light, are excellent candidates to fulfill this purpose. By tuning the geometry of 'meta–atoms', the building blocks of metamaterials, many different wave–manipulation effects can be achieved in electromagnetism, acoustics and elasticity. However, current methods for the design of metamaterials have significant drawbacks.

1.2 Outline of Thesis

In this thesis, we derive techniques for designing metamaterials, with an eye to a wide range of antenna applications. Our aim is to derive simple, intuitive, numerically efficient, methods for designing metamaterials to manipulate the radiation from simple emitters, making them more e.g. directive or multi–functional. The outline of the content is as follows:

- In **Chapter 2** we review the necessary background theory of electromagnetism, how Maxwell's equations can be solved under the assumption that the waves scatter from small dipolar particles and some powerful existing techniques for designing electromagnetic materials for specific applications.

- Next, in **Chapter 3**, we apply perturbation theory to the solutions of Maxwell's equations, deriving a method for designing metamaterials that perform single operations on the field of an emitter. We consider a wide range of problems related to antenna technology, such as improving emitted power, manipulating the radiation pattern and changing the coupling between nearby emitters.

- Extending our method, in **Chapter 4** we consider how to design passive metamaterials that can perform multiple operations on the field of an emitter, for example to produce different radiation patterns based on the polarisation of the emitter.

- The work of **Chapter 5**, undertaken jointly with Leanne Stanfield (University of Exeter), contains experimental validation of some of the devices designed using our method. Working at microwave frequencies, we demonstrate the ability of our method to design structures to control the radiation pattern of a simple antenna.

- In **Chapter 6**, we present a method for moving the resonances of scattering structures, based on the position of the modes in the complex frequency plane. This work, undertaken jointly with Dean Patient (University of Exeter), is useful for the design of resonators for sensing and emission, as well as for the design of meta–atoms with specific purposes.

- Finally, in **Chapter 7**, we evaluate the limitations of our proposed techniques and consider how the work of this thesis could be developed further.

Chapter 2

Background Theory

"It's still magic, even if you know how it's done."
– Terry Pratchett, 'A Hat Full of Sky'

Wave equations appear all over physics, describing a huge range of phenomena including water waves, elastic waves, acoustic pressure waves and quantum mechanical matter waves. One of the most important types of waves for modern life are electromagnetic waves. These are used for communications, cooking, sensing, medicine and much more. In this chapter, we review the background theory of electromagnetic radiation, formulating the wave equations for electric and magnetic fields. We then consider the interaction of the electromagnetic field with dipoles, both as emitters and as scattering objects. With this, we discuss how the electromagnetic wave equations can be solved for a collection of small dipolar scatterers. Considering next how materials can be designed to manipulate the electromagnetic field, we overview the field of metamaterials and key methods for designing them.

2.1 Wave Equations Across Physics

The findings in this thesis, and of metamaterial physics in general, extend across many domains of physics; almost anywhere the wave equation applies. To understand the implications of this statement, we now review the ubiquity of the wave equation; from quantum mechanics to elasticity and fluid dynamics. The wave equation for a scalar field $\phi(\boldsymbol{r}, t)$ is

$$\nabla^2 \phi(\boldsymbol{r}, t) = \frac{1}{c^2} \frac{\partial^2 \phi(\boldsymbol{r}, t)}{\partial t^2}, \tag{2.1}$$

where c is the speed of the wave. This equation can be read as nothing more than Newton's 2nd law. The right–hand side is a second time derivative so can be interpreted as the acceleration of the field ϕ, proportional to force. On the left, the Laplacian is a measure of the curvature of ϕ in space. Therefore, the wave–equation tells us that a larger curvature of the field ϕ corresponds to a larger restoring force upon the field. With this simple reasoning, we know that the solutions of this equation must oscillate in space and time. One can show this mathematically, by moving to the new variables

$$\xi = \boldsymbol{r} - \boldsymbol{c}t \qquad\qquad \eta = \boldsymbol{r} + \boldsymbol{c}t, \tag{2.2}$$

so that the wave equation becomes

$$\frac{\partial^2 \phi}{\partial \xi \partial \eta} = 0. \tag{2.3}$$

This has the general solution

$$\phi(\boldsymbol{r}, t) = f(\boldsymbol{r} - ct) + g(\boldsymbol{r} + ct), \tag{2.4}$$

where f and g are arbitrary functions. We see that the wave equation permits waves that travel both forwards and backwards in space as time progresses.

Much of the day–to–day physics we experience is wave physics. One of the most obvious examples of wave physics that we experience every day is sound (acoustic pressure waves). These kinds of waves are caused by small oscillations in compressible fluids, with the oscillation causing alternating compression and rarefaction. For sound waves in air, the individual air molecules only move by about 1μm. To derive the wave equation for sound, we need only consider the continuity of the mass of the fluid that the waves are propagating in [7]. Indeed, all of fluid mechanics can be derived from mass continuity, and its higher moments [7, 8]. Considering a finite volume V bounded by a surface S, the mass of fluid leaving this volume must be given by

$$\oint \rho \boldsymbol{v} \cdot d\boldsymbol{S}, \tag{2.5}$$

where $\boldsymbol{v}$ is the velocity of the fluid and ρ is the mass density of the fluid. The amount of fluid leaving the volume must produce a decrease in the total mass of the fluid inside that volume, per unit time, which can be written as

$$-\frac{\partial}{\partial t}\int \rho dV. \tag{2.6}$$

Equating these gives

$$-\frac{\partial}{\partial t}\int \rho dV = \oint \rho \boldsymbol{v} \cdot d\boldsymbol{S}, \tag{2.7}$$

which can be re–written using the divergence theorem[1] we have

$$-\frac{\partial}{\partial t}\int \rho dV = \int \nabla\cdot(\rho\boldsymbol{v})dV. \tag{2.8}$$

This must be true for any closed volume we choose, therefore

$$\frac{\partial\rho}{\partial t} + \nabla\cdot(\rho\boldsymbol{v}) = 0. \tag{2.9}$$

This is a statement that the mass of the fluid must be conserved. Now, if the fluid is under some pressure p, Newton's 2nd law can be written as

$$\rho\frac{\mathrm{d}\boldsymbol{v}}{\mathrm{d}t} = -\nabla p. \tag{2.10}$$

Re–writing the total derivative as

$$\frac{\mathrm{d}\boldsymbol{v}}{\mathrm{d}t} = \frac{\partial\boldsymbol{v}}{\partial t} + (\boldsymbol{v}\cdot\nabla)\,\boldsymbol{v}, \tag{2.11}$$

we arrive at Euler's equation

$$\frac{\partial\boldsymbol{v}}{\partial t} + (\boldsymbol{v}\cdot\nabla)\,\boldsymbol{v} = -\frac{1}{\rho}\nabla p. \tag{2.12}$$

This describes the effect of a pressure field upon the flow of a fluid. Assuming that the oscillations in pressure are small, we can expand the pressure and density variations of the fluid as

$$p = p_0 + p_1 \qquad \rho = \rho_0 + \rho_1 \qquad \boldsymbol{v} = \boldsymbol{v}_1, \tag{2.13}$$

---

[1] The divergence of a quantity in a volume V is equal to the flux of that quantity over a closed surface ∂S enclosing that volume: $\int_V \boldsymbol{\nabla}\cdot\boldsymbol{A}dV = \oint_{\partial S}\boldsymbol{A}\cdot\hat{\boldsymbol{n}}dS$, where $\hat{\boldsymbol{n}}$ is the normal vector of the surface.

where $p_1 \ll p_0$ and $\rho_1 \ll \rho_0$. Euler's equation then becomes

$$\frac{\partial \boldsymbol{v}_1}{\partial t} + \frac{1}{\rho_0}\nabla p_1 = 0, \tag{2.14}$$

and the continuity equation is

$$\frac{\partial \rho_1}{\partial t} + \nabla \cdot (\rho_0 \boldsymbol{v}_1) = 0. \tag{2.15}$$

In an ideal fluid, sound is adiabatic so that changes in pressure and mass density are connected by the thermodynamic relation

$$p_1 = \left(\frac{\partial p}{\partial \rho_0}\right)_S \rho_1, \tag{2.16}$$

with the subscript 'S' indicates that entropy is held constant while pressure and density vary. Substituting this into the continuity equation (2.15), we have

$$\frac{\partial p_1}{\partial t} + \left(\frac{\partial p}{\partial \rho_0}\right)_S \nabla \cdot (\rho_0 \boldsymbol{v}_1) = 0. \tag{2.17}$$

Differentiating this expression with respect to time, we arrive at the wave equation for pressure waves in a compressible fluid

$$\frac{\partial^2 p_1}{\partial t^2} + \left(\frac{\partial p}{\partial \rho_0}\right)_S \nabla \cdot \left(\rho_0 \frac{\partial \boldsymbol{v}_1}{\partial t}\right) = 0 \tag{2.18}$$

$$\Rightarrow \frac{\partial^2 p_1}{\partial t^2} = \left(\frac{\partial p}{\partial \rho_0}\right)_S \nabla^2 p_1. \tag{2.19}$$

We see that the speed of sound waves is given by $c^2 = \left(\frac{\partial p}{\partial \rho_0}\right)_S$, which can also be written in terms of macroscopic quantities as $c = \sqrt{K/\rho}$ where K is the bulk modulus.

Another type of wave we experience every day are the waves supported by solid bodies, elastic waves [9]. Inside a solid material, an elastic wave causes the distance between two points, described by the displacement vector $u_i = x'_i - x_i$, to change. Splitting the solid object into small blocks with surface S, the restoring force of each block is given by the stress tensor σ_{ik}

$$df_i = \sigma_{ik} dS_k, \tag{2.20}$$

where the first index is the direction the restoring force occurs in and the second index is the direction a force is applied in. Einstein summation notation is employed throughout this discussion. So the σ_{xx} element of the tensor describes the restoring force in the x direction due to a force applied in the x direction, while the σ_{xy} element describes the force exerted by the material in the x direction when a force is applied in the y direction. For an elastic material, Newton's 2nd law can then be written as

$$\frac{\partial}{\partial t} \int \left(\rho \frac{\partial u_i}{\partial t} \right) dV = \int \sigma_{ik} dS_k, \tag{2.21}$$

which can be re–written using the divergence theorem as

$$\rho \frac{\partial^2 u_i}{\partial t^2} = \frac{\partial \sigma_{ik}}{\partial x_k}. \tag{2.22}$$

To turn this into a wave equation, one needs constitutive relations between stress σ and strain u; for isotropic materials this is given by Hooke's law, stated as

$$\sigma_{ik} = K u_{ll} \delta_{ik} + 2\mu \left(u_{ik} - \frac{1}{3} \delta_{ik} u_{ll} \right). \tag{2.23}$$

Here, K is the bulk modulus, μ is the shear modulus and we have introduced the strain tensor

$$u_{ik} = \frac{1}{2} \left(\frac{\partial u_i}{\partial x_k} + \frac{\partial u_k}{\partial u_i} \right). \tag{2.24}$$

Putting this together, the stress tensor is now

$$\sigma_{ik} = K\frac{\partial u_l}{\partial x_l}\delta_{ik} + 2\mu\left(\frac{1}{2}\frac{\partial u_i}{\partial x_k} + \frac{1}{2}\frac{\partial u_k}{\partial x_i} - \frac{\delta_{ik}}{3}\frac{\partial u_l}{\partial x_l}\right). \tag{2.25}$$

To write down the wave–equation for elastic waves, we must calculate the divergence of the strain tensor, which is

$$\begin{aligned}\frac{\partial \sigma_{ik}}{\partial x_k} &= \left(K - \frac{2}{3}\mu\right)\frac{\partial^2 u_l}{\partial x_k \partial x_l} + \mu\left(\frac{\partial^2 u_i}{\partial x_k^2} + \frac{\partial^2 u_k}{\partial u_k \partial x_i}\right), &(2.26)\\ &= \left(K + \frac{1}{3}\right)\frac{\partial^2 u_l}{\partial x_k \partial x_l} + \mu\frac{\partial^2 u_i}{\partial x_k^2}. &(2.27)\end{aligned}$$

The wave equation for elastic waves in an isotropic material is therefore

$$\begin{aligned}\rho\frac{\partial^2 u_i}{\partial t^2} &= \left(K + \frac{1}{3}\mu\right)\frac{\partial^2 u_i}{\partial x_k \partial x_i} + \mu\frac{\partial^2 u_i}{\partial x_k^2} &(2.28)\\ \rho\frac{\partial^2 \boldsymbol{u}}{\partial t^2} &= \left(K + \frac{1}{3}\mu\right)\nabla(\nabla\cdot\boldsymbol{u}) + \mu\nabla^2\boldsymbol{u}. &(2.29)\end{aligned}$$

If we now break up the displacement vector into longitudinal and transverse parts $\boldsymbol{u} = \boldsymbol{u}_L + \boldsymbol{u}_T$, where

$$\nabla\cdot\boldsymbol{u}_T = 0 \qquad\qquad \nabla\times\boldsymbol{u}_L = 0, \tag{2.30}$$

we find that

$$\begin{aligned}\frac{\partial^2 \boldsymbol{u}_T}{\partial t^2} &= \frac{\mu}{\rho}\nabla^2\boldsymbol{u}_T, &(2.31)\\ \frac{\partial^2 \boldsymbol{u}_L}{\partial t^2} &= \frac{1}{\rho}\left(K + \frac{4}{3}\mu\right)\nabla^2\boldsymbol{u}_L. &(2.32)\end{aligned}$$

The transverse parts describe shear waves (S waves) and the longitudinal parts describe pressure waves (P waves). An interesting feature of elasticity is that at material interfaces, S and P waves couple [9], allowing for conversion between the two polarisations.

As well as waves in liquids (sound) and solids (elastics), more exotic waves are actively being studied. To begin to understand quantum mechanical waves, we can start from the dispersion relation for a massive relativistic particle

$$E^2 = p^2c^2 + m^2c^4, \tag{2.33}$$

where E is the energy, p is the momentum, m is the mass of the particle and c is the speed of light. Replacing energy and momentum with their operator representations [10] $E \rightarrow i\hbar\partial_t$ and $\boldsymbol{p} \rightarrow -i\hbar\nabla$, yields the Klein–Gordon equation

$$\left(-\frac{\partial^2\phi}{\partial t^2} + c^2\nabla^2\right)\phi = \frac{m^2c^4}{\hbar^2}\phi. \tag{2.34}$$

This describes a wave propagating with the speed of light, with a source term related to the particle mass, and is the starting point for much of relativistic quantum field theory [11, 12]. From this, we see that quantum mechanics is a theory of matter waves. The non–relativistic limit of the Klein–Gordon equation can be found by taking the non–relativistic limit of the dispersion relation

$$E = \sqrt{p^2c^2 + m^2c^4}. \tag{2.35}$$

Taking the limit when $v = p/m \ll c$, we find that

$$E = mc^2\sqrt{1 + \frac{p^2c^2}{m^2c^4}} \tag{2.36}$$

$$\approx mc^2 + \frac{p^2}{2m}. \tag{2.37}$$

The first term is a global offset that does not affect the dynamics of the fields. Replacing the momentum and energy with their operator representations, we arrive at the Schrödinger equation

$$i\hbar\frac{\partial\Psi}{\partial t} = \hat{H}\Psi, \tag{2.38}$$

which connects the time derivative of the wave function Ψ to the action of the Hamiltonian operator $\hat{H}$ upon the wave function Ψ. For a particle in an external potential V this can be written as

$$i\hbar\frac{\partial\Psi}{\partial t} = -\frac{\hbar^2}{2m}\nabla^2\Psi + \hat{V}\Psi. \tag{2.39}$$

While this is not of exactly the same form as the wave equation we opened this section with (the time derivative is first order rather than second), it shares many of the same features. For example, it has solutions of the form $f(\boldsymbol{r} - vt)$. It is easy to verify that

$$\Psi = \text{const} \times e^{\frac{i}{\hbar}(\boldsymbol{p}\cdot\boldsymbol{r} - Et)} \tag{2.40}$$

is a solution to the Schrödinger equation. This is a plane wave with wave–vector $\boldsymbol{k} = \boldsymbol{p}/\hbar$ with corresponding de–Brogilie wavelength $\lambda = 2\pi\hbar/p$.

2.2 Maxwell's Equations and Electromagnetic Waves

Electromagnetic phenomena have been a source of fascination since ancient times: lightening, electric eels, static electricity all puzzled our ancestors [13]. Not until much later was it realised that all of these phenomena are governed by the same fundamental laws. A complete theory of (classical) electromagnetism was proposed by Maxwell in the late 19th century [1], describing the interaction of charges and currents through the electromagnetic field. Written in the convenient vector notation first used by Heaviside, Maxwell's equations connect charges and currents to electromagnetic fields [14, 15] as follows

$$\nabla \cdot \boldsymbol{D}(\boldsymbol{r},t) = \rho(\boldsymbol{r},t), \tag{2.41a}$$

$$\nabla \cdot \boldsymbol{B}(\boldsymbol{r},t) = 0, \tag{2.41b}$$

$$\nabla \times \boldsymbol{E}(\boldsymbol{r},t) = -\frac{\partial \boldsymbol{B}(\boldsymbol{r},t)}{\partial t}, \tag{2.41c}$$

$$\nabla \times \boldsymbol{H}(\boldsymbol{r},t) = \frac{\partial \boldsymbol{D}(\boldsymbol{r},t)}{\partial t} + \boldsymbol{j}(\boldsymbol{r},t). \tag{2.41d}$$

Here, the charges and currents are given by: the free charge density $\rho(\boldsymbol{r},t)$, with units of Coulombs per unit volume; the free current density $\boldsymbol{j}(\boldsymbol{r},t)$, with units Coulombs per unit volume meters per second. From the units, it is clear that current $\boldsymbol{j}(\boldsymbol{r},t)$, is generated by a charge distribution in motion: $\boldsymbol{j} = \rho\boldsymbol{v}$, where $\boldsymbol{v}$ is a velocity. Taking the divergence of Ampere's law (2.41d), it is straightforward to show that [14] charge and current are not independent and obey the continuity equation

$$\nabla \cdot \boldsymbol{j}(\boldsymbol{r},t) + \frac{\partial \rho(\boldsymbol{r},t)}{\partial t} = 0. \tag{2.42}$$

The fields in the Maxwell equations are: the displacement field $\boldsymbol{D}$ with units of charge (Coulombs) per unit area, the electric field $\boldsymbol{E}$ with units of force per unit charge, the magnetic field strength $\boldsymbol{H}$ with units of charge per meter per second and the magnetic flux density $\boldsymbol{B}$ has units of force per meter per Ampere.

Since Maxwell's original formulation many approximations, simplifications and tricks have been used to solve Maxwell's equations [16–18].

When trying to solve Maxwell's equations in the presence of matter, the electromagnetic properties of the medium may be characterised in terms of macroscopic polarization $\boldsymbol{P}$ and magnetization $\boldsymbol{M}$ [16]. The quantity $\boldsymbol{P}$ represents the density of permanent or induced dipole moments within a material, and can be connected to bound and surface charge densities [15]. In this way, the macroscopic polarization $\boldsymbol{P}$ is simply the sum of all of the polarizations (dipole moments) of each molecule, per unit volume i.e. $\boldsymbol{P} = \sum_i \boldsymbol{p}_i / V = (1/V) \int_V dV \boldsymbol{p}(\boldsymbol{r})$. The direction of the vector $\boldsymbol{P}$ is obtained from the geometric addition of each of the individual vectors $\boldsymbol{p}_i$ [18]. Similarly, the quantity $\boldsymbol{M} = \sum_i \boldsymbol{m}_i / V = (1/V) \int_V dV \boldsymbol{m}(\boldsymbol{r})$, is the magnetic dipole moment per unit volume of a material. This can be connected to bound currents within the material [15].

The polarization density $\boldsymbol{P}$ and the magnetization density $\boldsymbol{M}$ can be related to the fields present in Maxwell's equations (2.41) through [15–18]

$$\boldsymbol{D}(\boldsymbol{r}, t) = \epsilon_0 \boldsymbol{E}(\boldsymbol{r}, t) + \boldsymbol{P}(\boldsymbol{r}, t), \tag{2.43a}$$

$$\boldsymbol{H}(\boldsymbol{r}, t) = \frac{1}{\mu_0} \boldsymbol{B}(\boldsymbol{r}, t) - \boldsymbol{M}(\boldsymbol{r}, t), \tag{2.43b}$$

where $\varepsilon_0 = 8.85 \times 10^{-12}\ \mathrm{Fm}^{-1}$ is the permittivity of free space and $\mu_0 = 4\pi \times 10^{-7}\ \mathrm{NA}^{-2}$ is the permeability of free space, both in SI units. This gives us all of the parts we need to construct and interpret the wave equations that follow from Maxwell's equations.

To form the wave equations, we take the curl of Faraday's law (2.41c) and of Ampere's Law (2.41d), then substitute from the constitutive relations (2.43). This procedure yields the linear inhomogeneous vector wave equations for the electric and magnetic fields, with the currents and charges forming the source terms:

$$\nabla \times \nabla \times \boldsymbol{E} + \frac{1}{c^2}\frac{\partial^2 \boldsymbol{E}}{\partial t^2} = -\mu_0 \frac{\partial}{\partial t}\left(\boldsymbol{j} + \frac{\partial \boldsymbol{P}}{\partial t} + \nabla \times \boldsymbol{M}\right), \tag{2.44a}$$

$$\nabla \times \nabla \times \boldsymbol{H} + \frac{1}{c^2}\frac{\partial^2 \boldsymbol{H}}{\partial t^2} = \nabla \times \boldsymbol{j} + \mu_0 \frac{\partial \boldsymbol{M}}{\partial t} + \nabla \times \frac{\partial \boldsymbol{P}}{\partial t}. \tag{2.44b}$$

We have introduced the speed of electromagnetic waves in free space $c = 1/\sqrt{\varepsilon_0 \mu_0} \approx 3 \times 10^8\ \mathrm{ms}^{-1}$. Interestingly, a very similar left-hand side can be obtained for elastic waves [9], although the expression for the wave speed is very different. The wave equations (2.44) have a simple general interpretation. Time varying free currents $\boldsymbol{j}$, bound currents $\boldsymbol{M}$ and bound charges $\boldsymbol{P}$ can all generate an electromagnetic field $(\boldsymbol{E}, \boldsymbol{H})$, which travels as a vector wave with a speed c in free space. The nature of the curl operator in (2.44) acts to mix components; for example it is clear that a source current $\boldsymbol{j}$ aligned along the Cartesian axis $\hat{\boldsymbol{x}}$ can produce an electromagnetic field with components along all three Cartesian axes.

While the wave equation (2.44) has a clear physical interpretation, it is still exactly equivalent to Maxwell's equations (2.41). We have therefore made no progress towards a solution. To do so, we assume that our wave has a single fixed period of oscillation T and equivalently a fixed angular frequency $\omega = 2\pi/T$, with units of oscillations per second [19]. A monochromatic wave of this form can be conveniently written as

$$\boldsymbol{E}(\boldsymbol{r}, t) = \mathrm{Re}\left\{\boldsymbol{E}_\omega(\boldsymbol{r}) e^{-i\omega t}\right\}, \tag{2.45}$$

where $\boldsymbol{E}_\omega(\boldsymbol{r})$ is a complex amplitude [14]. Assuming that all of the vector fields in the wave equations (2.44) can be written in this way we find that the complex amplitudes of each of the fields obey the same wave equation as the fields themselves

$$\boldsymbol{\nabla} \times \boldsymbol{\nabla} \times \boldsymbol{E}_\omega - \frac{\omega^2}{c^2}\boldsymbol{E}_\omega = i\omega\mu_0 \left(\boldsymbol{j}_\omega - i\omega\boldsymbol{P}_\omega + \boldsymbol{\nabla} \times \boldsymbol{M}_\omega\right), \tag{2.46a}$$

$$\boldsymbol{\nabla} \times \boldsymbol{\nabla} \times \boldsymbol{H}_\omega - \frac{\omega^2}{c^2}\boldsymbol{H}_\omega = \boldsymbol{\nabla} \times \boldsymbol{j}_\omega - i\omega\mu_0\boldsymbol{M}_\omega - i\omega\boldsymbol{\nabla} \times \boldsymbol{P}_\omega, \tag{2.46b}$$

with the time dependence removed. It is important to realise that the quantities with subscript ω are now complex so the physical interpretation of them becomes more complicated. For example $\boldsymbol{E}$ is a force per unit charge (a quantity that must be real), while $\boldsymbol{E}_\omega$ is not. In free space $\boldsymbol{j} = \boldsymbol{P} = \boldsymbol{M} = 0$, so equation (2.46) can be reduced to the Helmholtz equation for each component of the electric and magnetic field amplitudes

$$\left(\boldsymbol{\nabla}^2 + k^2\right) \boldsymbol{E}_\omega = 0, \tag{2.47a}$$

$$\left(\boldsymbol{\nabla}^2 + k^2\right) \boldsymbol{H}_\omega = 0, \tag{2.47b}$$

where $k = \omega/c$ is the wavenumber. With these rearrangements and simplifications, we are now ready to formulate solutions to the Helmholtz equation (2.47) and the monochromatic vector wave equation (2.46). In the subsequent sections, when $\boldsymbol{E}, \boldsymbol{H}, \boldsymbol{P}$ and $\boldsymbol{M}$ are used to we will be referring to the complex amplitudes of each of these fields, defined via (2.45), and the subscripts will be dropped. Since the complex nature of the quantities being discussed will be manifest, we hope there will be no confusion.

2.3 Solution of the Wave Equations

In this section we shall introduce the mathematical tools that will be used to solve the scalar and vector wave equations which follow from Maxwell's equations; equations (2.47) and (2.46) respectively. These tools are Green's functions. Originally developed in the 1820s to solve differential equations in electromagnetism [20], Green's functions are a powerful tool for solving inhomogeneous linear differential equations. As the electromagnetic Green's function is an important and fundamental object in this work (as well as many other areas of quantum and classical electromagnetism, condensed matter physics, the theory of elasticity etc.) this section will include its derivation. Having derived the electromagnetic Green's function, a few of its most important properties will be established.

Green's functions are a very general method of solving linear inhomogeneous differential equations [21]. This class of differential equation has the general form

$$\hat{O}u(\boldsymbol{r}) = s(\boldsymbol{r}). \tag{2.48}$$

Given some linear differential operator $\hat{O}$, with a given source term $s(\boldsymbol{r})$, our aim is to find the solution $u(\boldsymbol{r})$. This is done by defining the Green's function as the solution to the simpler differential equation

$$\hat{O}G(\boldsymbol{r}, \boldsymbol{r}') = \delta(\boldsymbol{r} - \boldsymbol{r}'). \tag{2.49}$$

The expression (2.49) immediately gives the interpretation of the Green's function. It is the response of the system to a single Dirac delta impulse (a 'kick'). For example, finding the Green's function of a harmonic oscillator where $\hat{O} = \partial_t^2 + \omega_0^2$, gives the response of the oscillator to a single impulse. To find the solution to the differential equation (2.48), $u(\boldsymbol{r})$, in terms of the Green's function one must multiply both sides of (2.49) by the source term

$s(\boldsymbol{r})$ and integrate over all space

$$\begin{aligned}\int_{V'} \hat{O}G(\boldsymbol{r},\boldsymbol{r'})s(\boldsymbol{r'})d\boldsymbol{r'} &= \int_{V'} \delta(\boldsymbol{r}-\boldsymbol{r'})s(\boldsymbol{r'})d\boldsymbol{r'},\\ \int_{V'} \hat{O}G(\boldsymbol{r},\boldsymbol{r'})s(\boldsymbol{r'})d\boldsymbol{r'} &= s(\boldsymbol{r}).\end{aligned} \tag{2.50}$$

Now, since the linear differential operator acts upon $\boldsymbol{r}$ and the integral is over $\boldsymbol{r'}$, the operator $\hat{O}$ can be brought outside the integral. As the equality must be true for all linear differential operators, we arrive at the solution in terms of the Green's function

$$\begin{aligned}\hat{O}u(\boldsymbol{r}) &= \hat{O}\int_{V'} G(\boldsymbol{r},\boldsymbol{r'})s(\boldsymbol{r'})d\boldsymbol{r'},\\ u(\boldsymbol{r}) &= \int_{V'} G(\boldsymbol{r},\boldsymbol{r'})s(\boldsymbol{r'})d\boldsymbol{r'}.\end{aligned} \tag{2.51}$$

We have found that the solution to an inhomogeneous linear differential equation is given by the convolution of the Green's function of the differential operator with the source term.

Next, we must address the problem of finding an explicit form of the Green's function. Our aim is to solve the vector wave equations (2.46) but first we shall solve the Helmholtz equation (2.47). The Green's function for the Helmholtz equation, by definition, satisfies

$$\left(\boldsymbol{\nabla}^2 + k_0^2\right) G_0(\boldsymbol{r},\boldsymbol{r'}) = \delta(\boldsymbol{r}-\boldsymbol{r'}). \tag{2.52}$$

We must solve this for the explicit form of $G_0(\boldsymbol{r},\boldsymbol{r'})$. This can be done by Fourier transforming the quantities in N spatial dimensions

$$G_0(\boldsymbol{r},\boldsymbol{r'}) = \frac{1}{(2\pi)^N}\int G_0(\boldsymbol{k})e^{i\boldsymbol{k}\cdot(\boldsymbol{r}-\boldsymbol{r'})}d\boldsymbol{k} \tag{2.53}$$

$$\delta(\boldsymbol{r}-\boldsymbol{r'}) = \frac{1}{(2\pi)^N}\int e^{i\boldsymbol{k}\cdot(\boldsymbol{r}-\boldsymbol{r'})}d\boldsymbol{k} \tag{2.54}$$

to turn the differential equation into an algebraic equation for $G_0(\boldsymbol{k})$. The measure of integration $d\boldsymbol{k}$ in 1D is dk, in 2D is $dk_x dk_y$ and so on. Re-arranging yields

$$G_0(\boldsymbol{k}) = \frac{1}{k_0^2 - \boldsymbol{k}^2 + i\eta}. \tag{2.55}$$

To find the explicit form of the Green's function in real space, one must evaluate the inverse Fourier transform of (2.55). This can be done using standard contour integration methods [22]. Notice that it has been necessary to introduce a small amount of loss $\eta \ll 1$ in order to ensure that we obtain outgoing (advanced) wave solutions [23]. This is an important feature of Green's functions: they are specific to the differential operator *and* the boundary conditions. If we instead required our solution to be incoming waves, the sign of the loss should be reversed (shifting the location of the poles in k space yielding the retarded solution). Evaluating the integral, then taking the limit where $\eta \to 0$, the explicit form of the Green's function for the Helmholtz operator with outgoing wave boundary conditions is

$$G_0(\boldsymbol{r},\boldsymbol{r}') = \begin{cases} \frac{1}{2ik_0} e^{ik_0|\boldsymbol{r}-\boldsymbol{r}'|}, & \text{(1D)} \\ \frac{1}{4i} H_0^{(1)}(k_0|\boldsymbol{r}-\boldsymbol{r}'|), & \text{(2D)} \\ \frac{-1}{4\pi|\boldsymbol{r}-\boldsymbol{r}'|} e^{ik_0|\boldsymbol{r}-\boldsymbol{r}'|}, & \text{(3D)} \end{cases} \tag{2.56}$$

where $H_0^{(1)}(z)$ is the Hanel funciton of the first kind of order 0.

Now that we have found the Green's function for the Helmholtz equation, we would like to find the Green's function for the vector wave equation (2.46), which has the form

$$\boldsymbol{\nabla} \times \boldsymbol{\nabla} \times \boldsymbol{u} - k^2 \boldsymbol{u} = \boldsymbol{s}(\boldsymbol{r}). \tag{2.57}$$

Applying the definition of Green's functions, the solution can be written as

$$\boldsymbol{u}(\boldsymbol{r}) = \int_{V'} \boldsymbol{G}(\boldsymbol{r},\boldsymbol{r'}) \cdot \boldsymbol{s}(\boldsymbol{r'}) d\boldsymbol{r'} = \sum_k \int_{V'} G_{jk}(\boldsymbol{r},\boldsymbol{r'}) s_k(\boldsymbol{r'}) d\boldsymbol{r'}. \tag{2.58}$$

Before we find the explicit form of $\boldsymbol{G}(\boldsymbol{r},\boldsymbol{r'})$, we can already see that it must have certain properties. Both the source term and the solution must be vectors, so can we choose $\boldsymbol{G}(\boldsymbol{r},\boldsymbol{r'})$ to be a scalar function? Clearly not: Maxwell's equations imply that a current along $\hat{\boldsymbol{x}}$ does not generate fields with exclusively $\hat{\boldsymbol{x}}$ components. We cannot choose $\boldsymbol{G}(\boldsymbol{r},\boldsymbol{r'})$ to be a vector either: the dimensions of the result would be incorrect (**vector** $\cdot$ **vector** $=$ scalar, or **vector** $\times$ **vector**^{T} = **matrix**). We are left with a single choice for the form of the Green's function: a 'dyad' (a second order tensor). Dyads can be thought of as operators that convert one vector to another [21]. In three dimensions, the new vector is related to the old one by the coefficients of the dyad G_{ij}. These objects are found across physics, for example the moment of inertia is a dyad. It will become clear in the following derivation of $\boldsymbol{G}(\boldsymbol{r},\boldsymbol{r'})$ that it must have this form, but these simple arguments tell us what to expect of the result.

The Green's function for equation (2.46) must, by definition, satisfy

$$\boldsymbol{\nabla} \times \boldsymbol{\nabla} \times \boldsymbol{G}(\boldsymbol{r},\boldsymbol{r'}) - k^2 \boldsymbol{G}(\boldsymbol{r},\boldsymbol{r'}) = \mathbf{1}\delta(\boldsymbol{r}-\boldsymbol{r'}), \tag{2.59}$$

where $\mathbf{1} = \operatorname{diag}(1,1,1)$ is the unit tensor. Again, we must calculate the explicit form of the Green's function. There are many ways to do this. For example, one may work directly from Maxwell's equations and utilise the scalar and vector potentials [24] or use a more abstract mathematical approach by taking the Fourier transform of (2.59) and using the properties of dyads [25]. In what follows we will use the elegant solution of Levine and

Schwinger [26], who were among the first to introduce the concept of an dyadic Green's function.

We begin by taking the divergence of (2.59) to find an expression for the divergence of $\boldsymbol{G}(\boldsymbol{r},\boldsymbol{r'})$

$$\boldsymbol{\nabla}\cdot\boldsymbol{G}(\boldsymbol{r},\boldsymbol{r'}) = -\frac{1}{k^2}\boldsymbol{\nabla}\cdot\left[\boldsymbol{1}\delta(\boldsymbol{r}-\boldsymbol{r'})\right]. \tag{2.60}$$

Now, re-writing (2.59) as[2]

$$-\boldsymbol{\nabla}^2\boldsymbol{G}(\boldsymbol{r},\boldsymbol{r'}) + \boldsymbol{\nabla}(\boldsymbol{\nabla}\cdot\boldsymbol{G}(\boldsymbol{r},\boldsymbol{r'})) - k^2\boldsymbol{G}(\boldsymbol{r},\boldsymbol{r'}) = \boldsymbol{1}\delta(\boldsymbol{r}-\boldsymbol{r'}), \tag{2.61}$$

and substituting (2.60) yields

$$(\boldsymbol{\nabla}^2+k^2)\boldsymbol{G}(\boldsymbol{r},\boldsymbol{r'}) = -\left(\boldsymbol{1}+\frac{1}{k^2}\boldsymbol{\nabla}\otimes\boldsymbol{\nabla}\right)\delta(\boldsymbol{r}-\boldsymbol{r'}) \tag{2.62}$$

where $\boldsymbol{\nabla}\otimes\boldsymbol{\nabla} = (\partial^2/\partial x_i \partial x_j)$, with $\otimes$ denoting the tensor outer product. Therefore, informed by (2.62), we seek a Green's function of the form

$$\boldsymbol{G}(\boldsymbol{r},\boldsymbol{r'}) = \left(\boldsymbol{1}+\frac{1}{k^2}\boldsymbol{\nabla}\otimes\boldsymbol{\nabla}\right)\psi(\boldsymbol{r},\boldsymbol{r'}), \tag{2.63}$$

where $\psi(\boldsymbol{r},\boldsymbol{r'})$ is a scalar function that we must determine. To do so, we simply substitute this form of $\boldsymbol{G}(\boldsymbol{r},\boldsymbol{r'})$ into (2.62) to find that $\psi(\boldsymbol{r},\boldsymbol{r'})$ must satisfy the Helmholtz equation with a delta function source

$$\left(\boldsymbol{1}+\frac{1}{k^2}\boldsymbol{\nabla}\otimes\boldsymbol{\nabla}\right)\left[(\boldsymbol{\nabla}^2+k^2)\psi = -\delta(\boldsymbol{r}-\boldsymbol{r'})\right]. \tag{2.64}$$

By comparing the contents of the square brackets with the definition of the Green's function for the Helmholtz equation (2.52) we can realise that

---

[2] Using the vector calculus identity $\boldsymbol{\nabla}\times\boldsymbol{\nabla}\times\boldsymbol{A} = \boldsymbol{\nabla}(\boldsymbol{\nabla}\cdot\boldsymbol{A}) - \boldsymbol{\nabla}^2\boldsymbol{A}$

$\psi(\boldsymbol{r},\boldsymbol{r}')$ is the Green's function we have already determined (2.56). So, the explicit form for the dyadic Green's function is

$$\boldsymbol{G}(\boldsymbol{r},\boldsymbol{r}') = \left(\mathbf{1} + \frac{1}{k^2}\boldsymbol{\nabla}\otimes\boldsymbol{\nabla}\right)\frac{e^{ik|\boldsymbol{r}-\boldsymbol{r}'|}}{4\pi|\boldsymbol{r}-\boldsymbol{r}'|}. \tag{2.65}$$

While it is possible to work entirely in terms of the electromagnetic Green's function $\boldsymbol{G}(\boldsymbol{r},\boldsymbol{r}')$, for certain problems it is convenient to define another Green's function. We call this $\boldsymbol{G}_{EH}(\boldsymbol{r},\boldsymbol{r}')$. The Green's function $\boldsymbol{G}_{EH}(\boldsymbol{r},\boldsymbol{r}')$ is defined as the solution to

$$\boldsymbol{\nabla}\times\boldsymbol{\nabla}\times\boldsymbol{G}_{EH}(\boldsymbol{r},\boldsymbol{r}') - k^2\boldsymbol{G}_{EH}(\boldsymbol{r},\boldsymbol{r}') = \boldsymbol{\nabla}\times\left[\mathbf{1}\delta(\boldsymbol{r}-\boldsymbol{r}')\right]. \tag{2.66}$$

This has the form of, for example, the term involving $\boldsymbol{\nabla}\times\boldsymbol{j}$ in (2.46b). Physically, this term describes the generation of a magnetic field due to an electric current with non-zero vorticity (denoted by the subscripts of $\boldsymbol{G}_{EH}$). To find the form of $\boldsymbol{G}_{EH}(\boldsymbol{r},\boldsymbol{r}')$, we apply the same method as before, finding that

$$\boldsymbol{\nabla}\cdot\boldsymbol{G}_{EH}(\boldsymbol{r},\boldsymbol{r}') = 0. \tag{2.67}$$

When substituted back into (2.66) this gives

$$(\boldsymbol{\nabla}^2 + k^2)\boldsymbol{G}_{EH}(\boldsymbol{r},\boldsymbol{r}') = -\boldsymbol{\nabla}\times\left[\mathbf{1}\delta(\boldsymbol{r},\boldsymbol{r}')\right], \tag{2.68}$$

leading us to seek a solution of the form

$$\boldsymbol{G}_{EH}(\boldsymbol{r},\boldsymbol{r}') = \boldsymbol{\nabla}\times\left[\mathbf{1}\psi(\boldsymbol{r},\boldsymbol{r}')\right], \tag{2.69}$$

where again $\psi(\boldsymbol{r}, \boldsymbol{r'})$ must be found. Once again, we find that $\psi(\boldsymbol{r}, \boldsymbol{r'})$ must be the Green's function for the Helmholtz equation

$$\boldsymbol{G}_{EH}(\boldsymbol{r}, \boldsymbol{r'}) = -\nabla \times \left[\mathbf{1} G_0(\boldsymbol{r}, \boldsymbol{r'})\right]. \tag{2.70}$$

By inspection, we can see that this is equivalent to the curl of the dyadic Green's function. We can therefore define

$$\boldsymbol{G}_{EH}(\boldsymbol{r}, \boldsymbol{r'}) = \boldsymbol{\nabla} \times \boldsymbol{G}(\boldsymbol{r}, \boldsymbol{r'}) = \begin{pmatrix} 0 & \partial/\partial z & -\partial/\partial y \\ -\partial/\partial z & 0 & \partial/\partial x \\ \partial/\partial y & -\partial/\partial x & 0 \end{pmatrix} \frac{e^{ik|\boldsymbol{r}-\boldsymbol{r'}|}}{4\pi|\boldsymbol{r}-\boldsymbol{r'}|} \tag{2.71}$$

Evaluating the derivatives in the expressions for the Green's functions, we have

$$\boldsymbol{G}(\boldsymbol{r}, \boldsymbol{r'}) = \left[\left(1 + \frac{ikR-1}{k^2R^2}\right)\mathbf{1} + \frac{3-3ikR-k^2R^2}{k^2R^2}\frac{\boldsymbol{R}\otimes\boldsymbol{R}}{R^2}\right]\frac{e^{ikR}}{4\pi R}, \tag{2.72a}$$

$$\boldsymbol{G}_{EH}(\boldsymbol{r}, \boldsymbol{r'}) = (\boldsymbol{R} \times \mathbf{1})\frac{k}{R}\left(i - \frac{1}{kR}\right)\frac{e^{ikR}}{4\pi R}, \tag{2.72b}$$

where $\boldsymbol{R} = \boldsymbol{r} - \boldsymbol{r'}$, $R = |\boldsymbol{R}|$ and $k = \omega/c$ is the wavenumber. These Green's functions are plotted in Figure 2.1. In terms of these Green's functions, solutions to the vector wave equations (2.46) for any source distribution can be found. We now derive some general properties of these Green's functions that will become useful in physical contexts. A far more thorough treatment can be found in Tai [24]; here we outline the key results.

In deriving the following properties, it is important to realise that the two Green's functions are tensors with two indices: one represented by the $\boldsymbol{r}$ coordinate and one by the $\boldsymbol{r'}$ coordinate. We would like to derive the effect of interchanging these tensor indices. Immediately, we notice that differentiating the Green's function for the Helmholtz equation (2.56) with

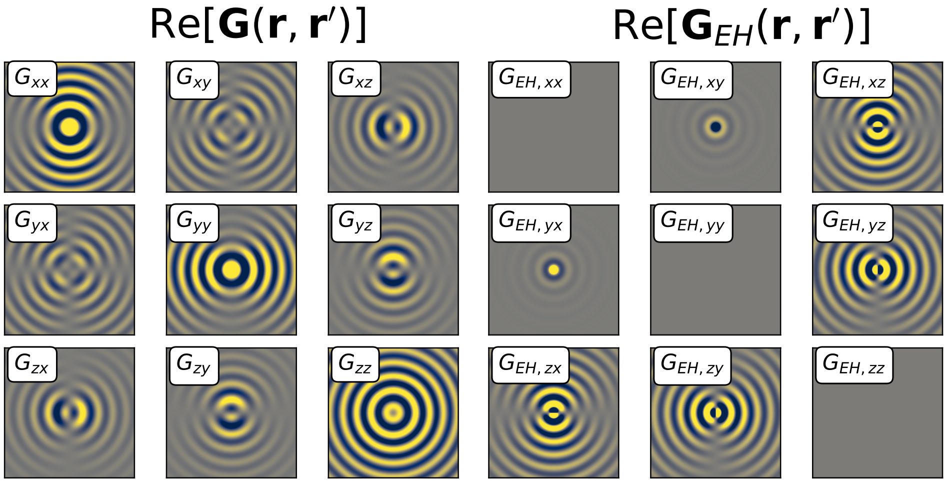

Figure 2.1: Real parts of the electromagnetic Green's functions, shown schematically. The figures are generated for a point source at $\boldsymbol{r}' = (0,0,0)$, observed in the $x-y$ plane at $z=1$. The symmetric nature of $\boldsymbol{G}(\boldsymbol{r},\boldsymbol{r}')$ as well as the anti-symmetric nature of $\boldsymbol{G}_{EH}(\boldsymbol{r},\boldsymbol{r}')$ are evident. The Green's functions can be interpreted as the response of the electromagnetic field to delta-like current excitations.

respect to the primed rather than the unprimed coordinates leads to a minus sign: $\boldsymbol{\nabla}' G_0 = -\boldsymbol{\nabla} G_0$, so $\boldsymbol{\nabla}'\boldsymbol{\nabla}' G_0 = \boldsymbol{\nabla}\boldsymbol{\nabla} G_0$. From this, we see that if we start from the tensor Green's function were $\boldsymbol{r}$ has been re–labelled as $\boldsymbol{r}'$ and vice–versa

$$\boldsymbol{G}(\boldsymbol{r}',\boldsymbol{r}) = \left(\boldsymbol{I} + \frac{1}{k^2}\boldsymbol{\nabla}' \otimes \boldsymbol{\nabla}'\right) G_0(\boldsymbol{r}',\boldsymbol{r}), \tag{2.73}$$

we can then exchange $\boldsymbol{r}$ and $\boldsymbol{r}'$ in the scalar Green's function G_0 and exploit the fact that two derivatives over the primed coordinate are equivalent to two derivatives over the unprimed coordinate. This leads to the observation that the tensor Green's function exhibits reciprocity

$$\boldsymbol{G}(\boldsymbol{r}',\boldsymbol{r}) = \left(\boldsymbol{I} + \frac{1}{k^2}\boldsymbol{\nabla} \otimes \boldsymbol{\nabla}\right) G_0(\boldsymbol{r},\boldsymbol{r}'), \tag{2.74}$$

$$\Rightarrow \boldsymbol{G}(\boldsymbol{r}',\boldsymbol{r}) = \boldsymbol{G}(\boldsymbol{r},\boldsymbol{r}'). \tag{2.75}$$

Now, since in free space $\boldsymbol{G}(\boldsymbol{r}',\boldsymbol{r})$ is also a symmetric dyadic (this is evident from both Figure 2.1 and equation (2.65)), it follows that

$$\begin{aligned}\left[\boldsymbol{G}(\boldsymbol{r}',\boldsymbol{r})\right]^T &= \boldsymbol{G}(\boldsymbol{r}',\boldsymbol{r}),\\ \left[\boldsymbol{G}(\boldsymbol{r}',\boldsymbol{r})\right]^T &= \boldsymbol{G}(\boldsymbol{r},\boldsymbol{r}').\end{aligned} \tag{2.76}$$

Applying the same reasoning to $\boldsymbol{G}_{EH}(\boldsymbol{r}',\boldsymbol{r})$, we see that as before an interchange of the primed and unprimed coordinates leads to a minus sign

$$\begin{aligned}\boldsymbol{G}_{EH}(\boldsymbol{r}',\boldsymbol{r}) &= \boldsymbol{\nabla}' \times \left[\mathbf{1}G_0(\boldsymbol{r}',\boldsymbol{r})\right],\\ &= -\boldsymbol{\nabla} \times \left[\mathbf{1}G_0(\boldsymbol{r},\boldsymbol{r}')\right],\\ \boldsymbol{G}_{EH}(\boldsymbol{r}',\boldsymbol{r}) &= -\boldsymbol{G}_{EH}(\boldsymbol{r},\boldsymbol{r}').\end{aligned} \tag{2.77}$$

Since $\boldsymbol{G}_{EH}(\boldsymbol{r},\boldsymbol{r}')$ is also clearly anti-symmetric (this can be seen in Figure 2.1 or equation 2.71) we can deduce that

$$\begin{aligned}\left[\boldsymbol{G}_{EH}(\boldsymbol{r}',\boldsymbol{r})\right]^T &= -\boldsymbol{G}_{EH}(\boldsymbol{r}',\boldsymbol{r}),\\ \left[\boldsymbol{G}_{EH}(\boldsymbol{r}',\boldsymbol{r})\right]^T &= \boldsymbol{G}_{EH}(\boldsymbol{r},\boldsymbol{r}').\end{aligned} \tag{2.78}$$

These symmetry properties of the Green functions (2.76), (2.78) can be interpreted as representing the important physical phenomena of reciprocity. In the next section, this will be discussed in the context of antenna radiation.

2.4 Dipole Antenna Radiation

As the main topic of this thesis is the manipulation of dipole radiation, in this section we develop a simple model for this radiation. We will use the electromagnetic Green's function derived in the previous section to solve Maxwell's equations for the fields produced by a small oscillating electrical current. This is the simplest model of dipole radiation.

The definition of a dipole is two charges of opposite sign, $\pm q$ separated by a distance d. Taking the oscillation of the dipole to be time harmonic and the charges to be point particles, we can write the charge density of a small dipole located at $\boldsymbol{r}_d$ as

$$\begin{aligned}\rho(\boldsymbol{r},t) &= q\left[\delta\left(\boldsymbol{r}-\boldsymbol{r}_d-\frac{d}{2}\hat{\boldsymbol{z}}\right)-\delta\left(\boldsymbol{r}-\boldsymbol{r}_d+\frac{d}{2}\hat{\boldsymbol{z}}\right)\right]e^{-i\omega t},\\ &= -qdz\partial_z\delta(\boldsymbol{r}-\boldsymbol{r}_d)e^{-i\omega t}.\end{aligned} \tag{2.79}$$

Using the continuity equation (2.42), we can convert this charge density into a current density

$$\boldsymbol{j} = -i\omega\boldsymbol{p}\delta(\boldsymbol{r})e^{-i\omega t}, \tag{2.80}$$

where we have defined the dipole moment as $\boldsymbol{p} = qd\hat{\boldsymbol{n}}$ with $\hat{\boldsymbol{n}}$ being a unit vector pointing along the dipole. By convention, this points from the negative charge to the positive charge. The units of $\boldsymbol{p}$ are therefore charge times distance.

Calculating the electric and magnetic fields due to this current distribution is now straightforward. One simply substitutes the dipole current density (2.80) into the vector wave equations (2.46)

$$\boldsymbol{\nabla}\times\boldsymbol{\nabla}\times\boldsymbol{E}(\boldsymbol{r})-k^2\boldsymbol{E}(\boldsymbol{r}) = \omega^2\mu_0\boldsymbol{p}\delta(\boldsymbol{r}-\boldsymbol{r}_d), \tag{2.81}$$

$$\boldsymbol{\nabla}\times\boldsymbol{\nabla}\times\boldsymbol{H}(\boldsymbol{r})-k^2\boldsymbol{H}(\boldsymbol{r}) = -i\omega\boldsymbol{\nabla}\times\left[\boldsymbol{p}\delta(\boldsymbol{r}-\boldsymbol{r}_d)\right], \tag{2.82}$$

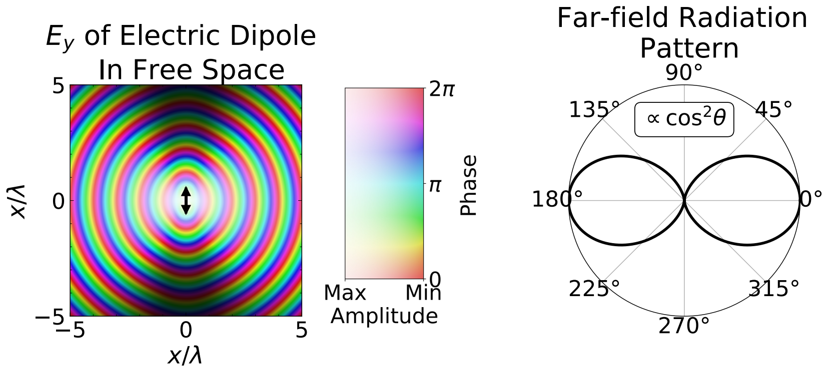

Figure 2.2: Electric field of an electric dipole in free space and the normalised far-field power distribution. Brightness indicates the magnitude of the field, while colour indicates the phase, given by the inset colour wheel. The dipole is indicated by a double-ended black arrow at the origin. Most radiation occurs along the axis perpendicular to the dipole moment.

and using the definitions of the Green's functions (2.59),(2.66) we can write down the solution immediately

$$\boldsymbol{E}(\boldsymbol{r}) = \omega^2 \mu_0 \boldsymbol{G}(\boldsymbol{r}, \boldsymbol{r}_d) \cdot \boldsymbol{p}, \tag{2.83}$$

$$\boldsymbol{H}(\boldsymbol{r}) = -i\omega \boldsymbol{G}_{EH}(\boldsymbol{r}, \boldsymbol{r}_d) \cdot \boldsymbol{p}. \tag{2.84}$$

The electric field of a dipole antenna in free space aligned along the $\hat{\boldsymbol{y}}$ axis is plotted in Figure 2.2, along with its far-field radiation pattern. The above results are valid when the antenna is small compared to the wavelength of light: the delta functions make evaluation of the convolution integrals of the source term and Green's function trivial. One can go beyond the point dipole approximation by employing the method of moments [6], although this is not treated in this thesis.

The symmetry conditions upon the Green's functions derived in the previous section, equations (2.76) and (2.78), are connected to reciprocity [15, 24, 27]. This is the property of the electromagnetic field that means when a source and an observer are interchanged, the field remains the same. This can be understood mathematically as follows. We start by writing Faraday's law (2.41c) and Ampere's law (2.41d) for two different time harmonic currents $\boldsymbol{j}_1$ and $\boldsymbol{j}_1$ as

$$\nabla \times \boldsymbol{E}_1 = i\omega \boldsymbol{B}_1 \qquad \nabla \times \boldsymbol{H}_1 = -i\omega \boldsymbol{D}_1 + \boldsymbol{j}_1, \tag{2.85a}$$

$$\nabla \times \boldsymbol{E}_2 = i\omega \boldsymbol{B}_2 \qquad \nabla \times \boldsymbol{H}_2 = -i\omega \boldsymbol{D}_2 + \boldsymbol{j}_2. \tag{2.85b}$$

Taking the dot product of (2.85a) with $\boldsymbol{H}_2$ and $\boldsymbol{E}_2$ respectively, and of (2.85b) with $-\boldsymbol{H}_1$ and $-\boldsymbol{E}_1$ respectively, adding the results gives

$$\begin{aligned}(\boldsymbol{H}_2 \cdot \nabla \times \boldsymbol{E}_1 - \boldsymbol{E}_1 \cdot \nabla \times \boldsymbol{H}_2) + (\boldsymbol{E}_2 \cdot \nabla \times \boldsymbol{H}_1 - \boldsymbol{H}_1 \cdot \nabla \times \boldsymbol{E}_2)& \\ = i\omega\left(\boldsymbol{B}_1 \cdot \boldsymbol{H}_2 - \boldsymbol{H}_1 \cdot \boldsymbol{B}_2\right) + i\omega\left(\boldsymbol{E}_1 \cdot \boldsymbol{D}_2 - \boldsymbol{D}_1 \cdot \boldsymbol{E}_2\right)& \\ + \left(\boldsymbol{j}_1 \cdot \boldsymbol{E}_2 - \boldsymbol{j}_2 \cdot \boldsymbol{E}_1\right).&\end{aligned} \tag{2.86}$$

The left hand side can be re-written using a vector identity [3]. Assuming that the background medium is linear so that $D_i = \varepsilon_{ik} E_k$ and $B_i = \mu_{ik} H_k$ then we see that $\boldsymbol{B}_1 \cdot \boldsymbol{H}_2 = \mu_{ik} H_{1k} H_{2k} = \boldsymbol{H}_1 \cdot \boldsymbol{B}_2$. The same is true of the second term on the right hand side. This means that we are left with

$$\nabla \cdot (\boldsymbol{E}_1 \times \boldsymbol{H}_2 - \boldsymbol{E}_2 \times \boldsymbol{H}_1) = \boldsymbol{j}_1 \cdot \boldsymbol{E}_2 - \boldsymbol{j}_2 \cdot \boldsymbol{E}_1. \tag{2.87}$$

Integrating this over all space, the divergence theorem can be applied to the left hand side. We are then free to choose a surface at $r \to \infty$ so that the integral vanishes [4] . This leaves us with the reciprocity theorem

$$\int_V \boldsymbol{j}_1(\boldsymbol{r}) \cdot \boldsymbol{E}_2(\boldsymbol{r}) = \int_V \boldsymbol{j}_2(\boldsymbol{r}) \cdot \boldsymbol{E}_1(\boldsymbol{r}). \tag{2.88}$$

---

[3] $\nabla \cdot (\boldsymbol{A} \times \boldsymbol{B}) = (\nabla \times \boldsymbol{A}) \cdot \boldsymbol{B} - (\nabla \times \boldsymbol{B}) \cdot \boldsymbol{A}$

[4] The Sommerfeld radiation condition demands that radiated power must decay to zero at infinite distances from the sources [23]. Since the Poynting vector is $\boldsymbol{S} = \boldsymbol{E} \times \boldsymbol{H}$, we see that the left-hand side of eq. (2.87) must vanish at infinity.

A very similar expression can be derived for magnetic dipoles and it should be noted that this applies to *only* dipole emission. If one has a source with higher multipolar moments, then an alternative form must be derived. This is beyond the scope of this thesis, but is considered in [15].

Before seeing that electromagnetic reciprocity makes the symmetry properties of the Green's functions inevitable, it will be useful to first interpret the reciprocity theorem (2.88). Let us say that our source current is $\boldsymbol{j}_1$, generating an electric field $\boldsymbol{E}_1$, the explicit form the electric field generated is given by equation (2.83). Our detector current is then $\boldsymbol{j}_2$. The reciprocity theorem tells us that interchanging the source and detector currents does not change the system or the fields at all. This is very useful when studying antenna radiation, as it implies that the behavior of an antenna as an emitter is the same as its behavior as a detector. To now show that reciprocity manifests in the symmetry of the electromagnetic Green's functions, we simply note that in equation (2.88), $\boldsymbol{j}_n \sim \delta(\boldsymbol{r}-\boldsymbol{r}_n)\boldsymbol{p}_n$ and $\boldsymbol{E}_n(\boldsymbol{r}) \sim \boldsymbol{G}(\boldsymbol{r},\boldsymbol{r}_n)\cdot\boldsymbol{p}_n$, as we have already shown. Prefactors can be neglected as they are the same on each side of the equality. Substituting these forms for current and electric field, we find that the reciprocity theorem (2.88) leads immediately to the symmetry of the electromagnetic Green's function

$$\boldsymbol{p}_1\cdot\boldsymbol{G}(\boldsymbol{r}_1,\boldsymbol{r}_2)\cdot\boldsymbol{p}_2 = \boldsymbol{p}_2\cdot\boldsymbol{G}(\boldsymbol{r}_2,\boldsymbol{r}_1)\cdot\boldsymbol{p}_1, \tag{2.89}$$

$$= \boldsymbol{p}_1\cdot\boldsymbol{G}^T(\boldsymbol{r}_2,\boldsymbol{r}_1)\cdot\boldsymbol{p}_2, \tag{2.90}$$

$$\boldsymbol{G}(\boldsymbol{r}_1,\boldsymbol{r}_2) = \boldsymbol{G}^T(\boldsymbol{r}_2,\boldsymbol{r}_1). \tag{2.91}$$

Since $\boldsymbol{G}(\boldsymbol{r}_1,\boldsymbol{r}_2)$ is a symmetric tensor this is equivalent to equation (2.76). Similar reasoning [24, 27] leads to the same reciprocity condition for $\boldsymbol{G}_{EH}(\boldsymbol{r},\boldsymbol{r}')$, given in equation (2.78). This also leads to a physical interpretation of the two indices of the electromagnetic Green's functions. The first index is the position of the observer/detector and second index is the position of the source.

We now proceed to introduce a useful tool in the characterisation of dipole radiation: the Polarized Local Density of Optical States (PLDoS). A clear and thorough review of this quantity and its application has been presented by Barnes and Horsley [28], so here we will only outline the key concepts. The time averaged power emission of a point dipole emitter, located at $\boldsymbol{r}_d$, can be evaluated by computing the integral

$$\begin{aligned}\langle P\rangle &= -\frac{1}{2}\mathrm{Re}\left\{\int_V \boldsymbol{j}(\boldsymbol{r})\cdot\boldsymbol{E}(\boldsymbol{r})d\boldsymbol{r}\right\}, &(2.92)\\ &= \omega^3\mu_0\mathrm{Im}\left\{\int_V \delta(\boldsymbol{r}-\boldsymbol{r}_d)\boldsymbol{p}\cdot\boldsymbol{G}(\boldsymbol{r},\boldsymbol{r}_d)\cdot\boldsymbol{p}\right\}, &(2.93)\\ &= \omega^3\mu_0\mathrm{Im}\left\{\boldsymbol{p}\cdot\boldsymbol{G}(\boldsymbol{r}_d,\boldsymbol{r}_d)\cdot\boldsymbol{p}\right\}. &(2.94)\end{aligned}$$

From this, the PLDoS is defined as

$$\rho_p(\hat{\boldsymbol{p}},\boldsymbol{r}_d,\omega) = \frac{2\omega n^2}{\pi c^2}\mathrm{Im}\left\{\hat{\boldsymbol{p}}\cdot\boldsymbol{G}(\boldsymbol{r}_d,\boldsymbol{r}_d)\cdot\hat{\boldsymbol{p}}\right\}, \tag{2.95}$$

where $\hat{\boldsymbol{p}}$ is a unit vector pointing along the dipole moment of the dipole emitter[5] and n is the refractive index of the background medium. This quantity gives the number of electromagnetic modes available per unit volume, for a given dipole polarization $\hat{\boldsymbol{p}}$ and a given frequency, ω. The strength of the coupling of the current in the dipole to the modes of the electromagnetic field is characterised by the PLDoS. The larger the PLDoS, the more electromagnetic modes are available for the emitter to couple into, so more power is radiated. Averaging the PLDoS over polarization and position allows one

---

[5] The vector $\hat{\boldsymbol{p}}$ has been left inside the Im deliberately: for chiral sources $\hat{\boldsymbol{p}}$ is complex.

to obtain a hierarchy of related densities of states, with reducing specificity

$$\rho_l(\boldsymbol{r},\omega) = \sum_{\hat{\boldsymbol{p}}} \rho_p(\hat{\boldsymbol{p}},\boldsymbol{r},\omega), \tag{2.96a}$$

$$\rho(\omega) = \int_V d\boldsymbol{r} \rho_l(\boldsymbol{r},\omega). \tag{2.96b}$$

Here, ρ_l gives the number of available states per unit volume for a given position and frequency, but for any polarization and $\rho(\omega)$ gives the total number of available states at a given frequency, averaged over position.

While the work of this thesis will focus upon the PLDoS in the context of electromagnetism, its applicability goes far beyond this. Indeed, the PLDoS has also been used to characterise thermal and acoustic emission. To emphasize this, the meaning of the PLDoS can be explained schematically with a simple mechanical analogy. Figure 2.3 shows two of the modes supported by a drum (vibrating membrane), denoted by $\omega_{0,1}$ and $\omega_{2,5}$. If the drum is struck at position $\boldsymbol{r}_1$, shown in red, then only the mode shown in pink, $\omega_{0,1}$, is excited. On the other hand, if the drum is struck at position $\boldsymbol{r}_2$, shown in blue, then both modes are excited. This is exactly the information given by the PLDoS: the number of available electromagnetic modes available for a certain location, frequency and polarization. A final interesting analogy to further exhibit the meaning of the PLDoS is revealed by slightly re-writing equation (2.94) by defining $\boldsymbol{p} = p_0\hat{\boldsymbol{p}}$ so that $\langle P\rangle = \omega^2\mu_0 p_0^2 \mathrm{Im}\left\{\hat{\boldsymbol{p}}\cdot\boldsymbol{G}(\boldsymbol{r}_d,\boldsymbol{r}_d)\cdot\hat{\boldsymbol{p}}\right\}$. This has the form $\langle P\rangle \sim A p_0^2\rho_p$, where A is a collection of prefactors. Writing Equation (2.94) in this way highlights the similarity with Fermi's Golden rule [29], which connects decay probabilities to the matrix elements of the initial and final states, as well as the

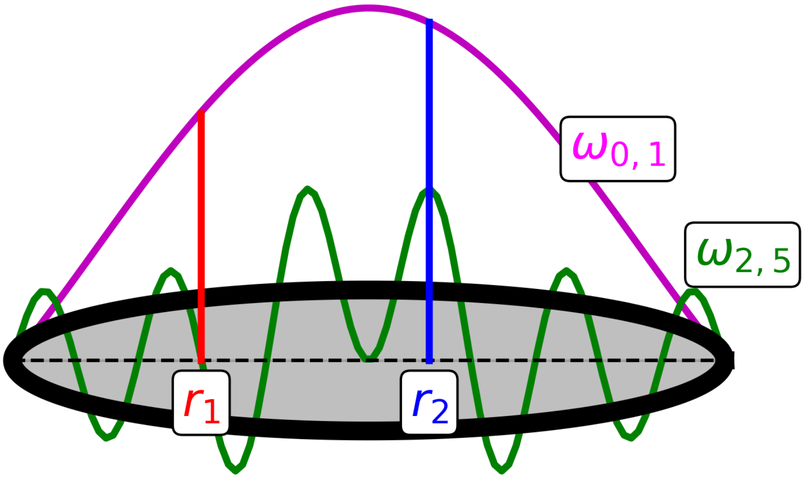

Figure 2.3: A mechanical analogy to explain the meaning of the Polarized Local Density of Optical States. A drum (vibrating circular membrane) supports several modes. Two are indicated by the pink and greens lines: $\omega_{0,1}$ and $\omega_{2,5}$ respectively. If the drum is struck at location r_1, shown in red, then only the mode $\omega_{0,1}$ is excited while if the drum is struck at r_2, shown in blue, then both modes are excited. This information about the local availability of modes is the information that the Polarized Local Density of Optical States gives about the electromagnetic field.

density of states into which the system can decay as

$$\Gamma_{i\to f} = \frac{2\pi}{\hbar}|M_{if}|^2\rho(E_f). \tag{2.97}$$

This has an identical form to $\langle P\rangle \sim Ap_0^2\rho_p$, and the interpretations of the terms are very similar. For a decaying atom, emitted power and decay probability are proportional. The matrix elements $|M_{if}|$ describe the strength of the coupling of the initial and final states, while the dipole moment p_0 describes how strongly the current in the dipole couples to the electric field. In both cases the densities of states give the number of modes (or states) into which the system can decay.

The PLDoS is a very useful tool in characterizing the effect of photonic environments upon antenna radiation. Modifying the environment around an antenna changes the availability of electromagnetic modes; this is clear from the study of waveguides and the Casimir effect [15]. This is shown in Figure 2.4, where the effect of placing a mirror below an emitter is demonstrated [30]. Although useful, PLDoS does not tell us where the radiation goes, only the availability of modes. For instance, it contains no information about which of the modes are occupied and which are empty. This means that while the power emission of a dipole can be well characterized using the PLDoS, the structure of the field cannot.

Now that we have formulated a way to solve Maxwell's equations for point dipole radiation, and seen how this radiation can be characterized we can move towards the main topic of this thesis: the manipulation of radiation properties.

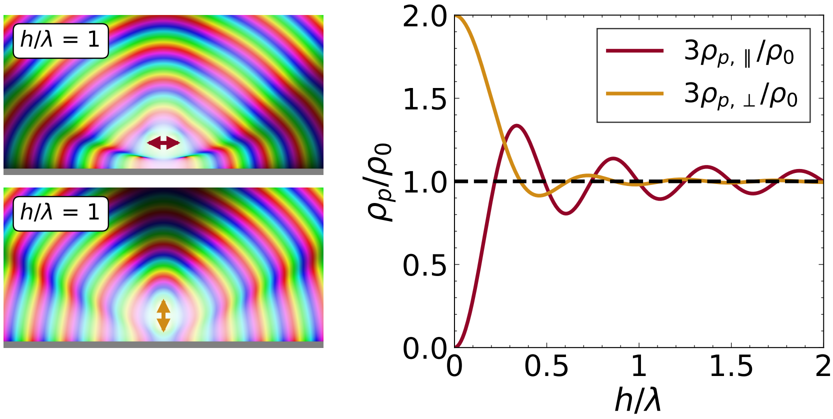

Figure 2.4: The variation of emitted power (or the polarized local density of optical states) of a dipole above a mirror. Two different polarizations of the dipole are shown: parallel (dark red) and perpendicular (orange). The dipole emits radiation with wavelength λ at a height h above the mirror. In both cases, the mirror is shown in grey. The complex electric field is plotted, with brightness indicating magnitude and colour indicating phase. For parallel polarization (red), when the dipole is on the mirror the image source cancels the emitter completely so that $\rho_p/\rho_0 \to 0$. For perpendicular polarization (orange) the image source acts to double the length of dipole leading to a doubling of the power emission when the dipole is on the mirror surface. As the distance of the dipoles above the mirror is increased, the power emission undergoes 'Drexhage oscillations' [30], before tending to free space emission as $h/\lambda \to \infty$.

2.5 Scattering: Mie Theory

In order to make analytic progress on a range of problems relevant to the design of metamaterials, some approximations will be necessary. The first of these has already been mentioned: our antenna can be modelled as a point dipole. This is valid as long as the length of the dipole is significantly smaller than the wavelength of radiation it emits. Now, when considering how we might place some scatterers around an antenna in order to have a desired effect upon the radiation we must make some assumptions about the scatterers themselves. We will assume that the scatterers are small compared to the wavelength of light. This means that we can treat the electric field as being constant over the volume of the scatterer. Also, we will assume that the scatterers are homogeneous, isotropic dielectric spheres. To understand these assumptions and state them more precisely it is necessary to sketch the full theory of electromagnetic scattering from spheres. This is one of a surprisingly small class of electromagnetic scattering problems that can be solved analytically.

The complete theory of electromagnetic scattering from spheres was derived by Mie in 1908 [31] and has since been reviewed in full detail (c.f. [32, 33]). Here, we follow the notation of Bohren and Huffman [32] to sketch the solution, outlining the parts important to the problems we will solve later in the thesis and to make it clear how the assumptions outlined in the paragraph above lead to a way of describing scattering from small spheres. The calculation is conceptually rather simple, however working with vector fields and several families of special functions can become somewhat involved.

Beginning from the vector equations for monochromatic waves in free space

$$(\nabla^2 + k^2)\boldsymbol{E} = 0 \qquad (\nabla^2 + k^2)\boldsymbol{H} = 0, \tag{2.98}$$

$$\nabla \cdot \boldsymbol{E} = 0 \qquad \nabla \cdot \boldsymbol{H} = 0, \tag{2.99}$$

where $\boldsymbol{E}$ and $\boldsymbol{H}$ are not independent, subject to

$$\nabla \times \boldsymbol{E} = i\omega\mu\boldsymbol{H} \qquad \nabla \times \boldsymbol{H} = -i\omega\varepsilon\boldsymbol{E}, \tag{2.100}$$

where $\varepsilon = \varepsilon_0\varepsilon_r$ and $\mu = \mu_0\mu_r$. The aim is to solve these equations under scattering from a sphere of dielectric of arbitrary size. To this end, one may introduce the vector spherical harmonics

$$\boldsymbol{M}_{\substack{e\\o}mn} = \nabla \times (\boldsymbol{r}\psi_{\substack{e\\o}mn}), \qquad \boldsymbol{N}_{\substack{e\\o}mn} = \frac{\nabla \times \boldsymbol{M}_{\substack{e\\o}mn}}{k}, \tag{2.101}$$

where

$$\psi_{emn} = \cos(m\phi)P_n^m(\cos(\theta))z_n(kr), \quad \psi_{omn} = \sin(m\phi)P_n^m(\cos(\theta))z_n(kr). \tag{2.102}$$

The subscript 'e' denotes that the solution is even and thus $\sim \cos m\phi$, 'o' denotes odd solutions that are $\sim \sin m\phi$, $z_n(kr)$ is any of the spherical Bessel functions and P_n^m are the Legendre polynomials. From these definitions, it is possible to show that $\boldsymbol{M}$ satisfies the vector Helmholtz equation as long as ψ is a solution to the scalar Helmholtz equation. One may decompose the scattered, incident and internal fields into these harmonics. For example, the scattered field can be written as

$$\boldsymbol{E}_s = \sum_{n=1}^{\infty} E_n(ia_n \boldsymbol{N}_{e1n}^{(3)} - b_n \boldsymbol{M}_{o1n}^{(3)}), \tag{2.103}$$

$$\boldsymbol{H}_s = \frac{k}{\omega\mu} \sum_{n=1}^{\infty} E_n(ib_n \boldsymbol{N}_{o1n}^{(3)} + a_n \boldsymbol{M}_{e1n}^{(3)}), \tag{2.104}$$

where a_n and b_n are the Mie scattering coefficients, which must be determined. To determine these, one must apply the Maxwell boundary conditions [15, 16] at the interface between the dielectric sphere and free space

$$[\boldsymbol{E}_2(\boldsymbol{r}) - \boldsymbol{E}_1(\boldsymbol{r})] \times \hat{\boldsymbol{n}} = 0, \quad [\boldsymbol{H}_2(\boldsymbol{r}) - \boldsymbol{H}_1(\boldsymbol{r})] \times \hat{\boldsymbol{n}} = 0, \quad \boldsymbol{r} \in \partial S. \tag{2.105}$$

This procedure yields the expressions for the Mie coefficients a_n and b_n, for each of the scattered modes in terms of the Riccati-Bessel functions [34]

$$\Psi_n(z) = zj_n(z) \qquad\qquad \xi_n(z) = zh_n^{(1)}(z), \tag{2.106}$$

as

$$a_n = \frac{m\Psi_n(mx)\Psi_n'(x) - \Psi_n(x)\Psi_n(mx)}{m\Psi_n(mx)\xi_n'(x) - \xi_n(x)\Psi_n'(mx)}, \tag{2.107}$$

$$b_n = \frac{\Psi_n(mx)\Psi_n'(x) - m\Psi_n(x)\Psi_n(mx)}{\Psi_n(mx)\xi_n'(x) - m\xi_n(x)\Psi_n'(mx)}. \tag{2.108}$$

In these expressions $x = ka$ is the size parameter, where a is the radius of the spherical scatterer and $m = n_1/n$ is the refractive index contrast of the scattering material n_1 and the background n. These expressions are plotted as functions of the size parameter in Figure 2.5. The coefficients a_n describe the electric multipole modes, where a_1 is the electric dipole mode, a_2 is the electric quadrupole and so on. The coefficients b_n describe the magnetic multipole modes in the same way. From Figure 2.5, it can be observed that

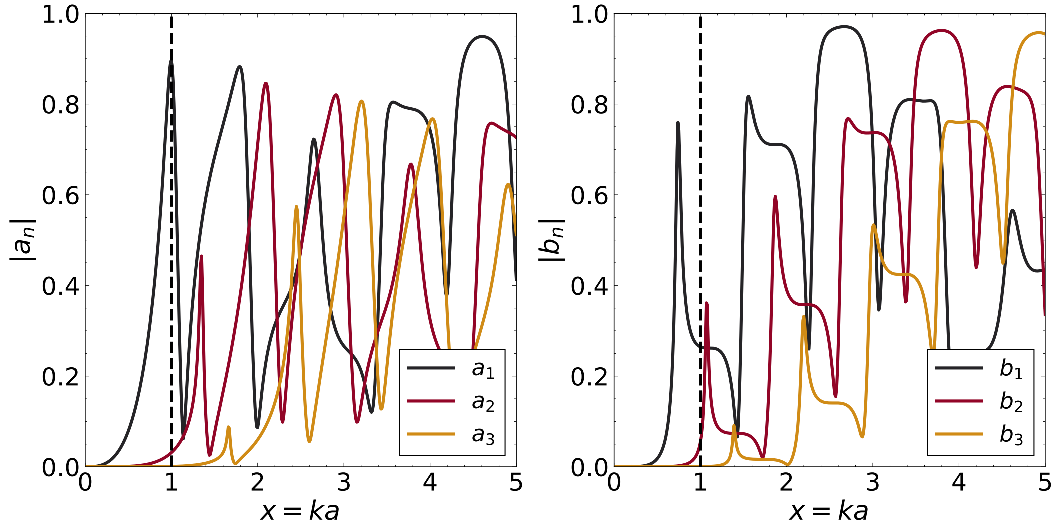

Figure 2.5: The absolute value of the Mie a_n and b_n coefficients, as functions of the size parameter. Background refractive index is free space $n = 1$ and scatterers are taken to be silicon at 550 nm, with $n \sim 4.1 + i0.041$. For $ka \leq 1$ (black dashed line), the dipole modes a_1, b_1 dominate the scattering response.

for $ka \leq 1$ the dipole response dominates. A convenient way to describe scattering from objects is through the extinction coefficient, which characterises the loss of field amplitude due to both absorption and scattering. In terms of the Mie coefficients, the extinction coefficient of a scatterer can be written as [32]

$$\sigma_{\text{ext}} = \frac{2\pi}{k^2} \text{Im} \left\{ \sum_{n=1}^{n=\infty} i(2n+1)(a_n + b_n) \right\}. \tag{2.109}$$

Noting this will be useful when connecting Mie's theory of scattering to an alternative method to describing scattering. For small scatterers, we need only consider the dipole a_1 and b_1 terms in the field expansions (2.103, 2.104). As these are the dipole terms, this assumption is called the dipole approximation.

In the dipole approximation, one can connect the electric and magnetic dipole moments, $\boldsymbol{p}$ and $\boldsymbol{m}$ respectively, acquired by a scatterer in response to applied fields as

$$\begin{pmatrix} \boldsymbol{p} \\ \boldsymbol{m} \end{pmatrix} = \begin{pmatrix} \boldsymbol{\alpha}_E & 0 \\ 0 & \boldsymbol{\alpha}_H \end{pmatrix} \begin{pmatrix} \boldsymbol{E} \\ \boldsymbol{H} \end{pmatrix}, \tag{2.110}$$

where $\boldsymbol{\alpha}_E$ is the electric polarizability tensor and $\boldsymbol{\alpha}_H$ is the magnetic polarizability tensor [35]. This picture is commonly used for analyzing the scattering from systems of several small dielectric scatterers (i.e. [36, 37]). Generally, one way to interpret the components α_{ij} is how strongly the scatterer polarizes along the direction i in response to an applied field in the j direction [6] . The coefficients, $\boldsymbol{\alpha}$ depend only upon the geometry of the scatterer, and for isotropic scatterers have no off-diagonal elements. This is the way of describing scattering that will be used throughout this thesis, as the macroscopic polarization of the scatterer is related to the dipole moment as $\boldsymbol{P} = \boldsymbol{p}\delta(\boldsymbol{r} - \boldsymbol{r'})$ [7] for a point scatterer. This immediately gives an expression for the source terms in the vector wave equation (2.46) in terms of the properties of the scatterers. One way to calculate the elements of the polarizability tensor for isotropic spherical scatterers is using the Mie coefficients.

The optical theorem [10, 38] connects the extinction cross-section of a scatterer with polarizability α as

$$\sigma_{ext} = k\text{Im}\left\{\alpha\right\}. \tag{2.111}$$

Simply comparing this with the expression one can derive from Mie theory for the extinction cross-section (2.109) one can write down the expressions for the electric and magnetic polarizabilities in terms of the Mie coefficients

---

[6] There is analogy between this and the stress tensor, for example [9]

[7] We have already stated that $\boldsymbol{P}$ should have units of dipole moment per volume. As the Dirac delta is a distribution with units of inverse volume, this expression clearly has the correct units.

as

$$\alpha_E = i\frac{6\pi}{k^3}a_1, \qquad \alpha_H = i\frac{6\pi}{k^3}b_1. \tag{2.112}$$

For isotropic scatterers, the polarizability tensor is diagonal, thus

$$\boldsymbol{\alpha}_E = \begin{pmatrix} 1 & 0 & 0 \\ 0 & 1 & 0 \\ 0 & 0 & 1 \end{pmatrix} \alpha_E, \qquad \boldsymbol{\alpha}_H = \begin{pmatrix} 1 & 0 & 0 \\ 0 & 1 & 0 \\ 0 & 0 & 1 \end{pmatrix} \alpha_H. \tag{2.113}$$

It is possible to generalize these expressions to materials which are not spherical (and therefore not isotropic) or exhibit bi-anisotropy [35]. It should also be noted that evaluation of a_n and b_n is not trivial. Numerical evaluation of the derivatives of the Bessel functions can be delicate, however excellent libraries exist in many programming languages. In this work, we make use of the python library 'PyMieScatt' to evaluate a_n and b_n [39].

2.6 The Discrete Dipole Approximation

To address the problem of designing metasurfaces, we begin by considering a metasurface composed of sub–wavelength discrete elements that support electric and magnetic dipole resonances. Maxwell's equations for a fixed frequency $\omega = ck$, where k is the wave–number, can then be written as

$$\begin{pmatrix} \nabla\times\nabla\times & 0 \\ 0 & \nabla\times\nabla\times \end{pmatrix} \begin{pmatrix} \boldsymbol{E} \\ \boldsymbol{H} \end{pmatrix} - k^2 \begin{pmatrix} \boldsymbol{E} \\ \boldsymbol{H} \end{pmatrix} = \begin{pmatrix} \boldsymbol{E}_s \\ \boldsymbol{H}_s \end{pmatrix} + \begin{pmatrix} \omega^2\mu_0 & i\omega\mu_0\nabla\times \\ -i\omega\nabla\times & k^2 \end{pmatrix} \begin{pmatrix} \boldsymbol{P} \\ \boldsymbol{M} \end{pmatrix}. \tag{2.114}$$

In this expression $\boldsymbol{E}_s$ and $\boldsymbol{H}_s$ represent the source fields, for example the field due to an emitter or a background plane wave. The source field is a solution of (2.114) with the right hand side equal to zero. The total electric field is then $\boldsymbol{E}_{\text{tot}} = \boldsymbol{E}_s + \boldsymbol{E}$. The properties of the metasurface are encoded in the polarisation density $\boldsymbol{P}$ and the magnetisation density $\boldsymbol{M}$. This is generally a difficult equation to solve, however the assumption that the scatterers are sub–wavelength $rk \leq 1$ means that the elements of the metasurface can be modelled as point–like. In general, the polarisation and magnetisation densities contain all multipole moments [40–42], however if we assume that only the dipole terms are present, then we can write the polarisation and magnetisation densities as

$$\boldsymbol{P} = \sum_n \boldsymbol{\alpha}_E \boldsymbol{E}(\boldsymbol{r}_n)\delta(\boldsymbol{r} - \boldsymbol{r}_n), \qquad \boldsymbol{M} = \sum_n \boldsymbol{\alpha}_H \boldsymbol{H}(\boldsymbol{r}_n)\delta(\boldsymbol{r} - \boldsymbol{r}_n), \tag{2.115}$$

where $\boldsymbol{E}(\boldsymbol{r}_n)$, $\boldsymbol{H}(\boldsymbol{r}_n)$ are the fields applied to the scatterer. This reduces the source terms in Maxwell's equations (2.114) to a summation of delta functions. As discussed in Section 2.3, equations of this form can be solved with the dyadic Greens function and its curl [24, 26]

$$\boldsymbol{G}(\boldsymbol{r}, \boldsymbol{r}') = \left[1 + \frac{1}{k^2}\nabla \otimes \nabla\right] \frac{e^{ik|\boldsymbol{r}-\boldsymbol{r}'|}}{4\pi|\boldsymbol{r} - \boldsymbol{r}'|}, \quad \boldsymbol{G}_{EH}(\boldsymbol{r}, \boldsymbol{r}') = \nabla \times \boldsymbol{G}(\boldsymbol{r}, \boldsymbol{r}'). \tag{2.116}$$

The solution to Maxwell's equations (2.114) with source terms given by (2.115) can then be written as

$$\begin{pmatrix} \boldsymbol{E}(\boldsymbol{r}) \\ \boldsymbol{H}(\boldsymbol{r}) \end{pmatrix} = \begin{pmatrix} \boldsymbol{E}_s(\boldsymbol{r}) \\ \boldsymbol{H}_s(\boldsymbol{r}) \end{pmatrix} + \sum_{n=1}^{n=N} \begin{pmatrix} \xi^2 \boldsymbol{G}(\boldsymbol{r},\boldsymbol{r}_n)\boldsymbol{\alpha}_E & i\xi \boldsymbol{G}_{EH}(\boldsymbol{r},\boldsymbol{r}_n)\boldsymbol{\alpha}_H \\ -i\xi \boldsymbol{G}_{EH}(\boldsymbol{r},\boldsymbol{r}_n)\boldsymbol{\alpha}_E & \xi^2 \boldsymbol{G}(\boldsymbol{r},\boldsymbol{r}_n)\boldsymbol{\alpha}_H \end{pmatrix} \begin{pmatrix} \boldsymbol{E}(\boldsymbol{r}_n) \\ \boldsymbol{H}(\boldsymbol{r}_n) \end{pmatrix} \tag{2.117}$$

where we have chosen units such that the impedance of free space is $\eta_0 = 1$ and work in terms of a dimensionless wavenumber $\xi = ka$, where a is a length scale we are free to choose. This solution is not yet closed, since the fields applied to each scatterer $(\boldsymbol{E}(\boldsymbol{r}_n), \boldsymbol{H}(\boldsymbol{r}_n))$ must be determined. To do this, the position of each scatterer $\boldsymbol{r}_m$ is substituted into (2.117) giving a system of simultaneous equations that can be solved for the fields applied to the scatterer. This procedure yields the following matrix equations connecting the source and total fields at each scatterer

$$\boldsymbol{R}_{nm} \begin{pmatrix} \boldsymbol{E}(\boldsymbol{r}_m) \\ \boldsymbol{H}(\boldsymbol{r}_m) \end{pmatrix} = \begin{pmatrix} \boldsymbol{E}_s(\boldsymbol{r}_n) \\ \boldsymbol{H}_s(\boldsymbol{r}_n) \end{pmatrix}, \tag{2.118}$$

where

$$\boldsymbol{R}_{nm} = \begin{pmatrix} \mathbf{1}\delta_{nm} - \xi^2 \boldsymbol{G}(\boldsymbol{r}_n,\boldsymbol{r}_m)\boldsymbol{\alpha}_E & -i\xi \boldsymbol{G}_{EH}(\boldsymbol{r}_n,\boldsymbol{r}_m)\boldsymbol{\alpha}_H \\ i\xi \boldsymbol{G}_{EH}(\boldsymbol{r}_n,\boldsymbol{r}_m)\boldsymbol{\alpha}_E & \mathbf{1}\delta_{nm} - \xi^2 \boldsymbol{G}(\boldsymbol{r}_n,\boldsymbol{r}_m)\boldsymbol{\alpha}_H \end{pmatrix}. \tag{2.119}$$

The self–consistency condition (2.118) can be solved with standard matrix methods [43] for the fields applied to each scatterer, which includes the source field as well as contributions from all of the other scatterers. Once these fields are found, the solution to Maxwell's equations given by (2.117) is fully specified.

The particular physical system we consider in many numerical examples is an arrangement of silicon spheres of radius 65 nm at a wavelength of 550 nm giving $kr \approx 0.75$. For this simple choice of metasurface element, the electric and magnetic polarisability tensors can be constructed from the Mie coefficients [31, 44] a_1 and b_1 as

$$\boldsymbol{\alpha}_E = \mathbf{1} i \frac{6\pi}{k^3} a_1 \qquad\qquad \boldsymbol{\alpha}_H = \mathbf{1} i \frac{6\pi}{k^3} b_1 \tag{2.120}$$

where $\mathbf{1} = \mathrm{diag}(1, 1, 1)$ is the unit tensor. Polarisability tensors for more complicated scatterers can be extracted from numerical modelling [38, 45], making this method applicable to a very wide range of systems. This is discussed in full detail in Appendix B. The key benefit is that an expensive full–wave simulation is required for only a single scatterer, not the entire metasurface.

2.6.1 Simple Example: Discrete Dipole Approximation For a Scalar Field

Many of the key results of the thesis will involve designing disordered structures consisting of discrete dipolar scatterers. As leveraging the numerical and conceptual benefits of the discrete dipole approximation will be crucial for what follows, in this section we will consider some of the implementation details of the multiple scattering problem. To retain conceptual simplicity, we will consider a scalar field obeying the Helmholtz equation. This could be a single component of the electromagnetic field, or an acoustic pressure wave. The wave field will be modified by several identical point scatterers located at $\{\boldsymbol{r}_n\}$, that scatter with strength $\alpha\phi(\boldsymbol{r}_n)$. Solving the multiple–scattering problem means finding the applied fields, which include both the source field as well as the effect of all of the other scatterers. The wave–equation is therefore

$$(\nabla^2 + k^2)\phi(\boldsymbol{r}) = j(\boldsymbol{r}) + \sum_n \alpha\delta(\boldsymbol{r} - \boldsymbol{r}_n)\phi(\boldsymbol{r}), \tag{2.121}$$

where k is the wave–number and $j(\boldsymbol{r})$ is the source current generating the incident field $\phi_i(\boldsymbol{r})$. This can immediately be solved using the Green's function, which for the 2D Helmholtz equation is the Hankel function of the first kind

$$G(\boldsymbol{r}, \boldsymbol{r'}) = \frac{1}{4i} H_0^{(1)}(k|\boldsymbol{r} - \boldsymbol{r'}|). \tag{2.122}$$

The solution to (2.121) is therefore

$$\phi(\boldsymbol{r}) = \phi_i(\boldsymbol{r}) + \sum_n \alpha G(\boldsymbol{r}, \boldsymbol{r}_n)\phi(\boldsymbol{r}_n). \tag{2.123}$$

To find the fields applied to each scatterer $\phi(\boldsymbol{r}_n)$, we form the linear system

$$\boldsymbol{R}\boldsymbol{\phi_n} = \phi_i, \tag{2.124}$$

where

$$\phi_n = \phi(\boldsymbol{r}_n) \qquad\qquad \phi_i = \phi_i(\boldsymbol{r}_n) \tag{2.125}$$

and the interaction matrix is

$$R_{nm} = \begin{cases} 1 & n = m, \\ -\alpha G(\boldsymbol{r}_n, \boldsymbol{r}_m) & n \neq m. \end{cases} \tag{2.126}$$

The code used to setup and solve this problem is given in Appendix A.

An example of using this formalism to find the fields of a collection of scatterers is shown in Figure 2.6. An incident plane wave, Figure 2.6 a), is incident upon 5 randomly positioned scatterers with polarisability $\alpha = 1 + i3$. The resulting scattering matrix is shown in Figure 2.6 b), with the scatterer positions and fields shown in Figure 2.6 c), d). The interaction matrix has 1 along the diagonal, then off–diagonal elements that reflect the strength of the coupling between the various scatterers. For example, just reading off elements of the interaction matrix tells us that the scatterer labelled 0 interacts more strongly with scatterer 4 than scatterer 1. This is because scatterer

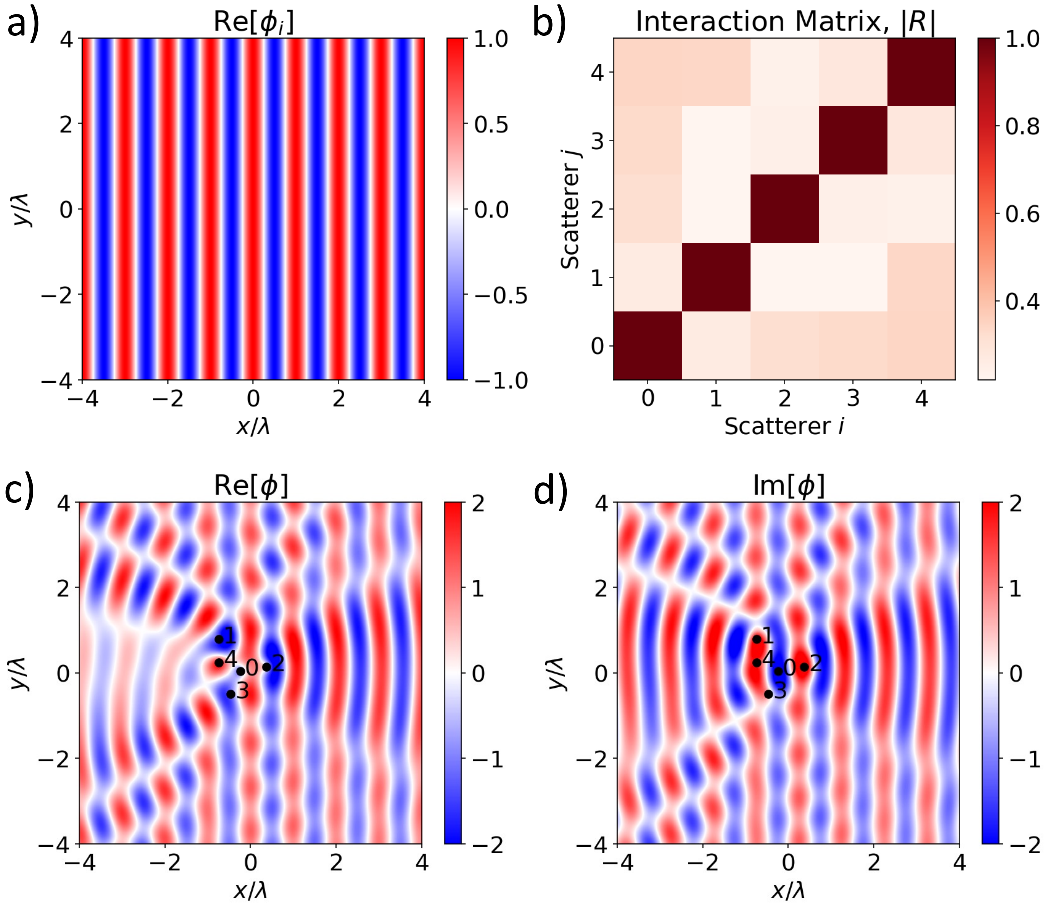

Figure 2.6: An example of solving the multiple scattering problem in 2D. a) An incident plane wave is disturbed by a random distribution of scatterers. To find the total (incident+scattered) field at each scatterer, we must form the interaction matrix shown in b). Solving the linear system (2.124) for the fields at the scatterers allows us to find all of the fields of the system, shown in c) and d).

4 is closer: the Greens function in 2D decays as $1/\sqrt{r}$ (in 1D there is no decay and in 3D there is a $1/r$ decay), meaning that one would expect scatterers closer together to couple more strongly.

With the model set up, we can ask "when are multiple scattering effects important?". To answer this, we consider two examples using just two scatterers. Firstly, we keep the polarisability of the scatterers fixed and vary the separation between them. Secondly, we keep the separation between the scatterers fixed and vary the polarisability. In each case, we compare full multiple scattering to the Born approximation [10, 46]. This is typically the weak scattering approximation, were no multiple scattering is present meaning that the total field is just

$$\phi_{\text{Born}}(\boldsymbol{r}) = \phi_i(\boldsymbol{r}) + \sum_n \alpha G(\boldsymbol{r}, \boldsymbol{r}_n)\phi_i(\boldsymbol{r}_n). \tag{2.127}$$

In this approximation it is unnecessary to perform a matrix inversion to find the field applied to each scatterer, as it is just equal to the incident field. The result of keeping the polarisability fixed to be $\alpha = 1 + i3$ and changing the separation is shown in Figure 2.7. Beginning with two scatterers separated by λ, Figure 2.7 a) and b) shows the field both with and without multiple scattering, and the error between the two characterised as

$$\text{Field Error} = |\phi(\boldsymbol{r}) - \phi_{\text{Born}}(\boldsymbol{r})|, \tag{2.128}$$

shown in Figure 2.7 c). Some error is observed, although it is reasonably small. The far–field radiation pattern from the multiple scattering approach and the Born approximation are compared in Figure 2.7 d), showing almost no difference. Performing the same comparison with two scatterers separated by $\lambda/3$ in Figure 2.7 e)-h), much larger field errors are observed, as

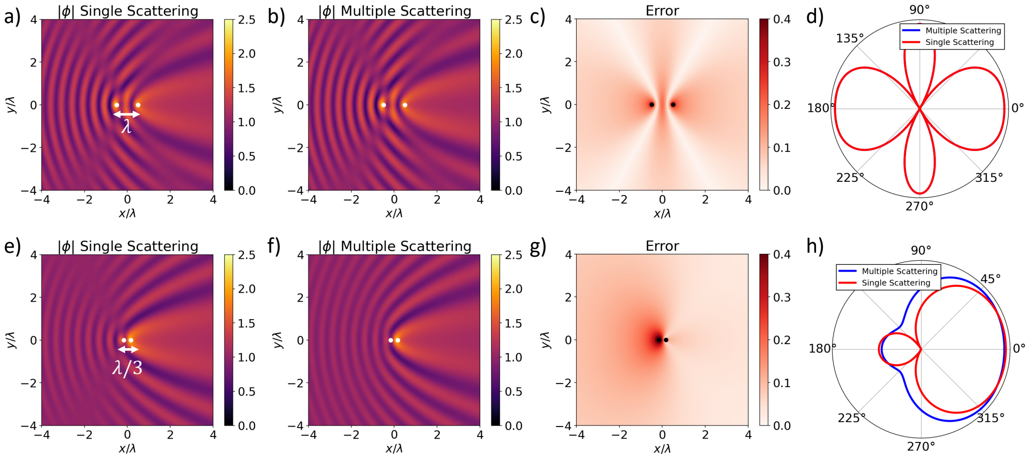

Figure 2.7: The effect of scatterer separation on the strength of multiple scattering effects. Considering two scatterers with polarisability $\alpha = 1 + i3$ separated by a)-d) λ and e)-h) $\lambda/3$, we investigate when multiple scattering effects become important to consider. The fields of the system under plane wave incidence are evaluated using a), e) the Born approximation and b), f) the full multiple–scattering formulation. The differences between the two approaches are shown in c) and g), with the radiation patterns compared in d) and h).

well as large differences in the radiation patterns. The dependence of the radiation pattern error, defined as the residual sum of square differences between the multiple scattering and single scattering solutions, on both separation and polarisability is shown in Figure 2.8. The effect of the spacing, shown in Figure 2.8 a) shows that for small scatterer spacing multiple scattering effects are important, diminishing for larger separations. Oscillations in the error are due to the multiple interaction term $\sim H_0^{(1)}(k|\boldsymbol{r}_1 - \boldsymbol{r}_2|)$ vanishing for certain separation values, related to the positions of the Bessel function zeros. Figure 2.8 b) shows the effect of keeping the scatterers separated by λ, but varying the real part of the polarisability. For weak scattering, or small polarisabilities, the Born approximation is valid. However, when scatterers are close together and/or the polarisability is large, multiple scattering effects must be taken into account.

These findings can be summarised as: multiple scattering effects become crucial when scatterers are close together and/or when scattering is very

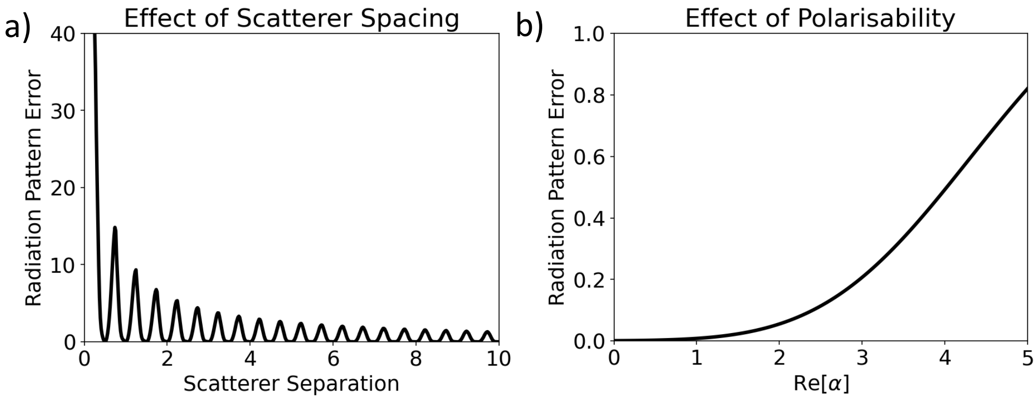

Figure 2.8: Effect of separation and polarisability on the radiation pattern of a two scatterer system. a) shows the sum of squares error between the radiation pattern, evaluated using the Born approximation and multiple scattering, as a function of scatterer separation for a fixed polarisability. Oscillations occur due to interference effects, although the an overall trend that multiple scattering is more important at smaller separations can be observed. b) shows the effect of changing the real part of the polarisability upon the error in radiation pattern, for a fixed scatterer separation of λ. As $Re[\alpha]$ gets larger, so does the error, leading to the conclusion that multiple scattering is important when scattering is strong.

strong, as is the case on resonance. Many electromagnetic systems rely on resonances to produce strong effects, and it is typical to have many such elements in close proximity to each other. Indeed, the field of metamaterials relies on closely packed resonant elements to achieve a wealth of wave manipulations.

2.7 Metamaterials

Most materials derive their electromagnetic properties from their chemical composition, understood through the Ewald–Oseen extinction theorem [46]. However, metamaterials derive their electromagnetic properties from their *structure*, rather than chemistry. Although a lively area of current research, many of the principles behind metamaterials have been known for a long time.

The Lucurgus cup, originating in 4th century Rome, shows a different colour depending on whether or not it is illuminated [47]. This effect is achieved without using dyes, but instead relies on the plasmon resonances of small gold and silver particles suspended in the cup. When excited at optical wavelengths small particulates of gold and silver, of diameter ~ 70 nm, support surface plasmon–polaritons changing how the material appears.

Over the last hundred years or so, ideas of metamaterials were developed greatly while also inspiring (or maybe taking inspiration from) science fiction. In his 1965 novel "Dune", Frank Herbert describes 'meta–glass', noting its use a selective radiation filter [48]. By the 1970s, science fiction had become science fact as many people had something that might fit the description of 'meta–glass' in their homes: the door of a microwave oven. Thin surfaces of periodically pattered metal, frequency selective surfaces [49], can be designed to reflect, transmit or absorb radiation based upon its frequency. Frequency selective surfaces (FSSs) have been extensively applied to microwave and radio wave problems, providing the framework for modern metasurfaces. The field of frequency selective surfaces has given birth to the active research topic of metasurfaces, 2D metamaterials. Extending the idea of FSSs by grading their elements in space, many novel reflection and transmission properties can be realised. For example, one can break Snell's law [50, 51], make metasurface holograms [52], create very thin optical components [53], perform polarisation conversion, perform image processing [54] and solve integral equations [55].

Another concept that appeared in science fiction long before it appeared in science is that of invisibility. H. G. Wells's "The Invisible Man" [56], published in 1897, describes a man who changes his refractive index such that he is invisible. Using the fact that Maxwell's equations in a material with

$\varepsilon = \mu$ take the same form as they do in a gravitational field, researchers developed the theory of transformation optics. This enabled both the design [57, 58] and experimental realisation [59] of an invisibility cloak, in the early 2000s. Grading refractive index in space has also enabled devices that sort incident fields by their wavelength [60] or perform mode conversions [61].

Great experimental progress has been made on the fabrication of metamaterials with complicated features and theoretical advances have produced many interesting analytic refractive index profiles for many different purposes. However, the problem of designing metamaterials that can easily be fabricated for specific purposes remains challenging, attracting much attention over the last two decades.

2.8 Inverse Design of Metamaterials

If metamaterials are to be used to solve the current problems in, for example, communications and stealth, techniques must be developed to design a metamaterial for a specific application. In this section, we outline some methods that have been developed to design metamaterials for a range of applications.

Exploiting the fact that Maxwell's equations retain their form under certain coordinate transformation, with different material properties, transformation optics emerged in the early 2000s with the seminal papers of Pendry [58] and Leonhardt [57] as a fully analytic method for designing metamaterials. Leonhardt used this idea to design an isotropic cloak in two dimensions using conformal mappings while Pendry designed a 3D cloak using anisotropic materials. While this is a very elegant design tool, the material properties required to deliver transformation optics can be hard to realise experimentally. The technique also lacks flexibility, as it relies on the ability to find a coordinate transform that solves a given problem. Although recent progress has seen made on this [62], it is in general an open challenge.

In addition to analytic techniques, many efficient numerical methods have been developed to solve the inverse design problem algorithmically. To do this, one must typically define a *figure of merit*: a physical quantity that one wishes to maximise or minimise. For lensing this could be the modulus of the field at a particular point, while for mode conversion it will be the overlap between the existing and desired mode. Different numerical techniques are used to address different design problems, which we now review.

Firstly, the Gerchberg–Saxton algorithm [63] has been used extensively [52, 53] to design metasurface holograms. This technique converts a desired image into a phase map that must be imparted onto a plane wave. To implement the required phase offset in a metamaterial, one typically uses as 'meta–atoms' elements that can be geometrically tuned. For example, one can change the angle or size of a resonator to change the phase of transmission. Each pixel of the phase map then corresponds to a single meta–atom with the correct geometric properties. This design technique is extremely efficient and produces devices that can be easily fabricated, but is limited to planar metamaterials that impart a phase offset. It also typically requires many full–wave simulations to build up the meta–atom library. Recently, the Gerchberg–Saxton algorithm was extended to include the ability to manipulate the amplitude [64] of the wave however arbitrary control of the electromagnetic field is still not possible within this framework.

Recently, it has become standard to design metamaterials with specific spectral properties using machine learning [65–67]. Designing a particular reflection coefficient as a function of wavelength, for example, can be done by generating many different meta–atom geometries, which are typically arrayed to form a metasurface. This is the training data. For each of the generated meta–atoms, the reflection coefficient as a function of wavelength is calculated using a full–wave solver (i.e. COMSOL [68]). With the test input and output, a neural network can be trained to map between the two. One can then use the neural network backwards, to predict a structure that will produce a certain spectral response. This technique works well, however generating the training data is time consuming and the method overall provides little physical insight. Indeed, machine learning tools are being applied to the output of machine learning tools to try to understand how they work [69].

Genetic algorithms have found application in designing materials that manipulate the field of small emitters [70] as well as a so called 'evolved' antenna [71]. One can construct a metamaterial from a collection of small discrete elements that can be arranged anywhere in space around an emitter. Genetic algorithms work by randomly generating many different configurations of these elements, selecting the best and then combining good solutions (crossover) and adding random changes (mutation). Currently, genetic algorithms are the only way to distribute large numbers of discrete scattering elements in space around an emitter to engineer its properties, and to date only various emission efficiencies have been tuned [70]. However, they suffer from similar drawbacks to machine learning techniques. The results of genetic algorithms are difficult to interpret physically, as they are based upon random number generators. Also, if the fields are found using full–wave simulations then the procedure can be inefficient as genetic algorithms typically require very many figure of merit calculations. It should also be noted they do not guarantee a global minima, as is shown in [70].

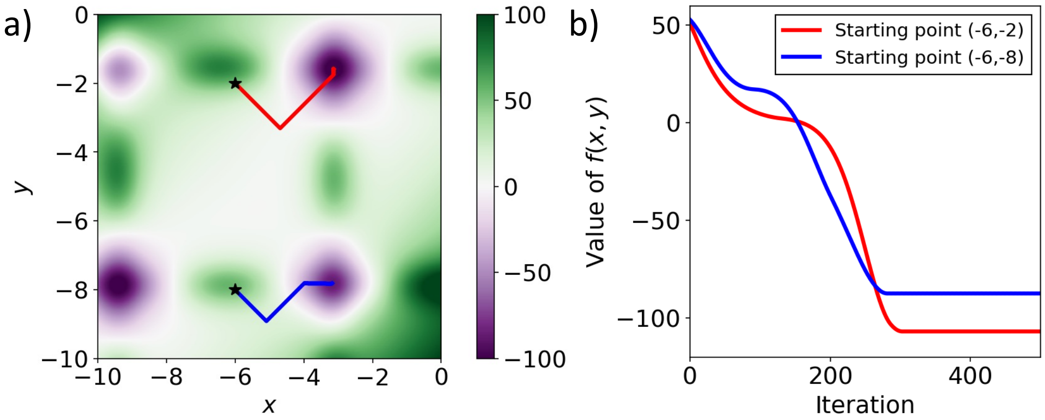

Figure 2.9: An example of gradient descent optimisation. The objective is to minimise the function given by Eq. 2.130. Starting from two different points, shown as black stars, steps of size $\gamma = 0.01$ in the direction of $-\nabla f(x, y)$ are taken iteratively, until a minima is reached. a) shows the function space and the two paths, b) shows the progression of the value of $f(x, y)$ along the two paths. The blue path ends in a local minima at $f(-3.17, -7.81) = -87.29$ while the red path finds the global minima at $f(-3.13, -1.58) = -105.76$.

Perhaps the simplest method of inverse design, understood as maximising or minimising a function, is gradient descent [72]. For some differentiable multi–variate function $f(\boldsymbol{x})$, the direction in which it decreases most quickly is given by $-\nabla f$, where the derivatives of the gradient are with respect to the variables $\boldsymbol{x}$. To find the set of variables $\{\boldsymbol{x}_{\text{min}}\}$ for which $f(\boldsymbol{x})$ is minimal, one can choose some starting point in parameter space $\boldsymbol{x}_{\text{initial}}$, evaluate the gradient of $f(\boldsymbol{x})$, take a small step in that direction according to

$$\boldsymbol{x}^{i+1} = \boldsymbol{x}^{i} + \gamma \nabla f(\boldsymbol{x}^{i}), \tag{2.129}$$

where i denotes the iteration number and γ is the step size. The procedure can then be repeated until a minimum is reached and the gradient vanishes. It should be noted that, depending upon the landscape of the function $f(\boldsymbol{x})$, this process may not find a global minimum and instead get stuck in a local one. The local minimum found could also depend upon the starting parameters one chooses. To illustrate this we consider an example: we seek to minimise Mishra's Bird function [73], given by

$$f(x,y) = \sin(y)e^{(1-\cos x)^2} + \cos(x)e^{(1-\sin y)^2} + (x-y)^2. \tag{2.130}$$

This is commonly used optimisation test function and exhibits several local minima as well as a global minimum at $f(-3.13, -1.58) = -105.76$. In Figure 2.9, the progress of gradient descent at two different starting points, shown as black stars, is illustrated. In each case, Eq. 2.129 is used to find a path to the minima, however the blue path finds a local minima at $f(-3.17, -7.81) = -87.29$ while the red path finds the global minima. This limitation of the gradient descent method should be kept in mind when it is applied to the inverse design of photonic systems.

While simple, applying this gradient descent optimisation to photonics problems can be challenging. To see why, say we would like to design a dielectric structure that increases the emitted power of a small dipole emitter with polarisation $\boldsymbol{p}$ at location $\boldsymbol{r}_\star$. Introduced in Section 2.4, the emitted power of a small dipole emitter can be characterised by the PlDoS. To increase the emitter power we seek to maximise the PLDoS at the location of the emitter. The figure of merit for this problem is therefore $\mathcal{F} \propto \text{Im}\left[\boldsymbol{p}^* \cdot \boldsymbol{E}(\boldsymbol{r}_\star)\right]$. Our aim is to maximise this function with respect to the design parameters, which here is the permittivity distribution. The figure of merit here is a functional $\mathcal{F}[\varepsilon(\boldsymbol{r})]$, a function of a function, nevertheless we can write the gradient descent for this problem as

$$\varepsilon(\boldsymbol{r})^{i+1} = \varepsilon(\boldsymbol{r})^{i} + \gamma \nabla_\varepsilon \mathcal{F}, \tag{2.131}$$

where ∇_ε denotes the gradient of the figure of merit with respect to the permittivity distribution. Evaluation of this gradient is challenging. To attempt to make progress, one could apply the chain rule, giving

$$\nabla_\varepsilon \mathcal{F} = \frac{\partial \mathcal{F}}{\partial \boldsymbol{E}} \frac{\partial \boldsymbol{E}}{\partial \varepsilon}. \tag{2.132}$$

The first of these derivatives $\partial \mathcal{F} / \partial \boldsymbol{E}$ can be easily evaluated, but evaluation of the second is not trivial. There are two strategies one could use to find the second derivative. Firstly, one could break up the dielectric structure into 'pixels', change the permittivity at each pixel and see how the field changes. This would allow one to build up the derivative bit–by–bit, however each pixel would require a full–wave simulation making this approach very slow. A far more efficient method, requiring only two simulations to find the entire gradient has been developed in recent years: the adjoint method.

2.9 The Adjoint Method

Originally developed in structural mechanics [74], the adjoint method has been widely applied to design a huge range of photonic devices in recent years [75, 76]. The adjoint method provides a very efficient way of deciding where to change a dielectric structure in order to increase a given figure of merit. In this section we derive the key results of the adjoint method, remembering that our overall aim is to find the derivative $\frac{\partial \mathcal{F}}{\partial \varepsilon}$.

We begin from the vector Helmholtz equation for the electric field $\boldsymbol{E}(\boldsymbol{r})$ and a permittivity distribution $\varepsilon(\boldsymbol{r})$, that was derived in Section (2.2) (c.f. (2.46)),

$$\nabla \times \nabla \times \boldsymbol{E}(\boldsymbol{r}) - k_0^2 \varepsilon(\boldsymbol{r}) \boldsymbol{E}(\boldsymbol{r}) = 0. \tag{2.133}$$

Next, we apply perturbation theory to see how a small change in the permittivity $\varepsilon(\boldsymbol{r}) \to \varepsilon(\boldsymbol{r}) + \delta\varepsilon(\boldsymbol{r})$ changes the field $\boldsymbol{E}(\boldsymbol{r}) \to \boldsymbol{E}(\boldsymbol{r}) + \delta\boldsymbol{E}(\boldsymbol{r})$. We find, to leading order, that the change the the field obeys the same vector

Helmholtz equation as before, with the addition of a source term produced by the change in permittivity

$$\nabla \times \nabla \times \delta \boldsymbol{E}(\boldsymbol{r}) - k_0^2 \varepsilon(\boldsymbol{r}) \delta \boldsymbol{E}(\boldsymbol{r}) = k_0^2 \delta\varepsilon(\boldsymbol{r}) \boldsymbol{E}(\boldsymbol{r}). \tag{2.134}$$

As discussed in Section 2.3, inhomogeneous linear differential equations can be solved using the Green's function, converting the differential equation into an equivalent integral one

$$\delta \boldsymbol{E}(\boldsymbol{r}) = k_0^2 \int d^3\boldsymbol{r'} \boldsymbol{G}(\boldsymbol{r}, \boldsymbol{r'}) \delta\varepsilon(\boldsymbol{r'}) \boldsymbol{E}(\boldsymbol{r'}). \tag{2.135}$$

Progress can be made by choosing a form for the perturbation to the permittivity: we change the permittivity at only a single point $\boldsymbol{r}_i$ by an amount $\Delta\varepsilon$. This means we can write $\delta\varepsilon(\boldsymbol{r}) = \Delta\varepsilon\delta(\boldsymbol{r} - \boldsymbol{r}_i)$, making the evaluation of the integral trivial

$$\delta \boldsymbol{E}(\boldsymbol{r}) = k_0^2 \boldsymbol{G}(\boldsymbol{r}, \boldsymbol{r}_i) \Delta\varepsilon \boldsymbol{E}(\boldsymbol{r}_i). \tag{2.136}$$

Now returning to the physical problem of interest, enhancing the emitted power of a dipole located at $\boldsymbol{r}_\star$, we can write down our figure of merit as

$$\mathcal{F} = \frac{\omega}{2} \mathrm{Im}\left[\boldsymbol{p}^* \cdot \boldsymbol{E}(\boldsymbol{r}_\star)\right]. \tag{2.137}$$

Expanding the figure of merit to first order under small changes in the field $\boldsymbol{E}(\boldsymbol{r}) \rightarrow \boldsymbol{E}(\boldsymbol{r}) + \delta \boldsymbol{E}(\boldsymbol{r})$ and substituting in the connection between a change in the field and a change in permittivity (2.136), we find

$$\delta\mathcal{F} = \frac{\omega}{2} \mathrm{Im}\left[\boldsymbol{p}^* \cdot \delta\boldsymbol{E}(\boldsymbol{r}_\star)\right], \tag{2.138}$$

$$= \frac{\omega k_0^2 \Delta\varepsilon}{2} \mathrm{Im}\left[\boldsymbol{p}^* \cdot \boldsymbol{G}(\boldsymbol{r}_\star, \boldsymbol{r}_i) \cdot \boldsymbol{E}(\boldsymbol{r_i})\right]. \tag{2.139}$$

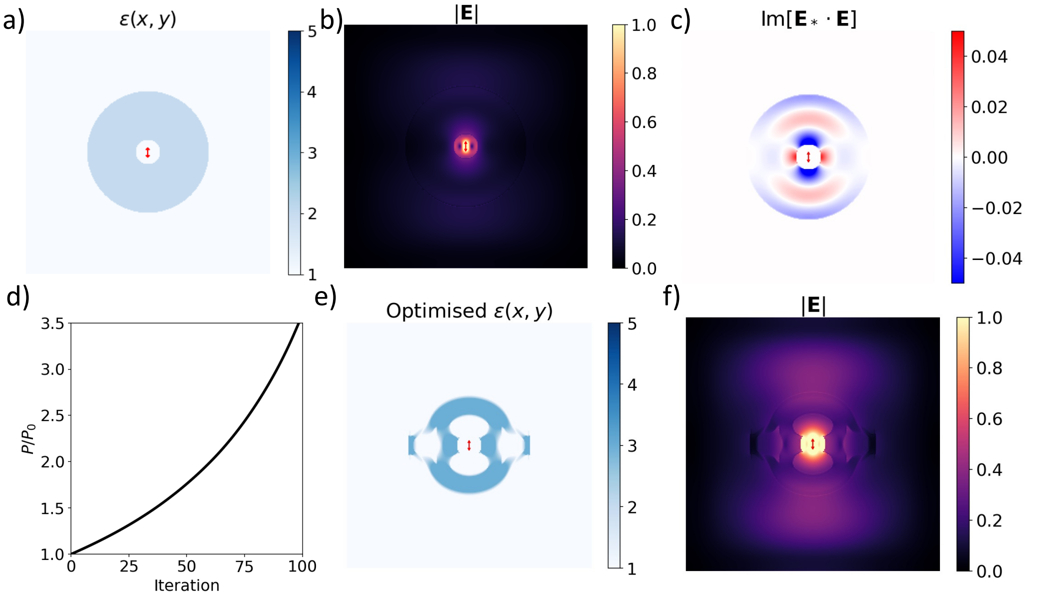

Figure 2.10: An example application of the adjoint method to increase the emitted power of a small dipole. Beginning from the permittivity structure shown in a), the dipole emitter produces the field shown in b). Iteratively applying 2.143 to update the permittivity, with the first step shown in c), the power enhancement is shown in d). The resulting graded index structure is shown in e), along with the optimised field in f). Comparing the initial field b) with the final field f), a clear enhancement at the emitter can be observed.

It does not look like we have made much progress, as we must still evaluate the Green's function for every single $\boldsymbol{r}_i$ we would like to change. However, we can use the reciprocity of the Green's function $\boldsymbol{G}(\boldsymbol{r}_i, \boldsymbol{r}_j) = \boldsymbol{G}^T(\boldsymbol{r}_j, \boldsymbol{r}_i)$ to re–write the expression as

$$\delta\mathcal{F} = \frac{\omega k_0^2 \Delta\varepsilon}{2} \mathrm{Im}\left[\boldsymbol{E}(\boldsymbol{r_i}) \cdot \boldsymbol{G}(\boldsymbol{r}_i, \boldsymbol{r}_\star) \cdot \boldsymbol{p}^*\right], \tag{2.140}$$

$$= \Delta\varepsilon \mathrm{Im}\left[\boldsymbol{E}(\boldsymbol{r}_i) \cdot \boldsymbol{E}_{\text{adjoint}}(\boldsymbol{r_i})\right], \tag{2.141}$$

where we have defined the adjoint field as

$$\boldsymbol{E}_{\text{adjoint}}(\boldsymbol{r}) = \frac{\omega k_0^2}{2} \boldsymbol{G}(\boldsymbol{r}, \boldsymbol{r}_\star) \cdot \boldsymbol{p}^*. \tag{2.142}$$

This can be interpreted as the field due to a point source at $\boldsymbol{r}_\star$ with a polarisation conjugate to that of the source we are trying to enhance. The adjoint field can therefore be interpreted as the 'time reverse' of the emitted field. Dividing through 2.141 by $\Delta\varepsilon$, we find that the gradient of our figure of merit is nothing but the dot product of the forwards field and the adjoint field

$$\frac{\partial \mathcal{F}}{\partial \varepsilon} = \operatorname{Im}\left[\boldsymbol{E}(\boldsymbol{r}_i) \cdot \boldsymbol{E}_{\text{adjoint}}(\boldsymbol{r_i})\right], \tag{2.143}$$

evaluated at the positions we would like to change the permittivity at $\boldsymbol{r}_i$. This means that to find how to change the permittivity, instead of needing many simulations we require only two. One to find the forwards field, with a source of polarisation $\boldsymbol{p}$ and another to find the adjoint field with a source of polarisation $\boldsymbol{p}^*$. The gradient can then easily be formed, and gradient descent optimisation used. An example of applying the adjoint method to enhance the power emission of a small dipole is shown in Figure 2.10. We begin from an initial permittivity distribution, shown in Figure 2.10 a), where the emitter is polarised in the y direction and denoted by a red arrow at the origin. The initial forwards field is shown in Figure 2.10 b). One can calculate both the forwards and adjoint fields, then form the dot product that gives the gradient, shown in Figure 2.10 c). In the regions shown in red, the permittivity should be increased and in the regions shown in blue the permittivity should be decreased, in order to increase the figure of merit. Repeating this, the emitted power of the dipole is increased as can be seen in Figure 2.10 d). The final permittivity distribution is shown in Figure 2.10 e) along with the field in Figure 2.10 f). The enhancement of the emission is evident in the field.

2.10 Summary & Conclusions

In this introductory chapter, we have given an overview of the wave equation in physics, noting that wave phenomena are ubiquitous and that the theoretical framework describing very different physical situations is remarkably similar. Throughout the thesis, analogies between wave behaviour in acoustics, electromagnetism and quantum mechanics will be exploited to develop new techniques and draw comparisons between seeming unrelated physical phenomena. Particular focus was placed on electromagnetic waves, their emergence from Maxwell's equations and certain interesting limiting cases such as the Helmholtz equation if we choose to work at a single frequency. Next, the solution of inhomogeneous equations using the Green's function approach was developed and the Green's functions for the vector and scalar Helmholtz equation were derived. We noted in particular the expression of reciprocity in the Green's function. Swapping the position of a source and detector of waves does not change the fields, thus the Green's function is symmetric under such an interchange. Having developed a way of solving the wave equations for a given source, we proceeded to derive a simple model for the kind of source we will be interested in: a dipole. This is a common, simple, model for an antenna. By analogy with Fermi's Golden Rule, we also introduced the concept of the Local Density of Optical States (LDOS) to describe the number of states into which an emitter may radiate. As noted by Purcell, one way to modify the LDOS is to change the photonic environment. Much of the work in this thesis will involve placing scatterers around emitters to change the radiation properties. We therefore introduced Mie theory as a model for the properties of a single isotropic spherical scatterers. Considering then the effect of many such scatterers, the discrete (or coupled) dipole approximation is formulated. After a brief review of metamaterials and methods for designing them for specific applications, we introduced the adjoint method. The adjoint method is a flexible and efficient tool for designing metamaterials.

Chapter 3

Designing Uni–functional Devices

> *"Talking nonsense is the sole privilege mankind possesses over the other organisms. It's by talking nonsense that one gets to the truth! I talk nonsense, therefore I'm human"* – Fyodor Dostoevsky, 'Crime and Punishment'

The results of this chapter have been published in:

- J. R. Capers, S. J. Boyes, A. P. Hibbins and S. A. R. Horsely "Designing the collective non-local responses of metasurfaces" Commn. Phys. **4** 209 (2021)
- J. R. Capers, S. J. Boyes, A. P. Hibbins and S. A. R. Horsely "Designing metasurfaces to manipulate antenna radiation" Proc. SPIE 12130, Metamaterials XIII, 121300H (2022)

Designer manipulation of electromagnetic radiation is key a to huge range of emerging and developing technologies, from sensing and optical computing, to next–generation communications and stealth. One way to manipulate radiation is using materials structured at the sub–wavelength scale: metamaterials. However, metamaterials typically have a very large number of geometric parameters that can be tuned to achieve a given scattering effect, making the modelling and design process extremely challenging. Existing design paradigms rely on either limiting approximations or numerically demanding full–wave simulations. In this chapter, we derive a semi–analytic method for designing metamaterials built from sub–wavelength magnetodielectric scattering elements. We then apply this to a large range of problems, manipulating the near and far–field of small sources as well as shaping plane waves.

3.1 Introduction

The emission properties of electromagnetic sources are not determined only by the geometry of the source. The photonic environment also affects how an emitter radiates. This effect was first noted by Purcell [77], who realised that atoms in a cavity had a different decay rate to atoms in free space. By changing the availability of the modes the emitter can radiate into, the cavity modifies the rate of emission. Drexhage observed that the decay rate of an emitter above a mirror varies based on the distance between the emitter and the mirror [30]. He understood this as a simple interference effect. The reflections from the mirror have a certain phase when they reach the source, which depends upon the distance from the emitter and the mirror. When the reflections are in phase with the emitter, the decay rate is enhanced and when the reflections are out of phase emission is suppressed.

This interference effect is not unique to electromagnetic waves, having also been observed for acoustic sources [78].

Modifiying the environment around an emitter to change its properties was known in the antenna community long before Purcell's observations. Invented in 1926, the Yagi–Uda antenna [79] exemplifies this idea. Constructed from a small number of metal rods, the Yagi–Uda antenna has a single driven element with a longer reflector behind it and several rods of decreasing length in front of the emitter. The result of this arrangement is a very strongly directional beam in the forwards direction. Since it is exceptionally simple to make, the Yagi–Uda antenna is widely used for broadcast TV reception. In recent years, with advances in nano–fabrication technology, common microwave or radio–wave antenna designs have been constructed on the nanoscale to manipulate light. Both the bow–tie antenna [80] and the Yagi–Uda antenna [81] have been realised on the nanoscale. Such plasmonic nanoantennas [82] hold great promise for on–chip optical technology and optical computing.

Greater control over the emission properties can be obtained through greater control over the structure surrounding the emitter using, for example, metamaterials. For a periodic metasurface made of electromagnetic dipoles, the usual Drexhage oscillations can be observed but are phase shifted [83]. Many features of emitters can be engineered by embedding them within [84] or on top of [85] metamaterials. For example, in a band gap, there is no radiation at all [84]. Switching mechanisms can be employed to adjust the coupling between emitters and the Mie resonances of the metasurfaces to allow tuneable emitter properties [85], useful in a wide range of optical devices. These approaches allow for directional and spectral shaping of light emitters [86, 87].

To achieve more exotic near–field manipulations, more complex geometries must be placed around the emitter. Design of such geometries is often facilitated using the adjoint method [75, 76], to find geometries of dielectric that manipulate the source radiation in several interesting ways. For example, cavities that enhance the efficiency of small emitters by factors of thousands have been designed at optical wavelengths [88] and realised at microwave frequencies [89]. Many quantum properties of emitters can also be engineered [90], such as coherence [91] and energy transfer [92], by structuring dielectric around an emitter. As well as the adjoint method, genetic algorithms are a well used design paradigm. For example they have been used to design disordered materials that enhance the decay rate of emitters [70, 93, 94], and to design highly directional antennas [95, 96].

While great progress has been made on the design of metamaterials that manipulate source properties, existing methods still have several drawbacks. Graded structures designed by algorithms can have very fine features [88] that can be difficult to manufacture. Genetic algorithms are very effective at designing disordered metasurfaces, however their operation and resulting structures can be difficult to interpret [69] using physical intuition.

In this chapter, we present a method for placing small dipolar scatterers around an emitter to change how it radiates. This is shown schematically in Figure 3.1. Considering an emitter near an array of initially periodic scatterers, Figure 3.1 a), we aim to find how to change the locations of the scatters to manipulate the radiation in a particular way. The scatterers themselves are taken to be silicon spheres of radius 65 nm so that their scattering properties, Figure 3.1 b), can be extracted analytically. Beginning with the prototypical problem of enhancing power emission, we derive both a design methodology, shown schematically in Figure 3.1, along with an accompanying interpretation framework. We then consider engineering both the

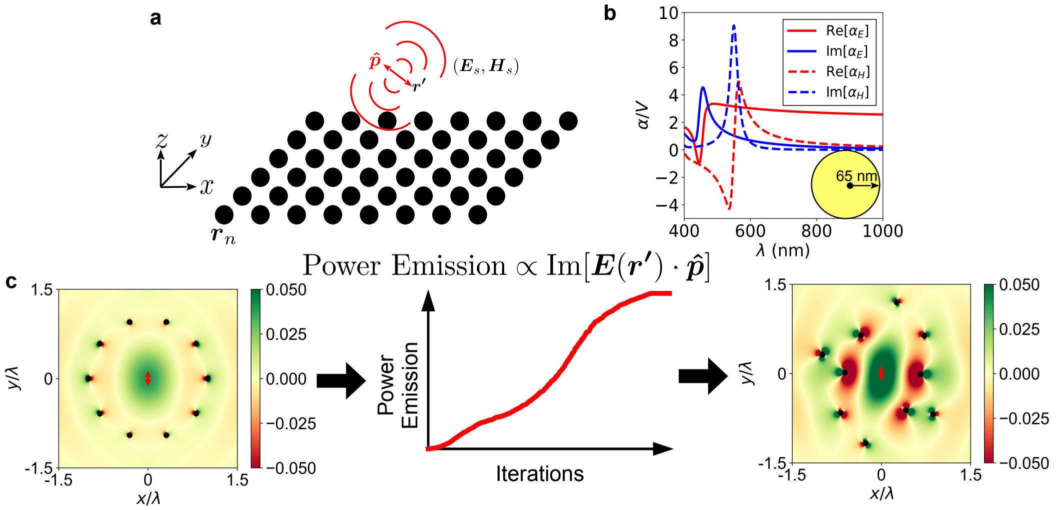

Figure 3.1: The system considered in our numerical examples. A schematic of the problem is shown in (a). A dipole emitter with polarization $\hat{\mathbf{p}}$ is located at $\mathbf{r}'$. This generates source fields ($\mathbf{E}_s$, $\mathbf{H}_s$), which are scattered by N silicon spheres located at $\mathbf{r}_n$. The scatters have optical properties shown in (b). The scatterers are assumed to be isotropic silicon spheres of radius 65 nm, with the frequency dispersion of the polarizability extracted from experimental data [97]. A simple example of the design process is shown in (c). The power emission of the emitter (red arrow) is enhanced by iteratively moving passive scatterers (black dots) from their initial positions (left) to some optimised positions (right). Colour plots show $\mathrm{Im}[\mathbf{E}(\mathbf{r}) \cdot \hat{\mathbf{p}}]$, which when evaluated at the emitter's location is proportional to power emission. The enhancement of this quantity at the location of the emitter is evident.

near and far–field of the emitter, manipulating directivity, coupling to other nearby emitters and lensing.

3.2 Designing Scattering Properties

The aim is to now find a way to choose the distribution of the scatterers $\{\boldsymbol{r}_n\}$ to achieve a desired wave–scattering effect. We consider choosing an initial distribution of scattterers and ask "how should the positions be changed to increase a particular figure of merit?". To answer this, we employ perturbation theory to find how a small change in the position of a scatterer changes the fields. This approach is similar to that of the adjoint method, described in Section 2.9, where the effect of a small change in the spatial distribution of the permittivity was considered. We work in our dimensionless system of units and begin by considering only the electric field and scatterers with $\boldsymbol{\alpha}_H = \mathbf{0}$. As in Section 2.6, we consider the governing equation

$$\nabla \times \nabla \times \boldsymbol{E} - \xi^2 \boldsymbol{E} = \boldsymbol{j}_{\text{source}}(\boldsymbol{r}) + \xi^2 \boldsymbol{P}(\boldsymbol{r}), \tag{3.1}$$

with the polarisation density given by

$$\boldsymbol{P}(\boldsymbol{r}) = \sum_n \boldsymbol{\alpha}_E \boldsymbol{E}(\boldsymbol{r}) \delta(\boldsymbol{r} - \boldsymbol{r}_n), \tag{3.2}$$

where $\boldsymbol{r}_n$ is the location of the scatterer, and $\boldsymbol{j}_{\text{source}}$ is the source current, which generates the incident electric field. Writing the dipole moment as

$$\boldsymbol{p} = \int dV \boldsymbol{P}(\boldsymbol{r}), \tag{3.3}$$

our aim is to find how the polarisation density is changed when a scatterer is moved by a small amount. To this end, we proceed in a similar fashion to how one derives the multipole expansion [41, 42], Taylor expanding the delta function as

$$\delta(\boldsymbol{r} - \boldsymbol{r}_n - \delta\boldsymbol{r}_n) = \delta(\boldsymbol{r} - \boldsymbol{r}_n) + (\delta\boldsymbol{r}_n \cdot \nabla)\delta(\boldsymbol{r} - \boldsymbol{r}_n) + \dots . \tag{3.4}$$

The polarisation density now has two parts: the first is the usual polarisation density of a dipole scatterer; the second is the small change in the polarisation density due to a small change in the scatterer location

$$\boldsymbol{p} = \sum_n \left[\int dV \boldsymbol{\alpha}_E \boldsymbol{E}(\boldsymbol{r}) \delta(\boldsymbol{r} - \boldsymbol{r}_n) + \int dV (\delta\boldsymbol{r}_n \cdot \nabla \delta(\boldsymbol{r} - \boldsymbol{r}_n)) \boldsymbol{\alpha}_E \boldsymbol{E}(\boldsymbol{r}) \right] . \tag{3.5}$$

To deal with the second term, we note it is a property of the derivative of the Dirac–delta function [98] that

$$f(x)\frac{\mathrm{d}}{\mathrm{d}x}\delta(x-x') = -\delta(x-x')\frac{\mathrm{d}f(x)}{\mathrm{d}x}, \tag{3.6}$$

which can be proven by integrating by parts as

$$\int_{-\infty}^{\infty}\phi(x)\frac{\mathrm{d}}{\mathrm{d}x}\delta(x-x')dx = \phi(x)\delta(x-x')|_{-\infty}^{\infty} - \int_{-\infty}^{\infty}\delta(x-x')\frac{\mathrm{d}}{\mathrm{d}x}\phi(x)dx. \tag{3.7}$$

The boundary term is zero as the delta function evaluated anywhere other than $x = x'$ is zero, leaving only the final term. Utilising this, the polarisation density is therefore

$$\boldsymbol{P}(\boldsymbol{r}) = \sum_n \delta(\boldsymbol{r}-\boldsymbol{r}_n)\left[\boldsymbol{\alpha}_E\boldsymbol{E}(\boldsymbol{r}) - \boldsymbol{\alpha}_E\delta\boldsymbol{r}_n\cdot\nabla\boldsymbol{E}(\boldsymbol{r})\right]. \tag{3.8}$$

Provided we choose $\delta\boldsymbol{r}_n \ll 0$, we can treat the change in polarisation density perturbatively. Inserting this into (3.1), then solving by integrating the source terms against the Dyadic Green's function, we find that

$$\boldsymbol{E}(\boldsymbol{r}) + \delta\boldsymbol{E}(\boldsymbol{r}) = \sum_n \xi^2\left[\boldsymbol{G}(\boldsymbol{r},\boldsymbol{r}_n)\boldsymbol{\alpha}_E\boldsymbol{E}(\boldsymbol{r}_n) - \boldsymbol{G}(\boldsymbol{r},\boldsymbol{r}_n)\boldsymbol{\alpha}_E\delta\boldsymbol{r}_n\cdot\nabla\boldsymbol{E}(\boldsymbol{r}_{\boldsymbol{n}})\right]. \tag{3.9}$$

So, the change in the electric field due to the change in the location of a scatterer is

$$\delta\boldsymbol{E}(\boldsymbol{r}) = -\xi^2\boldsymbol{G}(\boldsymbol{r},\boldsymbol{r}_n)\boldsymbol{\alpha}_E\delta\boldsymbol{r}_n\cdot\nabla\boldsymbol{E}(\boldsymbol{r}_{\boldsymbol{n}}). \tag{3.10}$$

Considering next a scatterer with $\boldsymbol{\alpha}_E = \boldsymbol{0}$ and $\boldsymbol{\alpha}_H \neq \boldsymbol{0}$, the governing equation is

$$\nabla\times\nabla\times\boldsymbol{E}(\boldsymbol{r}) - k^2\boldsymbol{E}(\boldsymbol{r}) = i\xi\sum_n\nabla\times\boldsymbol{M}, \tag{3.11}$$

and the magnetisation density is

$$\boldsymbol{M}(\boldsymbol{r}) = \sum_n \boldsymbol{\alpha}_H \boldsymbol{H}(\boldsymbol{r})\delta(\boldsymbol{r} - \boldsymbol{r}_n). \tag{3.12}$$

As with the electric case, we consider the total magnetic dipole moment and expand the delta functions to find

$$\boldsymbol{m} = \sum_n \left[\int dV \boldsymbol{\alpha}_H \boldsymbol{H}(\boldsymbol{r})\delta(\boldsymbol{r} - \boldsymbol{r}_n) + \int dV (\delta\boldsymbol{r}_n \cdot \nabla\delta(\boldsymbol{r} - \boldsymbol{r}_n))\boldsymbol{\alpha}_H \boldsymbol{H}(\boldsymbol{r}) \right]. \tag{3.13}$$

Integrating by parts to move the derivative from the delta function onto the field, we obtain the modified magnetisation density

$$\boldsymbol{M}(\boldsymbol{r}) = \sum_n \delta(\boldsymbol{r} - \boldsymbol{r}_n) \left[\boldsymbol{\alpha}_H \boldsymbol{H}(\boldsymbol{r}) - \boldsymbol{\alpha}_H \delta\boldsymbol{r}_n \cdot \nabla \boldsymbol{H}(\boldsymbol{r}) \right]. \tag{3.14}$$

Using this as a source term in (3.1), we can find the change in the field due to a small change in the position of a *magnetic* scatterer to be

$$\delta\boldsymbol{E}(\boldsymbol{r}) = -\sum_n i\xi \boldsymbol{G}_{EH}(\boldsymbol{r}, \boldsymbol{r}_n)\boldsymbol{\alpha}_H \delta\boldsymbol{r}_n \cdot \nabla \boldsymbol{H}(\boldsymbol{r}_n). \tag{3.15}$$

Therefore, the total change in the electric field due to a magnetodielectric scatterer being moved by a small amount is just the sum of (3.10) and (3.15), giving

$$\delta\boldsymbol{E}(\boldsymbol{r}) = -\sum_n \left[\xi^2 \boldsymbol{G}(\boldsymbol{r}, \boldsymbol{r}_n)\boldsymbol{\alpha}_E \delta\boldsymbol{r}_n \cdot \nabla \boldsymbol{E}(\boldsymbol{r}_n) + i\xi \boldsymbol{G}_{EH}(\boldsymbol{r}, \boldsymbol{r}_n)\boldsymbol{\alpha}_H \delta\boldsymbol{r}_n \cdot \nabla \boldsymbol{H}(\boldsymbol{r}_n) \right]. \tag{3.16}$$

Using identical arguments, the change in the magnetic field is

$$\delta\boldsymbol{H}(\boldsymbol{r}) = -\sum_n \left[\xi^2 \boldsymbol{G}(\boldsymbol{r}, \boldsymbol{r}_n)\boldsymbol{\alpha}_H \delta\boldsymbol{r}_n \cdot \nabla \boldsymbol{H}(\boldsymbol{r}_n) - i\xi \boldsymbol{G}_{EH}(\boldsymbol{r}, \boldsymbol{r}_n)\boldsymbol{\alpha}_E \delta\boldsymbol{r}_n \cdot \nabla \boldsymbol{E}(\boldsymbol{r}_n) \right]. \tag{3.17}$$

These expressions can be used to find how changing the location of a scatterer affects a given figure of merit, which is a functional of the field configurations $\mathcal{F}[\boldsymbol{E}, \boldsymbol{H}]$. Moving one scatterer produces a small change in the fields at every point in space, which in turn changes the figure of merit by a small amount

$$\mathcal{F}[\boldsymbol{E}, \boldsymbol{H}] \rightarrow \mathcal{F}[\boldsymbol{E}, \boldsymbol{H}] + \delta\mathcal{F}[\boldsymbol{E}, \boldsymbol{H}, \delta\boldsymbol{E}, \delta\boldsymbol{H}]. \tag{3.18}$$

The change in the figure of merit is linear in $\delta\boldsymbol{r}_n$, so once we have derived the analytic expression for $\delta\mathcal{F}$ it can be used to find an expression for a $\delta\boldsymbol{r}_n$ that leads to an increase in the figure of merit. Expressions for $\delta\mathcal{F}$ can be derived in the same way as in the expressions for the change in field were derived. Into the analytic expression for the figure of merit, we substitute $\boldsymbol{E} \rightarrow \boldsymbol{E} + \delta\boldsymbol{E}$ and $\boldsymbol{H} \rightarrow \boldsymbol{H} + \delta\boldsymbol{H}$, where $\delta\boldsymbol{E}$ and $\delta\boldsymbol{H}$ are given by (3.16) and (3.17). Dividing the resulting expression through by $\delta\boldsymbol{r}_n$ gives the gradient of the figure of merit with respect to the positions of all of the scatterers. In this way, we can begin from an initial distribution of scatterers and iteratively calculate the set of moves for each scatterer $\{\delta\boldsymbol{r}_n\}$ that increase the figure of merit.

To illustrate how these expressions can be used, we consider trying to enhance the emitted power of a small dipole emitter with polarisation $\boldsymbol{p}$ at position $\boldsymbol{r'}$. Our figure of merit is

$$P = -\frac{\omega}{2}\mathrm{Im}\left[\boldsymbol{p}^* \cdot \boldsymbol{E}(\boldsymbol{r'})\right]. \tag{3.19}$$

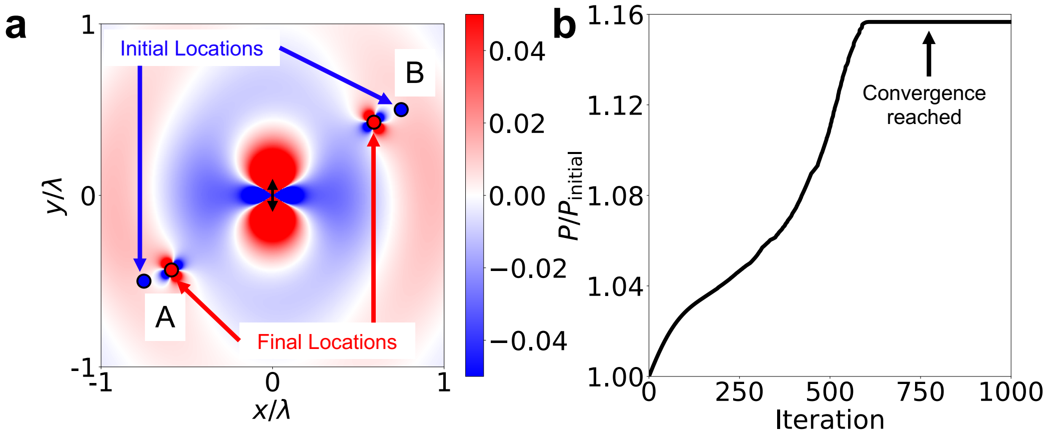

Figure 3.2: A simple example optimisation. The aim is to enhance the emitted power of the dipole emitter at the origin (black arrow). We consider two scatterers, labelled A and B, that support only an electric dipole ($\alpha_H = 0$). (a) shows the configuration change during the optimisation, with the colour indicated $\mathrm{Re}[E_y]$. (b) shows the evolution of the power emission.

To find the gradient of this figure of merit with respect to the locations of all of the scatterers, we expand it under small changes in the fields

$$P + \delta P = -\frac{\omega}{2}\mathrm{Im}\left[\boldsymbol{p}^* \cdot \left(\boldsymbol{E}(\boldsymbol{r}') + \delta\boldsymbol{E}(\boldsymbol{r}')\right)\right], \tag{3.20}$$

$$\delta P = -\frac{\omega}{2}\mathrm{Im}\left[\boldsymbol{p}^* \cdot \delta\boldsymbol{E}(\boldsymbol{r}')\right]. \tag{3.21}$$

Into this, we substitute the expression connecting the change in the field to a change in the position of a scatterer

$$\begin{aligned}\delta P = \frac{\omega}{2}\mathrm{Im}\Big[\boldsymbol{p}^* \cdot \Big\{&\xi^2 \boldsymbol{G}(\boldsymbol{r},\boldsymbol{r}_n)\boldsymbol{\alpha}_E \delta\boldsymbol{r}_n \cdot \nabla\boldsymbol{E}(\boldsymbol{r}_n) \\ &+ i\xi \boldsymbol{G}_{EH}(\boldsymbol{r},\boldsymbol{r}_n)\boldsymbol{\alpha}_H \delta\boldsymbol{r}_n \cdot \nabla\boldsymbol{H}(\boldsymbol{r}_n)\Big\}\Big].\end{aligned} \tag{3.22}$$

Dividing through by $\delta \boldsymbol{r}_n$, we arrive at the gradient of the figure of merit with respect to the position of all of the scatterers

$$\nabla_{\boldsymbol{r}_n} P = \frac{\omega}{2} \mathrm{Im} \left[\boldsymbol{p}^* \cdot \left\{ \xi^2 \boldsymbol{G}(\boldsymbol{r}, \boldsymbol{r}_n) \boldsymbol{\alpha}_E \nabla \boldsymbol{E}(\boldsymbol{r}_n) + i\xi \boldsymbol{G}_{EH}(\boldsymbol{r}, \boldsymbol{r}_n) \boldsymbol{\alpha}_H \nabla \boldsymbol{H}(\boldsymbol{r}_n) \right\} \right]. \tag{3.23}$$

This gradient can be used to update the positions of all the scatterers to increase the figure of merit using simple gradient descent optimisation, given by

$$\boldsymbol{r}_n^{i+1} = \boldsymbol{r}_n^i + \gamma \nabla_{\boldsymbol{r}_n} P, \tag{3.24}$$

where γ is a small step, chosen so that the change to the fields can be considered a small perturbation. We find that the choice of $\gamma \sim \lambda/500$ provides a good balance between convergence and computation time. Similarly to the adjoint method, our technique gives us a way to update the position of all of the scatterers at the same time, making it very efficient. Furthermore, only the derivative of the field is required not the derivative of the figure of merit.

An example of using this framework to place two electric scatterers ($\boldsymbol{\alpha}_H = 0$) around an emitter to enhance its emitted power is shown in Figure 3.2. The two scatterers, labelled A and B start in positions indicated by the blue dots and are shifted to the locations indicated by red dots. Power emission is enhanced by 16% , although it is clear that this is a local minimum meaning that another choice of initial condition could yield a better result. As was discussed in Section 2.8, this is a feature of gradient descent optimisation. Before proceeding to design more complex structures, we continue with this simple example and develop some tools that can be used to better understand the disordered structures we will design.

3.3 Understanding Scattering Structures

We consider what information can be extracted about the scattering system from the analytical formulation. Having the mathematical framework provided by the discrete dipole approximation, derived in Section 2.6, from which information can be extracted sets this method apart from design methods based on genetic algorithms or machine learning. While powerful, these techniques offer no physical insight into the disordered scattering system. The key object that characterises the system of scatterers is the interaction matrix, $\boldsymbol{R}$. All multiple scattering effects within the system are encoded within this matrix. To illustrate the physical meaning of the $\boldsymbol{R}$ matrix, we consider the simplest possible case: two scatterers with only an electric polarizability ($\boldsymbol{\alpha}_H = 0$). In this case, the response matrix connects the fields due to the the source, $(\boldsymbol{E}_s, \boldsymbol{H}_s)$, to the dipole moment induced in the scatterers $\boldsymbol{p}$ as,

$$\begin{pmatrix} \boldsymbol{p}(\boldsymbol{r}_1) \\ \boldsymbol{p}(\boldsymbol{r}_2) \end{pmatrix} = \boldsymbol{\alpha}_E \cdot \begin{pmatrix} \mathbf{1} & -\xi^2 \boldsymbol{G}(\boldsymbol{r}_1, \boldsymbol{r}_2) \cdot \boldsymbol{\alpha}_E \\ -\xi^2 \boldsymbol{G}(\boldsymbol{r}_2, \boldsymbol{r}_1) \cdot \boldsymbol{\alpha}_E & \mathbf{1} \end{pmatrix}^{-1} \cdot \begin{pmatrix} \boldsymbol{E}_s(\boldsymbol{r}_1) \\ \boldsymbol{E}_s(\boldsymbol{r}_2) \end{pmatrix}. \tag{3.25}$$

The eigenvalues of $\boldsymbol{R}^{-1}$ satisfy the characteristic polynomial

$$\boldsymbol{\lambda}^{-1} = \mathbf{1} \pm \sqrt{[\xi^2 \boldsymbol{G}(\boldsymbol{r}_1, \boldsymbol{r}_2) \cdot \boldsymbol{\alpha}_E] \cdot [\xi^2 \boldsymbol{G}(\boldsymbol{r}_2, \boldsymbol{r}_1) \cdot \boldsymbol{\alpha}_E]}. \tag{3.26}$$

This is exactly the same as (2.119) in Section 2.6, although we have used the fact that $\boldsymbol{p} = \boldsymbol{\alpha}_E \boldsymbol{E}$ to re-write the left–hand side in terms of the dipole moment rather than the field. Making use of the reciprocity of the Greens function [24], we see that the two terms under the square root are identical.

Therefore, the eigenvalues of $\boldsymbol{R}$ can be written down immediately

$$\boldsymbol{\lambda} = \mathrm{diag}\left\{\frac{\boldsymbol{\alpha}_E}{\mathbf{1} \pm \zeta^2 \boldsymbol{G}(\boldsymbol{r}_1, \boldsymbol{r}_2) \cdot \boldsymbol{\alpha}_E}\right\}. \tag{3.27}$$

One way to interpret the terms of (3.26) are as multiple scattering events between scatterer 1 and scatterer 2. An interaction between the two electric-dipole scatterers is comprised of scattering from $\boldsymbol{r}_1$ to $\boldsymbol{r}_2$, then back again. This is what is expressed by the product of the Green functions in the discriminant of the characteristic equation (3.26). This understanding can be extended to more electric scatterers, and also scatterers with both electric and magnetic dipoles, whence more complex scattering processes become available. However, this interpretation is still evident in the form of the characteristic polynomials. For example, for just two electromagnetic scatterers ($\boldsymbol{\alpha}_E, \boldsymbol{\alpha}_H \neq 0$), the characteristic equation is

$$
\begin{aligned}
&(1-\lambda)^4 \\
&+(1-\lambda)^2\Big[G(\boldsymbol{r}_1,\boldsymbol{r}_2)\alpha_E G(\boldsymbol{r}_2,\boldsymbol{r}_1)\alpha_E\xi^4 \\
&-G(\boldsymbol{r}_1,\boldsymbol{r}_2)\alpha_H G(\boldsymbol{r}_2,\boldsymbol{r}_1)\alpha_H\xi^4 \\
&-G_{EH}(\boldsymbol{r}_1,\boldsymbol{r}_1)\alpha_E G_{EH}(\boldsymbol{r}_1,\boldsymbol{r}_1)\alpha_H\xi^2 \\
&-G_{EH}(\boldsymbol{r}_1,\boldsymbol{r}_2)\alpha_E G_{EH}(\boldsymbol{r}_2,\boldsymbol{r}_1)\alpha_H\xi^2 \\
&-G_{EH}(\boldsymbol{r}_1,\boldsymbol{r}_2)\alpha_H G_{EH}(\boldsymbol{r}_2,\boldsymbol{r}_1)\alpha_E\xi^2 \\
&-G_{EH}(\boldsymbol{r}_2,\boldsymbol{r}_2)\alpha_E G_{EH}(\boldsymbol{r}_2,\boldsymbol{r}_2)\alpha_H\xi^2\Big] \\
&+(1-\lambda)\Big[-G(\boldsymbol{r}_1,\boldsymbol{r}_2)\alpha_E G_{EH}(\boldsymbol{r}_1,\boldsymbol{r}_1)\alpha_E G_{EH}(\boldsymbol{r}_2,\boldsymbol{r}_1)\alpha_H\xi^4 \\
&-G(\boldsymbol{r}_1,\boldsymbol{r}_2)\alpha_E G_{EH}(\boldsymbol{r}_2,\boldsymbol{r}_1)\alpha_E G_{EH}(\boldsymbol{r}_2,\boldsymbol{r}_2)\alpha_H\xi^4 \\
&-G(\boldsymbol{r}_1,\boldsymbol{r}_2)\alpha_H G_{EH}(\boldsymbol{r}_1,\boldsymbol{r}_1)\alpha_H G_{EH}(\boldsymbol{r}_2,\boldsymbol{r}_1)\alpha_E\xi^4 \\
&-G(\boldsymbol{r}_1,\boldsymbol{r}_2)\alpha_H G_{EH}(\boldsymbol{r}_2,\boldsymbol{r}_1)\alpha_H G_{EH}(\boldsymbol{r}_2,\boldsymbol{r}_2)\alpha_E\xi^4+ \\
&G(\boldsymbol{r}_2,\boldsymbol{r}_1)\alpha_E G_{EH}(\boldsymbol{r}_1,\boldsymbol{r}_1)\alpha_H G_{EH}(\boldsymbol{r}_1,\boldsymbol{r}_2)\alpha_E\xi^4 \\
&+G(\boldsymbol{r}_2,\boldsymbol{r}_1)\alpha_E G_{EH}(\boldsymbol{r}_1,\boldsymbol{r}_2)\alpha_H G_{EH}(\boldsymbol{r}_2,\boldsymbol{r}_2)\alpha_E\xi^4 \\
&-G(\boldsymbol{r}_2,\boldsymbol{r}_1)\alpha_H G_{EH}(\boldsymbol{r}_1,\boldsymbol{r}_1)\alpha_E G_{EH}(\boldsymbol{r}_1,\boldsymbol{r}_2)\alpha_H\xi^4 \\
&-G(\boldsymbol{r}_2,\boldsymbol{r}_1)\alpha_H G_{EH}(\boldsymbol{r}_1,\boldsymbol{r}_2)\alpha_E G_{EH}(\boldsymbol{r}_2,\boldsymbol{r}_2)\alpha_H\xi^4\Big] \\
&-G(\boldsymbol{r}_1,\boldsymbol{r}_2)\alpha_E G(\boldsymbol{r}_1,\boldsymbol{r}_2)\alpha_H G(\boldsymbol{r}_2,\boldsymbol{r}_1)\alpha_E G(\boldsymbol{r}_2,\boldsymbol{r}_1)\alpha_H\xi^8 \\
&-G(\boldsymbol{r}_1,\boldsymbol{r}_2)\alpha_E G(\boldsymbol{r}_1,\boldsymbol{r}_2)\alpha_H G_{EH}(\boldsymbol{r}_2,\boldsymbol{r}_1)\alpha_E G_{EH}(\boldsymbol{r}_2,\boldsymbol{r}_1)\alpha_H\xi^6 \\
&-G(\boldsymbol{r}_1,\boldsymbol{r}_2)\alpha_E G(\boldsymbol{r}_2,\boldsymbol{r}_1)\alpha_H G_{EH}(\boldsymbol{r}_1,\boldsymbol{r}_1)\alpha_E G_{EH}(\boldsymbol{r}_2,\boldsymbol{r}_2)\alpha_H\xi^6 \\
&+G(\boldsymbol{r}_1,\boldsymbol{r}_2)\alpha_H G(\boldsymbol{r}_2,\boldsymbol{r}_1)\alpha_E G_{EH}(\boldsymbol{r}_1,\boldsymbol{r}_1)\alpha_H G_{EH}(\boldsymbol{r}_2,\boldsymbol{r}_2)\alpha_E\xi^6 \\
&+G(\boldsymbol{r}_2,\boldsymbol{r}_1)\alpha_E G(\boldsymbol{r}_2,\boldsymbol{r}_1)\alpha_H G_{EH}(\boldsymbol{r}_1,\boldsymbol{r}_2)\alpha_E G_{EH}(\boldsymbol{r}_1,\boldsymbol{r}_2)\alpha_H\xi^6 \\
&+G_{EH}(\boldsymbol{r}_1,\boldsymbol{r}_1)\alpha_E G_{EH}(\boldsymbol{r}_1,\boldsymbol{r}_1)\alpha_H G_{EH}(\boldsymbol{r}_2,\boldsymbol{r}_2)\alpha_E G_{EH}(\boldsymbol{r}_2,\boldsymbol{r}_2)\alpha_H\xi^4 \\
&-G_{EH}(\boldsymbol{r}_1,\boldsymbol{r}_1)\alpha_E G_{EH}(\boldsymbol{r}_1,\boldsymbol{r}_2)\alpha_H G_{EH}(\boldsymbol{r}_2,\boldsymbol{r}_1)\alpha_H G_{EH}(\boldsymbol{r}_2,\boldsymbol{r}_2)\alpha_E\xi^4 \\
&-G_{EH}(\boldsymbol{r}_1,\boldsymbol{r}_1)\alpha_H G_{EH}(\boldsymbol{r}_1,\boldsymbol{r}_2)\alpha_E G_{EH}(\boldsymbol{r}_2,\boldsymbol{r}_1)\alpha_E G_{EH}(\boldsymbol{r}_2,\boldsymbol{r}_2)\alpha_H\xi^4 \\
&+G_{EH}(\boldsymbol{r}_1,\boldsymbol{r}_2)\alpha_E G_{EH}(\boldsymbol{r}_1,\boldsymbol{r}_2)\alpha_H G_{EH}(\boldsymbol{r}_2,\boldsymbol{r}_1)\alpha_E G_{EH}(\boldsymbol{r}_2,\boldsymbol{r}_1)\alpha_H\xi^4.
\end{aligned}
\tag{3.28}
$$

While this is much harder to interpret, we can see that if we set $\alpha_H = 0$, the purely electric case is retrieved.

Additionally, the terms can be interpreted physically: $-G(\boldsymbol{r}_1, \boldsymbol{r}_2)\alpha_H G(\boldsymbol{r}_2, \boldsymbol{r}_1)\alpha_H \zeta^4$ represents magnetic scattering between the two scatterers. Terms of the form $-G_{EH}(\boldsymbol{r}_1, \boldsymbol{r}_2)\alpha_E G_{EH}(\boldsymbol{r}_2, \boldsymbol{r}_1)\alpha_H \zeta^2$, read from left to right, indicate a magnetic field applied to scatterer 1 being scattered as an electric field, before being re–scattered as a magnetic field from scatterer 2. In what follows, we will consider the magnitude of the eigenvalues rather than the characteristic polynomials, due to their complexity, however all of the wave physics of the system is buried within these objects. Interestingly, scattering systems can also be understood using graph theory approaches [99]. This approach scales more conveniently than attempting to examine the characteristic equation directly.

Combining the fact that eigenvalues of the interaction matrix $\boldsymbol{R}$ contain information about the collective response of the particles with the expression for the eigenvalues (3.27), the value of eigenvalue itself can be interpreted as the collective polarizability of the two scatterers. The eigenvalue itself, $\boldsymbol{\lambda}$, can be viewed as the enhancement to the single scatterer polarizability due to multiple scattering effects. It is a dimensionless number that characterises how strongly interacting the system is. Therefore, $\boldsymbol{\alpha}_E^{-1} \cdot \boldsymbol{\lambda}$ gives the enhancement of the single particle polarizability due to the multiple scattering events between the two scatterers. So, if $\boldsymbol{\alpha}_E^{-1} \cdot \boldsymbol{\lambda} = 1$ there is no change to the single particle polarizability and multiple scattering events provide no enhancement. On the other hand, a large $\boldsymbol{\alpha}_E^{-1} \cdot \boldsymbol{\lambda}$ corresponds to a large enhancement to the response of a single scatterer, due to collective behaviour.

Additionally, the eigenmodes of the interaction matrix $\boldsymbol{R}$ represent configurations of field that produce a certain collective response of the system.

As $\boldsymbol{R}$ has no symmetries these eigenvectors do not form an orthogonal basis [100, 101], although the left and right eigenvectors of $\boldsymbol{R}$ do. Right eigenvectors are defined as satisfying

$$\boldsymbol{R}\boldsymbol{w}_n = \lambda_n \boldsymbol{w}_n, \tag{3.29}$$

and left eigenvectors can be defined as satisfying

$$\boldsymbol{v}_m^\dagger \boldsymbol{R} = \lambda_m \boldsymbol{v}_m^\dagger, \tag{3.30}$$

where '†' denotes the conjugate transpose (adjoint) of the vector. To see that these form a basis, we multiply the first by $\boldsymbol{v}_m^\dagger$ and the second by $\boldsymbol{w}_n$, giving

$$\boldsymbol{v}_m^\dagger \boldsymbol{R}\boldsymbol{w}_n = \lambda_n \boldsymbol{v}_m^\dagger \boldsymbol{w}_n, \tag{3.31}$$

$$\boldsymbol{v}_m^\dagger \boldsymbol{R}\boldsymbol{w}_n = \lambda_m \boldsymbol{v}_m^\dagger \boldsymbol{w}_n. \tag{3.32}$$

For these to both be true, we require that

$$\boldsymbol{v}_m^\dagger \boldsymbol{w}_n = \delta_{nm}. \tag{3.33}$$

In other words, the left and right eigen–vectors are orthogonal. Using a left and right pair, the source field can be decomposed into the basis of these eigenvectors, $\boldsymbol{w}_n$ as

$$(\boldsymbol{E}_s, \boldsymbol{H}_s)^T = \sum_{n=1}^{N} c_n \boldsymbol{w}_n, \tag{3.34}$$

where N is the number of scatterers and c_n is a complex expansion coefficient. To find c_n, we multiply each side of (3.34) by $\boldsymbol{v}_m^\dagger$

$$\boldsymbol{v}_m^\dagger \left(\boldsymbol{E}_s, \boldsymbol{H}_s\right)^T = \sum_{n=1}^{N} c_n \boldsymbol{v}_m^\dagger \boldsymbol{w}_n \tag{3.35}$$

$$= \sum_{n=1}^{N} c_n \delta_{nm} \tag{3.36}$$

$$\Rightarrow c_n = \boldsymbol{v}_n^\dagger \left(\boldsymbol{E}_s, \boldsymbol{H}_s\right)^T . \tag{3.37}$$

The expansion coefficient c_n indicates which eigenmodes contribute most strongly to the response of the system. Identifying these modes allows the response of the system to be understood and characterised by examining only a few eigenmodes, rather than the whole expansion (3.34). The expansion coefficient is a useful tool in characterising the response of the system. From this decomposition, one may find which modes are excited and how strongly so that the dominant scattering response of the system may be isolated and examined.

To demonstrate the utility of the eigenvalues of the interaction matrix and the expansion coefficient, we apply this framework to the simple scattering structure shown in Figure 3.2. Our aim is to gain insight into the optimisation procedure by considering i) the shapes of the eigenmodes of the interaction matrix, and ii) how the dominant modes change over the optimisation, characterised by the expansion coefficient. The modes of the two–scatterer system are shown in Figure 3.3. The labels ′A′ and ′B′ identify the scatterers and the modes are plotted as vectors indicating the direction of the electric field (equivalently, dipole moment) of each scatterer. Modes where the fields of the two scatterers are in the same direction are symmetric and are coloured red, while modes where the fields are not in the same

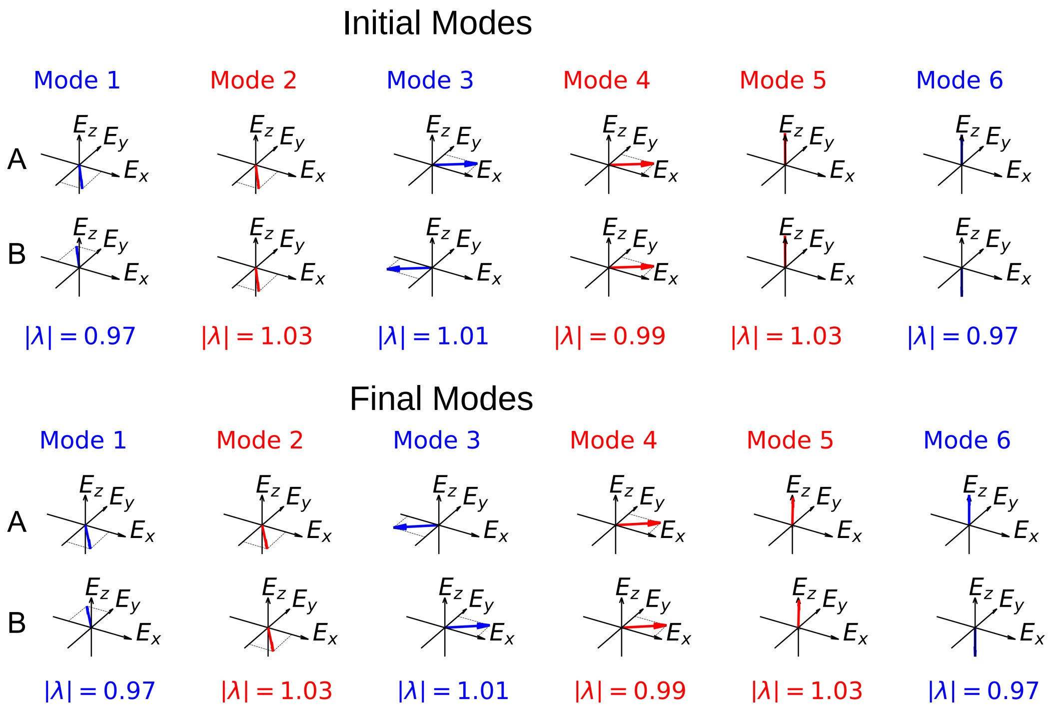

Figure 3.3: Eigenmodes of the simple example optimisation. Note the two classes of mode: anti-symmetric (i.e. initial mode 1) shown in blue and symmetric (i.e. initial mode 2) shown in red. Eigenmodes are indicated as pairs of 3D vectors, representing the components of the electric field in each scatterer.

direction are antisymmetric and are coloured blue. Magnitudes of the eigenvalues associated with each mode $|\lambda|$ are also indicated. We observe that the optimisation has little effect on the character of the modes. Before and after the optimisation there are 3 symmetric and 3 anti–symmetric modes and their associated eigenvalues are unchanged. This is not very surprising, as the configuration of the scatterers does not change drastically over the optimisation. If we look at the change in the expansion coefficients of the modes, shown in Figure 3.4, we see that which modes are excited changes. The effect of the optimisation is to promote excitation of the symmetric modes, with their expansion coefficients increasing while anti–symmetric modes are not excited. Enhancement of the coupling between the emitter and the

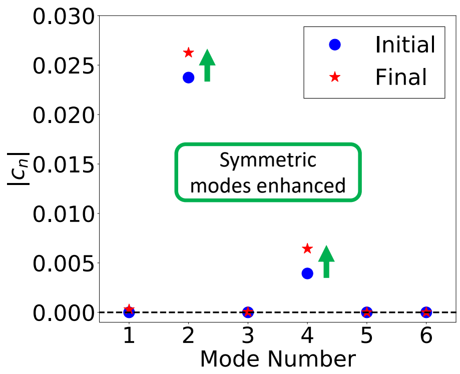

Figure 3.4: Demonstration of how the optimisation process changes the relative dominance of the modes in the response of the system, as characterised by their expansion coefficient.

symmetric modes of the systems is the mechanism for the power enhancement. The magnitude of the enhancement is relatively small since the magnitude of the eigenvalues associated with modes 2 and 4 is very close to unity, meaning that the collective response of these modes is small (i.e. the scatterers are weakly coupled). We might predict, then, that modes with larger $|\lambda|$ exhibit larger collective properties and if one could couple into such a mode a greater power emission enhancement could be achieved.

This discussion indicates two key ways we can understand how the optimisation procedure achieves the goals it is given. Either the character of the modes themselves could be changed, or which modes are excited could be modified, or both. These simple tools will be useful when we turn to the analysis of more complex structures.

In the next few sections, we will deploy our iterative framework and the associated elucidative tools to address some common antenna problems.

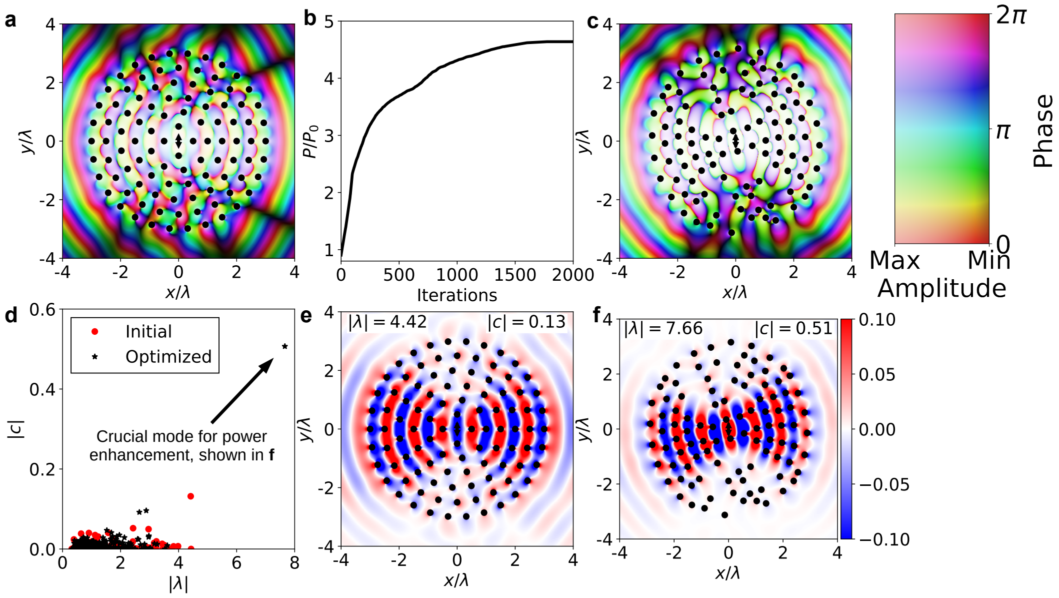

Figure 3.5: The result of applying our design methodology to enhance emitted power of a dipole using 100 scatterers. In all plots, scatterers are shown as black circles and the dipole emitter as a black arrow. (a) Shows the $\hat{y}$ component of the electric field in the initial configuration, (b) shows the progress of the power enhancement as the optimisation progresses and (c) shows E_y in the optimised configuration. (d) shows how the eigenvalues and expansion coefficients change due to the optimisation. (e) and (f) show $\mathrm{Re}[E_y]$ of the mode with the largest expansion coefficient in the initial and optimised structure respectively. The final mode, plotted in (f), with eigenvalue ~ 8 and expansion coefficient ~ 0.5 is responsible for the power enhancement.

3.4 Example: Emitted Power

The first problem we apply our method to is improving the emitted power of a small dipole emitter. In the context of antennas, this is useful as miniaturisation of antenna is well known to reduce their performance. We use parameters from optics, however our approach is length–scale agnostic, and will be demonstrated in other wave regimes later in the thesis. Working at a wavelength of 550 nm (green light), the scatterers are modelled as silicon spheres of radius 65 nm. For this choice of scatterer, the polarisability tensor is diagonal, due to the isotropy of the scatterer, and can be found analytically from Mie theory. We start from an arbitrary initial distribution of scatterers, shown in Figure 3.5 (a), then apply the method we have developed to re–distribute the scatterers to enhance radiated power.

The results of this are shown in Figure 3.5(a-c), with the progression of the eigenmodes shown in Figure 3.5(d). An arrangement of the 100 dipolar scatterers has been found, using our proposed framework, to provide a factor of $\sim \times 4.5$ enhancement of the power emission of the dipole emitter. This factor of enhancement is far smaller than can be achieved with 3D bulk structures [88, 89], but is of the order of studies with similar assumptions and constraints but which use genetic algorithms [70].

While the structure we have designed seems disordered, we can utilise the tools we have developed in the previous section to gain to insight into the device. Beginning by considering the change in the character of the eigenmodes of the interaction matrix, we compare the mode with the largest expansion coefficient before the optimisation, Figure 3.5(e), and after the optimisation Figure 3.5(f). Two key qualitative features of modes that enhance power emission can be determined. Firstly, the mode has a large eigenvalue corresponding to a large collective response of the scatterers. Secondly, this mode also exhibits a strong localisation at the location of the emitter. Clearly, this mode and the field from the dipole have a large overlap, expressed by the large expansion coefficient of the mode shown in Figure 3.5(f). The large collective response of the scatterer system, as well as being strongly coupled to the emitting dipole's field, leads to the enhancement of power emission. While not extremely surprising, these conclusions apply to a very wide variety of photonic structures designed to enhance power emission [88, 89, 102].

The results presented in Figure 3.5 also show the strength of designing aperiodic structures, rather than being limited to periodic ones. Design of aperiodic structures benefits from an improved exploration of the parameter space due to the removal of the restriction to periodic solutions. While it has been demonstrated that periodic structures can enhance antenna radiation [83], more compact and better performing solutions can be obtained with aperiodic structures, as we have demonstrated in Figure 3.5. The problem of antenna emission is not periodic, so one should not expect an emission enhancing structure to be periodic. To find an optimal, or even well performing, solution one is forced to consider aperiodic structures. Indeed, the bow-tie shape of the structure shown in Figure 3.5(c) is consistent with structures designed to enhance dipole radiation using genetic methods [102], simple phase arguments [88] and even the widely used bow–tie antenna [5]. The resulting structures have the same symmetry as dipole radiation: they are left-right symmetric, but not periodic. To further accelerate our method, one could impose the symmetry of the problem upon the solution. Such a constraint would be useful when designing metasurfaces with very large radius $\sim 100\lambda$, as only half of the field gradients would need to be calculated [103]. The additional parameters available to optimise when designing aperiodic structures can present a challenge for traditional methods based on gradient or look-up methods. However, in the method we have proposed, these additional degrees of freedom can be optimised while keeping the numerical problem efficient.

We now consider the bandwidth and sensitivity to perturbations of the structure we have designed. In Figure 3.6, we plot the power emission of a dipole in free space, governed by the Larmor equation [14]. Also plotted is the power emission of the dipole surrounded by the disordered structure we have designed, shown in black. The peak in power emission occurs at 550 nm, with a bandwidth of ± 5 nm. The narrow bandwidth is due to the fact

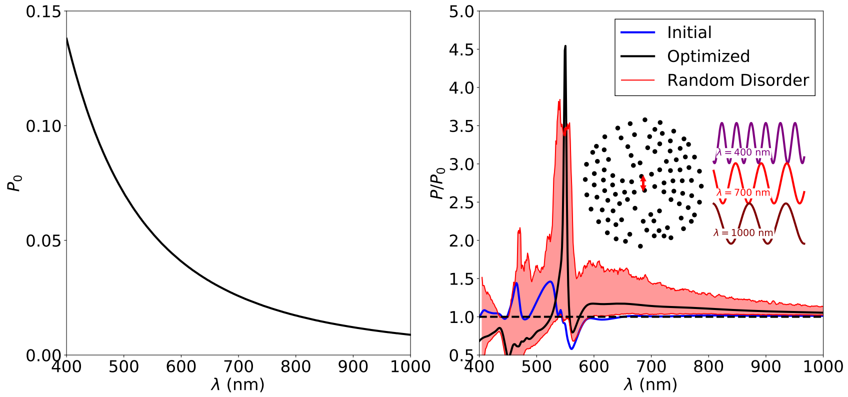

Figure 3.6: Bandwidth of power emission structure. Structure is shown inset, with scatterers as black dots and emitter as red arrow. For scale, three wavelengths are shown. The emitted power of the structure is compared relative to the emission in free space, given by Larmor's formula. A clear peak in performance is located at 550 nm, with a bandwidth of ~ 5 nm. An estimate for the upper and lower bounds on performance due to randomly shifting all scatterers by $\lambda/10$ is shown by the red region.

that power has only been optimised at a single wavelength, as well as the dependence of the enhancement upon interference effects of the scatterers. The delicacy of the interference effects is also evident from the impact small random perturbations have upon performance. Under random moves of all scatterers by a maximum of $\lambda/10$, the change in performance is indicated by the red band shown in Figure 3.6. Two features are of note. Firstly, the change in performance due to all of the scatterers being perturbed is pronounced, particularly at wavelengths < 600 nm. The power emission peak at 550 nm is smeared over a wider band and reduced by 20% in the best case (upper red line in Figure 3.6) and destroyed completely in the worst case (lower red line in Figure 3.6). Secondly, applying random perturbations does not lead to an increase in power emission at 550 nm. This implies that our optimised solution is a local minima, so small random changes do not improve the design.

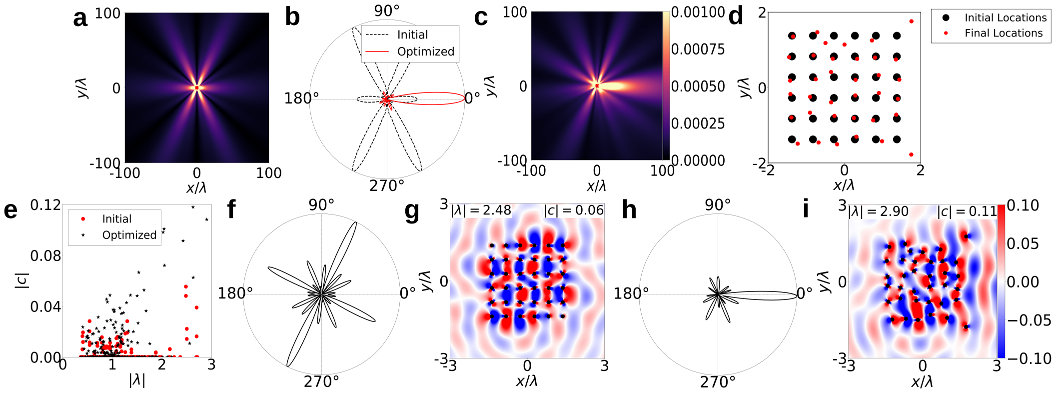

Figure 3.7: Re-structuring the far–field of a dipole emitter to radiated power in a particular direction. (a) shows $|\mathbf{E}|$ for the initial configuration (regular array), viewed from the far-field. (b) shows a comparison of the far-field distribution of the Poynting vector for the initial configuration (black dashed line) and the optimised configuration (red line). All far-field distributions are normalised to have unit amplitude. The width of the beam in the optimised structure is $\sim 20^{\circ}$. (c) shows $|\boldsymbol{E}|$ of the optimised structure, viewed from the far-field. The initial and final scatterer locations are shown in (d), and the change in eigenmodes and their expansion coefficients over the optimization are shown in (e). The evolution of the properties of the eigenmode with the largest expansion coefficient is shown in (f-i). Both the distribution of E_y in the plane of the scatterers and the normalized far-field Poynting vector are shown. (f-g) show the mode with the largest expansion coefficient in the initial structure, with (h-i) showing the mode with the largest expansion coefficient in the final structure. It is clear that the mode shown in (h-i) is responsible for the strong directivity along $\theta = 0^{\circ}$ in the optimised structure.

3.5 Far–field Beam

In the previous section, we demonstrated the ability of our method to manipulate the near–field of a small emitter. Next, we demonstrate the ability of our method to manipulate the *far-field* of an emitter. To do this, we take our figure of merit to be the modulus of the electric field at some target angle $\theta_{\star}$ in the far field

$$\mathcal{F} = |\boldsymbol{E}(\theta_{\star})| = \sqrt{\boldsymbol{E}^{*}(\theta_{\star}) \cdot \boldsymbol{E}(\theta_{\star})}. \tag{3.38}$$

To find, analytically, the gradient of this we expand the figure of merit under small changes in the fields

$$\mathcal{F} + \delta\mathcal{F} = \sqrt{(\boldsymbol{E}^*(\theta_\star) + \delta\boldsymbol{E}^*(\theta_\star)) \cdot (\boldsymbol{E}(\theta_\star) + \delta\boldsymbol{E}(\theta_\star))} \tag{3.39}$$

$$= \sqrt{|\boldsymbol{E}(\theta_\star)|^2 + \boldsymbol{E}^*(\theta_\star) \cdot \delta\boldsymbol{E}(\theta_\star) + \boldsymbol{E}(\theta_\star) \cdot \delta\boldsymbol{E}^*(\theta_\star) + \mathcal{O}(\delta\boldsymbol{E}^2)} \tag{3.40}$$

$$= \sqrt{|\boldsymbol{E}(\theta_\star)|^2 + 2\mathrm{Re}[\boldsymbol{E}^*(\theta_\star) \cdot \delta\boldsymbol{E}(\theta_\star)] + \mathcal{O}(\delta\boldsymbol{E}^2)} \tag{3.41}$$

$$= |\boldsymbol{E}(\theta_\star)|\sqrt{1 + \frac{2\mathrm{Re}[\boldsymbol{E}^*(\theta_\star) \cdot \delta\boldsymbol{E}(\theta_\star)]}{|\boldsymbol{E}(\theta_\star)|^2}}. \tag{3.42}$$

To linearise this, we use the fact that the change in the field $\delta\boldsymbol{E}(\theta_\star) \ll |\boldsymbol{E}(\theta_\star)|$ so the square root can be expanded in this limit. With this, the first order change in the figure of merit is

$$\mathcal{F} = \frac{\mathrm{Re}[\boldsymbol{E}^*(\theta_\star) \cdot \delta\boldsymbol{E}(\theta_\star)]}{|\boldsymbol{E}(\theta_\star)|}. \tag{3.43}$$

To then find the gradient, we substitute (3.16) to find

$$\begin{aligned}\nabla_{\boldsymbol{r}_n}\mathcal{F} = \frac{1}{|\boldsymbol{E}(\theta_\star)|}\mathrm{Re}\Big[\boldsymbol{E}^*(\theta_\star) \cdot \Big(&\xi^2\boldsymbol{G}(\boldsymbol{r}_\star, \boldsymbol{r}_n)\boldsymbol{\alpha}_E\nabla\boldsymbol{E}(\boldsymbol{r}_n) \\ &+ i\xi\boldsymbol{G}_{EH}(\boldsymbol{r}_\star, \boldsymbol{r}_n)\boldsymbol{\alpha}_H\nabla\boldsymbol{H}(\boldsymbol{r}_n)\Big)\Big].\end{aligned} \tag{3.44}$$

The position vector $\boldsymbol{r}_\star$ is the position in the $x - y$ plane corresponding to the angle $\theta_\star$, i.e. $x_\star = r_{\text{far}-\text{field}} \cos\theta_\star$. Radial distance of the evaluation plane of the far–field $r_{\text{far}-\text{field}}$ is chosen to be large, typically $\sim 100\lambda$. With this gradient, we can design structures that beam radiation into particular directions.

In the example shown in Figure 3.7 we have sought to enhance directivity along the $\theta = 0$ direction. Initially, the scatterers are arranged in a uniform square array with near and far–fields shown in Figure 3.7 (a) and (b) respectively. The near and far–fields of the optimised structure are shown in Figure 3.7 (b) and (c). There is a clear enhancement of the directivity along the $\theta = 0$ direction, shown in Figure 3.7(b-c), with the beam having a FWHM of $\sim 20^\circ$. The starting and optimised scatterer arrangements are shown in Figure 3.7(d).

As with the power emission result of the previous section, the designed structure is difficult to interpret but by considering the eigenmodes we can better understand how directivity can be enhanced. The change in the eigenvalues and expansion coefficients of the modes is shown in Figure 3.7(e). The eigenvalues and expansion coefficients do not change magnitude considerably as a result of the optimisation. This is demonstrated in Figure 3.7(f-i), where the leading order modes, characterised by expansion coefficient, of the system before and after the optimisation are plotted, along with the far-field Poynting vector of the mode in each case. Both of the modes have similar expansion coefficients and eigenvalues, but very different spatial distributions. Indeed, for this application the optimisation procedure aims to re-shape the modes rather than enhancing multiple scattering effects.

The bandwidth of the structure designed to enhance directivity along the 0° direction, shown in Figure 3.7, is plotted in Figure 3.8. Directivity is characterised as the fraction of power radiated into the $0^\circ \pm 10^\circ$ band

$$\text{Directivity} = \frac{\int_{-10^\circ}^{10^\circ} P(\theta) d\theta}{P_{\text{total}}}. \tag{3.45}$$

As with power emission, the directivity is strongly peaked at 550 nm, the wavelength we have chosen to work at, but with a wider bandwidth of ~ 10 nm. To investigate the effect of disorder, all of the scatterers are randomly perturbed by $\lambda/10$ several times. The average effect on directivity is shown

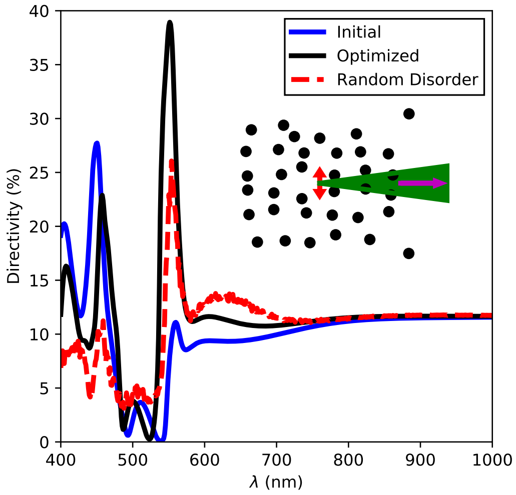

Figure 3.8: Bandwidth of directivity structure. Structure is shown inset, with the emitter shown as a red arrow. Directivity is the percentage of power radiated into the $\pm 10^\circ$ range, shown inset as the green region with the magenta arrow indicating the target direction. Performance is strongly peaked at 550 nm, with bandwidth ~ 10 nm. The effect of randomly perturbing all scatterer locations by $\lambda/10$ is shown as a red dashed line. There is a $\sim 40\%$ drop in performance at 550 nm due to disorder.

as a red dashed line in Figure 3.8. The result is little change in bandwidth but a $\sim$ 40% reduction in performance at 550 nm. The effect of random disorder on the radiation pattern at 550 nm is shown in Figure 3.9. The far-field distribution of the design without any disorder is shown in black and the bounds of the effect of random perturbations by $\lambda/10$ are shown in red. Random disorder has a very large effect on the performance due to the dependence of the designs upon interference conditions.

The previous examples have kept the emitter and the scatterers in a plane and focused on enginerring the effects in that plane. However, our proposed method is fully 3D and can be used to design radiation properties in or out of the plane of scatterers as well. As an example, Figure 3.10 shows the design of a structure which enhances directivity out of the plane. A dipole emitter is located at $(0, 0, \lambda/2)$ and the scatterers are constrained to the $z = 0$ plane, for simplicity. Using a procedure identical to that used to design the structure in Figure 3.7, although with the target point at $z \to \infty$,

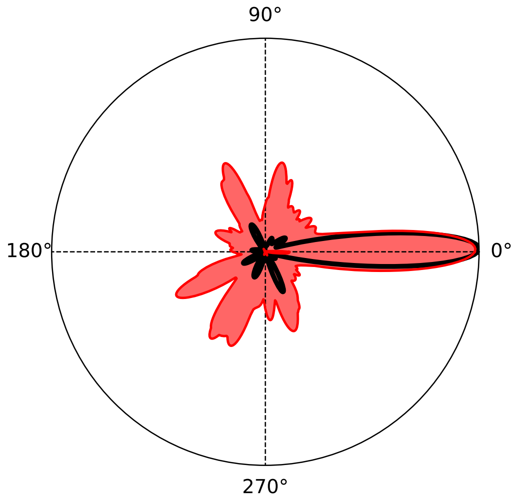

Figure 3.9: Effect of disorder on performance of beaming device. Change in far-field Poynting vector $|S|$ of the device shown in Figure 3.7 due to random perturbations of the designed scatterer locations by $\lambda/10$. All scatterers were randomly perturbed 1000 times to estimate the upper and lower bounds of performance. The black line indicates the Poynting vector for the structure with no perturbation to the design. The red region bounds the performance when all scatterers are randomly perturbed.

rather than $x \to \infty$, power emission out of the plane has been increased. This is demonstrated in Figure 3.10 (c), showing the Poynting vector in the H-plane and exhibiting a clear peak at $\theta = 90^\circ$.

3.6 Discrete 'Luneburg Lens'

Now, we shall demonstrate how the results of our optimisation procedure may be utilised to achieve more complex functionality. By rotating the structure designed to enhance directivity, as well as the source, a device can be constructed which has similar functionality to a Luneburg lens [104]. The Luneburg lens is a type of circular graded index lens that converts a point source to a directional plane wave. Rotating the point source around the edge of the lens allows the plane wave to be directed. This functionality

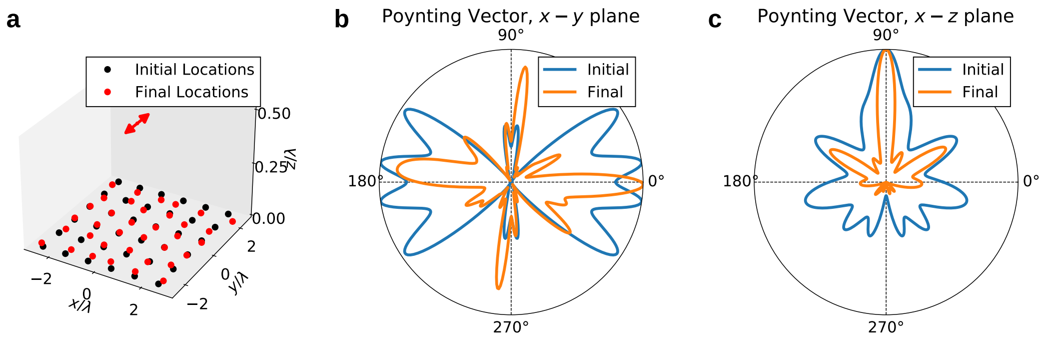

Figure 3.10: Demonstration of manipulating radiation properties out of the plane scatterers. The setup is shown in (a). A dipole emitter (red arrow) is located $\lambda/2$ above the scattering structure. Scatterers begin in the positions shown as black dots. The structure is then optimised to enhance directivity directly out of the plane: $z \to \infty$. The resulting structure is shown as red dots. (b) and (c) show the change in the Poynting vector in the E and H planes, respectively. In the E plane (b), some re-distribution occurs although without a clear aim. However in the H plane (c), there is a well-defined main lobe at $\theta = 90^\circ$, the target direction. In addition, the back lobes are suppressed.

is shown in Figure 3.11 (a). Luneburg lenses are used extensively on aircraft, so these is a desire to preserve their functionality while making them smaller and lighter. Multiplexing our result shown in Figure 3.7 to achieve a qualitatively similar functionality, is demonstrated in Figure 3.11(b-c). One can use the indicated structure to convert a dipole source into a beam directed along a single angle. By placing the source at different locations within the structure, with the correct orientation, the beam may be rotated. The structure proposed in Figure 3.11(b) can be fabricated without having to grade an index, instead 288 scatterers must be arranged as indicated. The multiplexed device has a radius comparable to conventional Luneburg lenses, at $\sim 6\lambda$. While the fabrication is more straightforward, the angular resolution is not continuous as for the usual Luneburg lens. Instead, an angular resolution of 45° can be achieved, although by making the structure larger a higher resolution could be achieved. By multiplexing more structures it was found that the relationship between device radius and angular

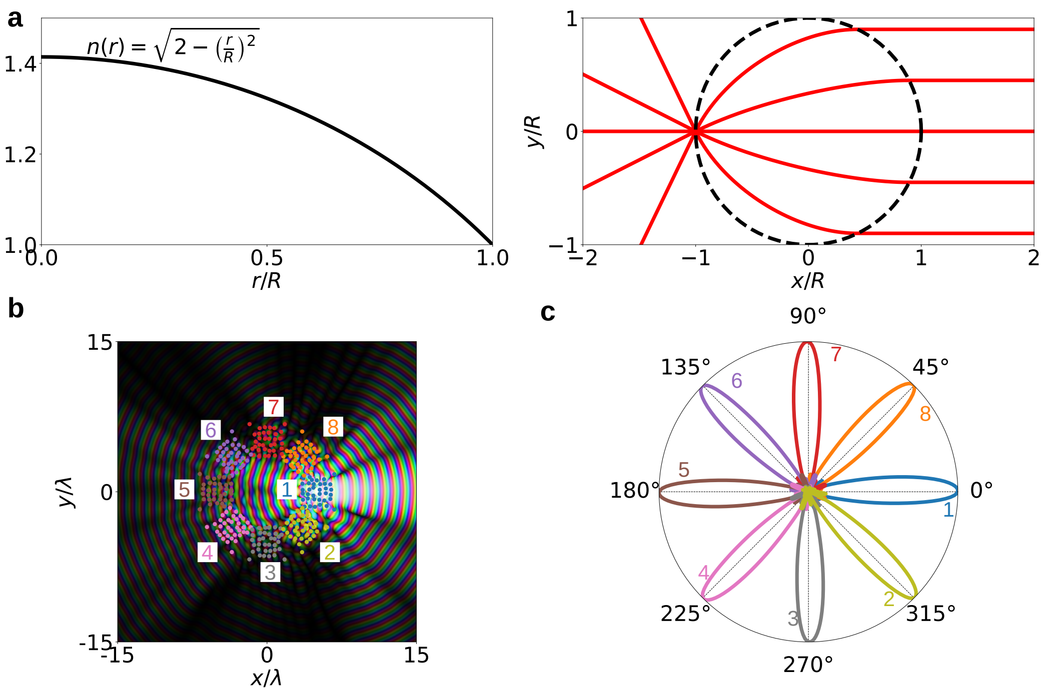

Figure 3.11: Multiplexing the design shown in Figure 3.7 to construct a Luneburg–like lens. (a) demonstrates the function of a normal Luneburg lens of radius R, with a refractive index graded according to the inset equation. A point source is converted into a beam in a single direction. (b) and (c) The result of multiplexing the structure proposed in Figure 3.7 to produce a Luneburg–like lens with a discrete angular resolution of 45°. By rotating the source and changing its location inside the array the far-field Poynting vectors indicated in (b) can be observed. For example, placing the emitter at the centre of array 2 in (b), and rotating it by 45° clockwise, results in the far-field directivity labelled as 2 in (c).

resolution, in degrees, was well approximated by the following power law

$$\left(\frac{R}{\lambda}\right) = 83.6 \times \text{resolution}^{-0.66}. \tag{3.46}$$

The relationship between resolution and radius is shown in Figure 3.12. Therefore, to achieve a resolution of 2°, the device would have to be $\sim 50\lambda$.

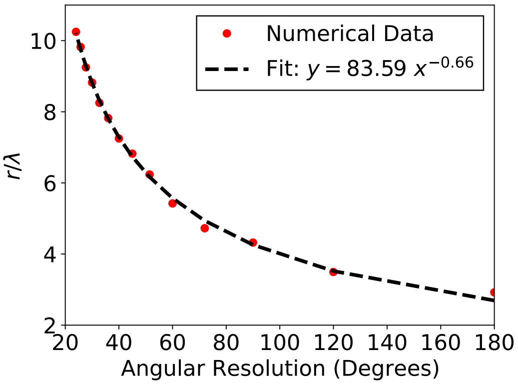

Figure 3.12: Estimating the relationship between angular resolution of the Luneburg lens structure and its radius.

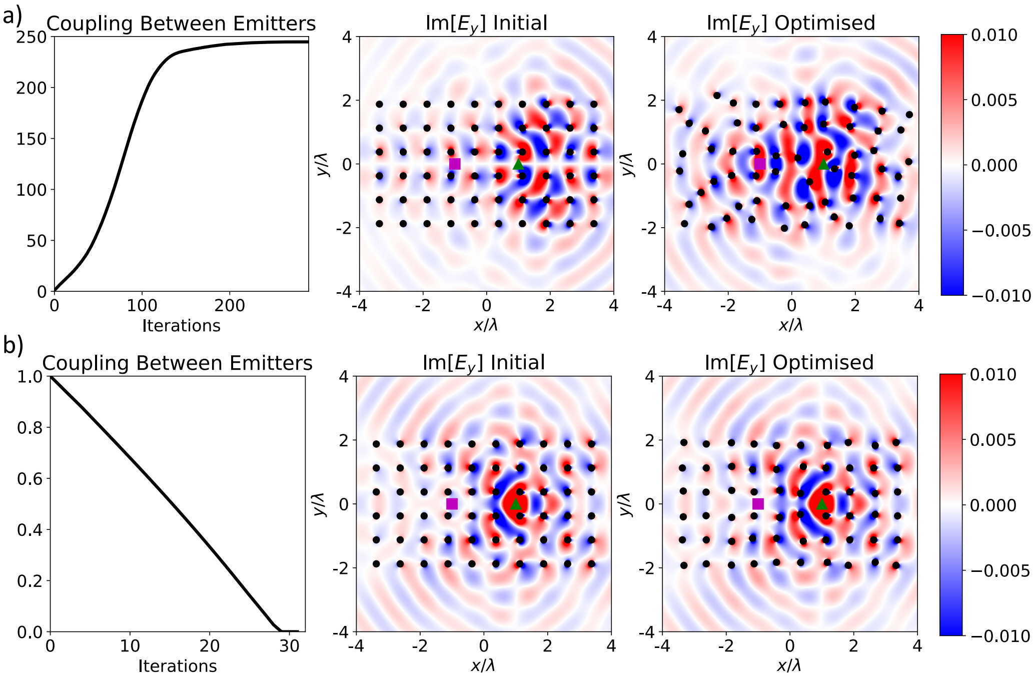

Figure 3.13: Designing dielectric structures that manipulate the coupling between two nearby emitters. Beginning from an initial distribution of scatterers, shown in the centre panels, the update equation (3.54) is used to iteratively move the scatterers to a) increase and b) decrease the coupling between two nearby emitters. The change in coupling over the optimisation procedure is shown in the left–hand panels and the optimised structure is shown in the right–hand panels. The two emitters are shown as a magenta square and a green triangle. The polarisation of the emitters in a) is $\boldsymbol{p} = \hat{\boldsymbol{x}}$ for the green triangle and $\boldsymbol{p} = \hat{\boldsymbol{y}}$ for the magenta square, while in b) is $\boldsymbol{p} = \hat{\boldsymbol{y}}$ for both emitters. In both cases, the y component of the field is re–shaped by moving the scatterers to exhibit either a null or peak at the location of the scatterer shown by the magneta square.

3.7 Nearby Emitters

Next, we consider designing a structure that manipulates the coupling between two nearby emitters. In the context of antennas, this is relevant to base–stations where many emitters are close together but must not cross–couple. On the other hand, increasing the coupling between nearby emitters is useful for sensing applications.

For this problem, we have two sources located at $\boldsymbol{r}_{s,1}$ and $\boldsymbol{r}_{s,2}$ and with electric polarisations $\boldsymbol{p}_{1,2}$. Employing the coupled dipole theory elucidated in Section 2.4, we immediately see that the source terms in Maxwell's equations are

$$\boldsymbol{E}_s(\boldsymbol{r}) = \xi^2 \boldsymbol{G}(\boldsymbol{r}, \boldsymbol{r}_{s,1}) \cdot \boldsymbol{p}_1 + \xi^2 \boldsymbol{G}(\boldsymbol{r}, \boldsymbol{r}_{s,2}) \cdot \boldsymbol{p}_2, \tag{3.47}$$

$$\boldsymbol{H}_s(\boldsymbol{r}) = -i\xi \boldsymbol{G}_{EH}(\boldsymbol{r}, \boldsymbol{r}_{s,1}) \cdot \boldsymbol{p}_1 - i\xi \boldsymbol{G}_{EH}(\boldsymbol{r}, \boldsymbol{r}_{s,2}) \cdot \boldsymbol{p}_2, \tag{3.48}$$

assuming that the sources are small compared to the wavelength. The coupling between the two sources is then given by the PLDoS introduced in Section 2.4

$$\rho_{12} = \mathrm{Im}\left[\boldsymbol{p}_1^* \cdot \boldsymbol{E}_2(\boldsymbol{r}_1)\right] = \mathrm{Im}\left[\boldsymbol{p}_2^* \cdot \boldsymbol{E}_1(\boldsymbol{r}_2)\right]. \tag{3.49}$$

where $\boldsymbol{E}_i(\boldsymbol{r}_j)$ is the field generated by the i^{th} emitter, along with the scattering structure, evaluated at the location of the j^{th} emitter [105]. In this way, ρ_{12} characterises the overlap of the fields generated by the emitters. To design a structure that manipulates the coupling between two emitters, we expand the figure of merit to first order under small changes in the fields at the second emitter

$$\mathcal{F}_{\text{coupling}} = \text{Im}\left[\boldsymbol{p}_1^* \cdot \left(\boldsymbol{E}_2(\boldsymbol{r}_1) + \delta\boldsymbol{E}_2(\boldsymbol{r}_1)\right)\right], \tag{3.50}$$

$$\delta F_{\text{coupling}} = \text{Im}\left[\boldsymbol{p}_1^* \cdot \delta\boldsymbol{E}_2(\boldsymbol{r}_1)\right]. \tag{3.51}$$

This is exactly the same idea behind the adjoint method, introduced in Section 2.9. Inserting the expression for the variation of the electric field (3.16), we find

$$\begin{aligned}\nabla_{\boldsymbol{r}_n} F_{\text{coupling}} = -\sum_n \text{Im}\Big[\boldsymbol{p}_1^* \cdot \Big\{&\xi^2 \boldsymbol{G}(\boldsymbol{r}_1, \boldsymbol{r}_n)\boldsymbol{\alpha}_E \nabla \boldsymbol{E}(\boldsymbol{r}_n) \\ &+ i\xi \boldsymbol{G}_{EH}(\boldsymbol{r}_1, \boldsymbol{r}_n)\boldsymbol{\alpha}_H \nabla \boldsymbol{H}(\boldsymbol{r}_n)\}\Big].\end{aligned} \tag{3.52}$$

This gives a way of calculating a move of the n^{th} scatterer so that the figure of merit is guaranteed to either increase or decrease. Using gradient descent optimisation, as defined in equation (2.129), we update the positions of the scatterers according to

$$\boldsymbol{r}_n^{i+1} = \boldsymbol{r}_{\boldsymbol{n}}^i \pm \gamma \nabla_{\boldsymbol{r}_n} F_{\text{coupling}}, \tag{3.53}$$

where i is the iteration number. Consequently, the update to the scatterer positions is taken to be

$$\delta\boldsymbol{r}_n \propto \mp \text{Im}\left[\boldsymbol{p}_1^* \cdot \left\{\xi^2 \boldsymbol{G}(\boldsymbol{r}_1, \boldsymbol{r}_n)\boldsymbol{\alpha}_E \nabla \boldsymbol{E}(\boldsymbol{r}_n) + i\xi \boldsymbol{G}_{EH}(\boldsymbol{r}_1, \boldsymbol{r}_n)\boldsymbol{\alpha}_H \nabla \boldsymbol{H}(\boldsymbol{r}_n)\right\}\right], \tag{3.54}$$

where the sign is determined by whether one wishes to increase or decrease the figure of merit over the optimisation. One can understand (3.54) physically, by noting that we are calculating gradients in the polarisation density, converting these to currents then propagating the field that these generate onto emitter 1. The ± in (3.54) ensures that the field arrives with the correct phase to constructively or destructively interfere. An example of applying this procedure to change the coupling between two emitters is shown in Figure 3.13. In Figure 3.13 (a), the coupling between an electric dipole with polarisation $\boldsymbol{p} = \hat{\boldsymbol{x}}$, shown as a green triangle, and an electric dipole with polarisation $\boldsymbol{p} = \hat{\boldsymbol{y}}$, shown as a magenta square, is enhanced. The scatterer positions are updated according to the upper sign of (3.54), leading to a redistribution of the scattered field. To increase the coupling, the $\hat{\boldsymbol{y}}$ component of electric field at the location of the emitter with polarisation $\hat{\boldsymbol{y}}$ is increased. Another case of interest might be to reduce the coupling between two similarly polarised nearby emitters. Taking the lower sign in the update equation (3.54) and decreasing the coupling between two emitters with the same polarisation, $\hat{\boldsymbol{y}}$, is demonstrated in Figure 3.13b. The scatterers are now redistributed to place a null in the field at the location of the emitter shown by the magenta square.

3.8 Lensing

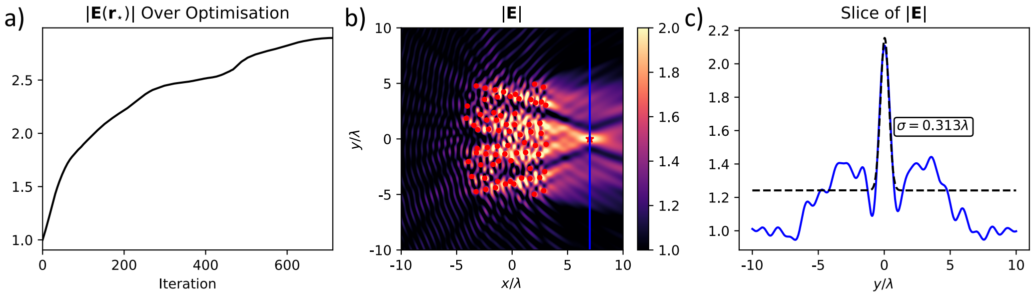

Figure 3.14: Designing a disordered metamaterial version of a lens. The device focuses the energy from a plane wave to a point, shown as the red star. The figure of merit for this optimisation is the modulus of the electric field at the target location (3.55); a) shows the increase of this quantity as a function of progressing optimisation and b) is the final design. A cut of the field along the blue line is given in c) showing the narrow focus.

We now consider the popular problem of lensing. Traditional lenses are made by shaping glass so that light entering it acquires a particular spatially varying phase offset so that it is focused to a point [106]. Much recent work has mimicked this behaviour using metamaterials, for optical [53] and acoustic [107] applications. Using metamaterials, rather than traditional optics, has a number of benefits. For example, metamaterials can be much thinner than glass optics making optical devices more compact. Also, much more complicated functionality can be achieved, including multiple foci, holograms and polarisation control [53, 64]. While not based on phase arguments, our method can be employed to design structures that focus plane waves to particular points in space, performing a similar function to a lens. The benefit of not being limited by simple phase arguments is that more precise control over the field can be achieved, beyond redirection.

For this lensing problem, the source fields in the solutions to Maxwell's equations (2.117) are plane waves, with a particular polarisation and wave–vector. For the example in Figure 3.14, we choose a TE polarised wave with wave–vector $\boldsymbol{k} = k\hat{\boldsymbol{x}}$. The figure of merit is the magnitude of the electric field at the target location $\boldsymbol{r}_\star$.

$$\mathcal{F}_{\text{lens}} = |\boldsymbol{E}(\boldsymbol{r}_\star)|. \tag{3.55}$$

This is similar to the figure of merit of the example in Section 3.5, where we wanted to beam into a particular far–field direction. Now instead, we select a point near the structure as the target location so that the radiation is focused there. The figure of merit can be expanded to first order under small changes in the fields as before

$$
\begin{aligned}
|\boldsymbol{E}(\boldsymbol{r}_\star)| &= \sqrt{\boldsymbol{E}(\boldsymbol{r}_\star)\cdot\boldsymbol{E}^*(\boldsymbol{r}_\star)}, && (3.56)\\
&= \sqrt{(\boldsymbol{E}(\boldsymbol{r}_\star)+\delta\boldsymbol{E}(\boldsymbol{r}_\star))\cdot(\boldsymbol{E}^*(\boldsymbol{r}_\star)+\delta\boldsymbol{E}^*(\boldsymbol{r}_\star))}, && (3.57)\\
&= \sqrt{|\boldsymbol{E}(\boldsymbol{r}_\star)|^2 + 2\mathrm{Re}\left[\delta\boldsymbol{E}(\boldsymbol{r}_\star)\cdot\boldsymbol{E}^*(\boldsymbol{r}_\star)\right]}, && (3.58)\\
&= |\boldsymbol{E}(\boldsymbol{r}_\star)|\sqrt{1+\frac{2\mathrm{Re}\left[\delta\boldsymbol{E}(\boldsymbol{r}_\star)\cdot\boldsymbol{E}^*(\boldsymbol{r}_\star)\right]}{|\boldsymbol{E}(\boldsymbol{r}_\star)|^2}}, && (3.59)\\
&\approx |\boldsymbol{E}(\boldsymbol{r}_\star)| + \frac{\mathrm{Re}\left[\delta\boldsymbol{E}(\boldsymbol{r}_\star)\cdot\boldsymbol{E}^*(\boldsymbol{r}_\star)\right]}{|\boldsymbol{E}(\boldsymbol{r}_\star)|}. && (3.60)
\end{aligned}
$$

Substituting the expression for the variation of the fields gives the following change in the figure of merit $\mathcal{F}_{\text{lens}}$

$$
\begin{aligned}
\delta\mathcal{F}_{\text{lens}} = \frac{-1}{|\boldsymbol{E}(\boldsymbol{r}_\star)|}\sum_n \mathrm{Re}\Big[\Big\{&\xi^2\boldsymbol{G}(\boldsymbol{r}_\star,\boldsymbol{r}_n)\boldsymbol{\alpha}_E\nabla\boldsymbol{E}(\boldsymbol{r}_n)\\
&+i\xi\boldsymbol{G}_{EH}(\boldsymbol{r}_\star,\boldsymbol{r}_n)\boldsymbol{\alpha}_H\nabla\boldsymbol{H}(\boldsymbol{r}_n)\Big\}\cdot\boldsymbol{E}^*(\boldsymbol{r}_\star)\Big]\,\delta\boldsymbol{r}_n.
\end{aligned}
\tag{3.61}
$$

As this is linear in $\delta\boldsymbol{r}_n$, we can choose $\delta\boldsymbol{r}_n$ to be proportional to the expression in the square brackets for each scatterer to guarantee that the gradient of the figure of merit has a particular sign. The result of applying this procedure is shown in Figure 3.14. A structure is designed that focuses the field to the desired location. Fitting a Gaussian of the form

$$
\mathcal{G}(y) = A\exp\left(\frac{(y-\mu)^2}{2\sigma^2}\right)+B \tag{3.62}
$$

to the peak, we find that the width of the focus is $\sigma\sim\lambda/3$.

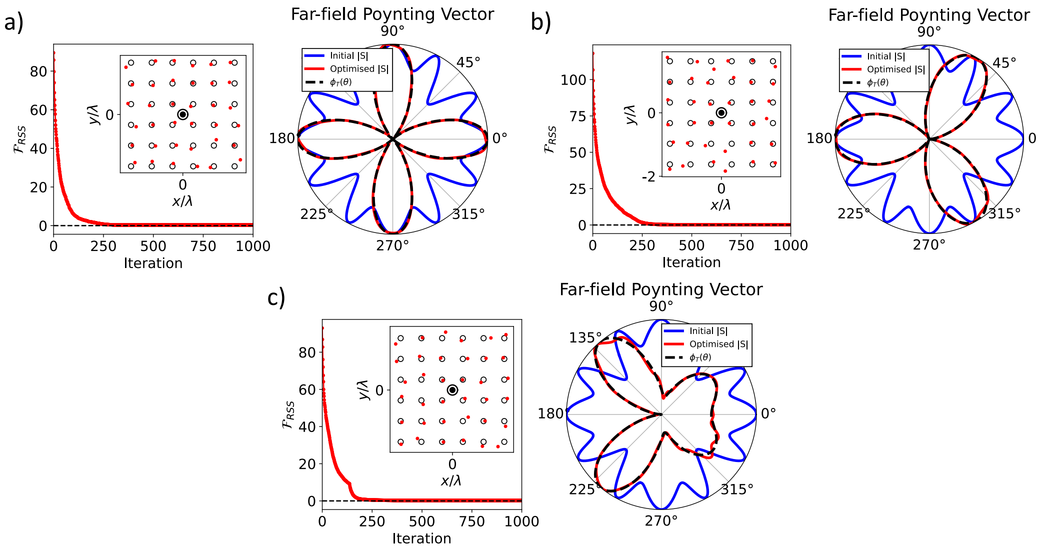

Figure 3.15: The design of a metamaterial with a chosen radiation pattern. In each case, the structure is driven by an emitter polarised along the z axis at the origin. For each of the target radiation patterns, black dashed lines, the scatterers begin at the locations indicated by black circles and are iteratively moved to reduce the difference between the radiation pattern and the desired pattern (3.63). The optimised locations of the scatterers are shown as red dots and the final radiation patterns as red lines.

3.9 Shaping the Far–field: Least Squares

The final problem we consider, is shaping the far–field Poynting vector of an emitter. We would like $|\boldsymbol{S}(\theta)|$ to have a particular shape, $\phi_T(\theta)$ in the far–field. Our aim is to design a scattering structure that produces a particular $|\boldsymbol{S}(\theta)|$ in the far–field, defined by a target angular distribution $\phi_T(\theta)$. With our framework, this can be achieved with two different figues of merit

1. The residual sum of squares between the current $|\boldsymbol{S}(\theta)|$ and the target $\phi_T(\theta)$.
2. The overlap integral between $|\boldsymbol{S}(\theta)|$ and $\phi_T(\theta)$.

These are equivalent ways of characterising how similar the two functions are. In this section, we use the residual sum of squares as the figure of merit, in the next we use the overlap integral.

Our figure of merit is therefore

$$\mathcal{F}_{\text{RSS}} = \sum_i \left[|\boldsymbol{S}(\theta_i)| - \phi_T(\theta_i)\right]^2 . \tag{3.63}$$

In order to use this figure of merit, both $|\boldsymbol{S}(\theta_i)|$ and $\phi_T(\theta_i)$ must be normalised to range from 0 to 1. To calculate how the scatterers should be moved to minimise this figure of merit, we expand it under small changes in $\delta|\boldsymbol{S}(\theta)|$

$$\begin{aligned}\sum_i \left[|\boldsymbol{S}(\theta_i)| - \phi_T(\theta_i)\right]^2 &= \sum_i \left(|\boldsymbol{S}(\theta_i)| + \delta|\boldsymbol{S}(\theta_i)| - \phi_T(\theta_i)\right) \\ &\quad \times \left(|\boldsymbol{S}(\theta_i)| + \delta|\boldsymbol{S}(\theta_i)| - \phi_T(\theta_i)\right), \\ &= \sum_i |\boldsymbol{S}(\theta_i)|^2 + \phi_T^2(\theta_i) + 2\delta|\boldsymbol{S}(\theta_i)|(|\boldsymbol{S}(\theta_i)| - \phi_T(\theta_i)),\end{aligned} \tag{3.64}$$

and retaining only first order terms, we find that

$$\delta\mathcal{F}_{\text{RSS}} = \sum_i \left[2\delta|\boldsymbol{S}(\theta_i)|(|\boldsymbol{S}(\theta_i)| - \phi_T(\theta_i)\right] . \tag{3.65}$$

It is then necessary to find $\delta|\boldsymbol{S}|$, the variation in the Poynting vector, in terms of the variations in the fields. Using the expression we obtained from expanding the modulus of the electric field (3.60), we know that

$$\delta|\boldsymbol{S}| = \frac{\text{Re}\left[\delta\boldsymbol{S}\cdot\boldsymbol{S}^*\right]}{|\boldsymbol{S}|}. \tag{3.66}$$

Then, $\delta\boldsymbol{S}$ can be derived from the expression for the Poynting vector

$$\boldsymbol{S} = \frac{1}{2}\boldsymbol{E}\times\boldsymbol{H}^* \tag{3.67}$$

$$= \frac{1}{2}(\boldsymbol{E}+\delta\boldsymbol{E})\times(\boldsymbol{H}^*+\delta\boldsymbol{H}^*), \tag{3.68}$$

$$\delta\boldsymbol{S} = \frac{1}{2}\left[\boldsymbol{E}\times\delta\boldsymbol{H}^* + \delta\boldsymbol{E}\times\boldsymbol{H}^*\right]. \tag{3.69}$$

Substituting this into (3.65) gives us the change of the figure of merit in terms of the changes in the fields, which are linear in $\delta \boldsymbol{r}_n$. As with the previous examples the expressions for the field variations, (3.16) and (3.17), can be substituted in to yield an expression for moving the scatterers to decrease this figure of merit. Figure 3.15 shows that structures exhibiting three arbitrary far-field radiation patterns can be generated using our method.

3.10 Shaping the Far–field: Overlap Integral

Figure of merit choices are not unique, and often in optimisation one should choose the one that is easier to evaluate. As well as using the residual sum of squares, one can use the overlap integral (inner product) to characterise how similar the far–field distribution of the Poynting vector is to the desired radiation pattern. We will define the 1D normalised overlap integral of two real scalar functions $\phi(\theta)$, $\phi_T(\theta)$ as

$$\mathcal{F} = \frac{\int d\theta \phi(\theta) \phi_{\mathrm{T}}(\theta)}{\sqrt{\int d\theta \phi^2(\theta) \int d\theta' \phi_{\mathrm{T}}^2(\theta')}}. \tag{3.70}$$

Here, the functions $\phi(\theta)$, $\phi_T(\theta)$ represent some quantities in the far-field: $\phi(\theta)$ is the current distribution of the quantity we are interested in, evaluated in the far-field, and $\phi_T(\theta)$ a target distribution. This figure-of-merit quantifies the similarity between the angular distribution of $\phi(\theta)$ and the target $\phi_T(\theta)$, ranging from 0 to 1. As will be shown, this figure-of-merit can be used to optimize a scatterer array to determine the exact shape of the far-field Poynting vector.

To use the figure-of-merit to calculate how to move a scatterer such that the merit function is guaranteed to increase, we expand under variation in

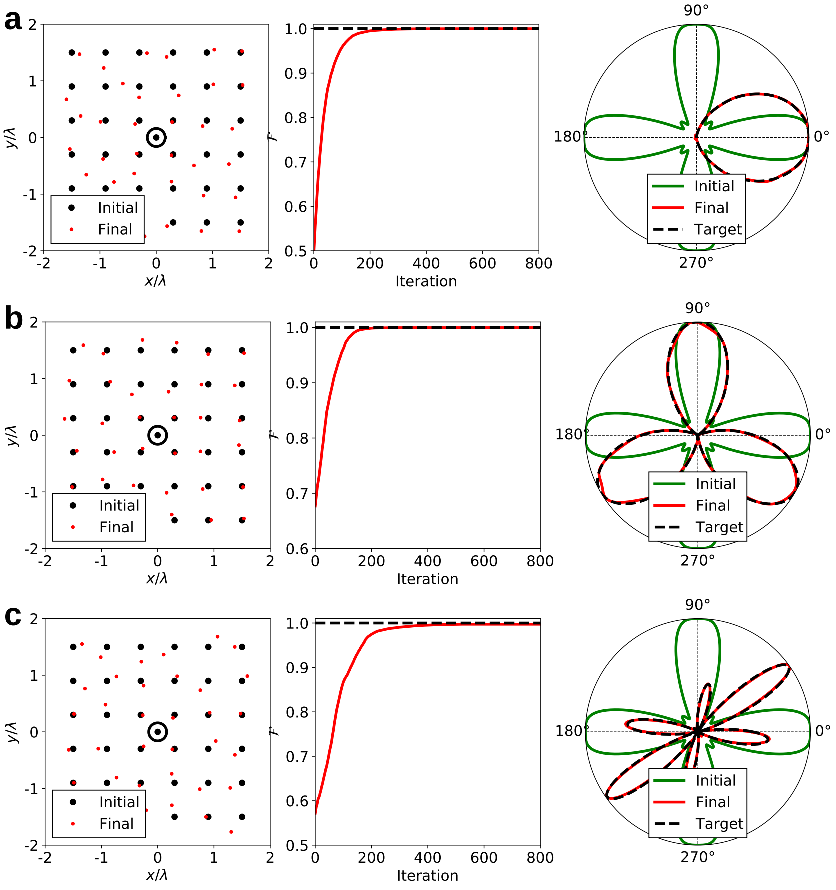

Figure 3.16: Design of far-field Poynting vector distribution, using an alternative figure of merit. (a-c) show examples of the same procedure for three different target distributions. In each case, the far-field power distribution of an isotropic emitter located at the origin in engineered. Beginning from some initial distribution of scatterers, shown as black dots, equation (3.72) is used to iteratively move the scatterers to enhance the figure-of-merit, defined as the overlap of the far-field Poyning vector $|\boldsymbol{S}(\theta)|$ and the target distribution $\phi_T(\theta)$. The optimized locations are shown as red dots. The change in the overlap integral with iteration number and far-field distributions are shown.

$\phi(\theta)$ to first order $\phi(\theta) \to \phi(\theta) + \delta\phi(\theta)$, giving

$$\delta\mathcal{F} = \frac{\int d\theta \delta\phi(\theta)\phi_{\mathrm{T}}(\theta) - \frac{\int d\theta\phi_{\mathrm{T}}(\theta)\phi(\theta)}{\int d\theta\phi^2}\int d\theta\phi(\theta)\delta\phi(\theta)}{\sqrt{\int d\theta\phi^2(\theta)\int d\theta'\phi_{\mathrm{T}}^2(\theta')}}. \tag{3.71}$$

The first term of (3.71) comes from expansion of the numerator of (3.70), while the second term is due to the expansion of the normalisation factor. To consider a specific use of this type of figure-of-merit, let us say that

$\phi(\theta) = |\boldsymbol{S}(\theta)| = \sqrt{\boldsymbol{S}\cdot\boldsymbol{S}^*}$: the modulus of the Poynting vector in the far-field. This describes the shape of how power is radiated. Expanding the Poynting vector to first order as in the previous section, we find that the expansion of the figure of merit is

$$\begin{aligned}\delta\mathcal{F} = \frac{1}{2\sqrt{\int d\theta|\boldsymbol{S}(\theta)|^2 \int d\theta'\phi_{\mathrm{T}}^2(\theta')}} \times \\ \left[\int \frac{d\theta}{|\boldsymbol{S}(\theta)|}\mathrm{Re}\left\{\boldsymbol{S}^*(\theta)\cdot[\delta\boldsymbol{E}\times\boldsymbol{H}^* + \boldsymbol{E}\times\delta\boldsymbol{H}^*]\right\}\phi_{\mathrm{T}}(\theta)\right. \\ \left. -\frac{\int d\theta\phi_{\mathrm{T}}(\theta)|\boldsymbol{S}(\theta)|}{\int d\theta|\boldsymbol{S}(\theta)|^2}\int d\theta\,\mathrm{Re}\left\{\boldsymbol{S}^*(\theta)\cdot[\delta\boldsymbol{E}\times\boldsymbol{H}^* + \boldsymbol{E}\times\delta\boldsymbol{H}^*]\right\}\right]\end{aligned} \tag{3.72}$$

Substituting into this the expressions connecting the variation of the fields due to scatterers being moved, we have an analytic expression for the gradient of the figure of merit, although the integrals need to be evaluated numerically. Figure 3.16 shows several examples of designing structures that shape the emssion of a dipole. An isotropic emitter aligned along the z axis (out of the plane) is surrounded by an array of scatterers. All numerical parameters are identical to those of Table 1 in the main paper. Applying (3.72) to calculate how to iteratively move the scatterers, several different angular distributions of the Poynting vector can be realised to a high degree of accuracy.

3.11 Comparison with Full–Wave Simulations

To validate our analytic work and to investigate the validity of our approximations, we present a comparison with full-wave simulations, shown in Figure 3.17. A simple design involving only 16 scatterers was generated using our design method, with the aim of enhancing directivity along the 0°

direction. Analytic results for both far-field radiation pattern and the complex fields were compared to results from COMSOL [68]. In the full-wave simulation, scatterers were modelled as finite silicon spheres of the correct radius and the emitter is treated as a point source. Near and far fields of

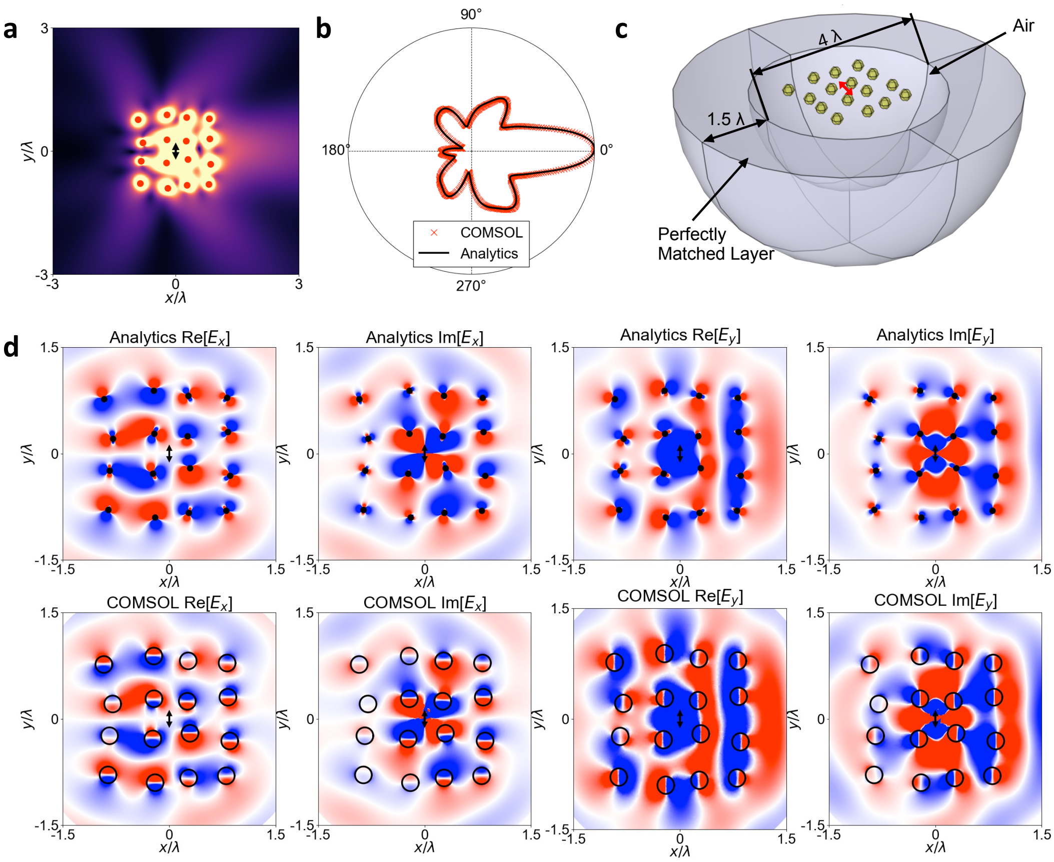

Figure 3.17: Comparison between our analytic results and a full-wave simulation. (a) shows the designed structure. (b) shows a comparison between $|\boldsymbol{S}|$ calculated in COMSOL and using analytic theory. Residual sum of square errors between the analytic results and numerical results is 0.044, demonstrating excellent agreement. (c) schematic setup of the full-wave simulation, with the emitter shown as a red arrow and the scatterers as yellow spheres. (d) shows a detailed comparison between the calculated fields of the analytic model compared to COMSOL. In all cases, the emitter is shown as a black arrow at the origin. For analytic plots, scatterers are represented as black dots indicating they are treated as points, while for COMSOL plots the scatterers are drawn as finite circles to show how they were modelled.

the designed structure are shown in Figure 3.17 (a) and (b) respectively. The COMSOL setup is shown in Figure 3.17 (c), with the point emitter shown as a red arrow. A perfectly matched layer (PML) is necessary to absorb boundary reflections to simulate an infinite medium. In the plane of the scatterers, the real and imaginary parts of the relevant components of the electric field generated from our analytic solutions to Maxwell's equations, within the coupled dipole approximation, are compared with COMSOL in Figure 3.17 (d). Even though in the analytic results the scatterers are modelled as points, while in COMSOL they have a finite size, the agreement between the fields is excellent. This demonstrates that for our choice of system the discrete dipole approximation works very well, and the approximations behind it are well justified.

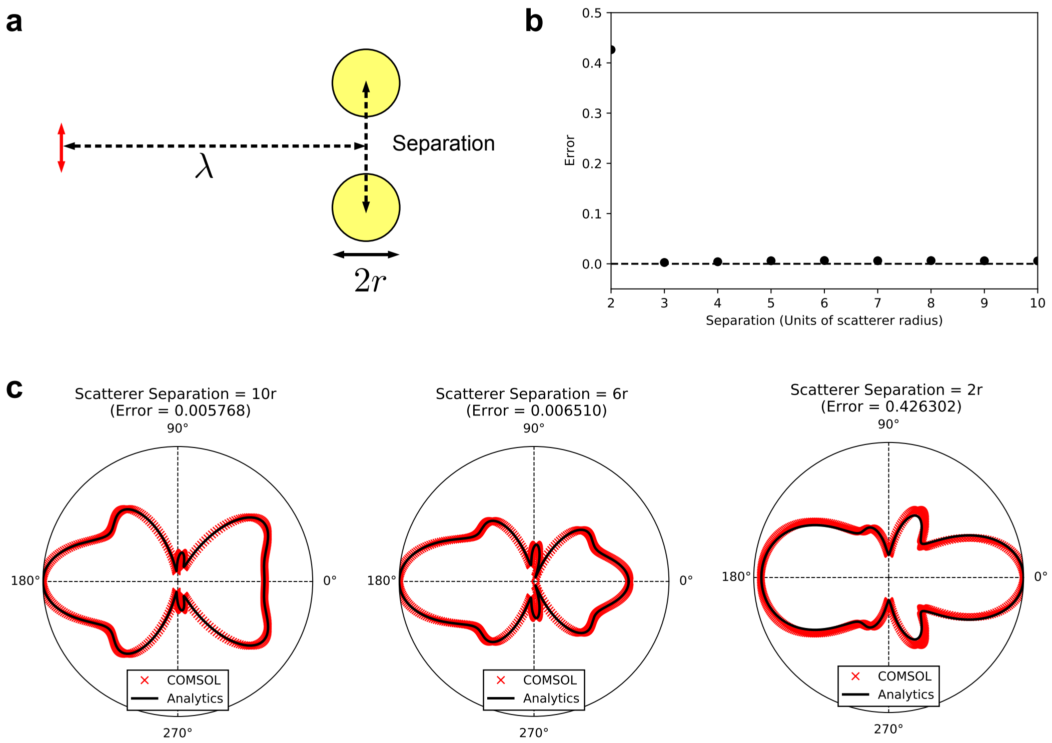

Figure 3.18: Investigating the validity of the dipole approximation. (a) shows the setup of the study. A point dipole emitter, aligned along the y axis is located at the origin. Two silicon spheres of radius 65 nm are placed at $(\lambda, \pm d/2)$, where d is the scatterer separation. As d is varied, the difference between the far-field Poynting vector calculated using COMSOL and using the analytic dipole approximation is recorded. (b) shows how the error, characterised as the sum of square errors between the analaytic and full-wave results, changes with separation. (c) Directly compares $|\boldsymbol{E}|$ in the far-field calculated using COMSOL and the dipole approximation.

During the optimisation procedure, we impose the constraint that scatterers cannot get too close. While the scatterers are *modelled* as points, they represent physical objects with spatial extent; in this case spheres of radius 65 nm. To preserve this, we stop the scatterers from sitting on top of each other or passing through each other. Scatterers, with radius r, are prevented from getting any closer than $3r$ to avoid this issue. In addition, some works have shown that the resonances of nearby resonators are shifted due to near–field coupling. To investigate the robustness of our setup to this coupling, a simple numerical investigation was performed using COMSOL. A dipole emitter, aligned along the y axis, was located at the origin. One scatterer was placed at $(\lambda, d/2)$ and another at $(\lambda, -d/2)$, where d is the separation between the scatterers. Both scatterers are modelled as silicon spheres of radius 65 nm. COMSOL's full-wave solver was used to extract the far-field radiation pattern and this was compared to analytic results based upon the dipole approximation, where the scatterers are treated as points. The error, characterised as the residual sum of squares, between analytic results and the full-wave solution was calculated for a range of separations. A schematic of the procedure, as well as the results, are shown in Figure 3.18. For separations $\geq 3r$ the error is small: of the order 10^{-3}. At a separation of $2r$, when the scatterers are touching, the error is much larger. However, qualitatively, the far-field radiation pattern is still reasonably well reproduced. These results indicate that the restriction on scatterer separation might be relaxed without causing much error. We note that closly spaced scatterers will interact in a manner not captured by the dipole approximation. However, it is possible to introduce correction terms [108] that allow the coupled dipole framework to be utilised for closely spaced scatterers.

3.12 Summary & Conclusions

In this chapter we began from Maxwell's equations and used perturbation theory to derive equations that connect a small change in the position of an electric and/or magnetic dipole scatterer to the change in the electric and magnetic fields. Utilising these analytic expressions to find an efficient optimisation framework, we considered figures of merit written in terms of the fields. Such figures of merit were expanded under small changes in the fields, into which we could substitute the expressions connecting small changes in the fields to small changes in scatterer locations. This gives an analytical expression for the gradient of a given figure of merit with respect to the positions of all of the scatterers. It is key that this can be evaluated for all scatterers simultaneously, making the resulting gradients very efficient to find numerically. Our semi–analytic gradients are then used to perform simple gradient descent optimisation, iteratively changing the positions of a collection of scatterers to increase many different figures of merit. Our optimisation framework is applied to a wide range of antennas related problems. For example: increasing the power emission from a small emitter, key to miniaturisation; manipulating the far–field radiation pattern of an emitter; reducing the coupling between nearby emitters, crucial to constructing base stations.

As well as a design framework, we also develop a simple paradigm for analysing the behaviour of strongly multiple scattering structures. Decomposing the response of the device into the eigenmodes of the scattering system yields three quantities of interest. First, the expansion coefficient describes how strongly a given eigenmode is excited. Second, the eigenvalue of the mode corresponds to an 'eigenpolarisability', characterising how strongly the structure responds to the input field when this mode is excited. Third, the spatial distribution of the field of the eigenmode dictates the response of the system. The performance of the device designed to enhance power emission is dominated by a single mode that has a large expansion coefficient, and therefore a large overlap with the source field, as well as a large eigenvalue, corresponding to a strong response. The structure designed to beam radiation into a particular direction has a handful of modes with large eigenvalue and large expansion coefficient. While some of these exhibit clear beaming into the desired direction, the resulting behaviour is clearly due to the interference of many eigenmodes. It remains to be seen whether this framework can add insight to other highly scattering, disordered, systems as well as whether it can be utilised directly to aid optimisations.

Chapter 4

Designing Multi–Functional Devices

"Nobody in this world can tell me what to think, but everyone has a lesson to teach me" – Lex Fridman

The results of this chapter have been published in:

- J. R. Capers, S. J. Boyes, A. P. Hibbins and S. A. R. Horsely "Designing Disordered Multi–Functional Metamaterials using the Discrete Dipole Approximation" New J. Phys. **24** 113035 (2022)

The ability to multiplex the functionality of electromagnetic materials is key to the eventual application of metamaterials to communications problems. While many techniques exist that design uni–functional metamaterials, the design of multi–functional materials remains challenging. Beginning from general considerations of wave–equations, we derive a hard constraint upon wave fields that are to be supported by the same material distribution. We then extend the method presented in the previous chapter to enable the design of multi–functional metamaterial devices. Two key examples are shown to illustrate the utility of our approach. Firstly, we design a device that beam steers based on the polarisation of an emitter. Secondly, we design a device that sorts radiation by its direction of incidence. Both of these devices have clear utility in communications applications.

4.1 Introduction

To achieve the speed and bandwidth required of next–generation communications networks, it will be necessary to multiplex functionality. This means carrying information in different wavelengths, polarisations or modes at the same time, to increase the amount of information that can be transmitted. One way to achieve such functionality is by using metamaterials to combine the transmitted field then to split it up again on the receiving end. As such, there has been much interest in the design of metamaterials that passively perform different operations on input fields based upon their wavelength [60, 109], polarisation [110], mode shape [61] or source position [111]. Such multi–functional materials can be used to design devices such as spectrometers [112] and even photonic computers [113]. Indeed, in optics, being able to 'spatially multiplex' or transmit data using multiple spatial modes [114–

118] has attracted significant attention. However, many of the solutions involve multi–mode fibers, which are not directly applicable to wireless communications problems. Instead, multi–functional metamaterials have been used to manipulate the radiation from a source directly. This has led to multi–functional antennas [119] that radiate differently at different wavelengths. If one can also modulate the material then real–time beam steering can also be achieved [120–122]. However, designing multi–functional metamaterials remains challenging.

To understand why the design of multi–functional materials is challenging, we consider an electric field $\boldsymbol{E}(\boldsymbol{r})$ of a fixed frequency $\omega = ck_0$, with wave number k_0, in a material with a spatially varying permittivty $\varepsilon(\boldsymbol{r})$. This wave obeys the vector Helmholtz equation,

$$\nabla \times \nabla \times \boldsymbol{E}(\boldsymbol{r}) + k_0^2 \varepsilon(\boldsymbol{r}) \boldsymbol{E}(\boldsymbol{r}) = 0. \tag{4.1}$$

The difficulty in the design of multi–functional materials is the problem of finding a single material distribution (here the permittivity, ε) that performs two (or more) desired wave transformations. This means that both of the desired wave behaviours, $\boldsymbol{E}_1(\boldsymbol{r})$ and $\boldsymbol{E}_2(\boldsymbol{r})$ must be solutions to the same Helmholtz equation,

$$\nabla \times \nabla \times \boldsymbol{E}_1(\boldsymbol{r}) + k_0^2 \varepsilon(\boldsymbol{r}) \boldsymbol{E}_1(\boldsymbol{r}) = 0, \quad \nabla \times \nabla \times \boldsymbol{E}_2(\boldsymbol{r}) + k_0^2 \varepsilon(\boldsymbol{r}) \boldsymbol{E}_2(\boldsymbol{r}) = 0. \tag{4.2}$$

From this statement, we can find a condition upon the two wave–fields for this to be possible. Multiplying the first of these by $\boldsymbol{E}_2(\boldsymbol{r})$ and the second by $\boldsymbol{E}_1(\boldsymbol{r})$, then taking the difference eliminates the material properties such that

$$\boldsymbol{E}_2(\boldsymbol{r}) \cdot [\nabla \times \nabla \times \boldsymbol{E}_1(\boldsymbol{r})] - \boldsymbol{E}_1(\boldsymbol{r}) \cdot [\nabla \times \nabla \times \boldsymbol{E}_2(\boldsymbol{r})] = 0. \tag{4.3}$$

Integrating this over all space, then using Green's vector identity [17], we find that

$$\oint_{\partial V} \left[\boldsymbol{E}_2(\boldsymbol{r}) \times \nabla \times \boldsymbol{E}_1(\boldsymbol{r}) - \boldsymbol{E}_1(\boldsymbol{r}) \times \nabla \times \boldsymbol{E}_2(\boldsymbol{r})\right] \cdot d\boldsymbol{S} = 0. \tag{4.4}$$

This condition, equivalent to reciprocity, places a stringent constraint on the two wave–fields if they are to be supported by the same material, which can be used to derive fundamental bounds on the performance of multi–functional devices [123]. Indeed (4.4) is a generalization of Poynting's theorem, representing the conservation of the norm of the system modes; ensuring for example, their orthogonality. To better understand the connection between the above equation and energy conservation, consider the special case where we demand the same permittivity distribution supports the solution $\boldsymbol{E}_1(\boldsymbol{r}) = \boldsymbol{E}$ and its complex conjugate (time reverse) $\boldsymbol{E}_2(\boldsymbol{r}) = \boldsymbol{E}^*$. The surface integral (4.4) can then be re–written using the divergence theorem,

$$\nabla \cdot \left(\boldsymbol{E} \times \nabla \times \boldsymbol{E}^* - \boldsymbol{E}^* \times \nabla \times \boldsymbol{E}\right) = 0. \tag{4.5}$$

Applying Maxwell's equations to convert the curls into magnetic fields $\nabla \times \boldsymbol{E} = -i\omega\eta_0\boldsymbol{H}$, where η_0 is the impedance of free space, we find

$$\nabla \cdot \left(\boldsymbol{E} \times \boldsymbol{H}^* + \boldsymbol{E}^* \times \boldsymbol{H}\right) = 0, \tag{4.6}$$

which is the usual expression for energy conservation expressed in terms of the Poynting vector $\boldsymbol{S} = \frac{1}{2}\mathrm{Re}\left[\boldsymbol{E} \times \boldsymbol{H}^*\right]$.

A direct application of Eq. (4.4) to design multi–functional materials is generally difficult. Instead several other design methodologies have emerged recently [124]. Typically, however, these methods either employ limiting assumptions such as only allowing the materials to impart a phase shift [63, 64], or require many full–wave simulations. Even with the efficiency of the adjoint method [76], at least two simulations are required. If one wants to design a material that performs different functions at i.e. two wavelengths, four full–wave simulations are required. Thus existing methods rapidly become intractable when used to design multi–functional metamaterials. In this chapter, we generalise the results of Chapter 3 to allow for the design of multi–functional devices. Beginning with some general comments about what is required in the design of a multi–functional device, we consider the toy example of increasing the efficiency of an antenna while also manipulating its radiation pattern. We then progress to design a device that beams radiation into different directions based upon the polarisation of the source, as well as a device that 'sorts' plane waves by their direction of incidence.

4.2 Multi–Objective Optimisation Considerations

Extending the method presented in Chapter 3 to apply to multi–functional metamaterials, requires one to seek to increase some set of figures of merit $\{F_1, F_2, F_3 \ldots\}$. A composite figure of merit can be constructed that is a weighted sum of these,

$$\mathcal{F} = \sum_i w_i F_i, \tag{4.7}$$

where w_i are the weights for each figure of merit. This composite figure of merit can be optimised in the same way as a single figure of merit, where the overall gradient becomes

$$\frac{\partial \mathcal{F}}{\partial \boldsymbol{r}_n} = \sum_i w_i \frac{\partial F_i}{\partial \boldsymbol{r}_n}. \tag{4.8}$$

Key to the success of this method is a sensible choice of the weights, w_i. An appropriate choice can be informed by considering the desired properties of the resulting device. Consider a simple example problem, shown in Figure 4.1. The goal is to distribute scatterers around a point emitter at location $\boldsymbol{r}'$ with polarisation $\boldsymbol{p} = \hat{\boldsymbol{z}}$ such that *two* figures of merit are simultaneously maximised. More specifically, the goal is to re–shape the radiation pattern of

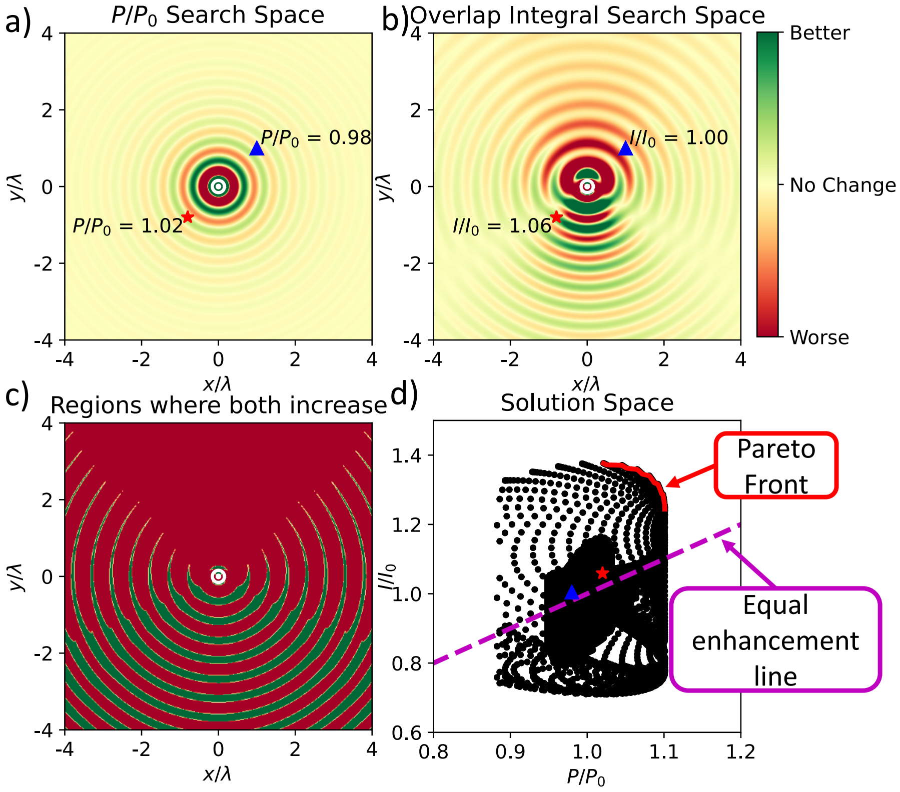

Figure 4.1: An example of a multi–objective optimisation problem. We seek to shape the radiation pattern of a dipole emitter pointing out of the plane along the z axis, while also increasing its efficiency. To achieve this, we consider placing a single isotropic scatterer near the emitter and explore the effect this has upon the figures of merit: the power emission and the radiation pattern. a) Shows how placing a scatterer at a particular point changes the power emission and b) shows how the overlap integral is changed. These represent the search spaces of the problem. The additional difficulty posed by *multi*, rather than single, objective problems is shown in c). A scatterer can only be placed in the green regions, where both figures of merit are enhanced. Each point in the search spaces corresponds to a point in solution space, shown in d). The blue triangle and red star are shown in both search and solution spaces to demonstrate this. Also shown in the solution space, d), is the diagonal 'line of equal enhancement' representing equal performance of each figure of merit and the Pareto front [125], which represents the acceptable solutions to the multi–objective problem.

an emitter, while simultaneously increasing the efficiency. The first figure of merit is the power emitted from the dipole, given by the PLDoS first derived in Section 2.4

$$F_1 = P = \frac{\omega}{2}\mathrm{Im}[\boldsymbol{p}^* \cdot \boldsymbol{E}(\boldsymbol{r'})]. \tag{4.9}$$

The second is the overlap integral between the angular distribution of the Poynting vector in the far–field, $|\boldsymbol{S}(\theta)|$ and a desired angular distribution $\psi_T(\theta)$

$$F_2 = I = \frac{\int d\theta |\boldsymbol{S}(\theta)| \psi_T(\theta)}{\sqrt{\int d\theta |\boldsymbol{S}(\theta)|^2}\sqrt{\int d\theta \psi_T^2(\theta)}}, \tag{4.10}$$

where the angle θ is in the same plane as the metasurface. In the following examples, the target distribution is

$$\psi_T(\theta) = \begin{cases} \cos^2\theta & 270^\circ < \theta < 90^\circ, \\ 0 & \text{otherwise.} \end{cases} \tag{4.11}$$

Both of these can be expanded to first order to find the gradient of the figure of merit with respect to the scatterer locations [126], as we saw in the previous chapter. For convenience, both will be normalised by their free–space values, P_0 and I_0: these are the values of the figures of merit without any scatterers present. Considering the effect of a single scatterer upon these figures of merit, Figure 4.1 (a) and (b) show how placing the scatterer in a particular location increases or decreases each figure of merit. These maps define the search space for the problem. For multi–functional problems, however, there is the additional constraint that a scatterer should only be placed where *both* figures of merit are increased. This is shown in Figure 4.1 (c); it is clear that multi–functional problems are significantly constrained and have complex search spaces. Each scatterer location in the search spaces Figure 4.1 (a) and (b) corresponds to a point in the solution space, shown in

Figure 4.1 (d). To demonstrate this correspondence, the red star and blue triangle are shown in the search and solution spaces. Each point in solution space corresponds to a configuration of scatterers, which in our example is one, but could be any number. The solution space, Figure 4.1 (d), has a few interesting features. The Pareto front [125], shown as a red line, are all acceptable solutions to the multi–objective optimisation problem (i.e. where one figure of merit cannot be improved without sacrificing the other). Along the diagonal, the dashed magenta line, enhancement of the two figures of merit is equal, which is often the desired outcome. It would not be very useful to select a solution point where the emitted power is large but the overlap is small, even if it lies on the Pareto front. This observation informs the choice of weights in the optimisation procedure. The weights are chosen to be proportional to the figure of merit itself,

$$w_i \propto \frac{1}{F_i}\text{ , and normalised so that}\sum_i w_i = 1. \tag{4.12}$$

Choosing the weights to be proportional to $1/F_i$ means that when the figure of merit is small the contribution of the gradient associated with that figure of merit to the sum (4.8) is large, but when the figure of merit is large the contribution is suppressed. Note that the figures of merit must be normalised so that their magnitudes can be meaningfully compared, for example by division by a free space value. Choosing the weights in this way allows for the design of multi–functional metamaterials built from discrete scatterers, for a variety of applications. A few examples are offered in the following section.

4.3 Multi–functional Devices

Continuing with the example developed in the previous section and shown in Figure 4.1, the multi–objective problem of designing a structure that re–shapes the radiation pattern of an emitter in the plane of the metasurface, while also increasing efficiency, is addressed. We work at a wavelength of $\lambda = 550$ nm and the scatterers are small silicon spheres of radius 65 nm. For this system, the polarisability tensor can be found analytically from the Mie a_1 and b_1 coefficients. Our figures of merit are the radiated power (4.9) and the overlap with the desired radiation pattern (4.10) and we choose the weights according to (4.12). As was done in Chapter 3, we expand these figures of merit to first order under small changes in the field to get for the power emission

$$P = \frac{\omega}{2}\mathrm{Im}\left[\boldsymbol{p}^* \cdot \boldsymbol{E}(\boldsymbol{r'})\right], \tag{4.13}$$

$$\delta P = \frac{\omega}{2}\mathrm{Im}\left[\boldsymbol{p}^* \cdot \delta\boldsymbol{E}(\boldsymbol{r'})\right], \tag{4.14}$$

so that

$$\begin{aligned}\nabla_{\boldsymbol{r}_n} P = \frac{\omega}{2}\mathrm{Im}\Big[\boldsymbol{p}^* \cdot \Big(&\xi^2 \boldsymbol{G}(\boldsymbol{r'},\boldsymbol{r}_n)\boldsymbol{\alpha}_E \nabla \boldsymbol{E}(\boldsymbol{r}_n) \\ &+ i\xi\nabla\times\boldsymbol{G}(\boldsymbol{r'},\boldsymbol{r}_n)\boldsymbol{\alpha}_H \nabla \boldsymbol{H}(\boldsymbol{r}_n)\Big)\Big].\end{aligned} \tag{4.15}$$

For the overlap integral, we write

$$\begin{aligned}\delta I = &\frac{1}{2\sqrt{\int d\theta |\boldsymbol{S}(\theta)|^2 \int d\theta' \phi_{\mathrm{T}}^2(\theta')}} \\ &\times \Bigg[\int \frac{d\theta}{|\boldsymbol{S}(\theta)|}\mathrm{Re}\left\{\boldsymbol{S}^*(\theta)\cdot\left[\delta\boldsymbol{E}\times\boldsymbol{H}^* + \boldsymbol{E}\times\delta\boldsymbol{H}^*\right]\right\}\phi_{\mathrm{T}}(\theta) \\ &- \frac{\int d\theta \phi_{\mathrm{T}}(\theta)|\boldsymbol{S}(\theta)|}{\int d\theta |\boldsymbol{S}(\theta)|^2}\int d\theta\, \mathrm{Re}\left\{\boldsymbol{S}^*(\theta)\cdot\left[\delta\boldsymbol{E}\times\boldsymbol{H}^* + \boldsymbol{E}\times\delta\boldsymbol{H}^*\right]\right\}\Bigg].\end{aligned} \tag{4.16}$$

Into these we substitute the expressions connecting the changes in the field to the changes in scatterer positions

$$\delta \boldsymbol{E}(\boldsymbol{r}) = \left[\xi^2 \boldsymbol{G}(\boldsymbol{r},\boldsymbol{r}_n)\boldsymbol{\alpha}_E \nabla \boldsymbol{E}(\boldsymbol{r}_n) + i\xi \nabla \times \boldsymbol{G}(\boldsymbol{r},\boldsymbol{r}_n)\boldsymbol{\alpha}_H \nabla \boldsymbol{H}(\boldsymbol{r}_n)\right] \delta \boldsymbol{r}_n, \tag{4.17}$$

$$\delta \boldsymbol{H}(\boldsymbol{r}) = \left[\xi^2 \boldsymbol{G}(\boldsymbol{r},\boldsymbol{r}_n)\boldsymbol{\alpha}_H \nabla \boldsymbol{H}(\boldsymbol{r}_n) - i\xi \nabla \times \boldsymbol{G}(\boldsymbol{r},\boldsymbol{r}_n)\boldsymbol{\alpha}_E \nabla \boldsymbol{E}(\boldsymbol{r}_n)\right] \delta \boldsymbol{r}_n, \tag{4.18}$$

giving analytic expressions for the gradients of the figures of merit.

Using these gradients, weights (4.12) and the gradient descent method, we design the structures shown in Figure 4.2. For comparison, we also consider the single–objective case where only the far–field radiation pattern is shaped. The resulting far–field radiation patterns are shown in Figure 4.2 a), with the path of the optimisation in solution space shown in Figure 4.2 b) and the two resulting structures shown in Figure 4.2 c) and d). Examining first the radiation pattern, we note that the multi–objective optimisation produces a slightly worse match to the target distribution than the single–objective case. This is due to the trade–off between the two figures of merit we seek to optimise. In solution space, Figure 4.2 b), we see that in the case where only the radiation pattern is shaped (blue line) only a very small change in emitted power is seen. Conversely, when both power and radiation pattern are optimised, the emitted power approximately doubles while the overlap integral also increases. Unlike the case for a single scatterer shown in Figure 4.1, it is impossible to plot the whole search space and visualise the location of the Pareto front. The scatterers have a diameter $\sim \lambda/4$ and our solution box has size 8λ, meaning that there are $32^2 = 1024$ possible 'pixels' a scatterer could occupy. This means that for N scatterers, the number of possible solutions is $1024!/(N!(1024-N)!)$. For $N = 64$,

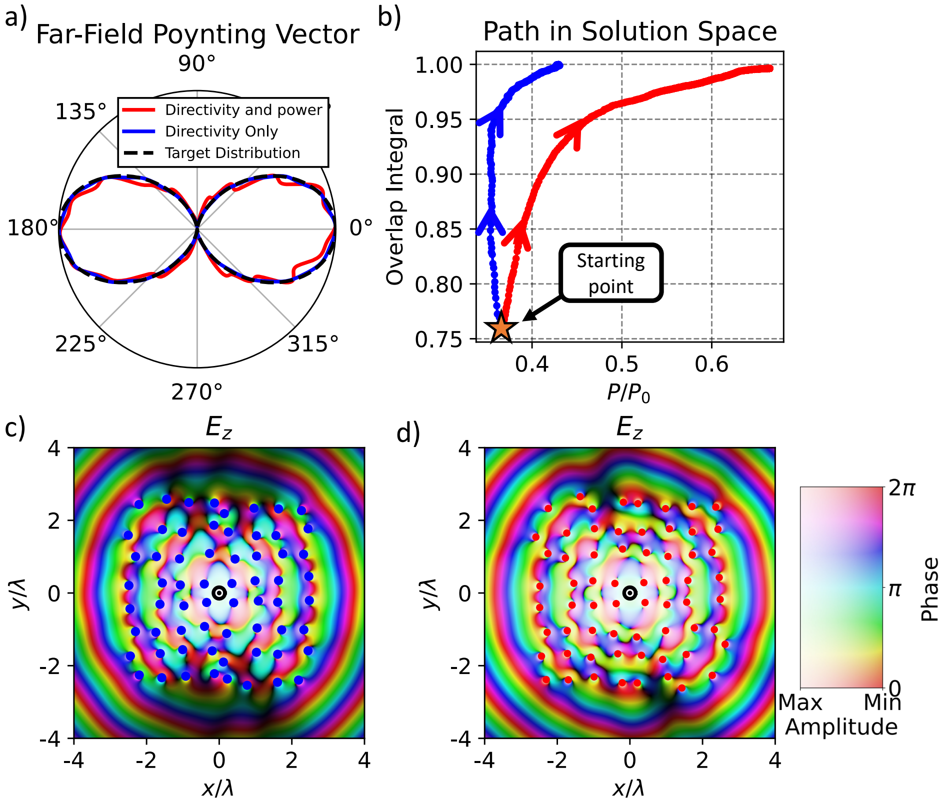

Figure 4.2: Multi–objective optimisation solutions, seeking to increase the emitted power from a dipole while also shaping the far–field radiation pattern into the desired double–lobed shape. For comparison, the single–objective case, where only the radiation pattern is shaped is shown. a) shows the far–field radiation pattern in the plane of the multi–functional structure (red) as well as the target radiation pattern (black dashes). The case where only radiation pattern is shaped is shown in blue. In b), the paths in solution space of the single and multi–objective cases are shown. It is clear that our choice of weightings works well: both figures of merit undergo similar enhancements from their starting values. When only radiation pattern is controlled (blue line) emitted power changes little over the optimisation, however when it is part of the composite figure of merit (red line) clear enhancement is seen at the same time as the overlap integral is increased. The single–objective structure is shown in c) and the multi–objective structure is shown in d), with the emitter polarised out of the page at the origin. In this example, we work at $\lambda = 550$ nm and the scatterers are silicon spheres of radius 65 nm.

this is $\approx 10^{21}$. Despite the exceedingly large search space, which even a genetic algorithm would explore only a very small portion of, our method has found a solution that performs well. A comparison between solving this problem using the method we present and a genetic algorithm is given in Section 4.5.

The second example we consider is manipulating the radiation pattern based on source polarisation. Again, we work at $\lambda = 550$ nm and use 65 nm silicon spheres as the scatterers. We aim to create beams at angles θ_i, associated with source polarisation $\boldsymbol{p}_i$. Our figures of merit are therefore

$$F_i = |\boldsymbol{S}(\theta_i)|. \tag{4.19}$$

The expansion of this to find analytically the gradient is

$$\begin{align}\delta F_i &= 2\mathrm{Re}\left[\boldsymbol{S}^*(\theta_i) \cdot \delta\boldsymbol{S}(\theta_i)\right] \tag{4.20}\\ &= 2\mathrm{Re}\left[\boldsymbol{S}^*(\theta_i) \cdot (\delta\boldsymbol{E}(\theta_i) \times \boldsymbol{H}^*(\theta_i) + \boldsymbol{E}(\theta_i) \times \delta\boldsymbol{H}^*(\theta_i))\right]. \tag{4.21}\end{align}$$

Substituting into this the expressions for the field variations (4.17, 4.18) gives analytic expressions for $\nabla_{\boldsymbol{r}_n} F_i$. We consider the source polarisation being either left or right circularly polarised, i.e.

$$\boldsymbol{p} = \frac{1}{\sqrt{2}} \begin{pmatrix} 1 \\ \pm i \\ 0 \end{pmatrix}. \tag{4.22}$$

The Poynting vector can then be expanded to first order to find the derivatives of the figures of merit for the optimisation procedure. Figure 4.3 a) shows the radiation patterns of the designed structure excited by each of

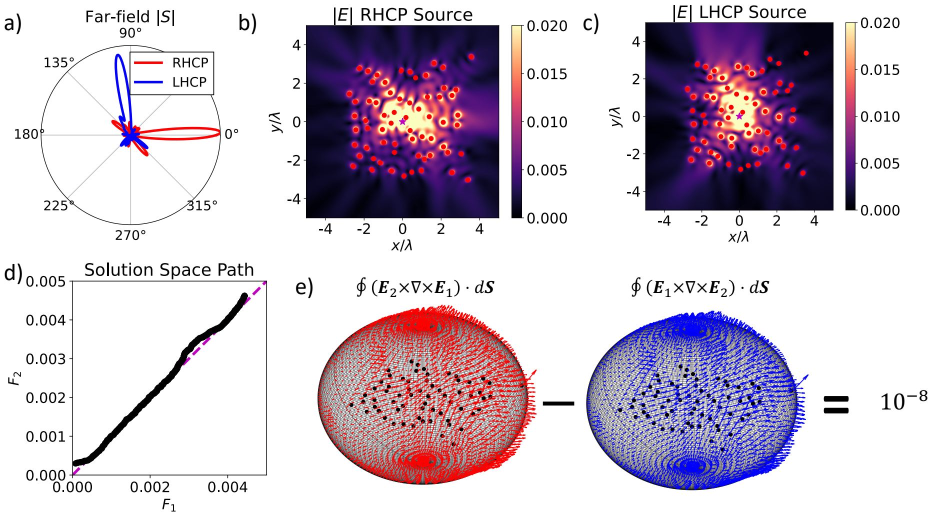

Figure 4.3: Solution to the multi–objective problem of beaming in different directions based on the polarisation of the source. We work at optical wavelengths $\lambda = 550$ nm, using silicon spheres of radius 65 nm as the scatterers. a) shows the far–field Poynting vector in the plane of the metamaterial. The aim was for a right handed source to beam into the 0° direction and for a left handed source to beam into the 100° direction. The optimised structure is shown in b) under a right–handed circular polarisation (RHCP) excitation and c) under left–handed circular polarisation (LHCP) excitation. The emitter is indicated by a magneta star at the origin. The path in solution space of the optimisation, d), shows that over the optimisation both figures of merit are enhanced equally, due to our choice of weights. The multi–functionality condition (4.4) is verified in panel e), by computing the integrals numerically. This yields 10^{-8}, which is small enough to be considered zero within the numerical error associated with evaluating the surface integral.

the two different sources we consider. For a right-handed source, the target angle is $\theta = 0^\circ$ and for a left–handed source, $\theta = 100^\circ$. The far–field Poynting vector in the plane of the metamaterial, Figure 4.3 a), also shows clear peaks at the desired locations, which are also evident in the near–fields shown in Figure 4.3 b) and c). The modulus of the Poynting vector on the far–field sphere, under both left hand (LHCP) and right hand (RHCP) excitation, is given in Figure 4.4. From this, it is clear that the radiation is being sent to the desired locations. The path in solution space, Figure 4.3 d), shows that the choice of weighting has ensured that the performance of both figures of merit remain similar over the optimisation and in the final result. The multi–functionality condition (4.4) is considered in Figure 4.3 e).

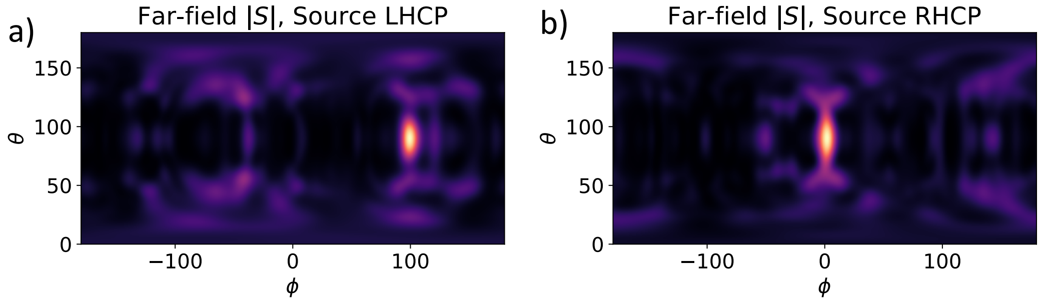

Figure 4.4: Modulus of the Poynting vector in the full far–field for the structure shown in Figure 4.3.

Forming the vector fields $\boldsymbol{E}_i \times \nabla \times \boldsymbol{E}_j$ on the surface of a sphere enclosing the structure, integrating over the surface and taking the difference yields a result of the order 10^{-8}, within expected numerical error.

The third and final example we consider is designing a device for beam sorting. Working at 15.5 GHz and using 'metacubes' [127] as the scattering element. The metacubes, formed of six metal faces joined by three connecting spokes, exhibit a strong dipole resonance at 15.5 GHz. Due to their complexity the polarisability tensor cannot be found analytically. Instead, one can model a single scatterer under plane–wave incidence using a full–wave solver such as COMSOL [68] and integrate over the currents to find the electric and magnetic dipole moments [38, 45], from which one can find the polarisability tensors. This is discussed in detail in Appendix B. Optimisation of a structure of many complex scatterers using such full–wave methods quickly becomes intractable. Our method presents the key benefit of being able to model large systems of potentially complicated scatterers, provided they can be approximated as dipoles, although it is possible to include higher order multipoles into the formalism [40–42]. We seek a structure of metacubes that takes plane waves from different directions and focuses them to distinct points. A device of this sort could be used, for example, to detect from which direction a signal is coming. The figures of merit for this problem are:

$$F_1 = |\boldsymbol{E}_1(\boldsymbol{r}_1)|^2, \qquad\qquad F_2 = |\boldsymbol{E}_2(\boldsymbol{r}_2)|^2, \tag{4.23}$$

where $\boldsymbol{r}_i$ denotes the location to focus the wave at for incident direction i and $\boldsymbol{E}_i$ is the electric field produced by the structure under incidence from direction i. The gradients of these figures of merit are

$$\begin{aligned} \delta F_i &= 2\mathrm{Re}\left[\boldsymbol{E}^*(\boldsymbol{r}_i)\cdot\delta\boldsymbol{E}(\boldsymbol{r}_i)\right], \\ \nabla_{\boldsymbol{r}_n} F_i &= 2\mathrm{Re}\Big[\boldsymbol{E}^*(\boldsymbol{r}_i)\cdot\Big(\xi^2\boldsymbol{G}(\boldsymbol{r}_i,\boldsymbol{r}_n)\boldsymbol{\alpha}_E\nabla\boldsymbol{E}(\boldsymbol{r}_n) \\ &\quad + i\xi\nabla\times\boldsymbol{G}(\boldsymbol{r}_i,\boldsymbol{r}_n)\boldsymbol{\alpha}_H\nabla\boldsymbol{H}(\boldsymbol{r}_n)\Big)\Big]. \end{aligned} \tag{4.24}$$

The structure resulting from this optimisation is shown in Figure 4.5. Operation of the device when driven by a TE plane wave incident at 20° is shown in Figure 4.5 a) and for a plane wave at -20° in Figure 4.5 b). The two different focus points are clearly visible in the fields. The path in solution space is shown in Figure 4.5 d), where again the choice of weighting has ensured roughly equal performance of F_1 and F_2. Slices of the fields from Figure 4.5 a),b) are shown in Figure 4.5 c), indicating the large main peaks at the desired focus locations. The initial and final structures are shown in 4.5 e),f). We begin from an ordered 3D arrangement of metacubes and the optimisation procedure introduces disorder to achieve the desired functionality. The validity of the multi–functionality condition is shown in Figure 4.5 g). Here, the numerical error is larger due to the highly oscillatory nature of the integrands.

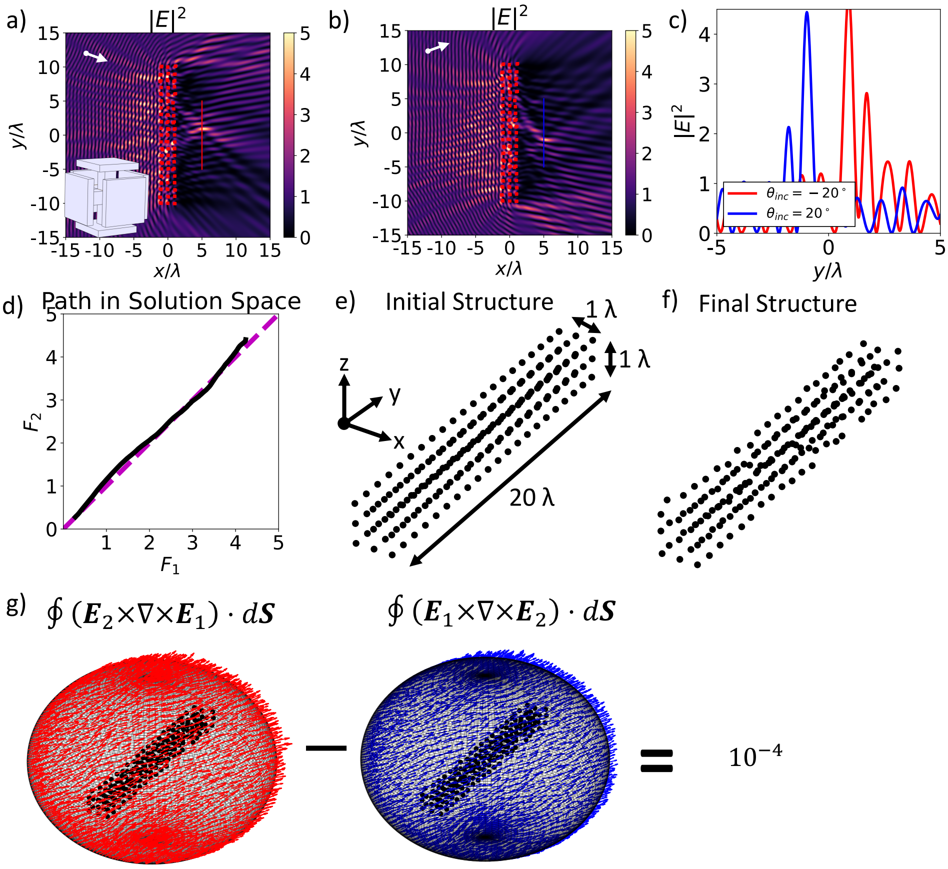

Figure 4.5: Design of a multi–functional device, with its operation depending upon the direction of incidence of a plane wave. If the wave is incident from ±20°, the wave is focused to different locations. The performance of the device under -20° incident is shown in a) and under 20° incidence in b), with direction of incidence shown as a white arrow. We work at 15.5 GHz using metacubes, shown inset in a), as the scatterers. Panel c), shows cuts of the fields under the two different incidence angles, demonstrating peaks at the target positions. The path in solution space, d), shows that the two figures of merit progress at the same rate over the optimisation, leading to a structure with roughly equal performance for each figure of merit. The initial and final structure are shown in e) and f). The multi–functionality condition (4.4) is verified in g) by evaluating the surface integrals. The numerical error here is larger than the results in Figure 4.3 due to the strongly oscillatory nature of the integrand, making evaluation of the surface integral more sensitive.

4.4 An Introduction to Differential Evolution

While we use gradient descent almost exclusively as our method of optimisation, genetic algorithms have been used extensively [70, 71, 95, 96] to design photonic systems. Gradient descent is simple and easy to implement, but can get stuck in local minima very easily. Genetic algorithms, are a particular class of so–called 'global optimisers', as they find global rather than local minima. To illustrate the difference between the two approaches, we consider optimising the Ackley function [128]

$$\begin{aligned} f(x,y) = &-20\exp\left[-0.2\sqrt{0.5(x^2+y^2)}\right] \\ &-\exp\left[0.5(\cos 2\pi x + \cos 2\pi y)\right] + 20 + e, \end{aligned} \tag{4.25}$$

shown in Figure 4.6. This is a difficult function to find the minima of, as it has very many local minima. We first try to apply gradient descent to find the global minima. Starting at 5 randomly chosen initial positions, we follow the directional gradient until a minima is found. Of the 5 starting conditions shown in Figure 4.6 (a), only 1 finds the global minima at $f(0,0) = 0$. The other 4 get stuck in local minima. Genetic algorithms present a solution to this issue, albeit at the cost of conceptual clarity.

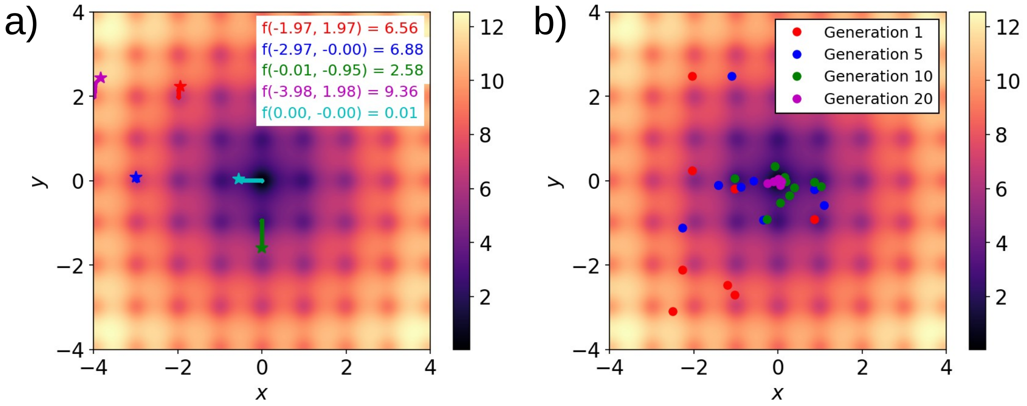

Figure 4.6: A comparison of minimising the Ackley function with gradient descent and a genetic algorithm. In a), gradient descent is used to find the minima, with 5 random starting positions within the search space. Each starting position finds a different minima, with many failing to find a global minima. b) Differential evolution is then used. Each dot represents a population member, with different colours representing different generations of the population. As 'evolution' progresses, the population converges on the global minimum.

Differential evolution is a prototypical genetic algorithm, developed by

Storn and Price [129] in the late 1990's. Today, many different genetic algorithms exist (i.e. particle swarm optimisation, Gaussian adaptation, cellular evolutionary algorithm etc.), however differential evolution is one of the simplest to understand and implement. The differential evolution algorithm requires the following ingredients

- **Figure of merit**: A function to be minimised $f(\boldsymbol{x})$. In our example, this is the Ackley function.
- **Candidate Solution**: A set of arguments that can be given to the merit function to evaluate the figure of merit. Here, each candidate solution is a point in the $x-y$ plane, $\boldsymbol{x} = (x, y)$.
- **Population**: A set of candidate solutions upon which the algorithm will act, $\{\boldsymbol{x}_1, \boldsymbol{x}_2, \boldsymbol{x}_3, \ldots\}$. The number of candidate solutions in the population is the population size, N_p.
- **Cross–over probability**: Denoted by $\mathrm{CR} \in [0, 1]$, this gives the probability that members of the population will combine.
- **Differential weight**: Denoted by $\mathrm{F} \in [0, 2]$, this parameter controls how combination works.
- **Maximum number of generations**: The maximum number of iterations of the algorithm we allow, N_g.

Population size, cross–over probability, differential weight and number of generations are all free parameters, meaning that for very complex problems they must be carefully tuned. Here, we use the standard values of

$$\mathrm{F} = 0.5 \qquad \mathrm{CR} = 0.7 \qquad N_p = 10 \qquad N_g = 1000. \tag{4.26}$$

The process of the algorithm is then

- Randomly initalise the population. For our example, we randomly choose N_p random positions in the $x - y$ plane.
- Until the stopping criteria is met (N_g reached or figure of merit smaller than an arbitrarily small number), for each member of the population $\boldsymbol{x}_i$, do
    1. Pick 3 population members at random $\boldsymbol{a}, \boldsymbol{b}, \boldsymbol{c}$.
    2. Choose a 4th random member of the population as the target $\boldsymbol{x}_\star$. This should be different from $\boldsymbol{a}, \boldsymbol{b}$ or $\boldsymbol{c}$.
    3. Generate a random index for the population R.
    4. Now perform the cross-over. Generate a random number $r \sim U(0, 1)$.
        (a) If $r < \text{CR}$ or $r = R$, set $\boldsymbol{y} = \boldsymbol{a} + F(\boldsymbol{b} - \boldsymbol{c})$. Otherwise set $y = \boldsymbol{x}_\star$.
    5. If $f(\boldsymbol{y}) < f(\boldsymbol{x}_\star)$ then replace $\boldsymbol{x}_i$ with $\boldsymbol{y}$.
- Pick the member of the population with the lowest figure of merit, and return it as the best solution.

Python code to perform this is given in Appendix A; differential evolution is also built into Scipy's 'optimize' toolbox [130].

Using this algorithm to find the minima of the Ackley function is shown in Figure 4.6 (b). The starting population, shown as red dots, are distributed randomly in space. As the generations progress, according to the differential evolution algorithm, they group around the global minima at $x = 0, y = 0$. Indeed, in very few iterations the algorithm finds the global minima.

For some problems, differential evolution has many advantages over gradient descent. As we have seen, it is much better at exploring complex search spaces and has the benefit of not requiring any gradient evaluations, although it does require many merit function evaluations. This is useful when figures of merit are faster to evaluate than their gradients. The merit function itself involves a single numerical integral, while its derivative requires two numerical integrals. However, the algorithm lacks the clarity of gradient descent and as it is based on random numbers can be difficult to repeat the results. Finally, for high-dimensional problems one must often perform a 'meta-optimisation' of the free parameters ($N_p, N_g, \mathrm{F}, \mathrm{CR}$), which is usually done using gradient descent.

In the next section, we compare the performance of differential evolution to our method, for designing multi-functional photonic devices.

4.5 Comparing our method to Differential Evolution

We compare the results of our optimisation for both emitted power and directivity with the results of a genetic algorithm solving the same problem. Using the differential evolution algorithm [129], with a population size of 20, and a maximum allowed iterations of 5000. The differential weight parameter is $F = 0.5$ and the crossover probability is CR = 0.7. This genetic algorithm was run several times and the best solution selected. The comparison between this result and the result of our local optimisation is shown in Figure 4.7. The genetic algorithm produces a slightly higher power emission but a slightly lower value of overlap integral. From the scatter of the solutions generated by the genetic algorithm in solution space, shown in Figure 4.7, it is evident that the genetic algorithm explores more of the search space

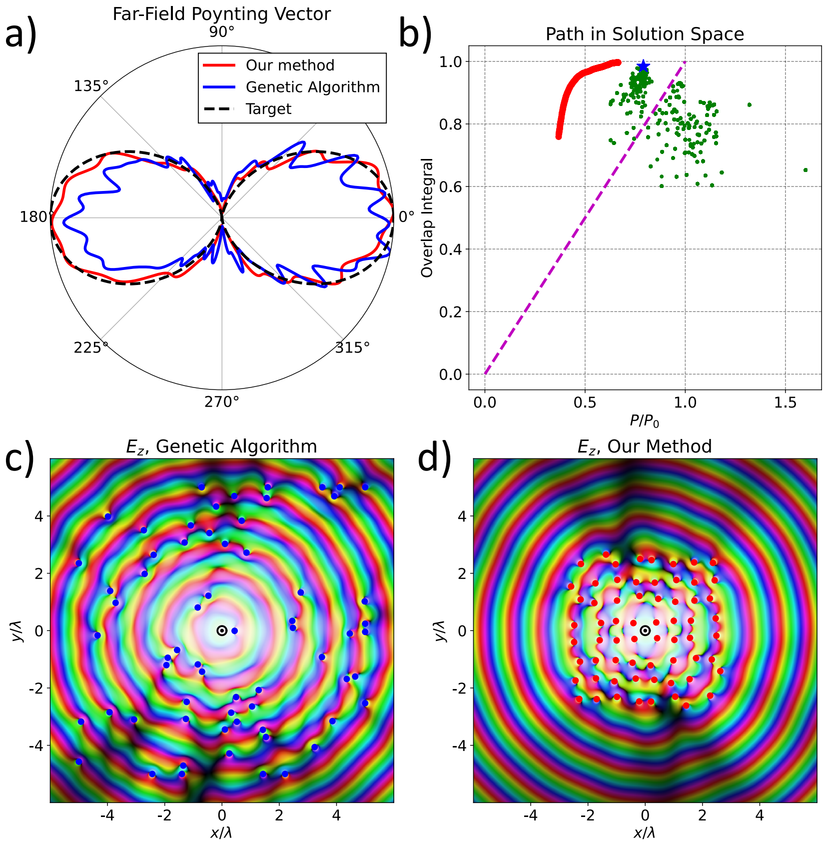

Figure 4.7: A comparison of the results of our optimisation and a genetic algorithm seeking to shape a far–field radiation pattern while also improving efficiency. The far–field radiation patterns are compared in a), and the solution space paths are shown in b). The progress of our method is shown in red, and the progress of the genetic algorithm as green dots. Each dot represents a single population member. The final result of the genetic algorithm is shown as a blue star. The resulting structures are shown in c) and d).

than our local optimisation. However, due to the size of the search space for multi–functional problems, this does not provide much advantage.

4.6 Validity of the Discrete Dipole Approximation

To verify the validity of the discrete dipole approximation, we compare our results with full–wave solutions using a finite element method numerical solver (COMSOL Multiphysics) [68].

The beaming device shown in Figure 4.3 has been validated by considering the nearest 20 scatterers to the source, due to memory considerations. For this reduced system, the comparison between the discrete dipole approximation and COMSOL is shown in Figure 4.8. The scatterers here are silicon spheres of radius 65 nm, for which the electric and magnetic polarisabilities can be found analytically.

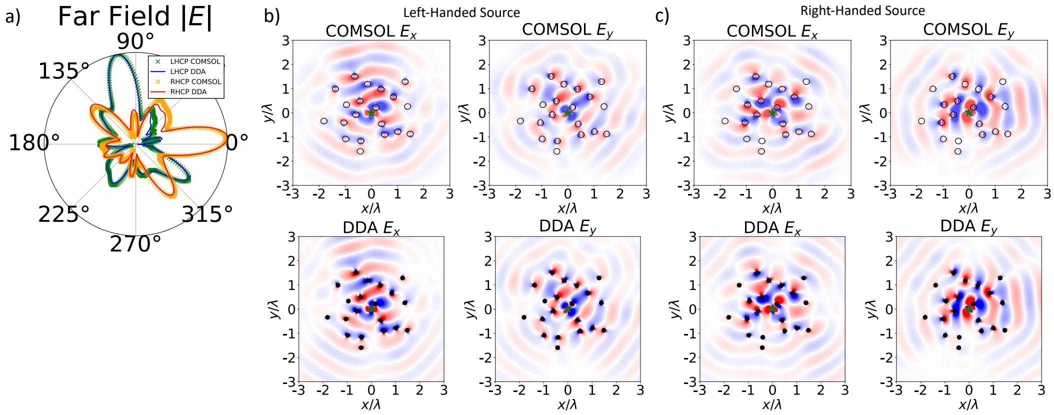

Figure 4.8: Comparison between our analytic results, based on the discrete dipole approximation, and full–wave simulations in COMSOL. Considering only the 20 (of 64) scatterers nearest to the source of the device shown in Figure 4.3 we compare a) the far–fields and b),c) the near–fields. For these scatterers, 65 nm radius silicon spheres, good agreement with the discrete dipole approximation is shown.

Validation of the 'lensing' device shown in Figure 4.5 of the main paper is shown in Figure 4.9. We consider a TE plane wave incident upon a small number of metacubes. Comparing the near and far fields in Figure 4.9 the main difference is in the field at the location of the scatterers, where the discrete dipole approximation is not valid anyway. The PEC boundary condition on the metal cubes in COMSOL ensures that the field inside the metacubes is zero. However, in the analytics, the field on one of the scatterers is proportional to $\boldsymbol{G}(\boldsymbol{r}_n, \boldsymbol{r}_n)$. The real part of this expression diverges, while the imaginary part remains finite. The divergence of the real part is what causes the difference in the fields at the scatterer locations.

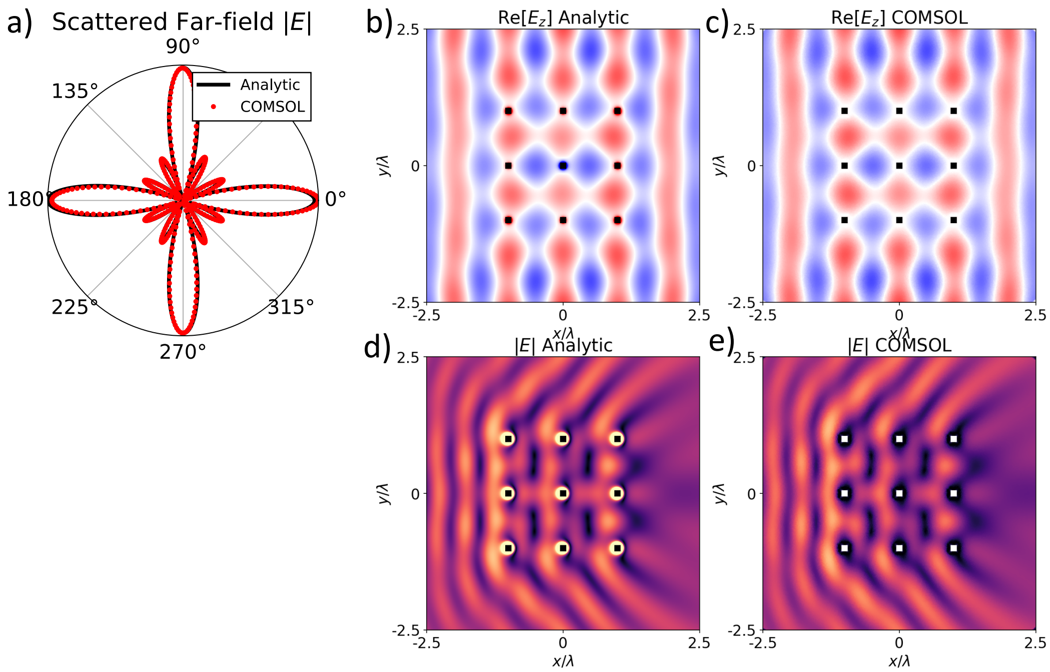

Figure 4.9: Comparison between the discrete dipole approximation and COMSOL for several metacubes under TE polarised plane wave incidence. Both a) the scattered field in the far–field and b)-e) the near–fields are shown. Excellent agreement between the analytics and full–wave simulations is found.

4.7 Summary & Conclusions

In this chapter, we generalised the results of Chapter 3 to enable the design of multi–functional photonic devices. Beginning with general considerations of multi–functional materials, we derived a rather restrictive constraint upon vector wave–fields that must be obeyed for multi–functionality. Taking as an illustrative example the problem of enhancing the emitted power of a small emitter while also shaping its far–field radiation pattern, we motivated a choice for how to weight the different components that make up the optimisation problem. Arguing that a good multi–functional device should perform each of its multiple roles well, we choose the weights to be proportional to one over the figure of merit at each optimisation step. Thus, if we begin from a point where emitted power is good but directivity is poor, directivity will be prioritised by the optimisation. Our weighted gradient descent optimisation procedure, with the gradients found semi–analytically as in Chapter 3, was compared favourably to a genetic algorithm, another popular method for multi–objective optimisation.

With the method developed through simple examples, we proceeded to design two multi–functional devices. Working at optical wavelengths, using small silicon spheres as the scatterers, we designed a device that beams radiation into different directions based upon the polarisation of the source emitter. Then at microwave wavelengths, using 'meta–cubes' as the scatterers, we design a 3D device that sorts waves by their direction of incidence. It is important to note that this device cannot be modelled using full–wave solvers such as COMSOL due to the different length scales involved. A very fine mesh must be used around the sub–wavelength scatterers, but then the device is tens of wavelengths across with over 100 scatterers. Leveraging the efficiency of being able to model a single scatterer at a time to extract the scattering properties, then using the coupled dipole approximation to find the fields, our method is extremely efficient at dealing with these length scale differences.

Chapter 5

Microwave Experiments

> *"...the triumphant vindication of bold theories – are these not the pride and the justification of our life's work?"* – Arthur Conan Doyle, The Valley of Fear

The work of this chapter was done jointly with Leanne D. Stanfield. JRC performed all numerical and analytical modelling. Experiments were carried out by LDS. Both authors contributed equally to the analysis of the data.

One of the most ubiquitous types of antenna is the Yagi–Uda antenna. Comprising a single driven element with several metal rods, forming the 'director', that generate a strongly directional beam in a particular direction. However, as the demand placed on communications networks has grown, so has the requirement for more specific antenna functionalities. In this chapter, we generalise the Yagi–Uda antenna, placing rods anywhere in a plane around an emitter to achieve arbitrary radiation patterns.

5.1 Introduction

One of the most common types of antenna is the Yagi–Uda antenna [79]. Shown in Figure 5.1 a), the antenna has one driven element surrounded by passive metal rods of varying length. All of the elements are uniformly spaced by $0.2\lambda_0$, were λ_0 is the desired working wavelength. The metal rods are held in place by a dielectric support. Parameters have been taken from the Yagi–Uda example in the COMSOL application gallery [131]. The reflection loss of the Yagi–Uda antenna, shown in Figure 5.1 b), shows that

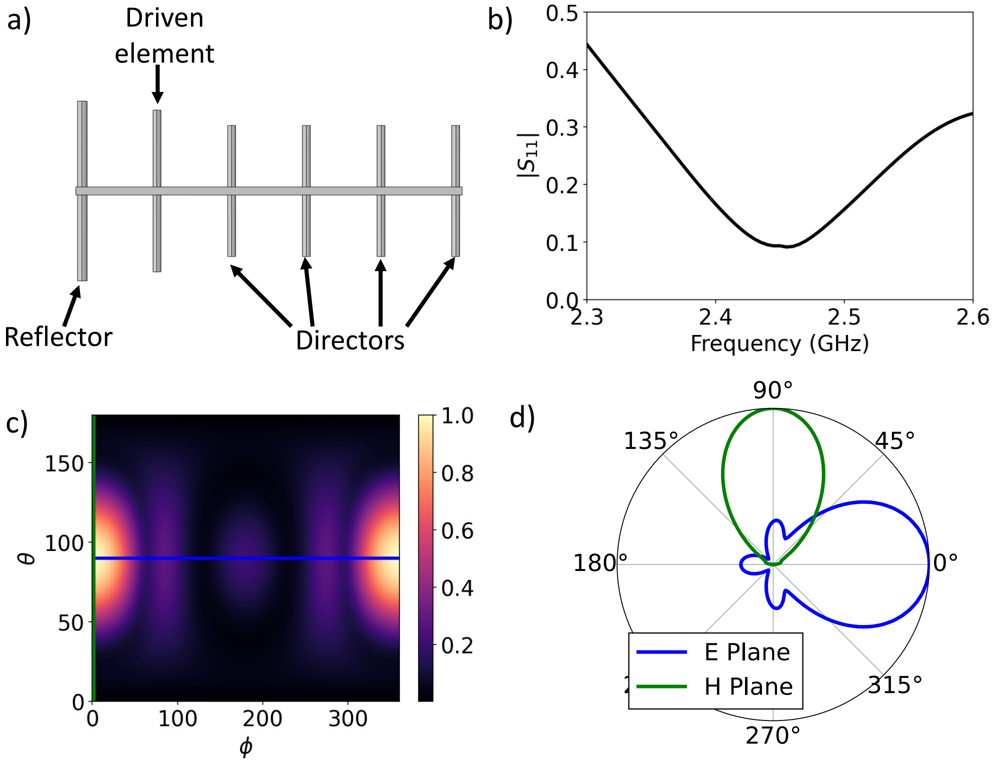

Figure 5.1: Behaviour of the Yagi–Uda antenna. a) Geometry of the antenna, comprising a single driven element and several passive metal rods acting as scatterers. The rods are arranged so that the scattered fields interfere constructively at the desired working frequency. b) Reflection loss of the driven element as a function of frequency. The minima corresponds to the desired working frequency of 2.45 GHz (a common WiFi frequency). c) The full far–field radiation pattern at $f = 2.45$ GHz shows a clear uni–directional beam. d) Cuts of the far–field along the E and H planes show the radiation pattern. Fitting Gaussians to each, we estimate that the beam width in the E plane is 44° and in the H plane is 29°.

the Yagi–Uda antenna is rather narrow band making it useful for applications what require frequency selectivity such as television broadcasting. The radiation pattern of the Yagi–Uda antenna, Figure 5.1 c), d) shows that a directional main beam is generated in the direction the rods are pointing, with a beam width of 44° in the E-plane and 29° in the H-plane.

Being simple to design and straightforward to build, the Yagi–Uda antenna has found great utlity over the last 100 years. However, the increasing congestion of communications frequencies requires antenna to be more directive and selective ideally while retaining the simplicity of the Yagi–Uda antenna. The ability to design antenna for specific applications that are easy to build, but have far more general radiation patterns than the Yagi–Uda antenna will be crucial to the next generation and generation beyond next communication systems. In this chapter, we apply the design framework presented in Chapter 3 to arrange metal rods around a simple emitter. We demonstrate the ability to engineer the far–field radiation pattern in many ways.

5.2 Modelling the Scatterers

We begin by considering how to model the elements we will use as the scatterers. Seeking to work at $\sim$ 10 GHz, we calculate the length of rod that will have its half–wavelength resonance at this frequency. A frequency of 10 GHz is equivalent to a wavelength of 30 mm, so the half–wavelength length is 15 mm. We therefore use as the scatterers rods of length 15 mm and diameter 3 mm. In order to use these scatterers in the semi–analytic design procedure, we must extract the polarisability numerically. The method we use to do this is described in Appendix B. A schematic of the model is shown in Figure 5.2. The metal rod is placed in an isotropic background

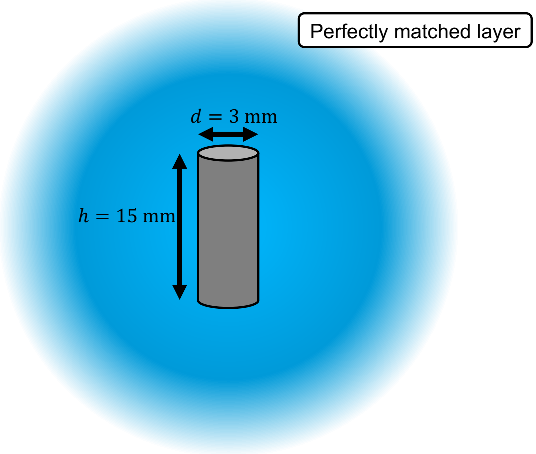

Figure 5.2: Schematic representation of how the scatterers are modelled to find their resonances. Following the method presented in Appendix B, the scatterer is placed in an isotropic background medium, then excited with plane waves. Integrating over the charges and currents allows one to calculate the elements of the polarisability tensor.

material and excited with plane waves of different polarisation and propagation directions to find elements of the polarisability tensor. As expected, this is anisotropic, with the structure

$$\boldsymbol{\alpha}_E^{\mathrm{rod}} = \begin{pmatrix} 0 & 0 & 0 \\ 0 & 0 & 0 \\ 0 & 0 & 1 \end{pmatrix} \alpha_E^{rod}, \tag{5.1}$$

where the long axis of the rod is aligned along the z axis. All of the x, y components, as well as the magnetic polarisability are negligible compared to the z component of electric polarisability. The resulting electric polarisability as a function of frequency is shown in Figure 5.3. The peak polarisability is at 7 GHz, red-shifted by the effect of the thickness of the rod, as well as end effects. Figure 5.3 shows how the modulus of the polarisability changes as the thickness of the rods is adjusted. As the rod becomes thinner, the resonance moves closer to the 10 GHz expected from elementary arguments.

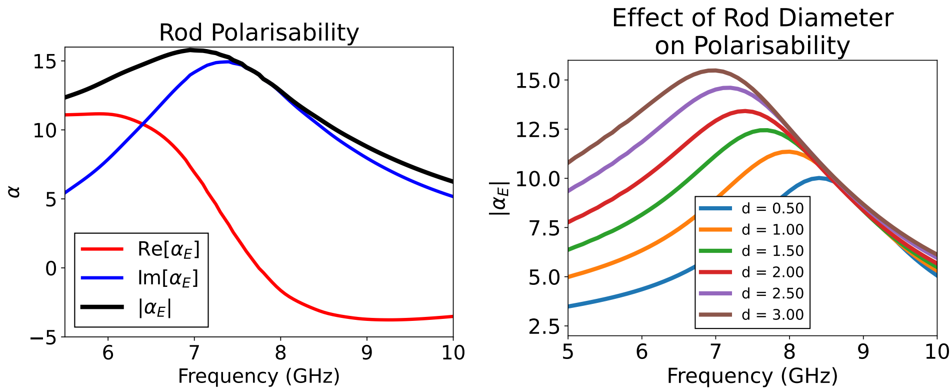

Figure 5.3: Polarisability of the metal rods, as a function of frequency. The effect of making the rods narrower is to shift the resonance towards to 10 GHz expected of an infinitely thin wire.

Since larger polarisability provides stronger scattering, and therefore more control over the wave-field, we elect to work at $f = 7$ GHz. At this frequency, we have

$$\alpha_E^{\mathrm{rod}} = 6.91 + i14.17 \qquad\qquad f = 7\,\mathrm{GHz}. \tag{5.2}$$

The other ingredient we need to include in the analytic framework is the source field. As we plan to use a non–standard emitter, this must also be extracted numerically.

5.3 Modelling the Emitter

All of the designs so far in this thesis have used idealised point emitters to generate the source fields. While this approximation can well describe the half–wavelength dipole antenna [5, 16], the radiation from more complex sources cannot be described in this way. It will therefore be necessary to numerically characterise the emitter we are using and incorporate this into the semi–analyic framework we have developed in Chapter 3. In the experiments of this chapter, we will use a balanced half–wavelength sleeve antenna, shown in Figure 5.4 a). The balun prevents currents from being generated down the length of the coaxial cable, which lead to additional resonances that perturb the performance. When one designs a sleeve antenna, the half–wavelength length includes both the radiation element and the balun [5]. To operate at a frequency of 7 GHz, corresponding to a wavelength of $\sim$ 4 cm, the radiating element plus the balun should have a length of 2 cm. Just like a dipole emitter, the radiation is predominantly perpendicular to the axis of the radiating rod. In previous chapters, the source was modelled as a point dipole meaning that the source fields could be found

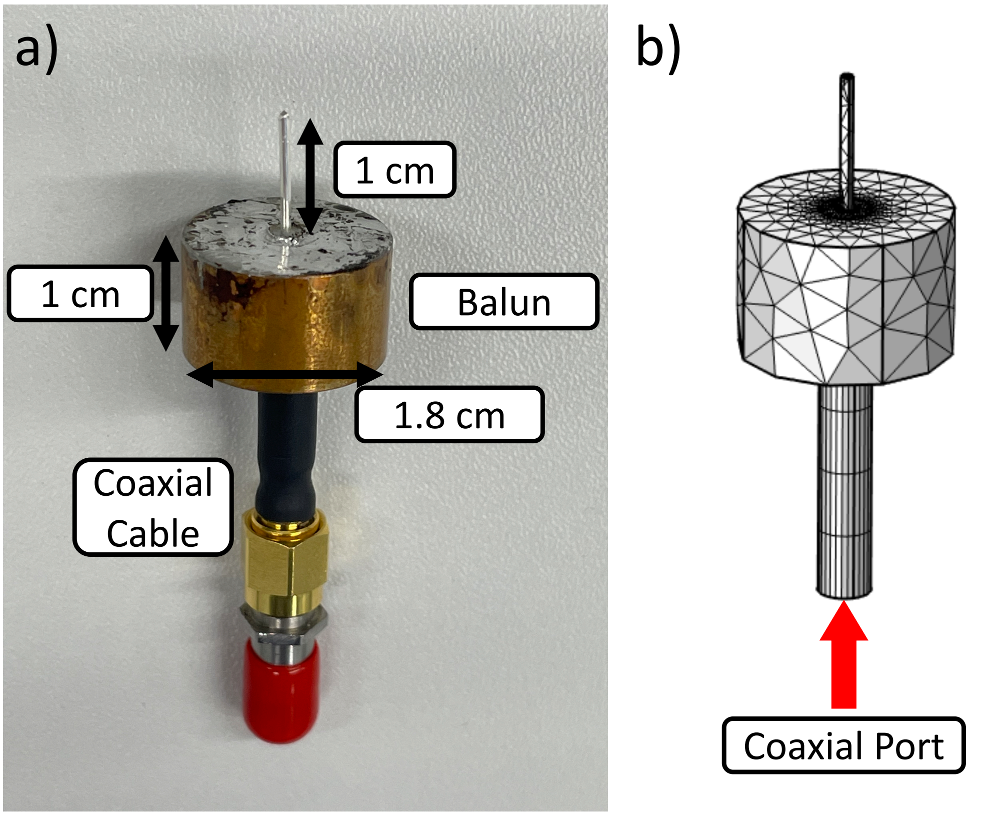

Figure 5.4: Sleeve antenna used in the experiments. For ease of measurement, we use a sleeve antenna with a balun to prevent standing waves along the length of the coaxial cable. The dimensions of the balun and rod have been chosen so that together they fulfill the half–wavelength condition at 7 GHz. The emitter is modelled numerically, to find the fields. The geometry and mesh used in COMSOL is shown in b), and a coaxial port is used to simulate the effect of the coaxial cable.

analytically using the dyadic Green's function. For more complicated emitters, such as the sleeve antenna, very few analytic results exist so it is necessary to numerically model the behaviour of the emitter. This was done using COMSOL Multiphysics [68]. The modelled geometry is shown in Figure 5.4 b). A coaxial port is used to excite the structure: this is an impedance boundary condition that simulates the effect of the coaxial cable.

Some key properties of the emitter are shown in Figure 5.5. Figure 5.5 a) shows $|S_{11}|$ as a function of frequency. This can be thought as the reflection loss of the antenna, a measure of how much input power gets radiated.

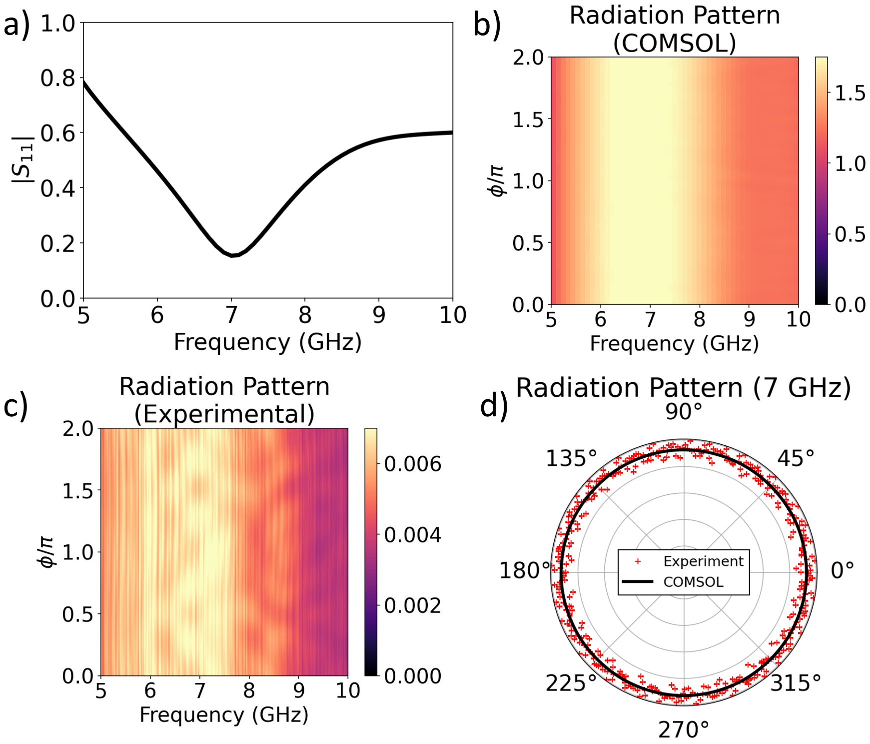

Figure 5.5: Key radiation properties of the sleeve antenna. a) the $|S_{11}|$ parameter shows a key dip at 7 GHz, indicating that the geometric dimensions of the balun and rod have been chosen correctly. The radiation pattern perpendicular to the plane of the antenna as a function of frequency was b) modelled and c) measured. There is a clear peak in amplitude around the 7 GHz resonance, with the radiation pattern being isotropic. Plotting d) the radiation pattern at 7 GHz, we see the isotropic behaviour along with some background noise.

A small $|S_{11}|$ corresponds to small reflection between the cable and the antenna, so a large amount of radiated power. We observe a dip in $|S_{11}|$ at 7 GHz, where the antenna has been designed to be resonant. Then, in Figure 5.5 b)-d), the radiation pattern of the emitter has been measured and compared with numerics. We consider the radiation pattern in the plane perpendicular to the axis of the antenna, as this is where the scatterers will be placed. The radiation patterns in Figure 5.5 b) and c) are isotropic, exhibiting an amplitude increase for all angles around the resonance frequency of 7 GHz. The radiation pattern at 7 GHz, shown in Figure 5.5 d), is isotropic although with some measurement noise.

To model the scattering system, we will require the fields of the emitter evaluated at the scatterer positions, which will change over the course of the optimisation. There are two approaches one could employ to calculate these fields. Firstly, one could model the emitter in COMSOL, then extract the currents within the source. Integrating these against the Green's function would allow one to calculate the field at any point in space. However, this requires many numerical integral evaluations which can be sensitive to the points on which one has chosen to export the field. Instead, we calculate all of the fields in COMSOL and export their spatial distributions. These are then interpolated so that one can very quickly evaluate the field at any $x-y$ position, or in the far–field. It should be noted that the far–fields were extracted separately, although one could use the near–to–far field transform [132] to map between the two. This would, however, require the calculation of a surface integral numerically. The fields of the sleeve antenna emitter with a balun at 7 GHz are shown in Figure 5.6. A small amount of x polarised field is generated, although as the scatterers have no x component of their polarisability tensor, this will not be modified by the scatterers. The

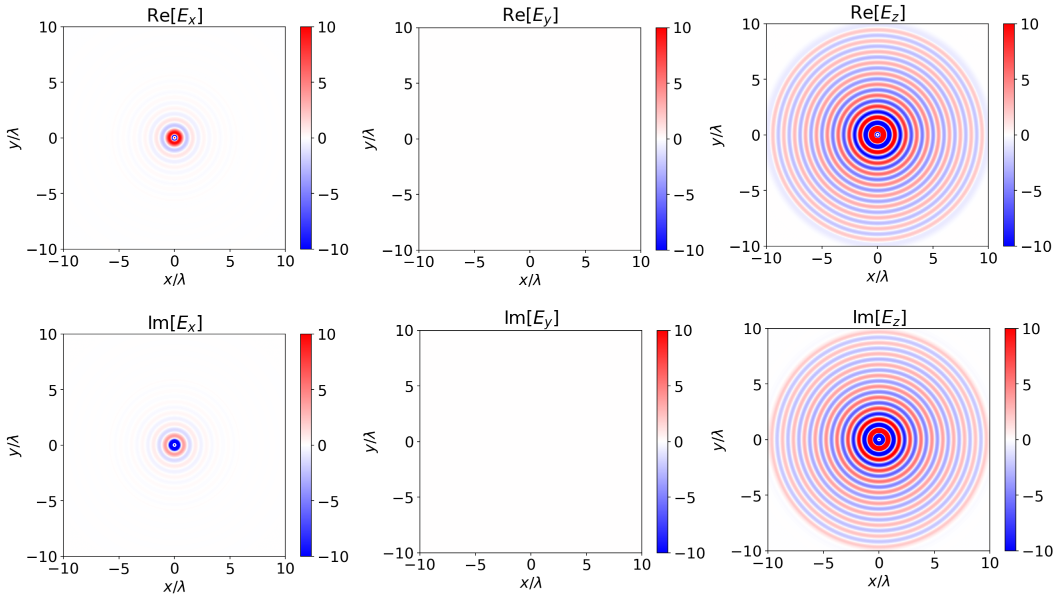

Figure 5.6: Electric field of the emitter, extracted from finite element modelling.

larger z component of the field will however couple strongly to the scatterers, exciting their dipole resonances.

5.4 Experimental Procedure

Once designed and constructed, the devices were experimentally characterised using an Anritsu MS46122B Vector Network Analyser (VNA), and a rotational table controlled by a Thorlabs APT Precision Motion Controller. To determine the far-field radiation pattern, the structure underwent a full 360° rotation in 1° increments about the z-axis, parallel to the axis of the source and the rod scatterers, in an anechoic chamber, with response measured by a Flann Dual Polarized Horn Antenna (Model DP240) for frequency range 4.0 GHz to 10.0 GHz in 0.05 GHz increments. The experimental setup is shown in Figure 5.7.

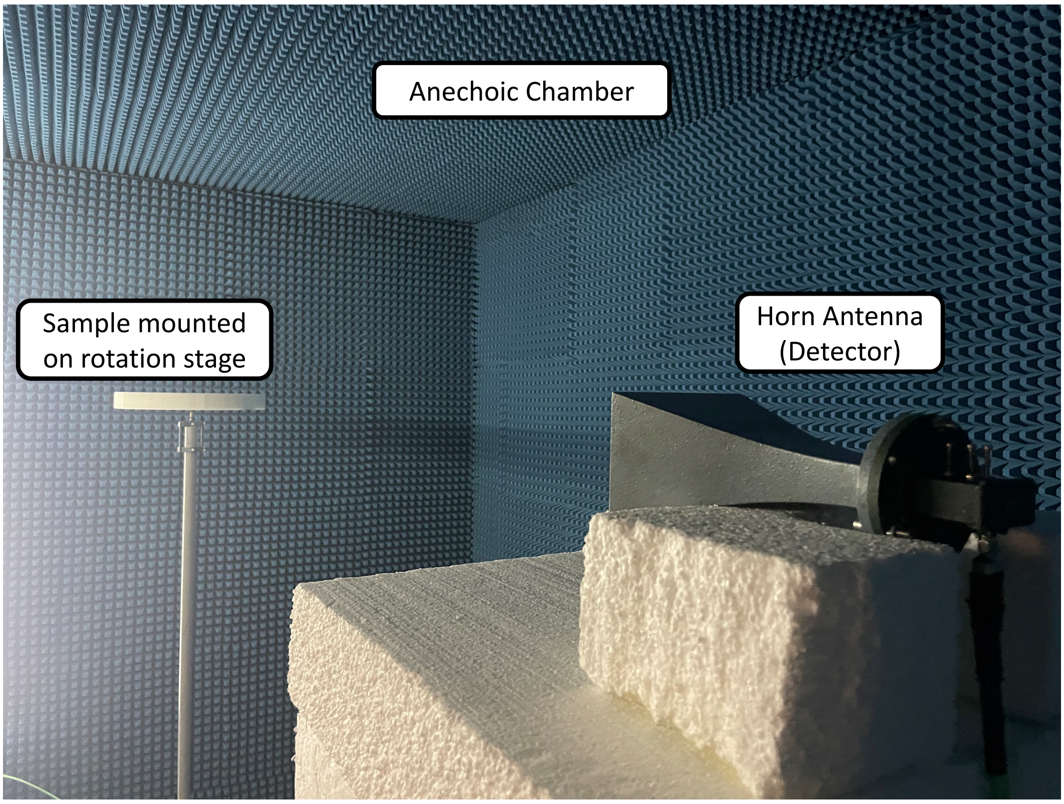

Figure 5.7: The experimental setup.

5.5 Experimental Demonstration of the Designs

Having established the key properties of the building blocks of the system, we proceed to utilise the methodology presented in Chapter 3 to design 'generalisations of the Yagi–Uda antenna'. Rather than arranging only a small number of rods to create a beam in a particular direction, we begin from a square array of 100 rods and design structures that have beams in arbitrary directions. While the numerical model is exactly the discrete dipole approximation described in Section 2.6, the source field is now extracted numerically and imported into the analytic framework. The first example of this is shown in Figure 5.8. The target radiation pattern is a beam at the 0° direction with a width of 10°. Figure 5.8 a) shows the progression of the figure of merit, defined as the overlap integral between the desired and current radiation patterns, over the optimisation. The initial and final structures are

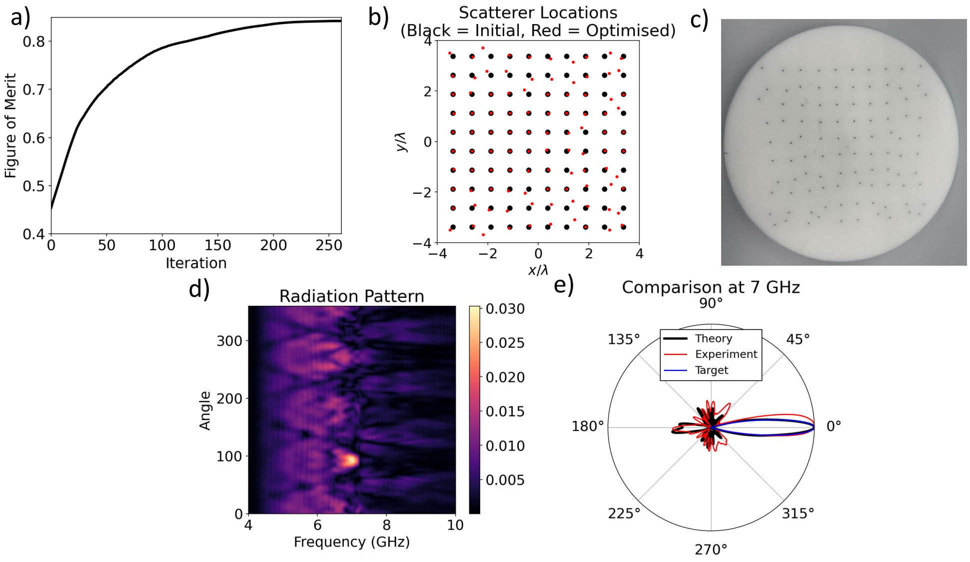

Figure 5.8: Designing an array of scatterers that beams in a single direction.

shown in Figure 5.8 b), with the experimental realisation shown in Figure 5.8 c). The measured radiation pattern is shown in Figure 5.8 d), exhibiting a clear peak at the design frequency of 7 GHz and at one particular angle. A comparison between analytics, experiment and the target distribution is shown in Figure 5.8 e). While similar to the behaviour of the conventional Yagi–Uda antenna, the inclusion of many more scatterers allows for direct control over the exact width of the beam.

Our next device illustrates the flexibility of our design procedure. The target radiation pattern now has two beams of width 15° at 10° and 260°. The progression of the overlap integral, final and initial scatterer positions and experimental sample are shown in Figure 5.9 a)-c). Measured radiation pattern, shown in Figure 5.9 d) shows two clear beams at 7 GHz. Comparison of the radiation patterns predicted and measured in Figure 5.9 e) show excellent agreement of the position and width of the main lobes, although larger back lobes are present in the experimental data.

Next, we consider attempting to design a device that has three beams of specified widths at specific positions, with pre–determined amplitudes. As

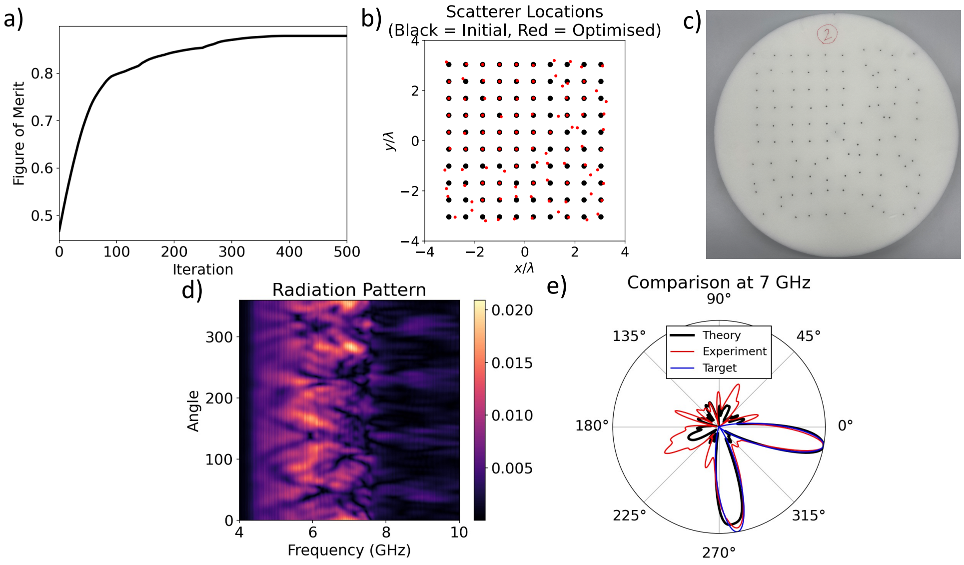

Figure 5.9: Designing an array of scatterers that beams in two directions, with defined width.

with the two beam design, we aim to place two beams of maximum amplitude and width 15° at 10° and 260°, in addition to a beam of half amplitude and width 45° at 80°. Figure 5.10 a)-c) shows the optimisation and experimental sample. The full measured far–field radiation pattern, shown in

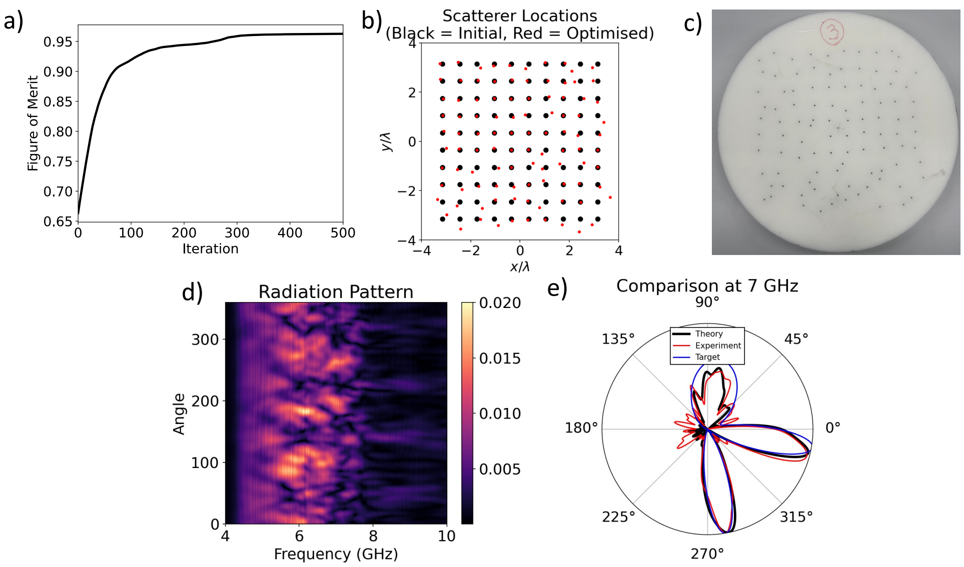

Figure 5.10: Designing an array of scatterers that beams in three directions, with defined widths and amplitudes.

Figure 5.10 d), is now harder to interpret. However the two maximum amplitude beams can be see at around 200° and 250°, with the half–amplitude beam appearing at around 100°. Comparing the radiation patterns in Figure 5.10 e), good agreement between analytics and experiment can be observed.

The full far–field radiation patterns (as functions of both polar angle θ and azimuthal angle ϕ) of each of the above designs is shown in Figure 5.11. These patterns were extracted from full-wave simulations in COMSOL [68]. In the radiation pattern for the single beam design, shown in Figure 5.11 a), a single clear beam at $\phi \sim 180°$, with little other radiation. For the two beam design, shown in Figure 5.11 b), two clear main beams can be observed. The three lobe design, shown in Figure 5.11 c), has the expected radiation pattern in the measurement plane, however there is significant radiation in out of plane directions. For example, there is a large lobe at around $\phi = 280°, \theta = 150°$.

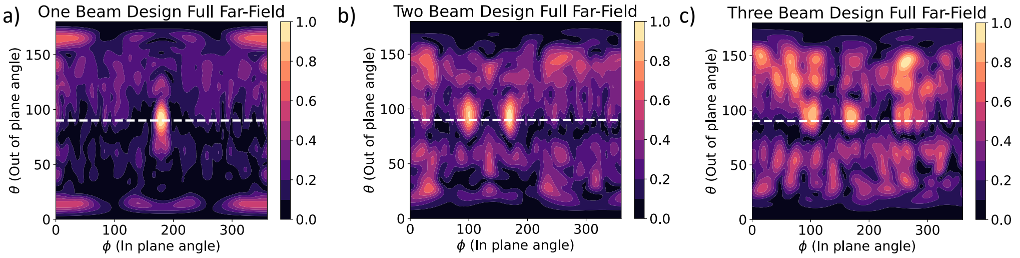

Figure 5.11: Full far–field radiation patterns of the designs presented in Figures 5.8, 5.9 and 5.10. White dashed line indicates the plane in which far–field measurements are taken.

Finally, we examine the effect of structuring the radiation pattern upon the mismatch loss of the emitter. These measurements are shown in Figure 5.12. In all cases we see that the effect of structuring the radiation pattern at 7 GHz is to reduce the efficiency of emission. This effect was also observed in the example consider at the start of Chapter 4, shown in Figure 4.2. To alleviate this, one could employ the multi–objective optimisation framework

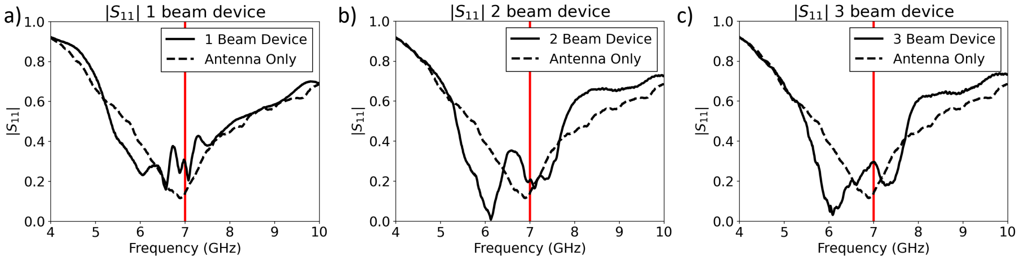

Figure 5.12: Measured reflection loss for the designs shown in Figures 5.8, 5.9 and 5.10. In all plots, the the reference of the antenna in free space is included. The working frequency of 7 GHz is indicated by the vertical red line.

presented in Chapter 4 to optimise both radiation pattern and power emission, although the system considered for experiments has fewer degrees of freedom that that considered in Figure 4.2.

5.6 Sources of Error

While the experimental results of the previous section show clear proof of concept, experimental and theoretical results do not perfectly align. Many steps in constructing the both the experiments and the semi–analytic design framework introduce non–negligible sources of error. In this section, we examine some of the key sources of error and consider how they have been addressed or could be further ameliorated.

Firstly, we consider the strength of the dipole approximation in correctly describing our system. This is a similar investigation to that presented in Section 3.11 of Chapter 3 and Section 4.6 of Chapter 4. The scatterers are treated as point dipoles, however have a length that is $\sim \lambda/2$ and a radius that is $\sim \lambda/20$. To check how well the dipole approximation works, we excite two scatterers with a point dipole source, polarised in the z direction. Varying the separation d between the scatterers we track the error between the far–field radiation pattern predicted by the point dipole approximation and full–wave simulations in COMSOL. Error is characterised by the residual sum of squared differences (RSS). The result of this study is shown in Figure 5.13. One can observe that for large separations the error is small, but not zero, even though we consider only two scatterers. Above separations of $d/r \sim 5$ (where r is the radius of the scatterers) the error is on the order of 0.1. As expected, for smaller separations $d/r < 5$ the error becomes large as the near–fields of the scatterers interact more strongly. The near fields of the scatterer are expressive of the exact geometry, which is an effect not captured in the dipole approximation where the scatterer is assumed to be a point. From this, we conclude that the dipole approximation works well provided that the scatterers are not too close, however is not perfect. For large numbers of scatterers, this error will be compounded. It should be noted that the minimum separation between the rods in the designs proposed in the previous section is $d/r \sim 10$.

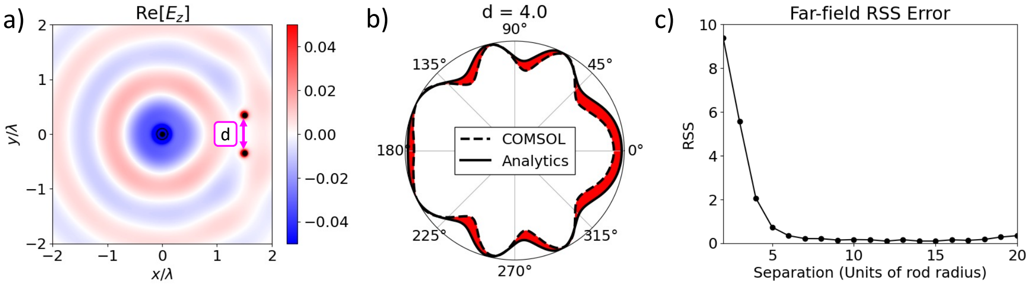

Figure 5.13: Investigating the strength of the dipole approximation. a) Exciting two rods of radius r with a point dipole source oriented in the z direction, the two scatterers are kept at $x = 1.5\lambda$ while the y distance d (in units of scatterer radius) between them is varied. b) Comparing the far–field predicted by the point dipole approximation with full–wave simulations in COMSOL, the error between the two is characterised by the residual sum of squared error (RSS), indicated in red. c) The error as a function of rod separation indicates that the dipole approximation works poorly when $d/r < 5$, when the near–fields couple. For larger separations, the dipole approximation has a consistent error of the order ~ 0.1.

As well as the inevitable limits of the dipole approximation, several other steps in constructing the semi–analytic design framework introduce error. The dielectric properties of the foam were measured and confirmed to match the values taken from the data sheet [133]. However small uncertainties may persist, leading to shifts in the resonances of the rods i.e. the peak of α_E will be shifted downwards as ε increases. Additionally, the properties of the emitter might have small errors in their representation. Modelling the emitter in COMSOL might introduce small numerical errors, then the fields must be exported and interpolated for use in the design procedure. This may introduce additional interpolation errors. While individually small, combined these effects might produce notable differences in the fields and radiation patterns. Although each of our simplifying assumptions introduces errors, it should be noted that the design of the structures presented in the previous section is intractable using full–wave simulations. Modelling the systems in COMSOL requires around 200 GB of RAM and simulations take around 3 hours. The ~ 500 iterations required for the optimisation procedure would therefore take around 60 days on a specialist computer. Conversely, our simplified framework uses only ~ 500 MB of RAM and runs in ~ 8 hours on a modest laptop.

In addition to the difficulties of modelling our system, the experimental procedure itself has several inherent challenges. Reflections within the anechoic chamber are a key concern, as they would destroy the radiation pattern. These were checked for by keeping the detector fixed, then measuring the radiation pattern of the sample. The sample is then rotated to a different starting position and measured again. If reflections are present then we expect a feature to appear at a fixed angle that is not affected by the rotation of the sample. This test is shown in Figure 5.14, demonstrating that no significant reflections were found. The other main experimental challenge is the alignment of the sample. If the sample is not mounted flat on the rotating table, then the radiation pattern will be slightly tilted. Laser

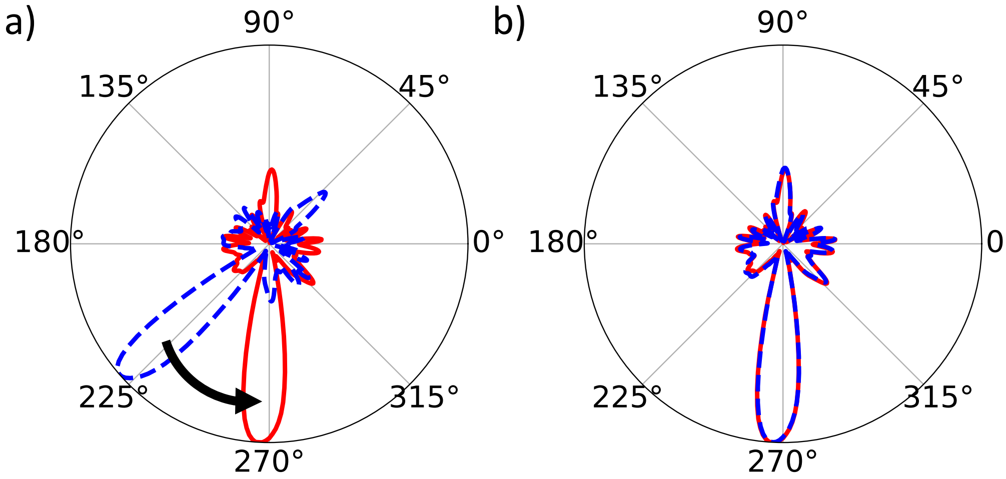

Figure 5.14: Checking for reflections within the anechoic chamber. a) The radiation pattern of the structure is measured from two different starting angles. If reflections are present, we would expect a feature to appear at an angle that does not depend upon the sample orientation. b) Rotating the two measurements onto each other, no persistent features are observed.

alignment was used to attempt to alleviate this and the reasonable spread of the beam above and below the plane of the emitter, evident in every panel of Figure 5.11, should make the measurements robust to small tilts. Nevertheless, the effect of this cannot be completely discarded.

5.7 Summary & Conclusions

In this chapter we have experimentally verified the utility of our proposed method for designing antenna. Taking for inspiration the Yagi–Uda antenna, we aimed to design and realise structures made of metal rods arranged around an emitter that could shape the far–field in non–trivial ways. We showed that radiation can be focused into beams at particular angles, of particular widths and amplitudes. Our devices express far more control than conventional Yagi–Uda antenna. Crucially, our semi–analytic framework has enabled the design of devices that would be otherwise inaccessible to numerical treatment.

While our theory is strongly predictive of experimental measurements, some differences remain. Several sources of error, both in the experiment and modelling have been discussed. Differences in material parameters, and the several numerical and interpolation steps are consider the key sources of error in this work.

To extend these results further, multi–functional devices could be designed using the framework of Chapter 4. However, the current implementation contains only the z component of the field. The ability to manipulate multiple components as well as the magnetic field would provide redundancy in degrees of freedom, providing more freedom to manipulate the radiation. This would require scatterers that have both electric and magnetic resonances, or could perform frequency conversion. Switching behaviour could be added by including PIN diodes into the scatterers, so they are either resonant or shorted. How such a system would be electrically controlled without interfering with performance or measurement remains an open question.

Chapter 6

Manipulating Quasi–Normal Modes

“...the developed method standing alone does not present scientific interest. Furthermore, the research topic addressed in the manuscript does not seem to be of interest to the broad optics and science community...” – A Deputy Editor of Optica

The results of this chapter have been published in:

- J. R. Capers, D. A. Patient, S. A. R. Horsely “Inverse Design in the Complex Plane: Manipulating Quasi–normal Modes” Phys. Rev. A **106** 053523 (2022).

All work was done jointly with D. A. Patient. Both authors contributed equally to the work of this chapter.

Many photonic devices rely on resonances to give a strong response. The frequency and linewidth of these resonances is determined by the refractive index and geometry of the resonator. Inverse design of photonic systems has attracted much attention over the previous decade, however little attention has been paid to how to manipulate the exact properties of resonances. In this chapter, we utilise the fact that the frequency response of a photonic device is directly related to the complex frequencies of the quasi–normal modes of the resonator. We present two methods to manipulate the locations of these modes, allowing for the control of frequency and linewidth simultaneously. Firstly, we employ an 'eigen-permittivity' method, to find how to shift the permittivity of a material so a quasi–normal occurs at a particular complex frequency. While this method is simple, it only allows for the manipulation of a single mode. To manipulate multiple modes, we develop an iterative procedure based on quasinormal mode perturbation theory.

6.1 Introduction

In the previous chapters we designed many structures built from resonant scattering elements. We chose to work at the resonant frequency of the scatterers as this is where the scattering response is strongest. The actual wavelength at which the scatterers are resonant is fixed by their geometry and material properties. In this chapter we consider applying inverse design techniques to the problem of manipulating the position and character of the resonances of photonic structures.

A very wide range of photonic devices rely on resonances for their operation. Some of the early examples of metamaterials relied upon plasmonic resonances [134, 135]. These are the collective resonances of electrons in metals. Such resonances have been used to realise a wide range of phenomena such as cavity tuneable lattice resonances [136], optical antennas [80], breaking Snell's law [50] and extreme field confinement [137]. However, at optical frequencies plasmonic resonances exhibit very high losses [138], limiting the efficiency of devices that rely upon them. Instead, materials based on dielectric Mie resonances [138–140] have become ubiquitous. Not only are the associated losses lower, nanofabrication of silicon has been developed by the electronics industry for decades and is now very advanced. As such, dielectric photonic devices have been built to e.g. control spontaneous emission [85] and construct antennas for light [141]. In dielectric systems there is a rich landscape of resonances is available. Interfering different multipoles can achieve, for example, invisibility due to the Kerker effect [142].

We will see in the next section that radiating resonant modes are characterised by complex wave–numbers, meaning that they grow in space. Consequently, deciding how to normalise them is not trivial, but required if one is to develop expansions or a perturbation theory for them. As such, there has been much theoretical work on developing both perturbative treatments [143, 144] and expansions of physical quantities in terms of the complex frequency resonances of specific systems such as spheres [145] as well as general open resonators [146, 147]. The mathematics of how to include 'killing functions' [148] into numerical simulations to make the normalisation of these modes easier is also an open problem. With such expansions, one can determine the effect of specific resonances on measurable quantities such as the Purcell factor [149]. Despite recent progress, some problems remain with these approaches. For example, the set of resonant modes do not form a complete basis. Recent insight from Chen et al. [150] shows that this problem can be avoided if one keeps the wave–number real but extends the permittivity of the structure into the complex plane. One can then expand in a complete set of bound states that are perfectly normalisable.

Beyond deriving field expansions in terms of quasi–normal mode fields, there are many reasons one may want to change the location and width of a resonance. The locations of resonances link directly to energy absorption: efficient energy harvesting requires high absorption over a large frequency band [151–155], while sensing requires narrow resonances at particular wavelengths [156–159]. However, little attention has been given to how to algorithmically design structures that exhibit resonances of particular widths at particular frequencies. Many current methods involve manually sweeping over geometric parameters to see how the resonances move [160–162]. Such procedures are slow and require many full–wave simulations. More recently, efforts have been made to apply perturbation theory [163] to efficiently explore parameter spaces. Expressing the optimisation problem in terms of the resonances of a system has a number of key benefits. Firstly, the optimisation procedure and result are easy to interpret as the entire paradigm is based on where resonances are located. Secondly, typically only a few resonances contribute to the response of a resonator over a small frequency band. This means that one only has to tune a few resonances, rather than consider full–fields as the adjoint method usually requires. It is only very recently that algorithmic methods for manipulating the locations of complex frequency resonances have emerged [164]. Such methods still require full–wave simulations to find the resonances, then perturbation theory can be used to evaluate their sensitivity to geometric parameters.

In this chapter we derive two methods for placing resonances of photonic systems at particular complex frequencies, allowing for the determination of both their resonance frequency and their spectral width. We begin by discussing the properties of the modes we would like to manipulate, and comparing multiple analytic and numerical methods for finding the resonances. We then develop a method based on the insight on Chen et al. [150] to determine an offset one can apply to the permittivity of a structure to place a particular resonance at a particular complex frequency. Next, by employing perturbation theory, we formulate an iterative procedure for designing graded index resonators with multiple resonances placed at desired complex frequencies. Initially, these ideas are formulated by considering dielectric slabs. We then extend this to consider radially symmetric resonators in 2D and 3D. Manipulating the resonances of radially symmetric resonators allows us to choose the multipolar character of the mode we move as well, making our method relevant for sensing as well as in the design of dielectric resonant antenna.

6.2 Quasi–Normal Modes: What and Why?

We will consider transverse electric fields propagating in 1D so that $\boldsymbol{E}(z) = \phi(z)\hat{\boldsymbol{x}}$. The boundary conditions are therefore that the electric and magnetic fields are continuous across a material boundary [15]. We will assume that all of our materials have $\mu = 1$, so we must impose that $\phi(z)$ and $\partial_z\phi(z)$ are continuous across boundaries. As was shown in Section 2.2, we can then consider solutions to the 1D Helmholtz equation

$$\left(\frac{d^2}{dx^2} + k^2\right)\phi(x) = 0, \tag{6.1}$$

of the form

$$\phi(x) = e^{ikx}. \tag{6.2}$$

If k is purely real, the solutions are just propagating plane waves. However if k is complex, with $k = k' + ik''$, then the solution is made of a complex and real exponential

$$\phi(x) = e^{ik'x}e^{-k''x}. \tag{6.3}$$

The sign of k'' dictates whether the exponential grows or decays: when $k'' > 0$ the mode is localised (bound), while when $k'' < 0$ the mode grows exponentially, leaking energy. For better physical insight, we put back the time–dependence of the solution to the wave equation, where now the frequency has inherited the complex nature of k through the dispersion relation $\omega = ck = \omega' + i\omega''$. Throughout, we will use ω, k and $\lambda = 2\pi/k$ interchangeably and assume they all become complex when we are discussing quasi–normal modes. The different physical quantities will be useful for describing different systems. With this, the full solution is then

$$\phi(t,x) = e^{i(k'x-\omega't)}e^{-k''x+\omega''t}. \tag{6.4}$$

Now, when $k'', \omega'' < 0$, we have a solution that has a propagating component and a part that grows in space but decays in time. These traits are characteristic of a quasi–normal mode (QNM). One can imagine a bell being struck at $t = 0$. Initially, the bell rings with a large amplitude resulting in sound waves of large amplitude moving outwards. At later times the

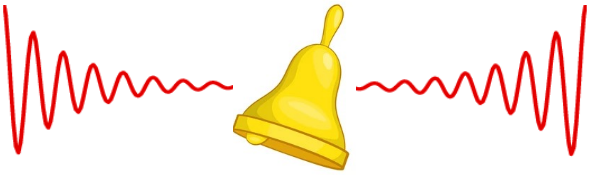

Figure 6.1: Schematic example of a quasi–normal mode. When a bell is struck, the initial amplitude of oscillation is large, producing radiating waves of a large amplitude. As damping within the bell reduces the amplitude of the oscillations, the amplitude of the radiating waves also decays. The result is a wave that seems to be growing in space, as a result of a temporal decay. The wavelength of the resonance is related to the wavelength of the radiating modes, with the decay rate of the mode being related to the rate of spatial growth.

amplitude of the bell's oscillation decays, radiating lower amplitude sound waves. Looking at the field at very long times, one sees the exponentially growing field shown in Figure 6.1.

With this broad physical insight, we explore the quasi–normal modes of a simple photonic system, considering the insight they provide. Perhaps the simplest example of a system supporting QNMs is a homogeneous dielectric slab (refractive index n_r in some background index n_b). To find the quasi–normal modes of a step of width L centered at $x = 0$, we calculate the reflection coefficient r by considering

$$\phi(x) = \begin{cases} A\left(e^{ikn_rx} + e^{-ikn_rx}\right) & |x| < L/2 \\ e^{-ikn_bx} + re^{ikn_bx} & x > L/2. \end{cases} \tag{6.5}$$

Applying continuity of the field and its derivative at $x = L/2$, we find that

$$r(k) = r_0 \frac{1 - e^{i2kLn_r}}{1 - r_0^2 e^{2ikLn_r}}, \tag{6.6}$$

where

$$r_0 = \frac{n_r - n_b}{n_r + n_b} \tag{6.7}$$

is the Fresnel coefficient. We can analytically continue this function into the complex plane, and consider for which $k \in \mathbb{C}$, $r(k) \to \infty$. In other words, we can find the poles of $r(k)$. These occur when the denominator of (6.6) vanishes, leading to an analytic expression [165, 166] for the poles

$$k_m L = \frac{2\pi m + i \ln\left[(n_r - n_b)^2 \,/\, (n_r + n_b)^2\right]}{2n_r}, \tag{6.8}$$

where m is an integer. Taking a slab of index $n_r = \pi$ and a background with index $n_b = 1$, the system and the poles are plotted in Figure 6.2. Several

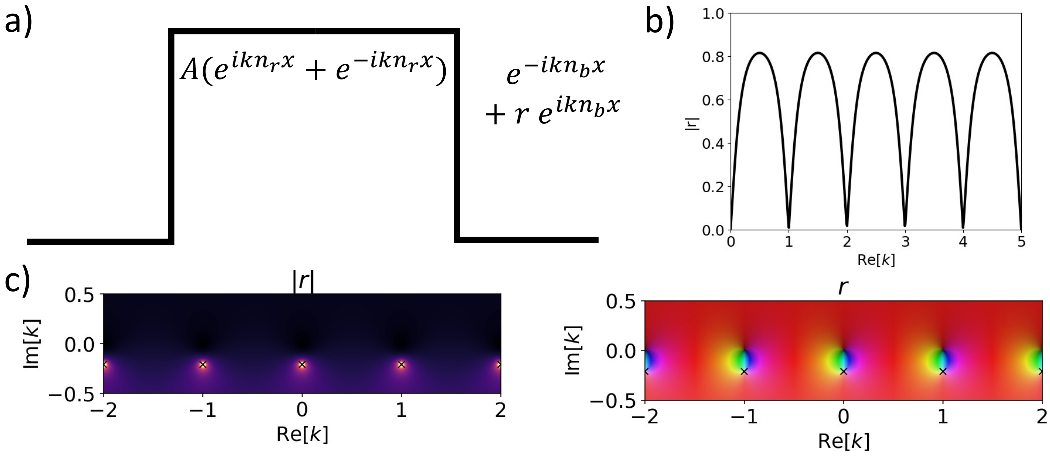

Figure 6.2: Example of a understanding a photonic system in terms of its quasi–normal modes. The system is shown in a): a dielectric slab of refractive index $n = \pi$ and width $L = 1$ has a wave incident from the right–hand side. Matching the field and it's derivative at the edge of the resonator allows one to calculate the reflection coefficient analytically, shown in b). Analytically continuing this into the complex plane, we show c) only the magnitude and d) both magnitude and phase. We see a row of simple poles, with their locations in the complex plane directly related to the k associated with the quasi–normal modes.

things are of note:

1. The poles of the reflection coefficient are located in the lower half of the complex plane. This means that $k'' < 0$, corresponding to a quasi–normal mode.
2. Associated with each pole is a zero in the reflection coefficient at $\mathrm{Re}[k_m]$.
3. The width of the zeros in reflection is determined by $\mathrm{Im}[k_m]$.

Knowing at which complex frequencies the quasi–normal modes occur at allows for the numerical calculation of the fields. It is also possible to do this analytically for this particular system [166], however we will proceed numerically. From our earlier discussion, we know that quasi–normal modes must be purely outgoing at the edge of the resonator: they must fulfil the radiation condition [167], which for N dimensions is

$$\lim_{r\to\infty} r^{(N-1)/2}\left(\frac{\partial}{\partial r} - ik\right)\phi(\boldsymbol{r}) = 0. \tag{6.9}$$

In 1D, this becomes

$$\frac{d\phi}{dx} = \pm ik\phi(x) \tag{6.10}$$

as $x \to \pm\infty$. Back–integration can be used to find the field numerically. Starting far away from the right–hand side of the sample, we set a field $\phi = e^{ik_m n(x)x}$, where k_m corresponds to the quasi–normal mode we would like to find the field of. We then integrate the 1D Helmholtz equation back to $x = 0$ to find the field. As this problem is left–right symmetric, the field on the left and right of the slab are identical. For a non–symmetric index profile $n(x)$, the same procedure could be applied, however one would need to impose continuity of field to connect the solutions. Code to perform this back–integration is given in Appendix A. The fields of the quasi–normal modes of the slab, found using this method, are shown in Figure 6.3. The modes exhibit the exponential growth in space that we expect.

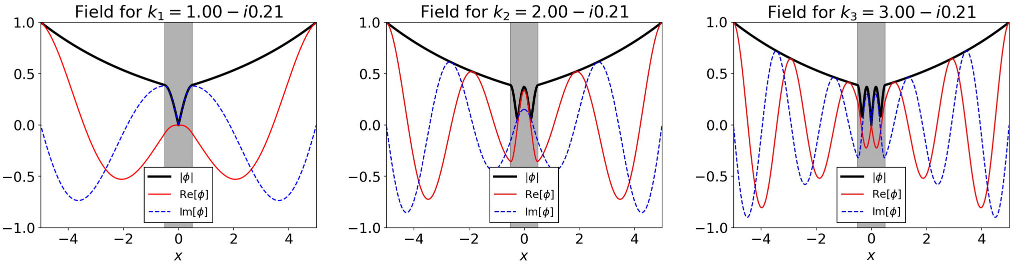

Figure 6.3: Fields associated with the quasi–normal modes of a dielectric slab. These are obtained by solving the Helmholtz equation with outgoing wave boundary conditions at particular complex frequencies.

Having characterised *what* quasi–normal modes are, we now consider *why* they have attracted such interest across physics in recent years. With the simple tools we have developed, more complicated systems can be analysed and understood with the help of quasi–normal modes. First used in quantum mechanics to describe alpha decay [168, 169], quasi–normal modes have since found utility in modelling radiation in many different systems, from black holes [165], photonic resonators [166] to leaky waveguides [170, 171]. Later in this chapter, we will consider how to design resonators that have QNMs at particular complex k values. To motivate this, we explore

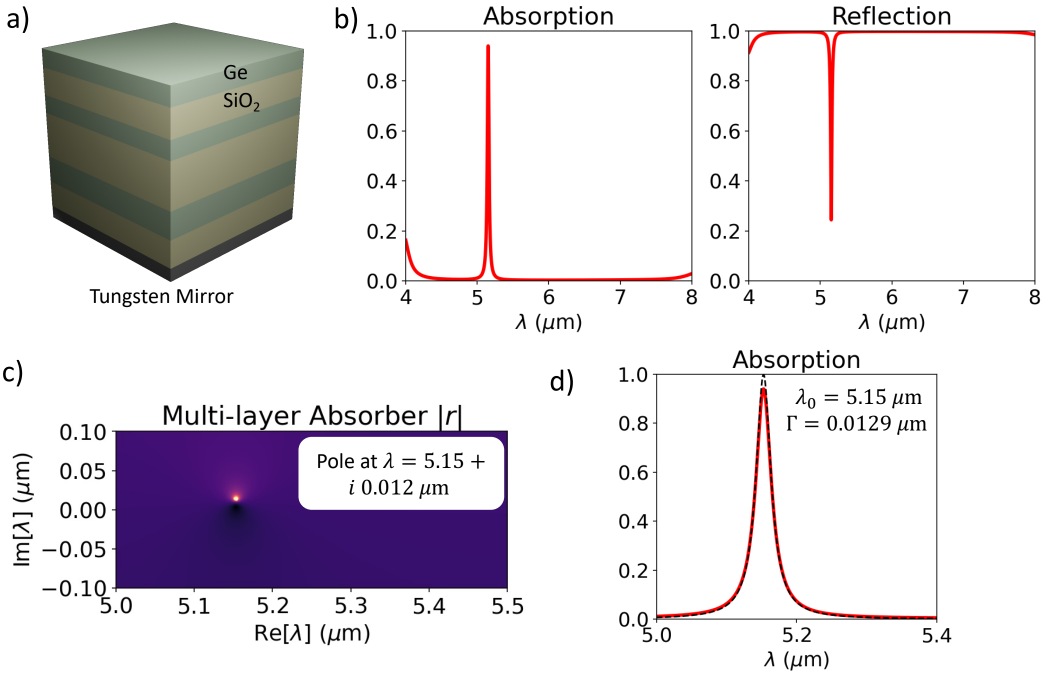

Figure 6.4: Understanding a more complicated structure using the quasi–normal mode framework. Sakurai et al. [172] designed the mirror–backed multi–layer structure shown in a) to function as an IR absorber. The absorption and reflection, shown in b), exhibit clear dips at around $\lambda = 5\mu$m. Extending the reflection coefficient into the complex wavelength plane, a pole is found at $\lambda = 5.15 + i0.015\mu$m, corresponding to a quasi–normal mode. Fitting a Lorentzian to the absorption peak, we find that the spectral properties are directly related to the position of the quasi–normal mode.

the multi–layer mid-IR absorber presented by Sakurai et al. [172], shown in Figure 6.4 a). This is a multi–layer structure, designed using a genetic algorithm, to absorb at partiuclar wavelengths. Shown in Figure 6.4 b), is a clear peak in absorption (and corresponding nadir in reflection) at the target wavelength of around 5 μm. We analyse the reflection coefficient by extending it into the complex wavelength plane. This is equivalent to extending k into the complex plane, as $k = 2\pi/\lambda$. Rather than expecting QNMs to appear in the lower half of the complex plane, we now expect them to appear in the upper half. The design procedure utilised in [172] employed little physical insight, however by looking at the reflection coefficient of the structure as a function of complex wavelength we can understand why the structure performs so well. Figure 6.4 shows a pole at the complex wavelength $\lambda = 5.15 + i0.012$ μm. Fitting a Lorentzian of the form

$$\mathcal{L}(\lambda) = \frac{\Gamma}{(\lambda - \lambda_0)^2 + \Gamma^2} \tag{6.11}$$

to the absorption peak, we find parameters

$$\lambda_0 = 5.15\ \mu\text{m} \qquad\qquad \Gamma = 0.0129\ \mu\text{m}. \tag{6.12}$$

The location of the quasi–normal mode in the complex wavelength plane directly relates to the properties of the resonance. This connection is a general property of quasi–normal modes at has been utilised to decompose the physical properties of a system into the quasi–normal modes [166]. For example, the effect of a structured environment upon the Purcell factor of an emitter can be decomposed in terms of the QNMs of the system [146], and through calculating how small changes in the system perturb the QNMs, deeper insight into sensing has been developed [173, 174].

6.3 Finding Quasi–Normal Modes Analytically

In the previous section, we outlined how to analytically find the quasi–normal modes of a 1D slab. The central idea was to find the complex wave–numbers at which the scattering (or reflection) coefficient had poles. This idea extends straightforwardly to higher dimensions and provides a useful way to analytically find the quasi–normal modes of uniform systems. We will consider the scalar Helmholtz equation

$$\left(\nabla^2 + k^2 n^2\right) \phi(\boldsymbol{r}). \tag{6.13}$$

Due to the extraordinary generality of wave phenomena, outlined in Section 2.1, this describes many types of time–harmonic waves including: pressure waves [7], single components of the electromagnetic field [15], longitudinal and transverse components of elastic waves [9], and even black holes [165].

6.3.1 2D: Cylinders

Consider a cylinder of index n and radius a.

$$\left(\nabla^2 + k^2 n^2\right) \phi(\boldsymbol{r}) = 0 \tag{6.14}$$

Where in 2D cylindrical coordinates the Laplacian is

$$\nabla^2 = \frac{\partial^2}{\partial r^2} + \frac{1}{r}\frac{\partial}{\partial r} + \frac{1}{r^2}\frac{\partial^2}{\partial \theta^2}. \tag{6.15}$$

As for the 1D slab, we consider the scattering of a plane wave from the cylinder and aim to find the expansion coefficients. To this end, we write the incident field as

$$\phi_i(\boldsymbol{r}) = e^{ikx} = e^{ikr\cos\theta}, \tag{6.16}$$

the scattered field as

$$\phi_s(\boldsymbol{r}) = \begin{cases} \sum_m a_m H_m^{(1)}(kr)e^{im\theta} & r > a \\ \sum_m b_m J_m(nkr)e^{im\theta} & r < a. \end{cases} \tag{6.17}$$

Our choice of functions to decompose the scattered field into ensures that $\phi_s(r = 0)$ does not diverge and that as $r \to \infty$, the radiation condition is met. The asymptotic form of the Hankel functions of the first kind [175] is

$$\lim_{z\to\infty} H_m^{(1)}(z) \sim \sqrt{\frac{2}{\pi z}} e^{i\left(z - \frac{m\pi}{2} - \frac{\pi}{4}\right)}, \tag{6.18}$$

which is manifestly an outgoing cylindrical wave. To find the expansion coefficients a_m, b_m, we re–write the incident plane wave using the Jacobi–Anger expansion [175]

$$e^{ikr\cos\theta} = \sum_m i^m J_m(kr)e^{im\theta}, \tag{6.19}$$

then impose continuity of the total field $\phi(\boldsymbol{r}) = \phi_i(\boldsymbol{r}) + \phi_s(\boldsymbol{r})$ and its derivative at $r = a$. This yields

$$a_m = -i^m \frac{J_m(nka)J_m'(ka) - nJ_m(ka)J_m'(nka)}{J_m(nka)H_m^{(1)}(ka) - nH_m^{(1)}(ka)J_m'(nka)}, \tag{6.20}$$

where primes denote derivative of the Bessel function with respect to the argument. Equation (6.20) is the cylindrical scalar field equivalent of Mie's multipole expansion that was derived in Section 2.5. This is the scattering coefficient for the m^{th} partial wave. As with the 1D case, the quasi–normal mode frequencies k_m occur when the scattering coefficient has a pole in the complex plane. Standard root–finding methods (i.e. Newton's method) can find the complex k values for which the denominator of (6.20) vanishes. This allows us to find the locations of the quasi–normal modes corresponding to specific multipoles: $m = 0$ is the monopole, $m = 1$ is the dipole and so on.

6.3.2 3D: Spheres

Considering the same scattering problem, now for a sphere of radius a and index n, the Helmholtz equation is

$$\left(\nabla^2 + k^2 n^2\right) \phi(\boldsymbol{r}) = 0, \tag{6.21}$$

where the Laplacian is written in spherical coordinates

$$\nabla^2 f = \frac{1}{r^2}\frac{\partial}{\partial r}\left(r^2 \frac{\partial f}{\partial r}\right) + \frac{1}{r^2 \sin\theta}\frac{\partial}{\partial \theta}\left(\sin\theta \frac{\partial f}{\partial \theta}\right) + \frac{1}{r^2 \sin^2\theta}\frac{\partial^2 f}{\partial \phi^2}, \tag{6.22}$$

with azimuthal angle ϕ and polar angle θ. As before, we consider the scattering of a plane wave, so the incident field is

$$\phi_i(\boldsymbol{r}) = e^{ikz} = e^{ikr\cos\theta}. \tag{6.23}$$

We decompose the scattered field as

$$\phi_s(\boldsymbol{r}) = \begin{cases} \sum_{\ell,m} a_{\ell,m} h_\ell^{(1)}(kr) P_\ell^m(\cos\theta) e^{im\phi} \\ \sum_{\ell,m} b_{\ell,m} j_\ell(kr) P_\ell^m(\cos\theta) e^{im\phi} \end{cases} \tag{6.24}$$

and the incident field into

$$e^{ikr\cos\theta} = \sum_\ell (2\ell+1) i^\ell j_\ell(kr) P_\ell(\cos\theta), \tag{6.25}$$

where $h_\ell(1)$ is the spherical Hankel function of the first kind, j_ℓ is the spherical Bessel function, P_ℓ^m are the associated Legendre polynomials. Once again, the asymptotic forms of the spherical Bessel and Hankel functions

$$\lim_{z\to 0} j_\ell(z) \sim \frac{z^\ell}{(2\ell+1)!!}, \tag{6.26}$$

$$\lim_{z\to\infty} h_\ell^{(1)}(z) \sim i^{-\ell-1}\frac{e^{iz}}{z}, \tag{6.27}$$

guarantee that the scattered field does not diverge and that the radiation condition is met. Applying continuity of the total field and its derivative at $r = a$, we find that

$$a_\ell = i^\ell(2\ell+1)\frac{j_\ell(nka)j_\ell'(ka) - nj_\ell(ka)j_\ell'(nka)}{j_\ell(nka)h_\ell^{(1)}(ka) - nh_\ell^{(1)}(ka)j_\ell'(nka)}. \tag{6.28}$$

Aside from the initial pre–factor, this is the same as the case of the 2D cylinder (6.20), with the Bessel and Hankel functions exchanged for the spherical Bessel and Hankel functions. Once again, Equation (6.28) is the spherical scalar field equivalent of Mie's multipole expansion that was derived in Section 2.5. Root finding can then be used to find the complex k values for which the denominator of (6.28) vanishes.

6.4 Finding Quasi–Normal Modes Numerically

In the previous section, we outlined how to find the locations of the quasi–normal modes of uniform slabs, discs and spheres. For graded media, analytic solution is no longer generally tractable so numerical techniques must be employed [176]. Here, we outline some simple finite difference schemes that can be used to find the locations of quasi–normal modes of certain graded systems. We then show how one can use finite element packages, such as COMSOL, to find the quasi–normal modes of any systems. While we make use of finite difference schemes, spectral methods [177] can also be used find the complex frequency resonances of a system. These methods have the benefit of using the whole grid to evaluate derivatives, rather than just neighbouring points as with finite difference methods. For conceptual simplicity we will proceed using finite difference methods, although future extensions might include developing spectral methods to manipulate quasi–normal modes.

To find quasi–normal modes numerically, one must formulate the Helmholtz equation as an eigenvalue problem for the wave–number k by discretising the Laplacian operator. There is, however, a key difficulty: the eigenvalue itself k is embedded within the Laplacian operator, as one must also impose the radiation condition at the boundary. As we will see, one must linearise the resulting expressions in terms of k, allowing for a quadratic eigenvalue problem [178] to be formed.

6.4.1 Finite Differences in 1D

To find the quasi–normal modes of a given permittivity $\varepsilon(x)$, we must discretise the wave–operator and impose the correct boundary conditions. Beginning from the 1D Helmholtz equation

$$\left(\frac{\mathrm{d}^2}{\mathrm{d}x^2}+\varepsilon(x)k^2\right)\phi(x)=0, \tag{6.29}$$

we use the usual finite difference discretisation [43] the Laplacian

$$\nabla^2\phi\approx\frac{\phi_{n+1}-2\phi_n+\phi_{n-1}}{\Delta x^2}, \tag{6.30}$$

where $\phi_i = \phi(x_i)$. Discretising space into only 4 points, we can write this in matrix form as

$$\frac{\mathrm{d}^2\phi}{\mathrm{d}x^2} \approx \frac{1}{(\Delta x)^2}\begin{pmatrix} -2 & 1 & 0 & 0 \\ 1 & -2 & 1 & 0 \\ 0 & 1 & -2 & 1 \\ 0 & 0 & 1 & -2 \end{pmatrix}\begin{pmatrix} \phi_1 \\ \phi_2 \\ \phi_3 \\ \phi_4 \end{pmatrix}. \tag{6.31}$$

This has the boundary condition that $\phi_0 = \phi_5 = 0$. Instead we would like to impose the boundary condition on the right–hand side that

$$\frac{\mathrm{d}\phi}{\mathrm{d}x} = ik\phi, \tag{6.32}$$

and on the left–hand side that

$$\frac{\mathrm{d}\phi}{\mathrm{d}x} = -ik\phi. \tag{6.33}$$

These are the Sommerfeld radiation conditions [167], which impose that energy cannot enter the system from infinity and the energy radiated by the system must scatter to infinity. Taking only the right–hand side we re-write the derivative using finite differences, then can re–arrange for ϕ_{n+1}

$$\frac{\phi_{n+1} - \phi_n}{\Delta x} = ik\phi_n \tag{6.34}$$

$$\phi_{n+1} = (ik\Delta x + 1)\phi_n. \tag{6.35}$$

Using this expression to eliminate ϕ_{n+1} in (6.30), we obtain a modified Laplacian matrix

$$\frac{\mathrm{d}^2\phi}{\mathrm{d}x^2} \approx \frac{1}{(\Delta x)^2}\begin{pmatrix} (ik\Delta x - 1) & 1 & 0 & 0 \\ 1 & -2 & 1 & 0 \\ 0 & 1 & -2 & 1 \\ 0 & 0 & 1 & (ik\Delta x - 1) \end{pmatrix}\begin{pmatrix} \phi_1 \\ \phi_2 \\ \phi_3 \\ \phi_4 \end{pmatrix}. \tag{6.36}$$

This now has the outgoing wave boundary condition at the edge of the slab.

To formulate the eigenvalue problem, we split this matrix into a part that is linear in k and a part that does not contain k. Defining

$$\mathcal{L} = \frac{1}{\Delta x^2}\begin{pmatrix} -1 & 1 & 0 & 0 \\ 1 & -2 & 1 & 0 \\ 0 & 1 & -2 & 1 \\ 0 & 0 & 1 & -1 \end{pmatrix} \tag{6.37}$$

$$\mathcal{L}' = \frac{1}{\Delta x^2}\begin{pmatrix} i\Delta x & 0 & 0 & 0 \\ 0 & 0 & 0 & 0 \\ 0 & 0 & 0 & 0 \\ 0 & 0 & 0 & i\Delta x \end{pmatrix} \tag{6.38}$$

the finite difference Helmholtz equation with outgoing wave boundary conditions becomes

$$\left(\mathcal{L} + k\mathcal{L}' + k^2\varepsilon(x)\right)\phi = 0. \tag{6.39}$$

This has the form of a quadratic eigenvalue problem [178] for k. If we define a new vector $(\phi, k\phi)^T$, we can form the eigenvalue problem as

$$\begin{pmatrix} \mathbf{0} & \mathbf{1} \\ -\mathcal{L}/\varepsilon(x) & -\mathcal{L}'/\varepsilon(x) \end{pmatrix} \begin{pmatrix} \phi \\ k\phi \end{pmatrix} = k \begin{pmatrix} \phi \\ k\phi \end{pmatrix}. \tag{6.40}$$

One can form this linear system and solve it using standard linear algebra methods [43] for the eigenvalues k, which give the complex frequencies at which the system supports a quasi–normal mode.

6.4.2 Finite Differences in 2D

We now formulate the method for 2D cylindrically symmetric permittivity profiles. The Helmholtz equation in 2D is

$$\left(\frac{\partial^2}{\partial r^2} + \frac{1}{r}\frac{\partial}{\partial r} + \frac{1}{r^2}\frac{\partial^2}{\partial \theta^2} + k^2 \varepsilon(\boldsymbol{r}) \right) \phi(\boldsymbol{r}) = 0. \tag{6.41}$$

We begin by separating the radial and angular variables using the ansatz

$$\phi(r, \theta) = \phi(r) e^{im\theta}, \tag{6.42}$$

giving

$$\left(\frac{\partial^2}{\partial r^2} + \frac{1}{r}\frac{\partial}{\partial r} - \frac{m^2}{r^2} + k^2 \varepsilon(\boldsymbol{r}) \right) \phi(\boldsymbol{r}) = 0. \tag{6.43}$$

We then make the substitution

$$\phi(r) = \frac{\psi(r)}{\sqrt{r}}, \tag{6.44}$$

which removes the first derivative

$$\left(\frac{\partial^2}{\partial r^2} + \frac{1}{4r^2} - \frac{m^2}{r^2} + k^2\varepsilon(r)\right)\psi(r) = 0. \tag{6.45}$$

The scattering boundary condition we must impose at $r = a$ is that

$$\phi(r = a) = H_m^{(1)}(ka), \tag{6.46}$$

so

$$\psi(r = a) = \sqrt{r}H_m^{(1)}(ka). \tag{6.47}$$

This means that

$$\frac{\partial\psi}{\partial r} = \psi(r)\left(\frac{1}{2r} + k\frac{H_m^{(1)'}(kr)}{H_m^{(1)}(kr)}\right). \tag{6.48}$$

This is the 2D equivalent of the $\phi' = ik\phi$ boundary condition we had to apply in 1D. To keep notation compact, we define

$$\gamma(k, r) = \left(\frac{1}{2r} + k\frac{H_m^{(1)'}(kr)}{H_m^{(1)}(kr)}\right). \tag{6.49}$$

To find how to modify the Laplacian matrix, we proceed as before, asserting that at $r = a$

$$\frac{\psi_{n+1} - \psi_n}{\Delta r} = \psi_n\gamma(k, a) \tag{6.50}$$

$$\psi_{n+1} = \psi_n(1 + \Delta r\gamma(k, a)). \tag{6.51}$$

Just plugging this into the Laplacian operator, however, will not allow us to set up the eigenvalue problem, as the eigenvalue k is still contained within the function $\gamma(k)$. To linearise the system, we Taylor expand $\gamma(k)$ around a particular complex $k_\star$ and group terms in powers of k

$$\begin{aligned} \gamma(k,a) &\approx \gamma(k_\star,a) + (k-k_\star)\partial_k\gamma(k_\star,a) + \dots && (6.52)\\ &= \gamma(k_\star,a) - k_\star\partial_k\gamma(k_\star,a) + k\partial_k\gamma(k_\star,a) && (6.53)\\ &= A + kB. && (6.54) \end{aligned}$$

The derivatives of $\gamma(k,a)$ with respect to k can be computed numerically using complex differentiation [179], or analytically as

$$\partial_k\gamma(k,r) = \frac{H_m^{(1)'}(kr)}{H_m^{(1)}(kr)} + (kr)\left[\frac{H_m^{(1)''}(kr)}{H_m^{(1)}(kr)} - \left(\frac{H_m^{(1)'}(kr)}{H_m^{(1)}(kr)}\right)^2\right]. \qquad (6.55)$$

Utilising this, we find that the boundary term in the Laplacian is

$$\psi_{n+1} = \psi_n(A\Delta r + 1) + kB\Delta r\psi_n. \qquad (6.56)$$

This leads to the modified Laplacian operator, with the correct outgoing boundary condition at $r=a$, which is

$$\frac{\partial^2}{\partial r^2} \approx \frac{1}{\Delta r^2}\begin{pmatrix} -2 & 1 & 0 & 0\\ 1 & -2 & 1 & 0\\ 0 & 1 & -2 & 1\\ 0 & 0 & 1 & (A\Delta r - 1) + kB\Delta r \end{pmatrix}. \qquad (6.57)$$

Splitting this into parts that are linear in k and parts that do not depend on k, we define

$$\mathcal{L} = \frac{1}{\Delta r^2}\begin{pmatrix} -2 & 1 & 0 & 0 \\ 1 & -2 & 1 & 0 \\ 0 & 1 & -2 & 1 \\ 0 & 0 & 1 & (A\Delta r - 1) \end{pmatrix}, \quad \mathcal{L}' = \frac{1}{\Delta r^2}\begin{pmatrix} 0 & 0 & 0 & 0 \\ 0 & 0 & 0 & 0 \\ 0 & 0 & 0 & 0 \\ 0 & 0 & 0 & B\Delta r \end{pmatrix}. \tag{6.58}$$

The 2D cylindrical Helmholtz equation with out–going wave boundary conditions is thus

$$\left(\mathcal{L} + k\mathcal{L}' + \frac{1}{4r^2} - \frac{m^2}{r^2} + k^2\varepsilon(r)\right)\psi(r) = 0. \tag{6.59}$$

The quadratic eigenvalue problem is therefore

$$\begin{pmatrix} \mathbf{0} & \mathbf{1} \\ -\frac{1}{\varepsilon(r)}\left[\mathcal{L} + \frac{1}{4r^2} - \frac{m^2}{r^2}\right] & -\frac{\mathcal{L}'}{\varepsilon(r)} \end{pmatrix}\begin{pmatrix} \psi \\ k\psi \end{pmatrix} = k\begin{pmatrix} \psi \\ k\psi \end{pmatrix}. \tag{6.60}$$

6.4.3 Finite Differences in 3D

We now consider the same problem as the previous section in 3 spatial dimensions, so the resonators are spherical. In spherical coordinates, with a solution of the form $\chi(\boldsymbol{r}) = \chi(r)Y_l^m(\theta,\phi)$, the Helmholtz equation can be written as

$$\frac{\partial^2\chi}{\partial r^2} + \frac{2}{r}\frac{\partial\chi}{\partial r} - \frac{l(l+1)}{r^2}\chi(r) + k^2\varepsilon(r)\chi(r) = 0. \tag{6.61}$$

Making the substitution $\chi = \psi/r$ to eliminate the first derivative, this becomes

$$\frac{\partial^2\psi}{\partial r^2} - \frac{l(l+1)}{r^2}\psi + k^2\varepsilon(r)\psi = 0. \tag{6.62}$$

The boundary condition for an outgoing wave is

$$\chi(r \to \infty) = h_\ell^{(1)}(kr), \tag{6.63}$$

$$\psi(r \to \infty) = r h_\ell^{(1)}(kr). \tag{6.64}$$

Using this to calculate the boundary condition in terms of the derivative, we find that

$$\frac{\partial \psi}{\partial r} = h_\ell^{(1)}(kr) \left[1 + (kr) \frac{h_\ell^{(1)'}(kr)}{h_\ell^{(1)}(kr)} \right] \tag{6.65}$$

$$= \psi \left[\frac{1}{r} + k \frac{h_\ell^{(1)'}(kr)}{h_\ell^{(1)}(kr)} \right] = \psi \gamma(k). \tag{6.66}$$

Using the same boundary condition as for the 2D case

$$\psi_{n+1} = \psi_n (1 + \Delta r \gamma(k)), \tag{6.67}$$

although with a slightly different expression for $\gamma(k)$. Linearising, we approximate $\gamma(k)$

$$\gamma(k) = \gamma(k_\star) + (k - k_\star) \partial_k \gamma(k_\star) = A + kB, \tag{6.68}$$

where $A = \gamma(k_\star) - k_\star \partial_k \gamma(k_\star)$ and $B = \partial_k \gamma(k_\star)$. Defining

$$\mathcal{L} = \frac{1}{\Delta r^2} \begin{pmatrix} -2 & 1 & 0 & 0 \\ 1 & -2 & 1 & 0 \\ 0 & 1 & -2 & 1 \\ 0 & 0 & 1 & (A\Delta r - 1) \end{pmatrix}, \quad \mathcal{L}' = \frac{1}{\Delta r^2} \begin{pmatrix} 0 & 0 & 0 & 0 \\ 0 & 0 & 0 & 0 \\ 0 & 0 & 0 & 0 \\ 0 & 0 & 0 & B\Delta r \end{pmatrix}. \tag{6.69}$$

we can split the Helmholtz equation into

$$\left(\mathcal{L} + k\mathcal{L}' - \frac{l(l+1)}{r^2} + k^2\varepsilon(r)\right)\psi = 0. \tag{6.70}$$

Which can be formed into a quadratic eigenvalue problem

$$\begin{pmatrix} \mathbf{0} & \mathbf{1} \\ -\frac{1}{\varepsilon(r)}\left(\mathcal{L} - l(l+1)/r^2\right) & -\mathcal{L}'/\varepsilon(r) \end{pmatrix} \begin{pmatrix} \psi \\ k\psi \end{pmatrix} = k \begin{pmatrix} \psi \\ k\psi \end{pmatrix}. \tag{6.71}$$

As our eventual aim is to manipulate the quasi–normal modes of spheres and cylinders by grading them or by shifting their permittivities, it is essential we are able to calculate the locations of the quasi–normal modes. The expressions derived in the previous two sections enable this for both cylinders and spheres. While Mie theory can be used to calculate the complex positions of the resonances for isotropic spheres, (6.60) and (6.71) allow us to calculate the quasi–normal modes of isotropic and graded spheres and give us the field of the mode ψ at the same time.

6.4.4 Finding Quasi–Normal Modes with COMSOL

Another way to find the eigenmodes of a system is to use finite element solvers, such as COMSOL. This provides a useful validation for the analytics and numerics we have developed in the previous few sections. Setting up a COMSOL model to validate our results involves four main steps:

1. Set up the geometry. If we consider the example of the cylinder, this means we need to define a cylinder of radius a, along with an air box outside it.

2. Define the materials. For our examples, We set the permittivity of the cylinder to be $\varepsilon = 4$. COMSOL's material library contains the properties of air.

3. Set the boundary conditions. In order to solve Maxwell's equations the boundary conditions must be specified. We only impose the radiation (Sommerfeld) condition at the edge of the mode. This is equivalent to the modification of the final element of the matrices in the previous sections to enforce the out going wave boundary condition. We must also add a perfectly matched layer (PML) to simulate scattering into free space. This ensures that there is no reflection from the edges of the computational domain.

4. Build the mesh. The system is discretised into small triangles. The size of these should be small enough to resolve the wavelength (i.e. minimum mesh size $\sim \lambda/6$.

Following these steps for a cylinder of radius $a = 550$ nm and permittivity $\varepsilon = 4$ we arrive at the COMSOL model shown in Figure 6.5. A very similar procedure can be followed for the sphere. The material domains and boundary conditions are shown in Figure 6.5 a) with the mesh shown in Figure 6.5 b). It can be noted that the mesh breaks the cylindrical symmetry of the resonator, affecting the modes that are found. Some of the eigenmodes this model finds are shown in Figure 6.6. Each mode has the correct character (i.e. $l = 1$ is a dipole etc.) and the frequency it occurs at matches with the analytic results shown in Figure 6.7. However, the modes are often found in pairs. This is due to the broken symmetry lifting the degeneracy of the eigenmodes of the system. Rather than a single $l = 1$ mode at f $97 + i21$ THz, two modes are found very close to this frequency. Also visible in Figure 6.6 is a drawback of using COMSOL to find quasi–normal

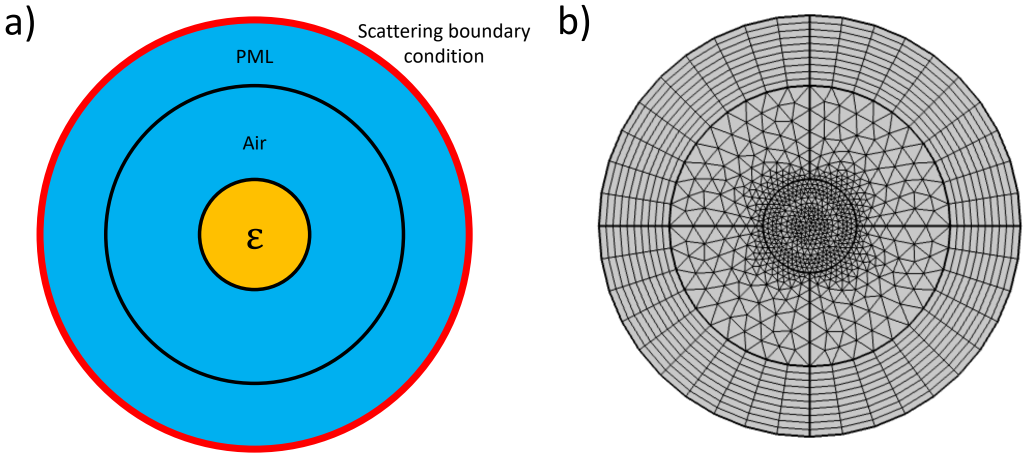

Figure 6.5: Finding quasi–normal modes in COMSOL. a) shows a schematic for how one sets up an eigenfrequency model in COMSOL to find quasi–normal modes. A resonator of permittivity ε is placed inside an air box, bounded by a perfectly matched layer (PML) to simulate radiation into free space. At the edge of the PML must be a scattering boundary condition, equivalent to the Sommerfeld radiation condition. The mesh, shown in b), should be fine enough to correctly resolve the wavelength in each material domain. This means it should be finer within the dielectric material.

modes. Since quasi–normal modes grow exponentially in space away from the resonator, the field magnitude at the internal PML edge is large. This means that the PML can fail to totally eliminate the reflections, shifting the eigen–frequencies. As the growth of the quasi–normal mode is dictated by $\mathrm{Im}[k]$, when this is large the growth is large and the numerical error is likely to be larger. Figure 6.6 shows this: all of the fields are plotted on the same colour scale, and the modes with smaller l have visibly larger fields within the PML layer.

6.4.5 Comparing the Methods

Figure 6.7 shows the comparision between the analytical, matrix and COMSOL methods for finding the quasi–normal modes of radially symmetric systems. Figure 6.7 a) shows the results for an infinite cylinder of radius $a = 550$ nm and permittivity $\varepsilon = 4$, while Figure 6.7 b) shows the results

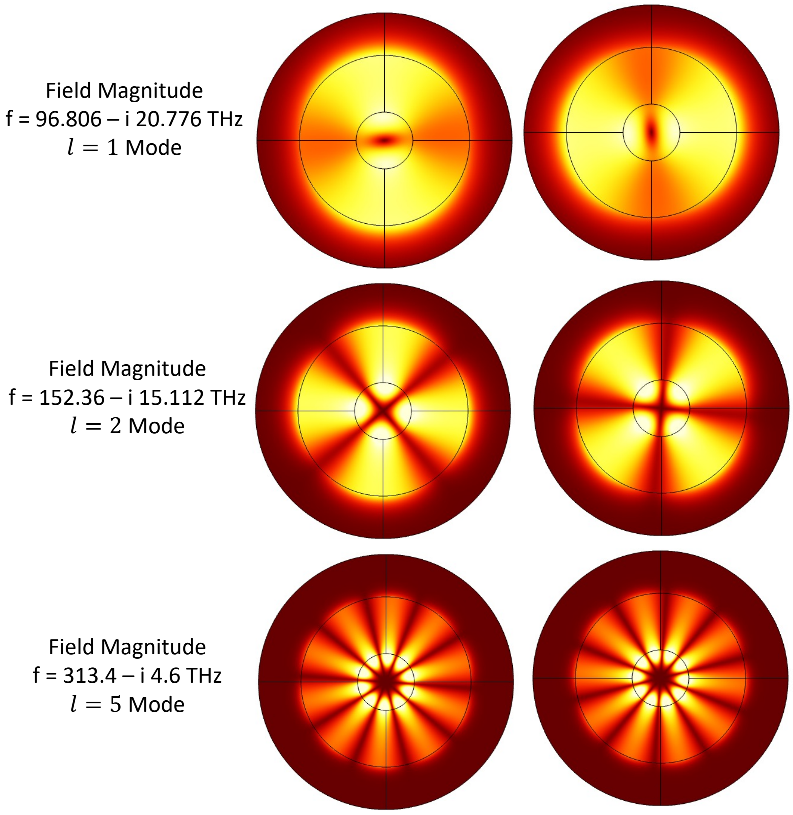

Figure 6.6: Fields of the quasi–normal modes of an isotropic dielectric cylinder. The structure we have modeled is shown in Figure 6.5.

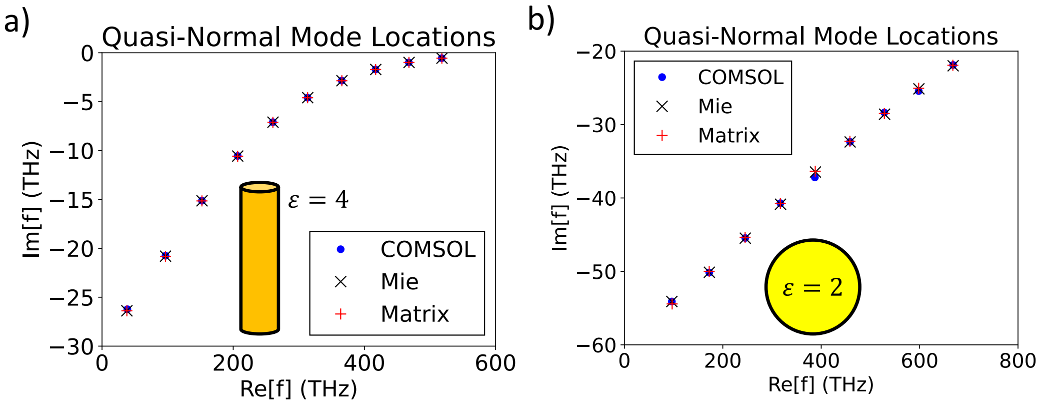

Figure 6.7: A comparison of different methods for finding the quasi–normal modes of isotropic cylinders or spheres. a) shows the comparison for a cylinder, and b) for a sphere.

for a sphere of radius $a = 550$ nm and permittivity $\varepsilon = 2$. All methods agree well, with some COMSOL points exhibiting larger error, due to the issues discussed in the previous section. It should be noted that the matrix method and COMSOL can find the mode locations for radially graded resonators too, while the analytics cannot.

Now that we have discussed in detail how one can find the quasi–normal modes of many different systems, we proceed to manipulate the properties of the resonator to place quasi–normal modes at desired frequencies. We begin with slabs of dielectric.

6.5 Moving the Quasi–Normal Modes of 1D Slabs by Finding Eigen–Permittivities

As we noted in the previous sections, finding the quasi–normal modes of general systems can be challenging [176]. To avoid solving a non–linear eigenvalue problem problem, Chen et al. [150] proposed, one could work in terms of real wave–numbers but extending the *permittivity* into the complex plane. Employing the insight of Chen et. al., we write the permittivity as a spatial variation plus a constant background $\varepsilon(x) = \varepsilon_s(x) + \varepsilon_b$ allows us to recast the Helmholtz equation as an eigenvalue problem for the permittivity

$$-\frac{1}{k^2}\left(\frac{d^2}{dx^2} + k^2\varepsilon_s(x)\right)\phi(x) = \varepsilon_b\phi(x). \tag{6.72}$$

Rather than using this to find the QNMs of a system, we show that this can be used to design the complex frequencies of the QNMs.

To do this, we take a known spatially varying permittivity, such as the dielectric step or absorber stack e.g. from [172], and choose a $k \in \mathbb{C}$ at which we would like a QNM to occur. We then numerically solve the eigenvalue problem Eq. (6.72) using the finite difference method Eq. (6.36), along with standard matrix libraries, to find a complex eigen–permittivity that allows us to form a structure with $\varepsilon(x) = \varepsilon_s(x) + \varepsilon_b$ with a pole at the chosen complex frequency.

We first apply the method to the homogeneous slab. In Fig. 6.8 we design the new structure to support a QNM at the frequency $k = 1.5 - 0.05i$. For the $N \times N$ Laplacian matrix, there are N possible values for ε_b that will satisfy this condition. Taking the lowest absolute valued background (to minimise numerical error) permittivity $\varepsilon_b = -4.99 - 2.32i$, we find that the new structure now supports a QNM at our chosen k. This is shown in Fig. 6.8(a). The transmission, Fig. 6.8(b), shows a large peak at the real frequency associated with the QNM and has values $|t| > 1$ due to the gain that has been added to the system. Although the location of the pole can be manipulated solely by changing the height of the barrier, in order to manipulate the real and imaginary parts independently, control over both the real and imaginary permittivity is required. As might be anticipated, in order to move a pole closer to the real frequency axis, without changing the resonant frequency, gain is required. Conversely, loss is required to move the pole further away from the real axis. The field profile, shown in Fig. 6.8(c), still has the exponential growth characteristic of QNMs.

Next, we apply the same eigen–permittivity method to the absorbing stack shown in Figure 6.4 a). For this structure, we must take care that the correct boundary conditions are imposed. The opaque metal substrate requires the Dirichlet boundary condition $\phi = 0$, while the outgoing wave boundary condition must be imposed at the top of the stack. Choosing two target bandwidths, for the same resonance wavelength, $\lambda_1 = (6.5 + 0.03i)\mu$m and $\lambda_2 = (6.5 + 0.15i)\mu$m, we obtain background permittivities of $\varepsilon_{b,1} = 3.27 - 0.01i$ and $\varepsilon_{b,2} = 3.28 + 0.29i$. The effect of the background shift on the pole locations is shown in Figure 6.9(a-b). Accordingly, the poles are

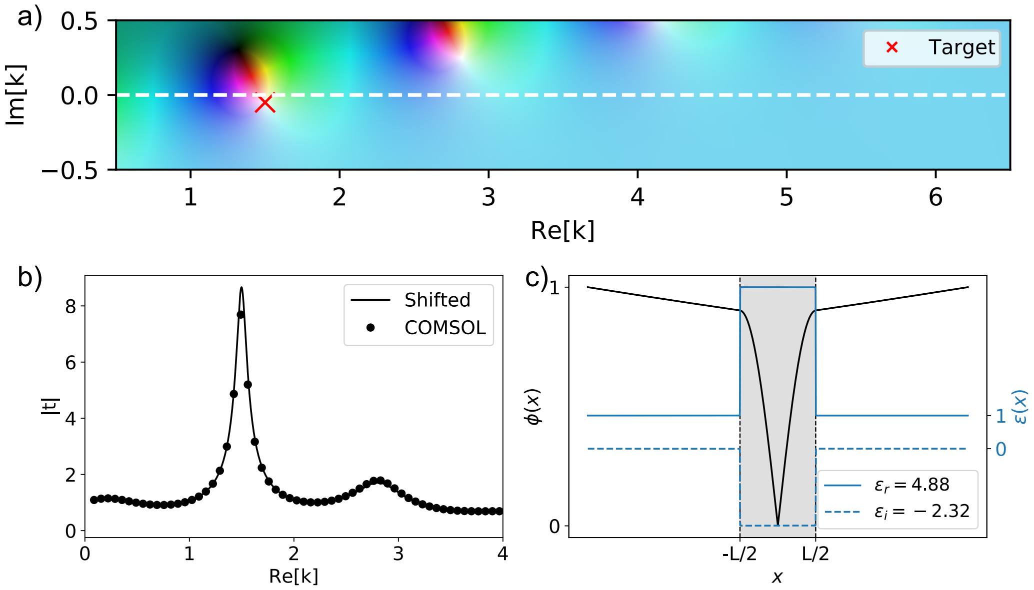

Figure 6.8: Shifting the resonances of a dielectric slab. A background permittivity $\varepsilon_b = -4.99 - 2.32i$ is found as a solution to Eq. (6.36) which, when combined with the original structure $\varepsilon_s(|x| < L/2) = \pi^2$ will contain a pole at the desired complex frequency of $k = 1.5 - 0.05i$. The reflection coefficient of the new structure is plotted in the complex plane (a). The transmission along the dashed white line, where $\mathrm{Im}[\mathrm{k}] = 0$ is plotted (b), alongside the field distribution plotted at the complex frequency k (c). Overlaid on the transmission calculations are results found using COMSOL Multiphysics [68].

found at the expected complex frequencies. The absorption, shown in Figure 6.9(c) plotted along the white dashed line ($\mathrm{Im}[\lambda] = 0$) is also provided, with a fitted Lorentzian to extract the properties of the resonances and verify that it corresponds to the QNM frequencies.

We can also apply this design procedure to impose the condition of coherent perfect absorption (CPA) at a given complex frequency. This can be understood as the time reverse of QNMs [180] were the wave is purely incoming rather than outgoing. The wavelengths at which a structure behaves as a perfect absorber are related to the locations of zeros on the real axis, rather than poles. With our eigen-permittivity formulation, we can find the background permittivity value required to make the device a perfect absorber at a frequency of choice. To do this, we simply take the outgoing

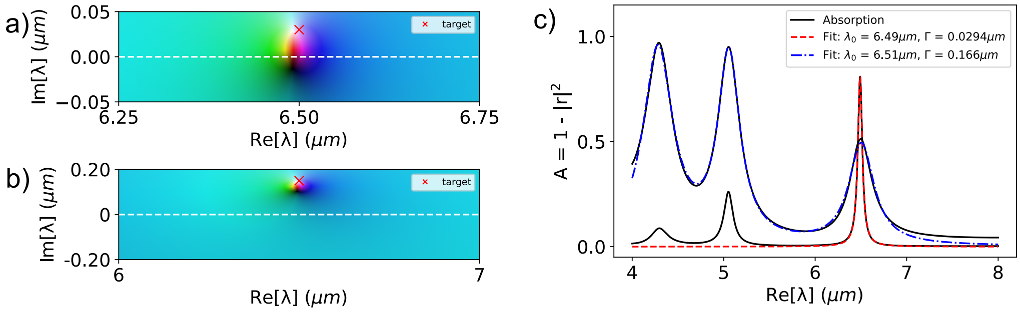

Figure 6.9: Shifting the resonances of the a multi–layer absorber. The original absorbing stack, shown in Figure 6.4 a) has been modified into two structures that contain a QNM at $\lambda_1 = (6.5 + 0.03i)\mu\text{m}$ and $\lambda_2 = (6.5 + 0.15i)\mu\text{m}$ respectively. The former is close to the real axis, corresponding to a narrow bandwidth, while the latter has a broader bandwidth. Plotted on (a) and (b) respectively are the reflection coefficients in the complex plane, showing that a QNM is indeed located at the chosen complex frequency. The absorption spectra of the two structures are plotted as a function of real wavelength (c). Fitted Lorentzians in dashed red (blue) correspond to fitting to the narrow (broad) resonance, verifying the complex frequencies of the QNMs. For the broadband case, we must fit a sum of 3 Lorentzians to accurately model the spectral profile, and obtain the correct fitting parameters.

boundary condition and replace it with the incoming boundary condition

$$\frac{d\phi(x)}{dx} = \mp ik\phi(x) \tag{6.73}$$

as $x \to \pm\infty$. This changes the boundary elements in the Laplacian Eq. (6.36) from $ik\Delta x - 1$ to $-ik\Delta x - 1$.

Applying the above changes to the Laplacian matrix, we can take e.g. a slab of dielectric, and rather than choose a complex frequency, pick a real frequency that we wish CPA to occur at. We take a dielectric slab of length $L = 1$ and initial permittivity π^2 and choose the arbitrary CPA frequency to be 125 MHz. The resulting background permittivity required is $\epsilon_b = -9.55 + i0.63$. To verify that there is coherent perfect absorption at the chosen frequency, we construct the scattering matrix for the slab under incidence from the left and right side

$$\begin{pmatrix} \phi_L^{\text{scattered}} \\ \phi_R^{\text{scattered}} \end{pmatrix} = \begin{pmatrix} r_L & t_R \\ t_L & r_R \end{pmatrix} \begin{pmatrix} \phi_L^{\text{in}} \\ \phi_R^{\text{in}} \end{pmatrix}, \tag{6.74}$$

noting that CPA occurs when an eigenvalue of the scattering matrix goes to zero [180]. The scattering matrix can be constructed analytically from the transfer matrix or found numerically in full–wave solvers such as COMSOL [68]. In Fig. 6.10 we plot the smallest eigenvalue of the scattering matrix of the slab as a function of frequency. A clear dip is seen at the desired frequency. We also show field profiles both under incidence from only one side and from both sides at different frequencies. Under incidence from only the left side, one can see the usual interference between reflected and incident field to the left of the slab and the constant transmitted field. Under excitation from both sides, but away from the target CPA frequency one can see reflection from both sides. At the target CPA frequency of 125 MHz, an almost constant field amplitude is observed, indicating perfect absorption.

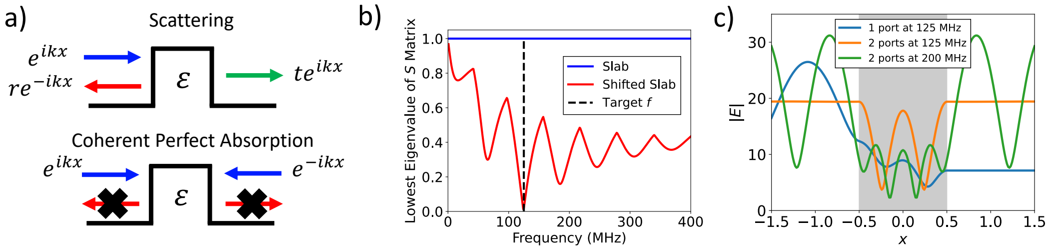

Figure 6.10: An example of using our eigen–permittivity method to design a structure that exhibits coherent perfect absorption (CPA). CPA is shown schematically in a). Under incidence from one direction, the structure scatters in the usual way, but under incidence from both sides reflection vanishes. We design a permittivity step of length $L = 1$ of permittivity $\varepsilon = \pi^2 + (-3.98 + i\,1.59)$ that exhibits this behaviour at the desired frequency of 125 MHz. To verify this, we show b) the smallest eigenvalues of the scattering matrix of the structure. Vanishing eigenvalue indicates coherent perfect absorption. This can be clearly observed at the target frequency of 125 MHz. The fields c), also indicate coherent perfect absorption. Under excitation from one side or off of the target frequency, reflections are observed. At the design frequency, there is a standing wave.

Although simple to implement, this eigen–permittivity method only allows you to choose the complex frequency of a single QNM. We now explore the possibility of applying an iterative method to move one or more QNMs to desired complex frequencies, by changing the spatial variation of the permittivity profile.

6.6 Can we move more than one mode?

One might naively expect that the eigen–permittivity method can easily be extended to move multiple modes. For a particular target wave–number k_i, we can write the eigen–value problem as

$$-\frac{1}{k_i^2}\left[\nabla_i^2 + k_i^2\varepsilon(x)\right]\phi_i = \varepsilon_b\phi_i. \tag{6.75}$$

We have included the index i on the Laplacian to indicate that it has been modified to exhibit the out–going wave boundary condition associated with wave–number k_i. To try to find a permittivity shift that moves more than one mode to a desired location, we can form a composite eigen–value problem

$$\begin{pmatrix} -\frac{1}{k_1^2}\left[\nabla_1^2 + k_1^2\varepsilon(x)\right] & 0 \\ 0 & -\frac{1}{k_2^2}\left[\nabla_2^2 + k_2^2\varepsilon(x)\right] \end{pmatrix}\begin{pmatrix}\phi_1 \\ \phi_2\end{pmatrix} = \varepsilon_b\begin{pmatrix}\phi_1 \\ \phi_2\end{pmatrix}. \tag{6.76}$$

This system can be constructed and solved for the eigen–values, however we find that each eigen–value only moves *one* of the two modes to the correct location. We demonstrate the behaviour in Figure 6.11. We choose, arbitrarily, the two target wave–numbers to be

$$k_1 = 0.5 - i0.5, \qquad k_2 = 1.3 - i0.08. \tag{6.77}$$

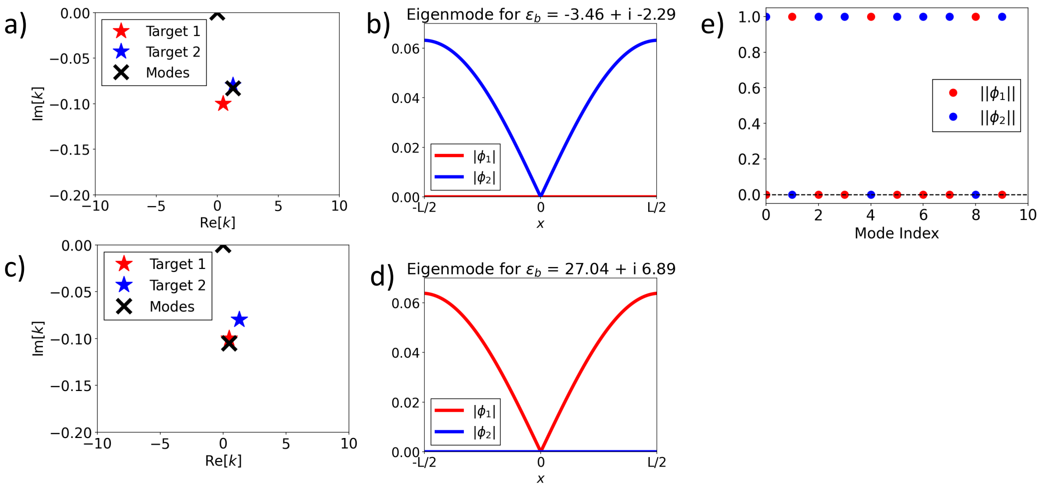

Figure 6.11: Attempting to move more than one mode using our 'eigen–permittivity' framework. a) For one of the eigen–permittivities, one mode is moved to the correct location, while the other mode has zero field, shown in b). c) Taking a different eigen–permittivity, the other mode is moved to the correct location, d) although the field associated with the second mode is zero. Looking at the norm of the fields for different choices of eigen–permittivity, we find that a mode with non–zero field is placed correctly, while the other mode has zero field associated with it, representing a trivial solution to the eigen–value problem.

For some values of ε_b, the first mode is placed correctly while for the others the second is placed correctly. To understand why, we examine the eigenvectors of the matrix we are using to calculate ε_b. Figure 6.11 a), b) show that when the second mode is placed correctly, only the ϕ_2 part of $(\phi_1, \phi_2)^T$ is non–zero. Similarly, when mode 1 is placed correctly only $\phi_1 \neq 0$, as shown in Figure 6.11 c), d). It is evident that if either of the ϕ_i's is zero everywhere, then the eigenvalue equation

$$-\frac{1}{k^2}\left[\nabla^2 + k^2\varepsilon(x)\right]\phi = \varepsilon_b\phi \tag{6.78}$$

will be automatically be satisfied for any k value. Figure 6.11 e) shows how the norm, defined as $||\boldsymbol{x}|| = \sqrt{\boldsymbol{x}^\dagger \cdot \boldsymbol{x}}$, of each of the eigenmodes is different for each of the eigen–permittivities. We find that the solutions alternate between ϕ_1 being zero and ϕ_2 being zero. This leads us to conclude that we cannot arbitrary place two (or more) modes of a system where the permittivity is restricted to be homogeneous, even if we are allowed to add gain or loss. Our conclusion is perhaps not surprising, as we can observe from Eq (6.8) that the spacing between modes is related to $2\pi/\sqrt{\varepsilon}$. We therefore cannot change the spacing *between* modes in any way we like, although we can place individual modes anywhere. This argument also holds for the homogeneous radially symmetric systems we will consider later in this chapter, as the spacing between the modes of those systems is governed by the spacing of the zeros of Bessel functions.

Noting these difficulties in placing multiple modes in systems of homogeneous permittivity, we now aim to develop a method for designing graded materials. Such a method should allow for the placement of multiple modes simultaneously.

6.7 Linking Perturbation Theory to Optimisation

In our discussion of the adjoint method in Section 2.9, we used perturbation theory to connect a small change in the permittivity to a small change in the fields. Here, we are interested in connecting a shift in a complex frequency due to a small change in the dielectric structure. Perturbation theory in quantum mechanics [10, 181] is well developed and connects changes in a potential to shifts in energy levels. As quasi–normal modes are a generalised case of this, where the energy is extended to the complex plane [168], we seek to develop a technique similar to the adjoint method to enable the design of graded structures with complex frequency resonances at particular locations. To this end, we begin by reviewing the key results of perturbation theory in quantum mechanics, before elucidating the connection between perturbation theory and inverse design.

Quantum mechanical systems are characterised by their Hamiltonian, which is usually the sum of kinetic and potential energy operators of the system

$$\hat{H} = \hat{E} + \hat{V}. \tag{6.79}$$

The discrete energy level spectrum of the system is then given by the eigenvalues of the Hamiltonian and the states of the system are the eigenvectors

$$\hat{H} \left|\psi_n\right\rangle = E_n \left|\psi_n\right\rangle. \tag{6.80}$$

A useful property of the eigenstates of the Hamiltonian is that they form an orthogonal basis

$$\langle\psi_n|\psi_m\rangle = \delta_{nm}. \tag{6.81}$$

As an example we consider a quantum harmonic oscillator, which has the

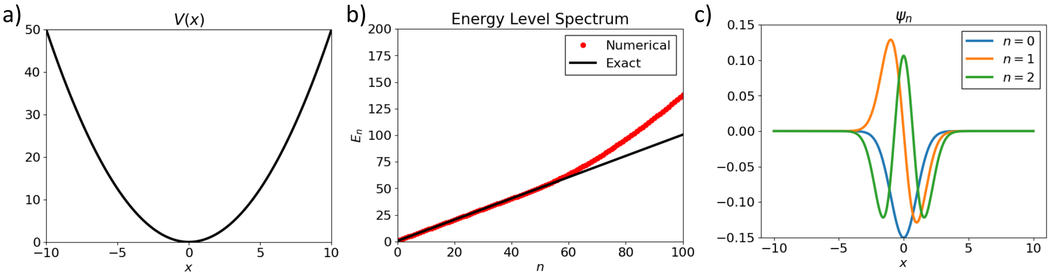

Figure 6.12: Numerically finding the eigenvalues and eigenstates of the harmonic oscillator. Discretising the Hamiltonian (6.84) with a quadratic potential shown in a), one can numerically find the energy levels b), comparing with the analytical result. Due to numerical error, the smaller energies are found correctly, while larger energies have larger errors. The eigen–vectors of the Hamiltonian matrix represent that eigen–states of the system, shown in c).

Hamiltonian

$$\hat{H} = \frac{\hat{p}^2}{2m} + \frac{1}{2}m\omega^2\hat{x}^2. \tag{6.82}$$

The momentum operator in 1 dimension is [10]

$$\hat{p} = -i\hbar\frac{\mathrm{d}}{\mathrm{d}x}. \tag{6.83}$$

Working in units where $\hbar = \omega = m = 1$, the Hamiltonian is

$$\hat{H} = -\frac{\mathrm{d}^2}{\mathrm{d}x^2} + \frac{1}{2}x^2. \tag{6.84}$$

Eigenvalues and eigenvectors of this operator can be found is discretising the second derivative as a matrix in exactly the same was as in Section 6.4. The potential, eigenvalue spectrum and first few eigenmodes are shown in Figure 6.12. We compare the numerical eigenvalue spectrum to the well–known analytic result

$$E_n = \hbar\omega\left(n + \frac{1}{2}\right), \tag{6.85}$$

where $n = 0, 1, 2, \ldots$. It should be noted that for large n the eigenvalues found numerically exhibit significant error. This is a consequence of the discretisation of space, which introduces numerical error. Higher eigenvalues can be made more accurate by increasing the number of points space is broken down into. Smaller eigenvalues exhibit lower errors. For this reason, when we calculate eigen–permittivities, we usually select the lowest eigenvalue, to avoid the effect of numerical errors.

Perturbation theory answers the question: "what happens to the energy levels and eigenstates if the Hamiltonian changes by a small amount?". Say we change the potential by a small amount $\hat{V} \to \hat{V} + \delta\hat{V}$. Expanding the eigenstates and the energy level to first order

$$\psi_n \to \psi_n + \delta\psi_n \qquad\qquad E_n \to E_n + \delta E_n \tag{6.86}$$

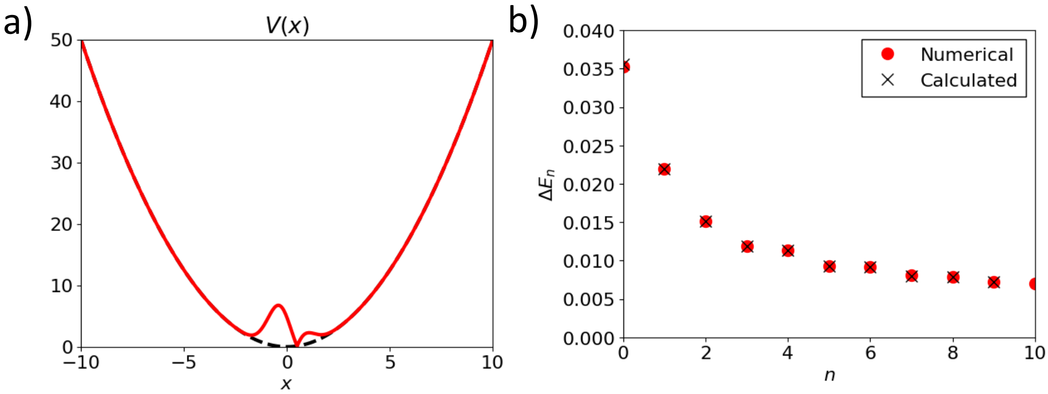

Figure 6.13: Using perturbation theory to calculate the shifts to the energy levels. For a given perturbation to the quadratic Hamiltonian, shown in a), the shifts to each energy level can be directly calculated using perturbation theory (6.89). b) The shifts calculated using perturbation theory are compared with numerically evaluating the energy with and without the perturbation, then subtracting the two energies. Provided the perturbation is small, the two methods yield the same changes to the energies.

we obtain

$$\hat{H} \left|\delta\psi_n\right\rangle + \delta\hat{V} \left|\psi_n\right\rangle = E_n \left|\delta\psi_n\right\rangle + \delta E_n \left|\psi_n\right\rangle . \tag{6.87}$$

Multiplying both sides by $\left\langle\psi_m\right|$, we get

$$\left\langle\psi_m\right| \hat{H} \left|\delta\psi_n\right\rangle + \left\langle\psi_m\right| \delta\hat{V} \left|\psi_n\right\rangle = E_n \left\langle\psi_m|\delta\psi_n\right\rangle + \delta E_n \left\langle\psi_m|\psi_n\right\rangle . \tag{6.88}$$

Using the fact that $\left\langle\psi_m\right| \hat{H} = \left\langle\psi_m\right| E_m$, the first terms on each side cancel. Then, applying orthogonality of the eigenstates, we arrive at the standard result

$$\delta E_n = \left\langle\psi_n\right| \delta\hat{V} \left|\psi_n\right\rangle . \tag{6.89}$$

Applying this framework to the harmonic oscillator example of Figure 6.12 is shown in Figure 6.13. To the usual $V(x) = x^2/2$ potential, shown as a black dashed curve in Figure 6.13 a), we add a small perturbation of the form

$$\delta V(x) = 0.1 \times \text{abs}\left[e^{-x^2} \sin(x - 0.5)\right] , \tag{6.90}$$

where $V(x) + \delta V(x)$ is plotted in red in Figure 6.13 a). The eigenstates can be found from the discretised Hamiltonian, then integrated against $\delta V(x)$, as in (6.89), to calculate the shifts in the energy levels. The calculated δE_ns, from (6.89), are compared with the numerical result, obtained by just finding the energy levels for the potential $V(x)$, then for $V(x) + \delta V(x)$ and subtracting them. This comparison is shown in Figure 6.13 b).

To connect the ideas of perturbation theory to optimisation, we re–write (6.89) as an integral

$$\delta E_n = \int_{-\infty}^{\infty} dx |\psi_n(x)|^2 \delta V(x). \tag{6.91}$$

Proceeding in the same way as we outlined in our discussion of the adjoint method in Section 2.9, we write the change in the potential as a delta function at a particular position x_i

$$\delta V(x) = \delta(x - x_i) \Delta V. \tag{6.92}$$

This allows us to connect a small change in the position of an energy level to a change in the potential as a continuous function given by the modulus squared of the eigenstate

$$\frac{\partial E_n}{\partial V} \approx |\psi_n(x)|^2. \tag{6.93}$$

One can use this gradient to design a potential that exhibits an energy level in a particular location. Defining the figure of merit

$$\mathcal{F}(V) = (E_n(V) - E_\star)^2, \tag{6.94}$$

where $E_\star$ is the target energy level. Differentiating with respect to the potential V we find the gradient of the figure of merit

$$\frac{\partial \mathcal{F}}{\partial V} = 2(E_n - E_\star)\frac{\partial E_n}{\partial V} = 2(E_n - E_\star)|\phi_n(x)|^2. \tag{6.95}$$

Using this expression, one can iteratively change the potential until an energy level occurs at a particular, pre–determined, energy. An example of doing this is shown in Figure 6.14. Beginning from the potential for a harmonic oscillator $V(x) = x^2/2$ shown in Figure 6.14 a), we seek to move the energy level $E_2 = 5/2$ to $E_2 = 2$. Using (6.95), finding the eigenstates numerically from the discretised Hamiltonian, we iteratively update the potential until the energy level is at the desired location. Figure 6.14 a) shows the new potential and 6.14 b) shows the new locations of the energy levels. It is evident that the $n = 2$ level is now located at $E = 2$. The progression of the optimisation is shown in Figure 6.14 c).

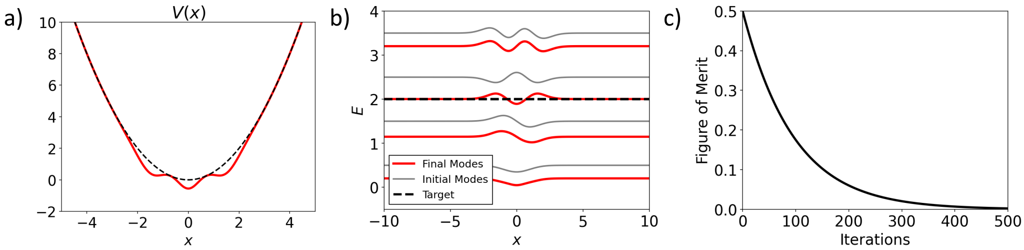

Figure 6.14: Using perturbation theory to optimise a potential. Beginning from a quadratic potential shown as a black dashed line in a), perturbation theory is used as an optimisation tool to design the potential shown as a solid red line in a). This potential has an energy level at the target energy $E = 2$, as shown by b) the energy levels and eigenstates. The progression of the figure of merit over the iterative optimisation procedure is shown in c).

The ideas we have developed in this section are basically a way of moving around the eigenvalues of an operator, so it is natural to ask whether the ideas could be extended to manipulate the locations of quasi–normal modes in the complex plane. Now, the eigenvalues we seek to manipulate are not real energies but complex wave–numbers (or, equivalently, frequencies). Perturbation theory, as we have reviewed it in this section is also not suitable for quasi–normal modes. Since they have exponential growth in space, the integrals diverge. In the next section we will review how one can develop perturbation theory for quasi–normal modes, so that we can use that framework to manipulate the locations of quasi–normal modes.

6.8 Perturbation theory for Quasi–Normal Modes

If one wants to use perturbation theory to manipulate quasi–normal modes, the usual Rayleigh-Schrödinger perturbation theory of quantum–mechanics is not suitable. Due to their characteristic exponential growth, the usual mode normalisation (6.81) is not physical: the integral diverges. To deal with this, perturbation theory must be re–formulated for quasi–normal modes. Such a reformulation was first presented by Zel–Dovich [182] in his study of alpha decay. Since then regularisation techniques have been used to apply perturbation theory to quasi–normal modes in both quantum mechanics [182, 183] and electromagnetism [184]. In this section, we briefly outline how one can derive a suitable expression for this, following closely [183, 185].

We begin from the 1D Helmholtz equation

$$\left(\frac{\mathrm{d}^2}{\mathrm{d}x^2}+k^2\varepsilon(x)\right)\phi(x)=0. \tag{6.96}$$

Making the substitution

$$f=\frac{\phi'}{\phi}, \tag{6.97}$$

where the prime denotes derivative with respect to x we re–cast this as the Riccati equation

$$f' + f^2 + \varepsilon k^2 = 0. \tag{6.98}$$

Expanding f, wave–number and permittivity in powers of μ

$$f = f_0 + \mu f_1 + \mu^2 f_2 + \dots, \tag{6.99}$$

$$\varepsilon = \varepsilon_0 + \mu \varepsilon_1 + \mu^2 \varepsilon_2 + \dots, \tag{6.100}$$

$$k = k_0 + \mu k_1 + \mu^2 k_2 + \dots, \tag{6.101}$$

to order $\mu = 1$ we obtain

$$f_1' + 2 f_0 f_1 + 2\varepsilon_0 k_0 k_1 + k_0^2 \varepsilon_1 = 0. \tag{6.102}$$

This is of the form

$$y'(x) + p(x) y(x) = q(x), \tag{6.103}$$

suggesting solution using an integrating factor. For the integrating factor, we choose

$$\exp\left[2 \int^{x} f_0(x') dx'\right] = \phi_0^2(x). \tag{6.104}$$

Multiplying both sides of (6.102) by the integrating factor and integrating over the finite region $x \in [L_-, L_+]$, we obtain

$$\phi_0^2(x) f_1(x)\Big|_{L_-}^{L_+} = -\int_{L_-}^{L_+} dx \phi_0^2(x) \left[k_0^2 \varepsilon_1 + 2\varepsilon_0 k_0 k_1\right]. \tag{6.105}$$

If we choose L_-, L_+ to be outside the resonator then the boundary condition upon ϕ is the radiation condition $\phi' = \pm ik\phi$ as $x \to \pm\infty$. Therefore the boundary condition on f_1 is that $f_1(x \to \pm\infty) \to \pm ik_1$. Substituting this into the boundary term (6.105),

$$ik_1\left(\phi_0^2(L_+)+\phi_0^2(L_-)\right)=-\int_{L_-}^{L_+}dx\phi_0^2(x)\left[k_0^2\varepsilon_1+2\varepsilon_0k_0k_1\right]. \tag{6.106}$$

Re-arranging for the perturbation to the wave–number we find

$$k_1=\frac{-1}{2k_0}\frac{k_0^2\int_{L_-}^{L_+}dx\phi_0^2(x)\varepsilon_1(x)}{\int_{L_-}^{L_+}\phi_0^2(x)\varepsilon_0(x)dx+\frac{i}{2k_0}(\phi_0^2(L_+)+\phi_0^2(L_-))}. \tag{6.107}$$

Comparing this with standard perturbation theory (6.91), we can note a number of key differences. Rather than depending the modulus squared of the wave–function, the shift in wave–number depends upon the square of the wave function. This ensures that the shift is complex. Furthermore, the normalisation factor of 1 due to orthogonality of the states in standard perturbation theory is replaced with a rather more complicated expression for quasi–normal modes. This is necessitated by the fact that $\phi(x)$ does not vanish at infinity. While quantitatively different, conceptually one can still use 6.107 to find the gradient of the wave–number's position in the complex with respect to the structure $\varepsilon(x)$. Choosing $\varepsilon_1(x)=\Delta\varepsilon\delta(x-x_i)$, one obtains the gradient

$$\frac{\partial k}{\partial\varepsilon}=\frac{-1}{2k_0}\frac{k_0^2\phi_0^2(x_i)}{\int_{L_-}^{L_+}\phi_0^2(x)\varepsilon_0(x)dx+\frac{i}{2k_0}(\phi_0^2(L_+)+\phi_0^2(L_-))}. \tag{6.108}$$

This is true for all x_i, so this expression gives a continuous function that can be easily calculated, and used to find how to change a structure to place a pole in a particular location.

6.9 An Optimisation Approach to Moving the Quasi–Normal Modes of 1D Slabs

Say we would like to move mode k_n to the complex frequency $k_\star$. We can write a suitable figure of merit and it's derivative as

$$\mathcal{F} = (k_n - k_\star)^2, \tag{6.109}$$

$$\frac{\partial \mathcal{F}}{\partial \varepsilon} = 2(k_n - k_\star)\frac{\partial k_n}{\partial \varepsilon}. \tag{6.110}$$

Updating the permittivity from iteration i to $i+1$ is done according to

$$\varepsilon^{(i+1)}(x) = \varepsilon^{(i)}(x) + \gamma \frac{\partial \mathcal{F}}{\partial \varepsilon}, \tag{6.111}$$

where γ is the step size. This makes the evaluation of the figure of merit gradients extremely efficient, similar to the adjoint method [76]. Combining this with gradient descent optimisation, we have found how to update the permittivty distribution in order to arbitrarily change the complex frequencies of the QNMs. This approach is very similar to the adjoint method presented in Section 2.9, as one can find how to change the whole structure in one calculation making evaluation of the gradient very efficient.

An example of this procedure is shown in Fig. 6.15. We begin by selecting a QNM of the system: the frequency of which we want to modify. The complex wave–number of this mode can be found by root–finding in the complex plane, using i.e. Newton's method. Specifying a target frequency of the pole $k_\star$, then using Eqns. (6.108, 6.110, 6.111) to iteratively update the permittivity distribution allows the pole to be moved to the desired complex frequency. At every iteration, ϕ_n and k_n must be re–calculated. In the example of Fig. 6.15 we move the pole originally at $k = 1 - 0.1i$ to $k_\star = 0.8 - 0.01i$,

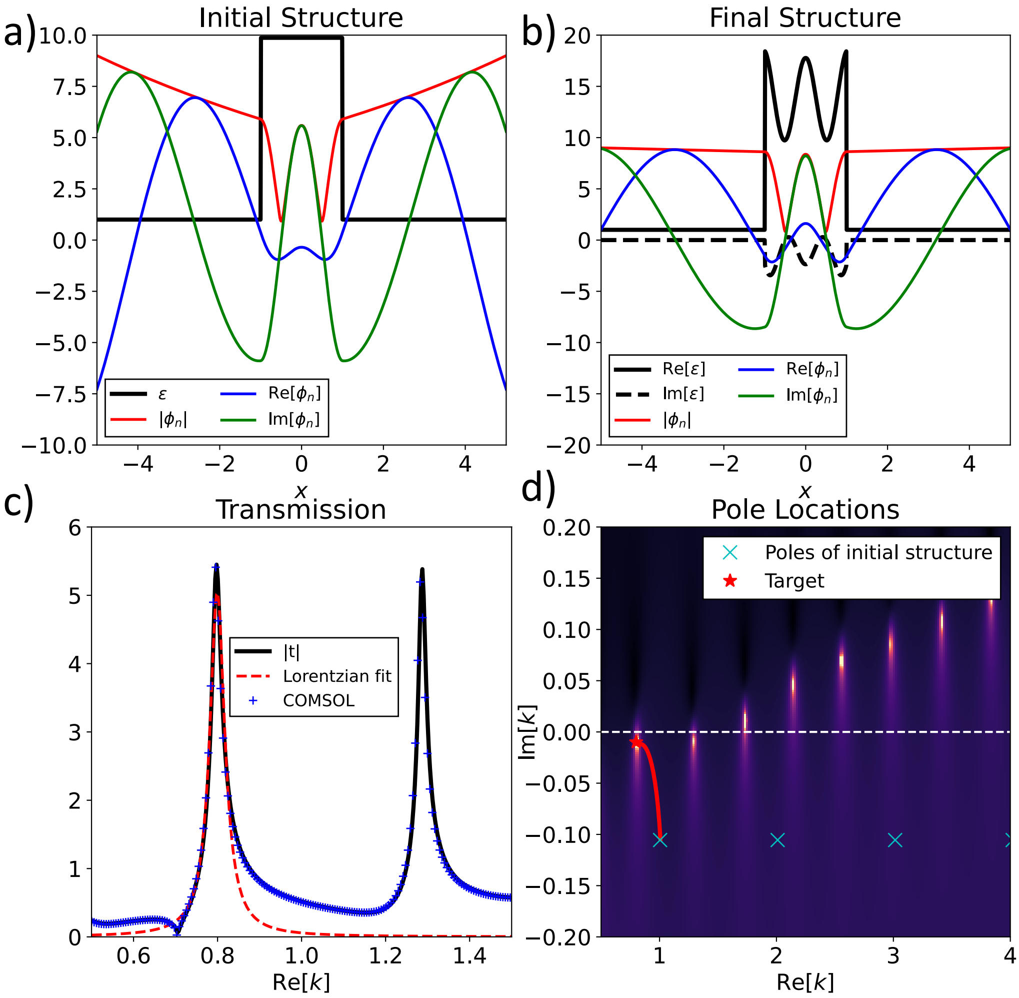

Figure 6.15: An example of using our iterative method to manipulate the poles of a dielectric slab. Beginning from a) a step of dielectric which supports a QNM at $k = 1 - 0.1i$, our iterative method designs the permittivity distribution shown in b), which supports a QNM at the desired frequency $k_\star = 0.8 - 0.01i$. The resulting transmission of the structure is shown in c), and compared to a full–wave solver. Fitting a Lorentzian to the transmission peak associated with $k_\star$, we extract find that the peak is at $k_0 = 0.799$ with width $\Gamma = 0.0109$. The path of the pole over the optimisation is shown in d).

and show that yields a structure with a peak in transmission at the designed frequency with the designed width. It should be noted that while we can move the pole to an arbitrary complex frequency, complete control of both the real and imaginary parts of the permittivity is required. While this remains experimentally challenging, a recent study [186] has demonstrated the ability to implement arbitrary loss and gain distributions in space.

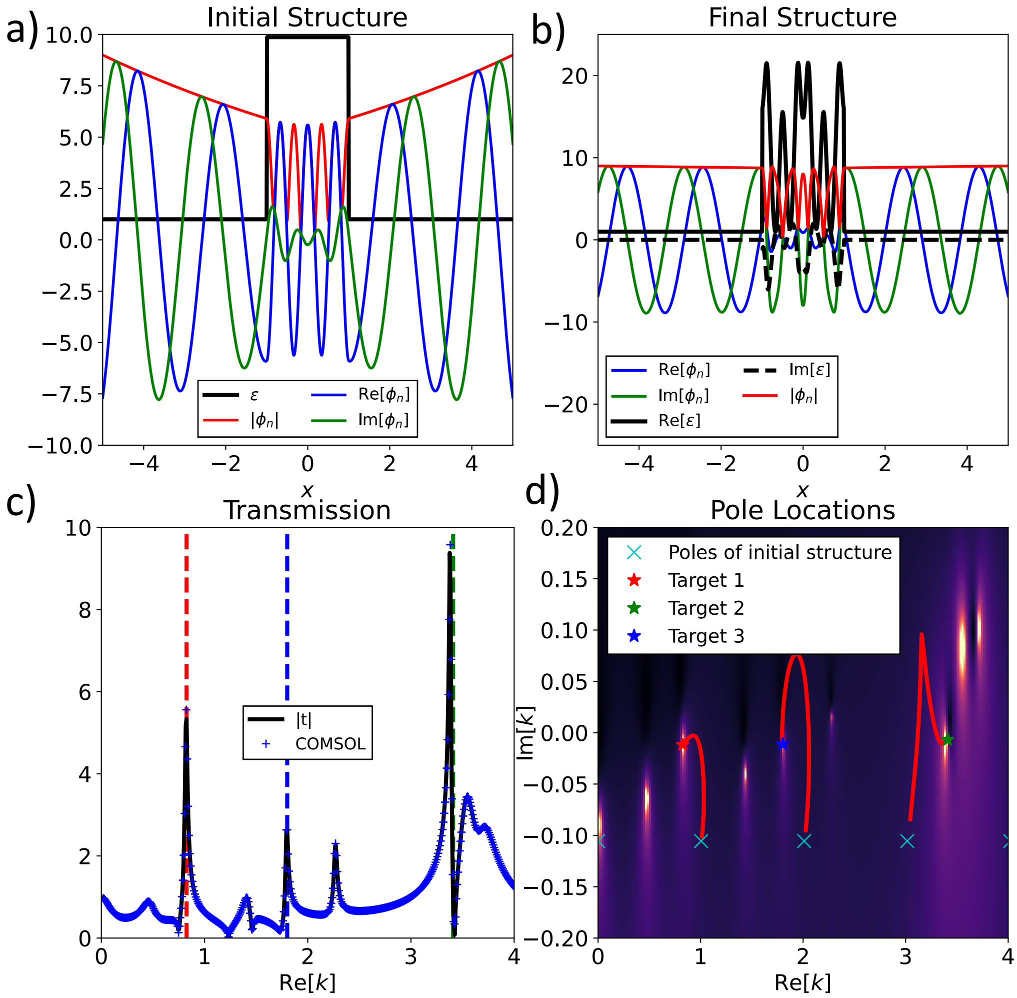

Figure 6.16: An example of using the iterative method we present to move 3 poles to desired complex frequencies at the same time. Beginning from a permittivity step shown in a), the real poles associated with $\mathrm{Re}[k] = 1, 2, 3$ are moved to the targets: $k_1 = 0.8 - 0.007i$, $k_2 = 3.5 - 0.008i$ and $k_3 = 1.8 - 0.009i$. The resulting permittivity profile is shown in b) and its transmission coefficient in c). Clear peaks are seen at the three target values of k. The path of the poles over the optimisation is shown in d).

As another example of this method, we consider trying to move several poles simultaneously. In Fig. 6.16 we take the poles originally at $k = 1 - 0.1i$, $2 - 0.1i$ and $3 - 0.1i$ and move them to three different values k_1, k_2 and k_3. Interestingly, due to the presence of other nearby poles, the transmission profile of the resulting structure becomes more complex, however a clear narrow transmission peaks associated with k_1, k_2 and k_3 are evident. If one controls all poles of interest over a given range of k values, almost complete control over the transmission profile can be obtained.

6.10 Moving the Quasi–Normal Modes of 2D Radially Symmetric Resonators

As we have already discussed, the method that was presented in the previous section can easily be adapted to spherically symmetric resonators. Using the results derived in Section 6.4.2, in this section we demonstrate that both the eigen–permittivity method and the iterative method can be applied to design isotropic or graded cylinders with resonances in particular locations. The key advantage of considering radially symmetric resonators is that we can choose the multipolar nature of the mode being manipulated.

Beginning with a cylinder of radius $r = 550$ nm and isotropic permittivity $\varepsilon = 4$, the initial modes are distributed in the complex frequency plane as shown in Figure 6.17 a). Applying the framework presented in Section 6.4.2 to move the $m = 1$ mode from $97 - i21$ THz to $100 - i$ THz, we find that one must apply a background permittivity of $\varepsilon_b = -0.046 + i0.483$. Once this has been added, the locations of the new modes are shown in Figure 6.17 b), where the target location is shown as a red star. Verification of the effect of moving the resonance on the scattering behaviour of the cylinder is shown in Figure 6.17 c). Using full–wave simulations in COMSOL, a plane wave is scattered from the cylinder with permittivity $\varepsilon = 4 + \varepsilon_b$ and the scattered power is calculated by integrating the power outflow from a closed loop around the cylinder. A clear peak is seen at $f = 100$ THz, with a width of 1 THz, corresponding to the $m = 1$ resonance we have moved. To verify that the scattering resonance has the correct multipolar nature, the field is shown inset in Figure 6.17 c). Next, we try to manipulate the $m = 3$

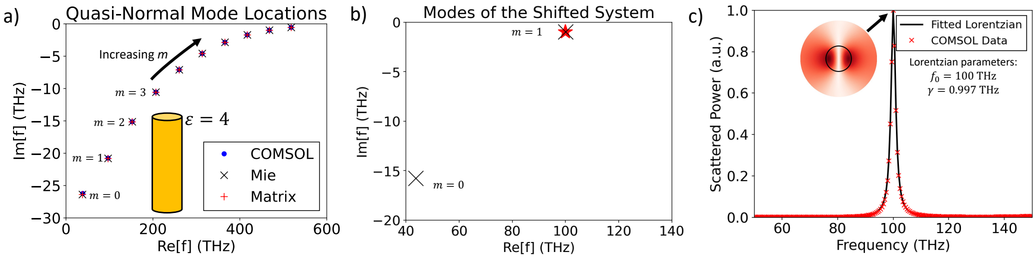

Figure 6.17: Using the eigen–permittivity method to move the dipole resonance of an isotropic cylinder. a) The original mode locations of the resonator. We seek to move the $m = 1$ mode from 97-i21 THz to 100-i THz. Solving the resulting eigenvalue problem, we find that this requires a background permittivity of $\varepsilon_b = -0.046 + i0.483$. b) shows the resonances of the new system. c) The scattering behaviour of the new resonator under plane wave incidence, with the field at 100 THz shown inset.

resonance. Beginning, as before, from a cylinder of radius $r = 550$nm and permittivity $\varepsilon = 4$ the $m = 3$ resonance is located at $f \sim 200 - i10$ THz. We aim to place this at $f = 150 - i2$ THz. Solving the associated eigenvalue problem, we find the background permittivity that must be added is $\varepsilon_b = 4.15 + i0.007$. Adding this, the locations of the modes are shown in Figure 6.18 a). The scattering behaviour of the resonator is shown in Figure 6.18 b), with the field associated with each resonance shown inset. Lorentzians are plotted (not fitted) with central frequencies and widths given by the real and imaginary parts of the resonances respectively. A mode indeed appears at $f = 150$ THz with the correct width and multipolar nature.

Next, we demonstrate that our iterative method can be applied to design graded cylinders that exhibit resonances at specific complex frequencies. For graded cylinders, both the position of the resonances and the associated field can be found from the results of Section 6.4.2. The perturbation theory developed in Section 6.8 can be utilised to manipulate cylindrical resonances without modification (indeed, Zel'Dovich's original calculation [182] was carried out for spherically symmetric potentials and arrived at an identical result). Figure 6.19 shows the application of this framework to design a graded cylinder with a quadrupole ($m = 2$) resonance at 100-i2 THz.

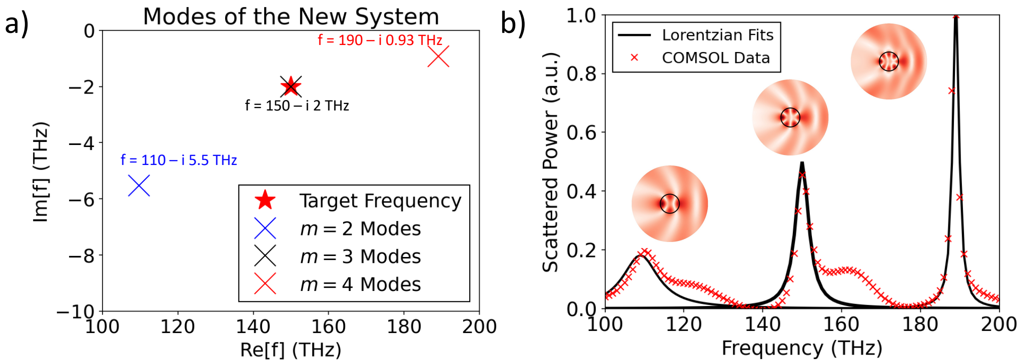

Figure 6.18: Using the eigen–permittivity method to place the $m = 3$ mode of an isotropic cylinder. We seek to move the $m = 3$ mode to 150-i2 THz, requiring a background permittivity of $\varepsilon_b = 4.15 + i0.007$. a) The locations of the quasi–normal modes. b) Full–wave simulations verifying the scattering behaviour of the cylinder. Peak locations and widths can be related directly to pole locations, and the fields shown inset verify the multipolar nature of the modes.

Beginning from a cylinder of radius $r = 550$nm and permittivity $\varepsilon = 4$, the permittivity profile is updated iteratively until the pole is in the correct location. The movement of the pole over the iterative optimisation is shown in

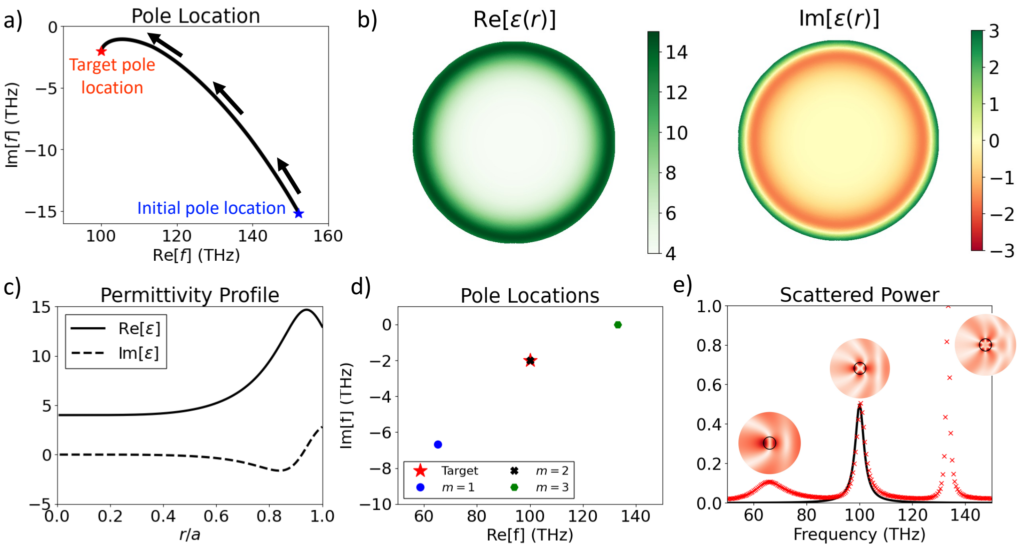

Figure 6.19: Designing a graded cylinder with a quadrupole resonance at 100-i2 THz. a) The iterative movement of the $m = 2$ mode from 152-i15 THz to the desired complex frequency of 100 - i2 THz. Panels b) and c) show the resulting permittivity distribution, which has the pole structure shown in d). Full–wave simulations of the scattered power indicate peaks corresponding to each pole, with inset fields show that each mode exhibits the expected multipolar nature.

Figure 6.19 a), with the resulting permittivity profile shown in b) and c). The pole locations of the graded cylinder are shown in Figure 6.19 d). Scattering from the graded cylinder was found using COMSOL and is shown in Figure 6.19 e). Clear peaks can be associated with the resonances shown in Figure 6.19 d) and correspond to strong scattering. Fields associated with each key scattering mode are shown inset, to that verify the multipolar nature of the modes is as expected.

6.11 General Resonators

So far we have discussed how to find and manipulate the quasi–normal modes of slabs of dielectric or radially symmetric resonators. In the final section of this chapter, we will indicate how one could extend our method to resonators or *any* shape in 1D, 2D or 3D. To illustrate this we consider a 2D square dielectric resonator, shown in Fig. 6.20(a). The resonator is a silicon cross inside a gallium arsenide square. To find how to change the permittivity to place a pole at a particular complex frequency, we must solve the eigenvalue problem Eq. (6.72) in 2D. To do this, we use COMSOL's coefficient form PDE interface, which allows one to solve problems of the form

$$\lambda^2 e_a \phi - \lambda d_a \phi + \nabla \cdot (-c\nabla\phi - \alpha\phi + \gamma) + \beta\nabla\phi + a\phi = f, \tag{6.112}$$

where λ is the eigenvalue. Choosing the coefficients to be $e_a = 0, c = 1, d_a = 1, a = -k^2\varepsilon$, this becomes exactly the eigenvlaue problem we would like to solve

$$\nabla^2\phi + k^2\varepsilon\phi = -\lambda\phi, \tag{6.113}$$

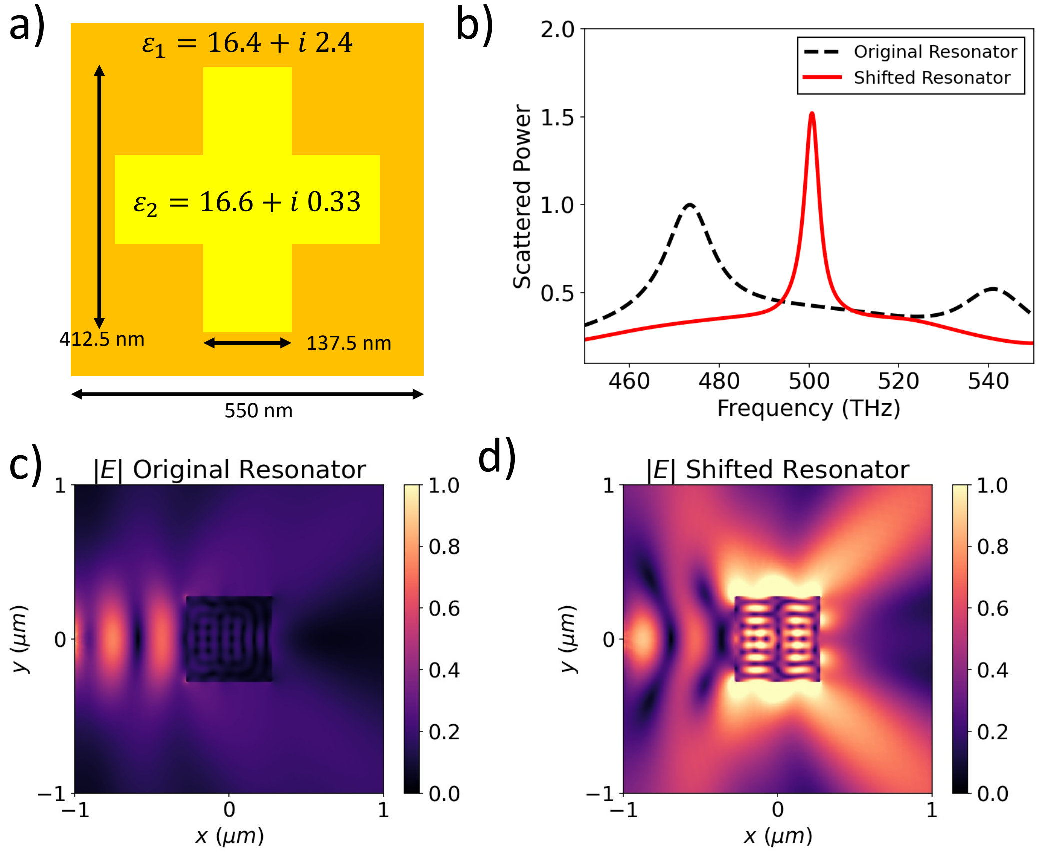

Figure 6.20: An example of using our eigen–permittivity framework to place the quasi-normal modes of a 2D resonator. The resonator, shown inset in a), is made of two different permittivities, ε_1 (silicon at 550 nm) and ε_2 (gallium arsenide at 550 nm). We apply our framework to find a permittivity offset to move a pole to the complex frequency (500 + 1i) THz. The background is $\varepsilon_b = -1.37 + i0.88$. To verify the location of the pole, we excite the resonator with a point electric dipole, located at (-1100 nm, 0), and calculate the total scattered power, shown in b). A clear peak is present in the spectrum of the shifted structure at the desired frequency of 500 THz, which is not present in the spectrum of the un–shifted structure. Examining the fields of the resonator driven by a nearby dipole at a frequency of 500 THz, c) and d), we see that the excitation of the mode in the sifted structure greatly increase the scattering.

where $\lambda = k^2\varepsilon_b$. The outgoing wave boundary condition can be applied to the outside edge of the resonator using the ‘flux/source’ boundary condition. Generally, this boundary condition is

$$-\boldsymbol{n}\cdot(-c\nabla\phi + \alpha\phi + \gamma) = g - \phi u, \tag{6.114}$$

where $\boldsymbol{n}$ is a unit–vector normal to the surface of the resonator at a given point. It is not necessary for $\boldsymbol{n}$ to be normal to the surface, it only needs to point outwards. With our parameter choices this becomes

$$\boldsymbol{n} \cdot \nabla \phi = -q\phi. \tag{6.115}$$

Setting $q = ik$ gives the correct out–going boundary condition. Solving this eigenvalue problem for the 2D geometry shown in Fig. 6.20(a), and choosing the location of the pole to be $f = 500 + 1i$ THz, we find a background permittivity of $\varepsilon_b = -1.37 + i0.88$. To verify that a QNM is now located at the correct complex frequency, we excite the resonator with a nearby point dipole and examine the total scattered power before and after the permittivity shift is applied. This is shown in Fig. 6.20(b). Once the shift is applied, there is a clear peak in scattered power at the desired wavelength. Additionally, the fields when the resonator is driven at 500 THz are shown in Fig. 6.20(c-d). Once the permittivty of the resonator is shifted, scattering at the desired frequency is greatly enhanced by the presence of the QNM.

6.12 Summary & Conclusions

Scattering from photonic resonators depends heavily upon the properties of the resonances supported by the structure. These resonances can be quasi–normal modes: complex frequency bound states of the system, with a characteristic negative imaginary part of the wavenumber. If one examines, for example, the scattering from an object, peaks in the scattering cross–section correspond to quasi–normal modes. The wavelength of peaks in scattering corresponds to the real part of the quasi–normal mode, while the width of the resonance is directly related to the imaginary part of the quasi–normal mode. Motivated by this direct correspondence, we have derived two methods for manipulating the locations of the resonances of dielectric slabs, cylinders and spheres.

The first method is based upon formulating an eigenvalue problem for a shift to the permittivity so that the structure supports a resonance at a particular location. The second method is an iterative procedure, based on perturbation theory for quasi–normal modes. While the iterative technique is slower, it has the benefit of being able to move multiple modes at the same time.

Chapter 7

Conclusions & Future Work

"Education never ends, Watson. It is a series of lessons, with the greatest for the last." – Arthur Conan Doyle, His Last Bow

7.1 Thesis Summary

The aim of this thesis was to develop simple and efficient techniques to design electromagnetic materials. Usually, there are great numerical problems posed by the large difference in scales between the sub–wavelength resonant elements that make up the metamaterial, and the size of the metamaterial itself which could have dimensions of the order of tens or hundreds of wavelengths. To overcome this, we employ the coupled–dipole framework to separate the modelling of the scatterer and the entire metamaterial.

To this end, in **Chapter 2** we introduce the key theoretical tools that are used throughout the thesis. This includes a brief review of Maxwell's equations and Mie scattering theory to describe the scattering from a single resonant object, characterised by its electric and magnetic polarisability tensors. Calculating the scattering of a source field (i.e. a plane wave or a dipole source) from a metasurface made of such elements is then facilitated using the coupled–dipole formalism. We conclude this introductory chapter with a brief review of inverse design techniques in the context of electromagnetism, indicating the key challenges they face.

Seeking to address the challenges of numerical complexity while preserving conceptual simplicity, in **Chapter 3** we derive a simple, efficient and versatile method for designing metamaterial devices. Applying perturbation theory to the coupled–dipole approximation, we can derive analytic expressions for gradients of figures of merit, enabling efficient optimisations. To illustrate the utility of our framework, we design devices that shape the near and far–field of a small emitter as well as manipulate plane waves.

Extending these ideas, in **Chapter 4**, we develop a framework for designing multi–functional metamaterial devices. We design a device that operates at optical wavelengths to produce different radiation patterns based on the polarisation of the source emitter. Using more complex scatterers, we also design a device at microwave wavelengths that sorts waves by their angle of incidence. We also find that our method compares favourably to the widely used inverse design paradigm, a genetic algorithm.

In **Chapter 5** we experimentally realise some uni–functional designs at microwave wavelength, using metal rods as the scattering elements and a complicated monopole emitter as the source.

Finally, in **Chapter 6** we consider how to shift the resonances of photonic structures, by directly manipulating the locations of their quasi–normal modes in the complex plane. We present both a semi–analytic eigen–permittivity framework as well as an iterative numerical technique based on perturbation theory to manipulate the resonances of arbitrary structures. The ability to tune the resonances of photonic resonators is key to multi–band behaviour as well as to designing structures that could be used to form a metasurface.

7.2 Future Work

Many outstanding challenges remain, which can be broadly divided into two categories. Firstly, there are many incremental changes to our inverse design frameworks that could be made. Secondly, different physical challenges could be addressed using our methods.

Beginning with the first category: incremental changes. Our dipole based inverse design framework, developed in Chapters 3-5, would benefit from many improvements. A key problem we have not solved is how to best choose the initial distribution of the scatterers. Where the scattering elements begin is key to the result of the optimisation, although throughout this thesis initial distributions have been chosen arbitrarily. This is a general problem in inverse design in photonics. While some progress has been made on how to choose initial graded permittivity distributions [187], how to do this for discrete scatterers is unclear. It may be possible to develop an additive procedure, such as Bennett et al. [90], although this has not been explored. Furthermore, it has been noted that convergence is affected by many properties of the problems [188–190], particularly the learning rate [92, 191]. Little attention has been given to these features of our optimisation framework, as we have instead focused on the application of our techniques. For instance, due to recent interest in optimisation for fitting machine learning models [72], it is known that for many optimisation problems better results can be obtained using stochastic gradient descent [192], simulated annealing [43] or the 'Adam' optimiser [193], instead of basic gradient descent. The immediate next steps of our method for manipulating the resonances of photonic structures, presented in Chapter 6, are as follows. As it has been formulated, our methods are immediately applicable to design graded cylinders or spheres. With this development, one could overlap modes to construct anapole resonances [194], super–scatterers [195, 196] or Kerker effects [197]. To make the results of the optimisation easier to build, our search could be restricted to lossy materials however the framework could be easily extended to include material dispersion effects [176].

In addition to adjustments to our methods, many different physical challenges could be addressed using the frameworks we have developed in this thesis. Key to the next generation of communication systems is the ability to widen the bandwidth of emitters. This is something that has not been addressed: all of our designs are optimised at only a single frequency. One way to do this might be to vary the size, and thereby resonance frequency, of the constituent elements of the metamaterial. The theory for doing this is well developed [198, 199], and has recently been applied to design photonic devices [200] although not with an eye to improving bandwidth. Such an approach may allow for the saturation of performance limits on size and bandwidth, such as the Chu–Harrington limit [201–203] for antennas and the Rozanov limit [204] for absorbers.

As well as addressing antenna bandwidth, the frameworks we have developed might find utility in modelling electromagnetic systems with large length scale separations. Being able to model and characterise individual 'meta–atoms' then assemble them into larger structures allows one to model the behaviour of systems that are otherwise numerically inaccessible. As communications frequencies are pushed upwards into mm–waves and beyond, atmospheric scattering will become an important effect. Current channel models do not properly account for multiple scattering effects [205], presenting a key challenge for next–generation communications. The power of our frameworks to include all scattering effects at small length scales, as well as effects over very many wavelengths make the methods we have used throughout the thesis attractive candidates to address this problem. Our methods also have the benefit that they scale with the number of scatterers, not the volume of space one wishes to model. Thus, modelling propagation over long distances, normally numerically impossible, does not increase the computational burden.

Beyond electromagnetism, our design methods may find utility in engineering other wave regimes such as acoustics or elasticity. Even though the field on inverse design began in the field of structural mechanics [74], it is under utilised to manipulate elastic waves. In the field of elastic metamaterials, there have been many great advances in engineering the band–structures for energy harvesting [206], roton–like dispersion [207] and the observation of topological effects [208, 209], to name only a few. Much work focuses on modelling elastic materials as thin plates [9], on which flexural waves can propagate. These waves can be manipulated by grading the thickness of the sheet [210] or by pinning masses to the sheet [211–215]. The inverse design problem, of how to grade or pin a sheet in particular places in order to manipulate the waves in a particular way has not been extensively addressed: the methods we have presented are immediately applicable to such problems. Such approaches would have utility for energy harvesting, vibration isolation and sensing if one could manipulate surface acoustic waves. Furthermore, it has recently been noted that elastic resonances can also be understood in terms of quasi–normal modes [216, 217]. The methods we present in Chapter 6 might also be applicable to elastic systems, with some modification.

With some generalisation, the methods we have developed might also be applicable to the design of time–varying materials. There has been much recent interest in time–varying materials within the metamaterials community due to the unique physics they can exhibit. For example, time–varying materials can exhibit wave–amplification without gain [218] and mimicking black–hole physics [219]. Recent experiments in acoustics [220, 221] have realised such materials using arrays of dipoles where the response function can be tuned, demonstrating amplification and frequency conversion. In principle, our approach to optimisation within the coupled–dipole framework could be extended to dipoles that are distributed in space, but also have a temporal response that can be tuned. Such a system could be realised in electromagnetism with fast–switching diodes.

Appendix A

Code Snippets

Many results throughout this thesis were generated using custom Python code. In this appendix, some snippets are collected to aid reproducibility. Key to the results of Chapters 3–5 is the solution of the multiple scattering problem. Section A.1 contains code that solves the multiple scattering problem for a scalar field. In Chapter 4, the results of our multi–functional design method are compared to a genetic algorithm. The code for the genetic algorithm was written from scratch, and is included in Section A.2. Finally, one way the fields of the quasi–normal modes were calculated in Chapter 6 was using back–integration. The code that performs this is given in Section A.3.

A.1 Multiple Scattering Code

Here, we include code that solves the multiple scattering problem for a simple scalar field. Extension to full vector electromagnetism is conceptually straightforward, although the Green's function becomes a tensor.

```
import numpy as np
import scipy.linalg as spl
import scipy.special as sps
```

```
lm                    = 1.0 # Wavelength
k                     = 2.0*np.pi/lm # Wave number
alpha                 = 1.0+3*1j #  Polarisability
Ns                    = 5 # Number of scatterers
 scatterer_locations  = 2.0*np.random.random((Ns,2))−1.0 # Random
    scatterer positions

# Define the Green's function
def G(x,xp,y,yp,k):
    z = (x−xp)+1j*(y−yp)
    r = np.abs(z)
    return (1.0/(4.0*1 j))*sps.hankel1(0, k*r)

# Define the incident field
def phii(x,y,k):
    return np.exp(1j*k*x)

# Calculate the total field
def phi(x,y,k,pts,alpha):
    # Evaluate the incident field at the scatterers
     inc_field = phii(pts [:,0], pts [:,1], k)

    # Construct the interation matrix
    A = np.zeros((Ns, Ns), dtype=complex)
    for i in range(Ns):
        for j in range(Ns):
```

```
            A[i,j] = −alpha∗G(pts[i,0], pts[j,0], pts[i,1], pts[j,1], k)
    np.fill_diagonal(A, 1.0)

    # Solve the linear system for the fields applied to each scatterer
    applied_field = spl.solve(A,inc_field)

    # Construct the total field
    total_field = phii(x,y,k)
    for n in range(Ns):
        total_field += alpha ∗ G(x,pts[n,0],y,pts[n,1],k) ∗ applied_field
            [n]

    return total_field
```

A.2 Differential Evolution Algorithm

This code performs global optimisation of a function using the differential evolution genetic algorithm, propose by Storn and Price [129]. This code was written by JRC, with reference to [222].

```
import numpy as np
import numpy.random as npr


class DifferentialEvolution:


    def __init__(self, bounds, popsize, max_generations, merit_func,
        args):
        self.bounds            = bounds
```

```
        self .pop_size          = popsize
        self .individual_size   = len(bounds)
        self .max_generations   = max_generations
        self .merit_func        = merit_func
        self .args              = args

        self .F                 = 0.5
        self .CR                = 0.7

    def _x_to_pts(self ,x):
        N = len(x)
        Np = int(N/2)
        pts  = np.asarray(x).reshape((Np, 2))
        return pts

    def printInfo( self ):
        print("Population Size :  %i" %self.pop_size)
        print("Max. Generations : %i" %self.max_generations)
        print("Individual Size  :  %i" %self.individual_size)
        print("F  :  %lf"  %self.F)
        print("CR : %lf"  %self.CR)
        print("Bounds : ",  self .bounds)

    def make_initial_population(self):
        self .population = []
        for  i  in  range(self .pop_size):
            individual  =  []
```

```
            for j in range(self.individual_size):
                individual.append(npr.uniform(self.bounds[j][0], self.
                    bounds[j][1]))
            self.population.append(individual)

    def impose_bounds(self, vec, bounds):
        for i,elem in enumerate(vec):
            if elem < self.bounds[i][0]:
                vec[i] = self.bounds[i][0]
            elif elem > self.bounds[i][1]:
                vec[i] = self.bounds[i][1]

    def solve(self):
        # Generate a random population
        self.make_initial_population()
        self.fom_hist    = []
        self.pop_hist    = []

        for iteration in range(self.max_generations):

            for i,indiv in enumerate(self.population):

                ## Perform the mutation
                # Can choose to either loop through the population in
                    order, or select an index at random to be the target

                idx_options     = np.arange(0, self.pop_size).tolist()
```

```
R                = npr.choice(idx_options)

# Just loop over the population in index order
if False:
    idx_options.remove(i)
    idxs             = npr.choice(idx_options, size=3)
    target_idx       = i
    x_t          = self .population[target_idx] # Target
        individual
    x1, x2, x3   = np.array(self .population[idxs[0]]), np.
        array(self .population[idxs[1]]), np.array(self .
        population[idxs[2]])

# Choose a random member of the population as the target
if True:
    idxs             = npr.choice(idx_options, size=4)
    target_idx       = idxs[3]
    x_t          = self .population[target_idx] # Target
        individual
    x1, x2, x3   = np.array(self .population[idxs[0]]), np.
        array(self .population[idxs[1]]), np.array(self .
        population[idxs[2]])

v            = list (x1 + self .F *(x2 − x3))

# Impose the bounds
self .impose_bounds(v, self.bounds)
```

```
            ## Crossover
            x_trial = []
            for j,element in enumerate(x_t):
                r = npr.uniform(0,1)
                if r <= self.CR or r == R:
                    x_trial.append(v[j])
                else:
                    x_trial.append(x_t[j])

            ## Check
            fom_xt     = self.merit_func(x_t, *self.args)
            fom_xtrial = self.merit_func(x_trial, *self.args)
            if fom_xtrial < fom_xt:
                self.population[target_idx] = x_trial

        foms_it = []
        for indiv in self.population:
            foms_it.append( self.merit_func(indiv, *self.args) )
        self.fom_hist.append(foms_it)
        self.pop_hist.append(self.population.copy())

    foms = []
    for i,element in enumerate(self.population):
        foms.append(self.merit_func(element, *self.args))
    mx = np.argmax(np.array(foms))
```

```
        # Outputs
        self.fom_hist    = np.asarray(self.fom_hist)
        self.result      =  self.population[mx]
        self.final_fom   = foms[mx]

def fom(params):
    x = params[0]
    y = params[1]
    return -20*np.exp(-0.2*np.sqrt(0.5*(x**2+y**2))) - np.exp(0.5*(np.cos
        (2.0*np.pi*x)+np.cos(2.0*np.pi*y))) + np.e + 20

if __name__=="__main__":
    # Define the bounds array
    Ns = 1
    bounds = []
    xi  = 2*( np.random.rand(2*Ns) - 1 )
    for i,xi in enumerate(xi):
        bounds.append((-4, 4))

    opt     = DifferentialEvolution(bounds, popsize=10, max_generations
        =1000, merit_func=fom, args=())
    opt.solve()
    sln     = opt.result

    f1      = fom(sln)
    print("Minima found: f(%lf,%lf) = %lf" %(sln[0], sln[1], f1))
```

A.3 Back–Integration for Quasi–Normal Modes

This code numerically calculates the fields associated with quasi–normal modes, by back integrating the field. To implement this using Python's 'odeint' function, one must break up the real and imaginary parts of the differential equation one seeks to solve.

```
# Import modules
import numpy as np
from scipy.integrate import odeint


# Define slab properties
nr = np.pi
nb = 1.0
L = 1.0


# We're finding the field of the mth mode
midx = 4


# Analytic expression for the QNM frequencies
def roots(m):
    r0 = (nr-nb)/(nr+nb)
    return 1j*np.log(r0**2)/(2.0*nr) + np.pi*m/nr


# Refractive index profile
def n(x):
    if np.abs(x) < L/2:
        return nr
    elif np.abs(x) > L/2:
```

```
        return nb
n=np.vectorize(n)


km = roots(midx)


# Split the x coordinates into left and right
x_right = 5*np.linspace(0, 1, 500)
x_left = -1.0*x_right[1:]
x = np.concatenate((np.flip(x_left),x_right))


# Define the field and its derivative
def dpsi(psi, x):
    ph = psi[0]+1j*psi[1]
    dph = psi[2]+1j*psi[3]
    Dph = dph
    D2ph = -n(x)**2*km**2*ph
    return [ np.real(Dph), np.imag(Dph), np.real(D2ph), np.imag(D2ph) ]


# Back-integrate using odeint
sln_r = odeint(dpsi, [1.0, 0.0, -np.imag(km), np.real(km)], x_right
    [::-1])
sln_l = odeint(dpsi, [1.0, 0.0, np.imag(km), -np.real(km)], x_left[::-1])


# Results are the left and right solutions
phir = ( sln_r[:,0] + 1j * sln_r[:,1] )[::-1]
phil = ( sln_l[:,0] + 1j * sln_l[:,1] )[::-1]
```

Appendix B

The Finite Element Method

In several chapters of the main thesis, the finite element solver COMSOL is used extensively to validate numerical or analytical results and when designing experiments, the electric and magnetic polarisabilities of complex resonators are calculated numerically. This chapter introduces the principles of the finite element method, though a simple example, then outlines how the properties of complex resonators can be extracted.

B.1 A Simple Example

Consider trying to solve the inhomogeneous Helmholtz equation

$$\left(\nabla^2 + \varepsilon(\boldsymbol{r})k^2\right) u(x) = s(\boldsymbol{r}) \tag{B.1}$$

numerically. If one discretises the differential operator using finite differences [43], then the grid points are uniformly spaced. The resulting matrix equation

$$\boldsymbol{A}\boldsymbol{u} = \boldsymbol{s} \tag{B.2}$$

will be sparse, but may still be too large to invert, particularly in 2D or 3D. Instead, it is beneficial to be able to change the size of the mesh in different regions of space so that a dense mesh can be focused where it is needed and a sparse mesh used elsewhere. For example, if the system is made of two materials with different refractive indices $n_1 = 1$ and $n_2 = 10$ then the wave length in material 2 is 10 times smaller than that in material 1. Rather than having to discretise *all* space finely enough to capture the smaller wavelength, the ability to change the size of the mesh in space makes the solution far more efficient. To do this, one can break space up into finite elements, the size of which does not have to be uniform. Following closely Burnett [223], we consider a simple example to explain the key steps in constructing a finite element solution to a differential equation. A detailed and comprehensive discussion of the finite element method is beyond the scope of this thesis.

We will construct the finite element solution to the 1D inhomogeneous Helmholtz equation with the following boundary conditions

$$\left(\frac{\mathrm{d}^2}{\mathrm{d}x^2} + k^2\varepsilon(x)\right) u(x) = 1, \qquad u(0) = 0, \qquad u(1) = 0. \tag{B.3}$$

We being by finding the weak form of (B.3) by multiplying both sides by a test function $\phi_i(x)$ then integrating the first term by parts, to find

$$\int_0^1 \phi_i(x)\frac{\mathrm{d}^2u}{\mathrm{d}x^2}dx + \int_0^1 \varepsilon(x)\phi_i(x)u(x)dx = \int_0^1 \phi_i(x)dx \tag{B.4}$$

$$\phi_i(x)\frac{\mathrm{d}u}{\mathrm{d}x}\bigg|_0^1 - \int_0^1 \frac{\mathrm{d}\phi_i}{\mathrm{d}x}\frac{\mathrm{d}u}{\mathrm{d}x}dx + \int_0^1 \varepsilon(x)\phi_i(x)u(x)dx = \int_0^1 \phi_i(x)dx \tag{B.5}$$

The test functions, $\phi_i(x)$, are chosen to satisfy the boundary conditions (B.3), so the boundary term vanishes [1]. The simplest choice for the test functions

---

[1] For other boundary conditions such as the radiation boundary condition $u' = iku$, this term does not vanish and is moved to the right–hand side as an additional source term [223].

is piecewise linear functions of the form

$$\phi_i(x) = \begin{cases} 0 & x < x_{i-1} \\ \frac{x - x_{i-1}}{x_i - x_{i-1}} & x_{i-1} < x < x_i \\ \frac{x_{i+1} - x}{x_{i+1} - x_i} & x_i < x < x_{i+1} \\ 0 & x > x_i. \end{cases} \tag{B.6}$$

These are plotted in Figure B.1 for a uniform discretisation. Preemptively

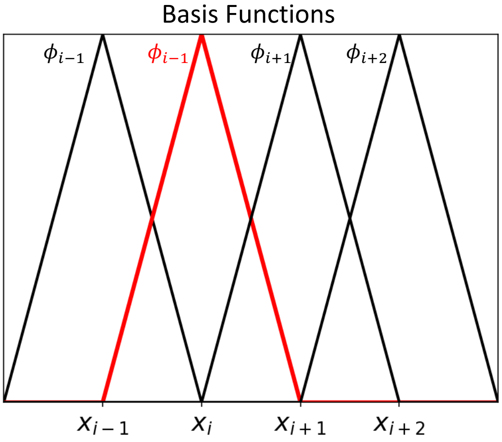

Figure B.1: Piecewise linear basis functions used to perform the finite element discretisation.

calculating the derivative of these we find

$$\frac{\mathrm{d}\phi_i}{\mathrm{d}x} = \begin{cases} 0 & x < x_{i-1} \\ \frac{1}{x_i - x_{i-1}} & x_{i-1} < x < x_i \\ -\frac{1}{x_{i+1} - x_i} & x_i < x < x_{i+1} \\ 0 & x > x_i. \end{cases} \tag{B.7}$$

Now, writing the solution as a decomposition of the test functions

$$u(x) = \sum_j c_j \phi_j(x), \tag{B.8}$$

and substituting this, we have

$$\left(-\int_0^1 \frac{\mathrm{d}\phi_i}{\mathrm{d}x}\frac{\mathrm{d}\phi_j}{\mathrm{d}x}dx + k^2\int_0^1 \phi_i(x)\phi_j(x)dx\right)c_j = \int_0^1 \phi_i(x)dx. \tag{B.9}$$

This is now a matrix system that can be assembled and solved for the coefficients c_j that define the solution. All that remains is to evaluate the integrals, which are nothing but integrals over the triangular basis functions or their derivatives. Three cases can be considered $i = j$ and $i = j \pm 1$. It is evident from the choice of basis functions and Figure B.1 that there is no overlap between basis function i and $i \pm 2$. Therefore, the linear system will be tridiagonal like the finite difference case but the elements will be numerically different, based on how the systems is discretised.

To obtain and explicit form of the matrix that must be inverted to obtain the coefficients c_j, we now evaluate the integrals. This gives

$$\int_0^1 \phi_i(x)dx = \frac{x_{i+1} - x_{i-1}}{2}. \tag{B.10}$$

$$\int_0^1 \frac{\mathrm{d}\phi_i}{\mathrm{d}x}\frac{\mathrm{d}\phi_j}{\mathrm{d}x}dx = \begin{cases} \frac{1}{x_i - x_{i-1}} + \frac{1}{x_{i+1}-x_i} & i = j \\ -\frac{1}{x_{i+1}-x_i} & |i-j| = 1. \end{cases} \tag{B.11}$$

$$\int_0^1 \phi_i(x)\phi_j(x)dx = \begin{cases} \frac{x_i - x_{i-1}}{3} - \frac{x_{i+1}-x_i}{3} & i = j \\ \frac{x_{i+1}-x_i}{6} & |i-j| = 1. \end{cases} \tag{B.12}$$

Choosing a wavelength of $\lambda = 1/2$, so $k = 4\pi$, this system can be constructed and solved using standard matrix methods. The solution is shown in Figure B.2, compared with the analytical solution

$$u_{\text{analytic}}(x) = 0.00633257 - 0.00633257\cos(kx), \tag{B.13}$$

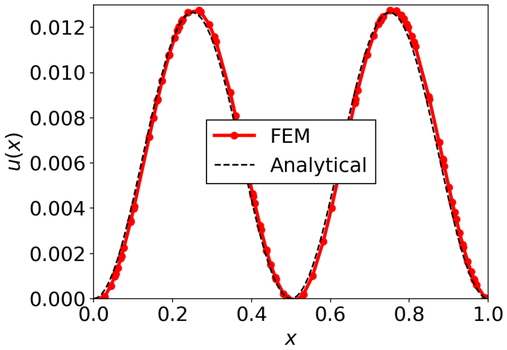

Figure B.2: Comparison of the finite element and analytic solution.

which was obtained using Mathematica. The finite element solution used for comparison is in a random irregular grid with 100 nodes.

While this section has illustrated the key concepts behind the finite element method, extension to higher dimensions and more complicated boundary conditions is far from trivial. Rather than triangles, the basis functions become tetrahedrons so the integrals are more complicated. Additionally, while we have used linear basis functions greater accuracy can be achieved with higher orders i.e. quadratic or cubic basis functions. Some of the issues around extensions to higher dimensions are discussed in [224].

B.2 Perfectly Matched Layers

Many of the COMSOL models in the main thesis are terminated by perfectly matched layers (PMLs). In this section, we will briefly review why they are used and how they work, following [225, 226].

PMLs are reflectionless layers one puts at the edge of simulations to simulate scattering into free space. When analytically solving Maxwell's equations, one could choose to use the radiation condition, which prevents radiation arriving to the system. PMLs fulfill the same condition in numerical solutions: preventing artificial reflections from the edge of the computational domain, they can the thought of as 'numerical anechoic material'. PMLs were originally introduced in the 1990's [227] using a 'split field' formulation, whereby the usual electromagnetic field acquired additional artificial terms due to the absorbing boundary layer. However, a conceptually neater way of understanding PMLs as coordinate transformations was soon realised by Chew et al. [228].

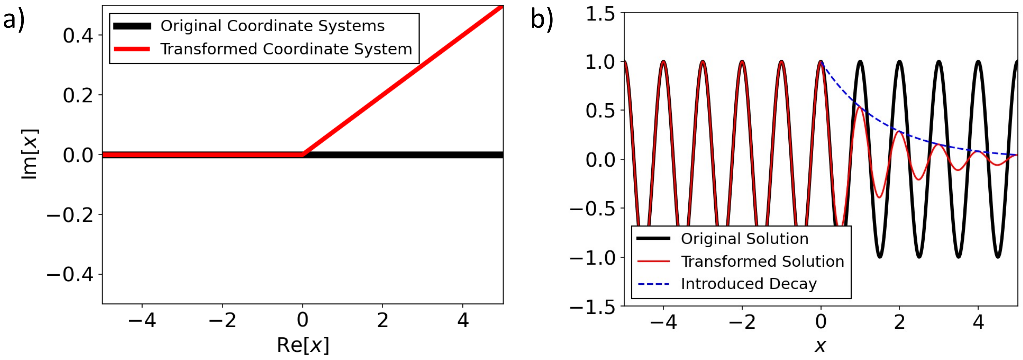

Figure B.3: Coordinate mapping description of perfectly matched layers. a) shows how the x coordinate is deformed at $x = 0$ to acquire a linear imaginary part. b) The effect of this mapping upon a propagating wave is to introduce a spatial decay, without reflection. This simulates emission into free space.

To understand the action of PMLs, we can consider the 1D wave equation

$$c^2 \frac{\partial^2 \phi}{\partial x^2} = \frac{\partial^2 \phi}{\partial t^2}, \tag{B.14}$$

which has a usual plane wave solution

$$\phi = e^{i(kx - \omega t)} \tag{B.15}$$

with $\omega = ck$. Analytically continuing the spatial coordinate into the complex plane $\tilde{x} = x' + ix''$ we see that the solution acquires a decay

$$\phi = e^{i(kx' - \omega t)} e^{-kx''}. \tag{B.16}$$

As long as $x'' > 0$, this is like having an absorbing material. We write the coordinate mapping from the real x coordinate to the complex $\tilde{x}$ as

$$\tilde{x} = x + if(x). \tag{B.17}$$

A possible mapping is illustrated in Figure B.3 a). Aiming to see how the coordinate mapping affects the wave equation in real space, we re–write the derivative

$$\partial\tilde{x} = \left(1 + i\frac{\mathrm{d}f}{\mathrm{d}x}\right)\partial x, \tag{B.18}$$

where we also define $df/dx = \sigma(x)/\omega$. Therefore, the coordinate transformation changes the x derivatives in the wave equation to

$$\frac{\partial}{\partial x} \to \left(\frac{1}{1 + i\frac{\sigma(x)}{\omega}}\right)\frac{\partial}{\partial x}. \tag{B.19}$$

The wave–equation, for a fixed frequency therefore becomes

$$\left[\frac{\partial^2}{\partial x^2} + \left(1 + i\frac{\sigma(x)}{\omega}\right)^2 k^2\right]\phi(x) = 0. \tag{B.20}$$

This is equivalent to the wave being in a material with refractive index

$$n(x) = 1 + i\frac{\sigma(x)}{\omega}. \tag{B.21}$$

In the regions where $f(x) = 0$, and therefore $\sigma(x) = 0$, the coordinate stretching has no effect upon the solution to the wave equation. However, in the PML regions where $f(x), \sigma(x) \neq 0$, making the spatial coordinate complex introduces an artificial lossy material that has no reflection. This is shown in Figure B.3 b). Since $df/dx = \sigma(x)/\omega$, we know that

$f(x) = \int^x \sigma(x')dx'/\omega$, we can write the solution to the wave equation as

$$\phi(x) = e^{ik(x+if(x))} \tag{B.22}$$

$$= e^{ikx}e^{-\frac{k}{\omega}\int^x \sigma(x')dx'}. \tag{B.23}$$

This shows us that in regions where $\sigma = 0$, the solution is just the usual propagating wave, while the wave gets absorbed in the PML region. We also note that introducing the factor of $1/\omega$ in the definition of σ means that the decay within the PML is governed by (inverse) wave speed k/ω, making the behaviour of the PML frequency independent. This means that all wavelengths are attenuated at the same rate. Now, we can tuncate the computational domain so only the exponential tails will reflect from the edge, and the reflections will be attenuated on their return. So, provided the PML is an appropriate thickness, the reflections from the edge of the domain will be exponentially small.

B.3 Calculating Polarizability

While the polarisability of simple systems can be extracted analytically from the Mie coefficients, for more complicated systems it must be found numerically. This was done in Chapter 4, to find the polarisability of the meta–cubes to design a multi-functional 'beam sorter' and in Chapter 5 to find the polarisability of metal rods. In each case, we followed closely the methods proposed by Yazdi and Komjani [229, 230]. One can calculate the polarisability tensor by exciting the scatterer with a plane wave, then evaluating the induced electric and magnetic dipole moments. The dipole moments can then be easily connected to the components of the polarisability, as

$$\boldsymbol{p} = \boldsymbol{\alpha_E E} \qquad\qquad \boldsymbol{m} = \boldsymbol{\alpha_H H}. \tag{B.24}$$

The direction and polarisation of the plane wave is chosen to give certain components of the tensors $\boldsymbol{\alpha}_E, \boldsymbol{\alpha}_H$. For example, to find the z components one chooses a plane wave polarised in the z direction and propagating as $e^{ik_y y}$, so that the field over the scatterer in the z direction is uniform. This procedure can easily be followed in full–wave solvers, such as COMSOL: the dipole moments can be found by numerically integrating either charge or polarisation density in the dipole case

$$\boldsymbol{p} = \int dV \boldsymbol{r} \rho(\boldsymbol{r}) = \int \boldsymbol{P}(\boldsymbol{r}) dV \tag{B.25}$$

and the cross product of position with current for the magnetic dipole.

$$\boldsymbol{m} = \frac{1}{2} \int dV \boldsymbol{r} \times \boldsymbol{j}. \tag{B.26}$$

To test this method, we evaluate the polarisability of a silicon sphere of radius 65 nm, across optical frequencies. Mie theory can be used to analytically calculate the polarisability of such a scatterer, so the numerics and analytics can be meaningfully compared to validate the method. Since the scatterer is isotropic, the polarisability tensor is diagonal with the elements along the diagonal all being equal. The numerical and anlytical results are compared in Figure B.4. Figure B.4a) shows a schematic of the model: the scatterer is excited with the plane wave, which induces charge and current densities. The dispersive nature of the refractive index of silicon, Figure B.4b), is taken into account with data from Green [97], being used for both the analytical and numerical calculations. The resulting polarisabilities are

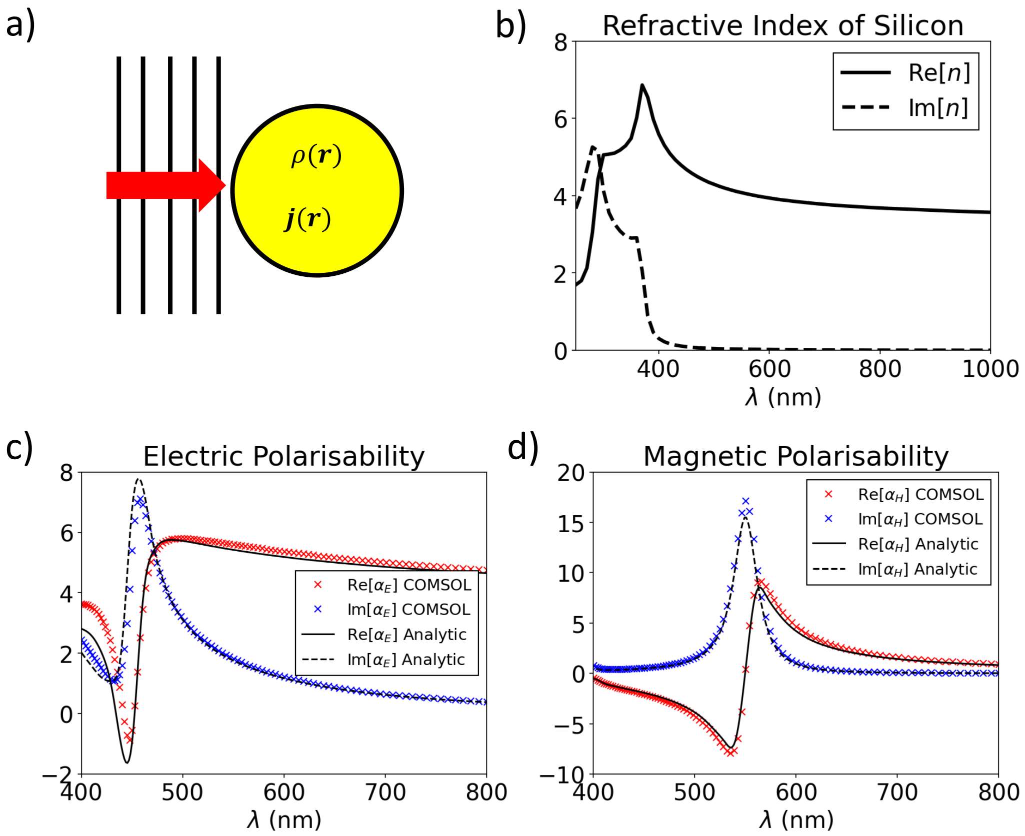

Figure B.4: Numerical calculation of the electric and magnetic polarisability of isotropic silicon spheres. a) shows the method. The scatterer is illuminated with a plane wave in a particular direction with a particular polarisation, related to which column of the polarisability tensor one wants to calculate. The incident field excites charges and currents within the resonator. Integrating over these over space yields the electric and magnetic dipole moments, which are used to form the polarisability. b) shows the dispersion of the refractive index of silicon, which must be included in the model. The numerically calculated electric and magnetic polarisabilities are shown in c) and d) respectively, and compared with the analytic solutions from Mie theory.

shown in Figure B.4c), d). With this method, the polarisabilities of more complicated scatterers can be found. The cases we will consider are reasonably simple, however even anisotropic and bianisotropic scatterers can be addressed using this framework.

Bibliography

1. Maxwell, J. C. *A Treatise on Electricity and Magnetism* (Oxford University Press, Oxford, 1873).
2. Poynting, J. H. On the Transfer of Energy in the Electromagnetic Field. *Philosophical Transactions of the Royal Society of London* **175,** 343–361 (1884).
3. Hertz, H. *Electric Waves: Being Researches on the Propagation of Electric Action with Finite Velocity Through Space* (Dover, New York, 1962).
4. Cyber and Electromagnetic Activities. *Joint Doctrine Note 1/18* (2018).
5. Kraus, J. D. & Marhefka, R. J. *Antennas for all applications* (McGraw Hill, New York, 2003).
6. Kraus, J. D. Antennas Since Hertz and Marconi. *IEEE Transactions on Antennas and Progagation* **33,** 131–137 (1985).
7. Landau, L. D. & Lifshitz, E. M. *Fluid Mechanics* (Pergamon Press, Oxford, 1966).
8. Landau, L. D. & Lifshitz, E. M. *Physical Kinetics* (Pergamon Press, Oxford, 1981).
9. Landau, L. D. & Lifshitz, E. M. *Theory of Elasticity* (Pergamon Press, Oxford, 1970).
10. Landau, L. D. & Lifshitz, E. M. *Quantum Mechanics* (Pergamon Press, Oxford, 1976).

11. Lancaster, T. & Blundell, S. J. *Quantum Field Theory for the Gifted Amateur* (Oxford University Press, Oxford, 2014).
12. Ryder, L. H. *Quantum Field Theory* (Cambridge University Press, Cambridge, 1996).
13. Whittaker, E. T. *A History of the Theories of Aether and Electricity: The Classical Theories* (Thomas Nelson and Sons, London, 1951).
14. Landau, L. D. & Lifshitz, E. M. *The Classical Theory of Fields* (Pergamon Press, New York, 1994).
15. Landau, L. D. & Lifshitz, E. M. *Electrodynamics of Continuous Media* (Butterworth-Heinemann, Oxford, 2008).
16. Jackson, J. D. *Classical Electrodynamics* (John Wiley and Sons, New York, 1998).
17. Stratton, J. A. *Electromagnetic Theory* (John Wiley and Sons, New York, 2007).
18. Sommerfeld, A. *Electrodynamics* (Academic Press Inc., New York, 1956).
19. Pierce, J. R. *Almost all about waves* (Dover, New York, 1981).
20. Green, G. *An Essay on the Application of mathematical Analysis to the theories of Electricity and Magnetism* (Wheelhouse, Nottingham, 1828).
21. Morse, P. M. & Feshbach, H. *Methods of Theoretical Physics* (McGraw-Hill Book Company, New York, 1953).
22. Ablowitz, M. J. & Fokas, A. S. *Complex Variables: Introduction and Applications* (Cambridge University Press, Cambridge, 2003).
23. Sommerfeld, A. *Partial Differential Equations in Physics* (Academic Press, New York, 1949).

24. Tai, C.-T. *Dyadic Green Functions in Electromagnetic Theory* (IEEE Press, New York, 1994).
25. Faryad, M. & Lakhtakia, A. *Infinite-Space Dyadic Green Functions in Electromagnetism* (IOP Publishing, Bristol, 2018).
26. Levine, H. & Schwinger, J. On the Theory of Electromagnetic Wave Diffraction by an Aperature in an Infinite Plane Conducting Screen. *Communications of Pure and Applied Mathematics* **3,** 355 (1950).
27. Chew, W. C. *Waves and Fields in Inhomogeneous Media* (IEEE Press, New York, 1995).
28. Barnes, W. L., Horsley, S. A. R. & Vos, W. L. Classical antennas, quantum emitters, and densities of optical states. *Journal of Optics* **22,** 7 (2020).
29. Dirac, P. A. M. The quantum theory of the emission and absorption of radiation. *Proceeding of the Royal Society A* **114,** 243–265 (1927).
30. Drexhage, K. H. Influence of a dielectric interface on fluorescence decay time. *Journal of Luminescence* **1-2,** 693–701 (1970).
31. Mie, G. Beiträge zur Optik trüber Medien, speziell kolloidaler Metallösungen. *Annalen der Physik* **3,** 377–445 (1908).
32. Bohren, C. F. & Huffman, D. R. *Absoproption and Scattering of Light by Small Particles* (John Wiley and Sons, New York, 1998).
33. Van de Hulst, H. C. *Light Scattering by Small Particles* (Dover, New York, 1981).
34. Abramowitz, A. & Stegun, I. A. *Handbook of Mathematical Functions* (Dover, New York, 1972).

35. Lindell, I. V., Sihvola, A. H., Tretyakov, S. A. & Viitanen, A. J. *Electromagnetic Waves in Chiral and Bi-Isotropic Media* (Artech House, Boston, 1994).

36. Evlyukhin, A. B., Reinhardt, C., Seidel, A., Luk'yanchuk, B. S. & Chichkov, B. N. Optical response features of Si-nanoparticle arrays. *Physical Review B* **82,** 045404 (2010).

37. Lunnemann, P. & Koenderink, A. F. The local density of optical states of a metasurface. *Scientific Reports* **6,** 20655 (2016).

38. Arango, F. B. & Koenderink, A. F. Polarizability tensor retrieval for magnetic and plasmonic antenna design. *New Journal of Physics,* 073023 (2013).

39. Sumlina, B. J., Heinsona, W. R. & K.Chakrabartya, R. Retrieving the aerosol complex refractive index using PyMieScatt: A Mie computational package with visualization capabilities. *Journal of Quantitative Spectroscopy and Radiative Transfer* **205,** 127–134 (2018).

40. Raab, R. E. & de Lange, O. L. *Multipole Theory in Electromagnetism* (Oxford University Press, Oxford, 2005).

41. Evlyukhin, A. B., Reinhardt, C. & Chichkov, B. N. Multipole light scattering by nonspherical nanoparticles in the discrete dipole approximation. *Phys. Rev. B* **84,** 235429 (2011).

42. Evlyukhin, A. B., Reinhard, C., Evlyukhin, E. & Chichkov, B. N. Multipole analysis of light scattering by arbitrary-shaped nanoparticles on a plane surface. *J. Opt. Soc. Am. B* **30,** 2589–2598 (2013).

43. Press, W. H., Teukolsky, S. A., Vetterling, W. T. & Flannery, B. P. *Numerical Recipes: The Art of Scientific Computing* (Cambridge University Press, Cambridge, 2007 (third edition)).

44. Bohren, C. F. & Huffman, D. R. *Absorption and Scattering of Light by Small Particles* (John Wiley and Sons, New York, 1983).

45. Liu, X.-X., Zhao, Y. & Alù, A. Polarizability tensor retrieval for subwavelength particles of arbitrary shape. *IEEE Trans. Antennas Propag.* **64,** 2301–2310 (2016).

46. Born, M. & Wolf, E. *Principles of Optics* (Cambridge University Press, 2009).

47. Savage, N. Photonics: Trick of the light. *Nature* **495.** `https://doi.org/10.1038/495S8a` (2013).

48. Herbert, F. *Dune* (Chilton Books, 1965).

49. Munk, B. A. *Frequency Selective Surfaces: Theory and Design* (John Wiley and Sons, New York, 2000).

50. Yu, N. *et al.* Light Propagation with Phase Discontinuities: Generalized Laws of Reflection and Refraction. *Science* **334,** 333–337 (2011).

51. Díaz-Rubio, A., Li, J., Shen, C., Cummer, S. A. & Tretyakov, S. A. Power flow–conformal metamirrors for engineering wave reflections. *Science Advances* **5,** eaau7288 (2019).

52. Ni, X., Kildishev, A. V. & Shalaev, V. M. Metasurface holograms for visible light. *Nature Communications* **4** (2013).

53. Chen, W. T., Zhu, A. Y. & Capasso, F. Flat optics with dispersion-engineered metasurfaces. *Nature Reviews Materials* (2020).

54. Padilla, W. J. & Averitt, R. D. Imaging with metamaterials. *Nature Reviews Physics* **4.** `https://doi.org/10.1038/s42254-021-00394-3` (2021).

55. Cordaro, A. *et al. Solving integral equations in free-space with inverse-designed ultrathin optical metagratings* 2022. `https://arxiv.org/abs/2202.05219`.

56. Wells, H. G. *The Invisible Man* (Pearson, 1897).

57. Leonhardt, U. Optical Conformal Mapping. *Science* **312,** 1777–1780 (2006).

58. Pendry, J. B., Schurig, D. & Smith, D. R. Controlling Electromagnetic Fields. *Science* **312,** 1780–1782 (2006).

59. Schurig, D. *et al.* Metamaterial Electromagnetic Cloak at Microwave Frequencies. *Science* **314,** 977–980 (2006).

60. Piggott, A. Y. *et al.* Inverse design and demonstration of a compact and broadband on-chip wavelength demultiplexer. *Nature Photon.* **9,** 374–377. `https://doi.org/10.1038/nphoton.2015.69` (2015).

61. Frellsen, L. F., Ding, Y., Sigmund, O. & Frandsen, L. H. Topology optimized mode multiplexing in silicon-on-insulator photonic wire waveguides. *Opt. Express* **24,** 16866–16873. `https://doi.org/10.1364/OE.24.016866` (2016).

62. Krešić, I., Makris, K. G., Leonhardt, U. & Rotter, S. Transforming Space with Non-Hermitian Dielectrics. *Physical Review Letters* **128,** 183901 (2022).

63. Gerchberg, R. W. & Saxton, W. O. A practical algorithm for the determination of the phase from image and diffraction plane pictures. *Optik* **35,** 237 (1972).

64. Liu, M. *et al.* Multifunctional metasurfaces enabled by simultaneous and independent control of phase and amplitude for orthogonal polarization states. *Light Sci. Appl.* **10,** 107. `https://doi.org/10.1038/s41377-021-00552-3` (2021).

65. Xu, L. *et al.* Enhanced Light-Matter Interactions in Dielectric Nanostructures via Machine Learning Approach. *Advanced Photonics* **2,** 026003 (2020).

66. Estrada-Real, A., Khaireh-Walieh, A., Urbaszek, B. & Wiecha, P. R. Inverse design with flexible design targets via deep learning: Tailoring of electric and magnetic multipole scattering from nano-spheres. *Photonics and Nanostructures - Fundamentals and Applications* **52,** 101066 (2022).

67. Dinsdale, N. J. *et al.* Deep Learning Enabled Design of Complex Transmission Matrices for Universal Optical Components. *ACS Photonics* **8,** 283–295 (2021).

68. COMSOL Multiphysics v. 6.0, `http://www.comsol.com`.

69. Yeung, C. *et al.* Elucidating the Behavior of Nanophotonic Structures through Explainable Machine Learning Algorithms. *ACS Photonics* **7,** 2309–2318. `https://doi.org/10.1021/acsphotonics.0c01067` (2020).

70. Wiecha, P. R., Arbouet, A., Cuche, A., Paillard, V. & Girard, C. Decay rate of magnetic dipoles near nonmagnetic nanostructures. *Physical Review B* **97,** 1–7 (2018).

71. Hornby, G. S., Globus, A., Linden, D. S. & Lohn, J. D. Automated Antenna Design with Evolutionary Algorithms. *Space.* `http://alglobus.net/NASAwork/papers/Space2006Antenna.pdf` (2006).

72. Sra, S., Nowozin, S. & Wright, S. J. *Optimization for Machine Learning* (The MIT Press, Cambridge, MA, 2012).
73. Mishra, S. Some new test functions for global optimization and performance of repulsive particle swarm method. *MPRA.* `https://mpra.ub.uni-muenchen.de/2718/` (2006).
74. Bendsøe, M. P. & Sigmund, O. *Topology optimization: Theory, methods and applications* (Springer, 2003).
75. Miller, O. D. *Photonic Design: From Fundamental Solar Cell Physics to Computational Inverse Design* PhD thesis (University of California, Berkeley, 2013).
76. Lalau-Keraly, C. M., Bhargava, S., Miller, O. D. & Yablonovitch, E. Adjoint shape optimization applied to electromagnetic design. *Opt. Express* **21,** 21693–21701. `https://doi.org/10.1364/OE.21.021693` (2013).
77. Purcell, E. M. Spontaneous emission probabilities at radio frequencies. *Physical Review* **69,** 681 (1946).
78. Langguth, L., Fleury, R., Alù, A. & Koenderink, A. F. Drexhage's Experiment for Sound. *Physical Review Letters* **116,** 224301 (2016).
79. Yagi, H. & Uda, S. Projector of the Sharpest Beam of Electric Waves. *Proceedings of the Imperial Academy* **2,** 49–52 (1926).
80. Novotny, L. & van Hulst, N. Antennas for light. *Nat. Photon.* **5,** 83–90 (2011).
81. Kullock, R., Ochs, M., Grimm, P., Emmerling, M. & Hecht, B. Electrically-driven Yagi-Uda antennas for light. *Nat. Comms.* **11,** 115 (2020).

82. Giannini, V., Fernández-Domínguez, A. I., Heck, S. C. & Maier, S. A. Plasmonic Nanoantennas: Fundamentals and Their Use in Controlling the Radiative Properties of Nanoemitters. *Chem. Rev.* **6,** 3888—3912 (2011).

83. Lunnemann, P. & Koenderink, A. F. The local density of optical states of a metasurface. *Sci. Rep.* **6** (2016).

84. Lodahl, P. *et al.* Controlling the dynamics of spontaneous emission from quantum dots by photonic crystals. *Nature* **430,** 654–657 (2004).

85. Bohn, J. *et al.* Active Tuning of Spontaneous Emission by Mie-Resonant Dielectric Metasurfaces. *Nano Lett.* **18,** 3461–3465 (2018).

86. Vaskin, A. *et al.* Directional and Spectral Shaping of Light Emission with Mie-Resonant Silicon Nanoantenna Arrays. *ACS Photonics* **5,** 1359–1364 (2018).

87. Vaskin, A., Kolkowski, R., Koenderink, A. F. & Staude, I. Light-emitting metasurfaces. *Nanophotonics* **8,** 1151–1198 (2019).

88. Mignuzzi, S. *et al.* Nanoscale Design of the Local Density of Optical States. *Nano Lett.* **19,** 1613–1617 (2019).

89. Stanfield, L. D., Powell, A. W., Horsley, S. A. R., Sambles, J. R. & Hibbins, A. P. Microwave Demonstration of Purcell Effect Enhanced Radiation Efficiency. *arXiv* **2209.13670** (2022).

90. Bennett, R. & Buhmann, S. Y. Inverse design of light–matter interactions in macroscopic QED. *New J. Phys.* **22,** 093014 (2020).

91. Bennett, R. Inverse design of environment-induced coherence. *Phys. Rev. A* **103,** 013706 (2021).

92. Matuszak, J., Buhmann, S. Y. & Bennett, R. Shape optimizations for body-assisted light-matter interactions. *Phys. Rev. A* **106,** 013515 (2022).

93. Wiecha, P. R. *et al.* Enhancement of electric and magnetic dipole transition of rare-earth-doped thin films tailored by high-index dielectric nanostructures. *Applied Optics* **58,** 1682–1690 (2019).

94. Brûlé, Y., Wiecha, P., Cuche, A., Paillard, V. & des Francs, G. C. Magnetic and electric Purcell factor control through geometry optimization of high index dielectric nanostructures. *Optics Express* **30,** 20360–20372 (2022).

95. Wiecha, P. R. *et al.* Design of plasmonic directional antennas via evolutionary optimization. *Optics Epxress* **27,** 29069–29081 (2019).

96. Wiecha, P. R. *et al.* Multi-resonant silicon nanoantennas by evolutionary multi-objective optimization. *Proc. SPIE 10694, Computational Optics II* **1069402** (2018).

97. Green, M. A. Self-consistent optical parameters of intrinsic silicon at 300 K including temperature coefficients. *Sol. Energy Mater. Sol. Cells* **92,** 1305–1310 (2008).

98. Gel′fand, I. M. & Vilenkin, N. Y. *Generalized Functions Vol. 1: Properties and Operations* (Academic Press, 1964).

99. Scali, S., Anders, J. & Horsley, S. A. R. Graph theory approach to exceptional points in wave scattering. *arXiv* **2301.08257** (2023).

100. Markel, V. A. Antisymmetrical optical states. *J. Opt. Soc. Am. B* **12,** 1783 (1995).

101. Merchiers, O., Moreno, F., González, F. & Saiz, J. M. Light scattering by an ensemble of interacting dipolar particles with both electric and magnetic polarizabilities. *Phys. Rev. A* **76,** 043834 (2007).

102. Gondarenko, A. *et al.* Spontaneous Emergence of Periodic Patterns in a Biologically Inspired Simulation of Photonic Structures. *Phys. Rev. Lett.* **96** (2006).

103. Lin, Z., Liu, V., Pestourie, R. & Johnson, S. G. Topology optimization of freeform large-area metasurfaces. *Opt. Express* **27,** 15765 (2019).

104. Luneburg, R. K. & Herzberger, M. *Mathematical Theory of Optics* (University of California Press, Berkely and Los Angeles, 1964).

105. Novotny, L. & Hecht, B. *Principles of Nano–Optics* (Cambridge University Press, Cambridge, 2006).

106. Smith, A. M. *From Light to Sight: The Passage from Ancient to Modern Optics* (The University of Chicago Press, Chicago, 2015).

107. Chaplain, G. J., Craster, R. V., Cole, N., Hibbins, A. P. & Starkey, T. A. Underwater Focusing of Sound by Umklapp Diffraction. *Phys. Rev. Applied* **16,** 064029 (2021).

108. Schnitzer, O. & Brandão, R. Absorption characteristics of large acoustic metasurfaces. *Phil. Trans. R. Soc. A* **380,** 20210399 (2022).

109. Pandey, G., Choudhary, A. & Dixit, A. Wavelength Division Multiplexed Radio Over Fiber Links for 5G Fronthaul Networks. *IEEE Journal on Selected Areas in Communications* **39,** 2789–2803 (2021).

110. Li, J.-S. & Zhong, M. Airy Beam Multifunctional Terahertz Metasurface. *IEEE Photonics Technology Letters* **35,** 245–248 (2023).

111. Pande, D., Gollub, J., Zecca, R., Marks, D. L. & Smith, D. R. Symphotic Multiplexing Medium at Microwave Frequencies. *Phys. Rev. Applied* **13,** 024033. `https://doi.org/10.1103/PhysRevApplied.13.024033` (2020).

112. Hadibrata, W., Noh, H., Wei, H., Krishnaswamy, S. & Aydin, K. Compact, High-resolution Inverse-Designed On-Chip Spectrometer Based on Tailored Disorder Modes. *Laser and Photonics Reviews* **15,** 2000556 (2021).

113. Bai, Y. *et al.* Photonic multiplexing techniques for neuromorphic computing. *Nanophotonics* (2023).

114. Puttnam, B. J., Rademacher, G. & Luís, R. S. Space-division multiplexing for optical fiber communications. *Optica* **8,** 1186–1203 (2021).

115. Richardson, D. J., Fini, J. M. & Nelson, L. E. Space-division multiplexing in optical fibres. *Nature Photonics* **7,** 354–362 (2013).

116. Luo, L.-W. *et al.* WDM-compatible mode-division multiplexing on a silicon chip. *Nature Communications* **5,** 3069 (2014).

117. Xiang, J. *et al.* Metamaterial-enabled arbitrary on-chip spatial mode manipulation. *Light: Science and Applications* **11,** 168 (2022).

118. Liu, Y. *et al.* Arbitrarily routed mode-division multiplexed photonic circuits for dense integration. *Nature Communications* **10,** 3263 (2019).

119. Liberal, I., Ederra, I., Teniente, J. & Gonzalo, R. Multi-Functional Antennas Based on Meta-Surfaces. *IEEE Transactions on Antennas and Propagation* **60,** 3020–3024 (2012).

120. Li, H., Fan, Y., Zhuang, Y., Zhou, T. & Denidni, T. A. Experimental Validation of an Active Parallel-Plate-Waveguide-Loaded Metasurfaces Lens for Wide-Angle Beam Steering. *IEEE Antennas and Wireless Propagation Letters* **21,** 2156–2160 (2022).

121. Zhou, F., Xu, J. & Song, Z. Terahertz Multiple Beam Steering Using Graphene Pancharatnam-Berry Metasurfaces. *IEEE Photonics Journal* **14,** 2231306 (2022).

122. Li, S.-Q. *et al.* Phase-only transmissive spatial light modulator based on tunable dielectric metasurface. *Science* **364,** 1087–1090. `https://doi.org/10.1126/science.aaw6747` (2019).

123. Shim, H., Kuang, Z., Lin, Z. & Miller, O. D. Fundamental limits to multi-functional and tunable nanophotonic response. *arXiv:2112.10816v1.* `https://arxiv.org/pdf/2112.10816` (2021).

124. Molesky, S. *et al.* Inverse design in nanophotonics. *Nature Photonics* **12,** 659–670 (2018).

125. Hwang, C.-L. & Masud, A. S. *Multiple Objective Decision Making: Methods and Applications* (Springer–Verlag, 1979).

126. J. R. Capers S. J. Boyes, A. P. H. & Horsley, S. A. R. Designing the collective non-local responses of metasurfaces. *Communications Physics* **4,** 209. `https://doi.org/10.1038/s42005-021-00713-1` (2021).

127. Powell, A. W. *et al.* Strong, omnidirectional radar backscatter from subwavelength, 3D printed metacubes. *IET Microw. Antennas Propag.* **14,** 1862–1868 (2020).

128. Ackley, D. H. *A connectionist machine for genetic hillclimbing* (Kluwer Academic Publishers, Boston, 1987).

129. Storn, R. & Price, K. Differential Evolution – A Simple and Efficient Heuristic for global Optimization over Continuous Spaces. *Journal of Global Optimization* **11,** 314–359. `https://doi.org/10.1023/A:1008202821328` (1997).

130. Virtanen, P. *et al.* SciPy 1.0: Fundamental Algorithms for Scientific Computing in Python. *Nature Methods* **17,** 261–272 (2020).

131. *Wi-Fi Booster Yagi–Uda Antenna, COMSOL Application Gallery* `https://www.comsol.com/model/wi-fi-booster-yagi-8211-uda-antenna-99891`, *Accessed 18th Apr. 2023.*

132. Taflove, A. & Hagness, S. C. *Computational Electrodynamics: The Finite–Difference Time–Domain Method* (Artech House, 2005).

133. *Dielectric Properties of Rohacell* `https://www.yumpu.com/en/document/read/20310696/dielectric-properties-of-rohacell-ig-a-hf-and-wf`, *Accessed 18th Apr. 2023.*

134. Auguié, B. & Barnes, W. L. Collective Resonances in Gold Nanoparticle Arrays. *Phys. Rev. Lett.* **101,** 143902 (2008).

135. Meinzer, N., Barnes, W. L. & Hooper, I. R. Plasmonic meta-atoms and metasurfaces. *Nature Photonics* **8,** 889–898 (2014).

136. Mann, C.-R., Sturges, T. J., Weick, G., Barnes, W. L. & Mariani, E. Manipulating type-I and type-II Dirac polaritons in cavity-embedded honeycomb metasurfaces. *Nature Communications* **9,** 2194 (2018).

137. Khurgin, J., Tsai, W.-Y., Tsai, D. P. & Sun, G. Landau Damping and Limit to Field Confinement and Enhancement in Plasmonic Dimers. *ACS Photonics* **4,** 2871–2880 (2017).

138. Staude, I. & Schilling, J. Metamaterial-inspired silicon nanophotonics. *Nature Photonics* **11,** 274–284 (2017).

139. Staude, I., Pertsch, T. & Kivshar, Y. S. All-Dielectric Resonant Meta-Optics Lightens up. *ACS Photonics* **6,** 802–814 (2019).

140. A. I. Kuzentsov A. E. Miroshnichenko, M. L. B., Kivshar, Y. S. & Luk'Yanchuk, B. Optically resonant dielectric nanostructures. *Science* **354,** aag2472 (2016).

141. Krasnok, A. E., Miroshnichenko, A. E., Belov, P. A. & Kivshar, Y. S. All-dielectric optical nanoantennas. *Optics Express* **20,** 20599–20604 (2021).

142. Shamkhi, H. K. *et al.* Transverse Scattering and Generalized Kerker Effects in All-Dielectric Mie-Resonant Metaoptics. *Phys. Rev. Lett.* **122,** 193905 (2019).

143. Weiss, T. *et al.* From Dark to Bright: First-Order Perturbation Theory with Analytical Mode Normalization for Plasmonic Nanoantenna Arrays Applied to Refractive Index Sensing. *Phys. Rev. Lett.* **116,** 237401 (2016).

144. Kristensen, P. T., de Lasson, J. R. & Gregersen, N. Calculation, normalization, and perturbation of quasinormal modes in coupled cavity-waveguide systems. *Optics Letters* **39,** 6359–6362 (2014).

145. Sztranyovszky, Z., Langbein, W. & Muljarov, E. A. Optical resonances in graded index spheres: A resonant-state-expansion study and analytic approximations. *Phys. Rev. A* **105,** 033522 (2022).

146. Zschiedrich, L. *et al.* Riesz-projection-based theory of light-matter interaction in dispersive nanoresonators. *Phys. Rev. A* **98,** 043806. `https://link.aps.org/doi/10.1103/PhysRevA.98.043806` (4 2018).

147. Sauvan, C., Wu, T., Zarouf, R., Muljarov, E. A. & Lalanne, P. Normalization, orthogonality, and completeness of quasinormal modes of open systems: the case of electromagnetism. *Optics Express* **30,** 6846–6885 (2022).

148. Mcphedran, R. C. & Stout, B. 'Killing Mie Softly': Analytic Integrals for Complex Resonant States. *Q. J. Mech. Appl. Math.* **73,** 119–139 (2020).

149. Sauvan, C., Hugonin, J. P., Maksymov, I. S. & Lalanne, P. Theory of the Spontaneous Optical Emission of Nanosize Photonic and Plasmon Resonators. *Phys. Rev. Lett.* **110,** 237401 (2013).

150. Chen, P. Y., Bergman, D. J. & Sivan, Y. Generalizing Normal Mode Expansion of Electromagnetic Green's Tensor to Open Systems. *Phys. Rev. Appl.* **11.** `https://doi.org/10.1103/PhysRevApplied.11.044018` (2019).

151. Zoysa, M. D. *et al.* Conversion of broadband to narrowband thermal emission through energy recycling. *Nature Photon.* **6.** `https://doi.org/10.1038/nphoton.2012.146` (2021).

152. Aydin, K., Ferry, V. E., Briggs, R. M. & Atwater, H. A. Broadband polarization-independent resonant light absorption using ultrathin plasmonic super absorbers. *Nat. Commun.* **2.** `https://doi.org/10.1038/ncomms1528` (2011).

153. Pala, R. A., White, J., Barnard, E., Liu, J. & Brongersma, M. L. Design of Plasmonic Thin-Film Solar Cells withBroadband Absorption Enhancements. *Adv. Mater.* **21.** `https://doi.org/10.1002/adma.200900331` (2009).

154. Zhou, Y. *et al.* Ultra-broadband metamaterial absorbers from long to very long infrared regime. *Light Sci Appl* **10.** `https://doi.org/10.1038/s41377-021-00577-8` (2021).

155. Ding, F. *et al.* Broadband near-infrared metamaterial absorbers utilizing highly lossy metals. *Scientific Reports* **6.** `https://www.nature.com/articles/srep39445` (2016).

156. Liu, N., Mesch, M., Weiss, T., Hentschel, M. & Giessen, H. Infrared Perfect Absorber and Its Application As Plasmonic Sensor. *Nano. Lett.* **10.** `https://doi.org/10.1021/nl9041033` (2010).

157. Landy, N. I., Sajuyigbe, S., Mock, J. J., Smith, D. R. & Padilla, W. J. Perfect Metamaterial Absorber. *Phys. Rev. Lett.* **100.** `https://doi.org/10.1103/PhysRevLett.100.207402` (2008).

158. Luo, S., Zhao, J., Zuo, D. & Wang, X. Perfect narrow band absorber for sensing applications. *Opt. Express* **24.** `https://doi.org/10.1364/OE.24.009288` (2016).

159. Lochbaum, A. *et al.* On-Chip Narrowband Thermal Emitter for Mid-IR Optical Gas Sensing. *ACS Photonics* **4.** `https://pubs.acs.org/doi/abs/10.1021/acsphotonics.6b01025` (2017).

160. Grigoriev, V. *et al.* Optimization of resonant effects in nanostructures via Weierstrass factorization. *Phys. Rev. A* **88.** `https://doi.org/10.1103/PhysRevA.88.011803` (2013).

161. Wu, T., Baron, A., Lalanne, P. & Vynck, K. Intrinsic multipolar contents of nanoresonators for tailored scattering. *Phys. Rev. A* **101.** `https://doi.org/10.1103/PhysRevA.101.011803` (2020).

162. Ming, X. & Sun, L. Optimization of Broadband Perfect Absorber by Weierstrass Factorization. *IEEE Photonics J.* **11.** `https://doi.org/10.1109/JPHOT.2019.2945492` (2019).

163. Yan, W., Lalanne, P. & Qiu, M. Shape Deformation of Nanoresonator: A Quasinormal-Mode Perturbation Theory. *Phys. Rev. Lett.* **125,** 013901. `https://link.aps.org/doi/10.1103/PhysRevLett.125.013901` (1 2020).

164. Binkowski, F. *et al.* Computation of eigenfrequency sensitivities using Riesz projections for efficient optimization of nanophotonic resonators. *Communications Physics* **5,** 202 (2022).

165. Chandrasekhar, S. & Detweiler, S. The quasi-normal modes of the Schwarzschild black hole. *Proc. R. Soc. Lond. A* **344.** `https://doi.org/10.1098/rspa.1975.0112` (1975).

166. Kristensen, P. T., Herrmann, K., Intravaia, F. & Busch, K. Modeling electromagnetic resonators using quasinormal modes. *Adv. Opt. Photonics* **12.** `https://doi.org/10.1364/AOP.377940` (2020).

167. Sommerfeld, A. *Partial Differential Equations in Physics* (Academic Press, 1949).

168. Gamow, G. Zur quantentheorie des atomkernes. *Zeitschrift für Physik* **51.** `https://link.springer.com/article/10.1007/BF01343196` (1928).

169. Bethe, H. A. Nuclear Physics B: Nuclear Dynamics, Theoretical. *Rev. Mod. Phys* **9.** `https://doi.org/10.1103/RevModPhys.9.69` (1937).

170. Ghatak, A. K. Leaky Modes in Optical Waveguides. *Opt. Quantum Electron.* **17.** `https://doi.org/10.1007/BF00620394` (1985).

171. Hu, J. & Menyuk, C. R. Understanding leaky modes: slab waveguide revisited. *Adv. Opt. Photonics* **1.** `https://doi.org/10.1364/AOP.1.000058` (2009).

172. Sakurai, A *et al.* Ultranarrow-Band Wavelength-Selective Thermal Emission with Aperiodic Multilayered Metamaterials Designed by Bayesian Optimization. *ACS Cent. Sci.* **5,** 319–326. `https://pubs.acs.org/doi/full/10.1021/acscentsci.8b00802` (2019).

173. Yang, J., Giessen, H. & Lalanne, P. Simple Analytical Expression for the Peak-Frequency Shifts of Plasmonic Resonances for Sensing. *Nano Lett.* **15.** `https://doi.org/10.1021/acs.nanolett.5b00771` (2015).

174. Both, S. *et al.* Nanophotonic Chiral Sensing: How Does It Actually Work? *ACS Nano.* **16.** `https://doi.org/10.1021/acsnano.1c09796` (2022).

175. *NIST Digital Library of Mathematical Functions* *`https://dlmf.nist.gov`*

176. Lalanne, P. *et al.* Quasinormal mode solvers for resonators with dispersive materials. *J. Opt. Soc. Am. A* **36.** `https://doi.org/10.1364/JOSAA.36.000686` (2019).

177. Adamou, A. T. I. & Craster, R. V. Spectral methods for modelling guided waves in elastic media. *J. Acoust. Soc. Am.* **116,** 1524–1535 (2004).

178. Tisseur, F. & Meerbergen, K. The quadratic eigenvalue problem. *SIAM Review* **43,** 235–286 (2001).

179. Ablowitz, M. J. & Fokas, A. S. *Complex Variables: Introduction and Applications* (Cambridge University Press, 2003).

180. Chong, Y. D., Ge, L., Cao, H. & Stone, A. D. Coherent Perfect Absorbers: Time-Reversed Lasers. *Phys. Rev. Lett.* **105.** `https://doi.org/10.1103/PhysRevLett.105.053901` (2010).

181. Dirac, P. A. M. *Principles of Quantum Mechanics* (Oxford University Press, Oxford, 1947).

182. Zel'Dovich, Y. B. On the theory of unstable states. *Soviet Physics JETP* **12.** `http://jetp.ras.ru/cgi-bin/dn/e_012_03_0542.pdf` (1961).

183. Leung, P. T., Liu, Y. T., Suen, W. M., Tam, C. Y. & Young, K. Logarithmic perturbation theory for quasinormal modes. *J. Phys. A* **31.** `https://iopscience.iop.org/article/10.1088/0305-4470/31/14/013` (1998).

184. Muljarov, E. A., Langbein, W. & Zimmermann, R. Brillouin-Wigner perturbation theory in open electromagnetic systems. *EPL* **92.** `https://doi.org/10.1209/0295-5075/92/50010` (2010).

185. Perelomov, A. M. & Zel'Dovich, Y. B. *Quantum Mechanics: Selected Topics* (World Scientific, 1998).

186. Steinfurth, A. *et al.* Observation of photonic constant-intensity waves and induced transparency in tailored non-Hermitian lattices. *Sci. Adv.* **8,** eabl7412 (2022).

187. Wang, Z., Wang, B.-Z., Liu, J.-P. & Wang, R. Method to obtain the initial value for the inverse design in nanophotonics based on a time-reversal technique. *Optics Letters* **46,** 2815–2818 (2021).

188. Yang, J. & Fan, J. A. Topology-optimized metasurfaces: impact of initial geometric layout. *Optics Letters* **42,** 3161–3164 (2017).

189. Zhao, N., Verweij, S., Shin, W. & Fan, S. Accelerating convergence of an iterative solution of finite difference frequency domain problems via schur complement domain decomposition. *Optics Express* **26,** 16925–16939 (2018).

190. Verweij, S. & Fan, S. Impact of objective bandwidth and frequency sampling density on search landscape structure and search performance in design optimization of optical structures. *Journal of Optics* **20,** 115002 (2018).

191. Boutami, S., Zhao, N. & Fan, S. Determining the optimal learning rate in gradient-based electromagnetic optimization using the Shanks transformation in the Lippmann–Schwinger formalism. *Optics Letters* **45,** 595–598 (2020).

192. Bottou, L. *Stochastic Learning: Advanced Lectures on Machine Learning* (Springer Verlag, Berlin, 2004).

193. Kingma, D. P. & Ba, J. Adam: A Method for Stochastic Optimization. *arXiv* **1412.6980** (2014).

194. Kaelberer, T., Fedotov, V. A., Papasimakis, N., Tsai, D. P. & Zheludev, N. I. Toroidal dipolar response in a metamaterial. *Science* **330,** 1510–1512 (2010).

195. Powell, A. W., Hibbins, A. P. & Sambles, J. R. Multiband superbackscattering via mode superposition in a single dielectric particle. *Applied Physics Letters* **118,** 251107 (2021).

196. Powell, A. W., Mrnka, M., Hibbins, A. P. & Sambles, J. R. Superscattering and Directive Antennas via Mode Superposition in Subwavelength Core-Shell Meta-Atoms. *Photonics* **9,** 6 (2022).

197. Liu, W. & Kivshar, Y. S. Generalized Kerker effects in nanophotonics and meta-optics. *Optics Express* **26,** 13085–13105 (2018).

198. Gower, A. L., Smith, M. J. A., Parnell, W. J. & Abrahams, I. D. Reflection from a multi-species material and its transmitted effective wavenumber. *Proceedings of the Royal Society A* **474,** 20170864 (2018).

199. Gower, A. & Kristensson, G. Effective waves for random three-dimensional particulate materials. *New Journal of Physics* **23,** 063083 (2021).

200. Zhu, Y., Chen, Y., Gorsky, S., Shubitidze, T. & Negro, L. D. Inverse design of functional photonic patches by adjoint optimization coupled to the generalized Mie theory. *arXiv* **2302.02835** (2023).

201. Chu, L. J. Physical limitations of omni-directional antennas. *Journal of Applied Physics.* **19,** 1163–1175 (1948).

202. Harrington, R. F. Effects of antenna size on gain, bandwidth, and efficiency. *Journal of the National Bureau of Standards* **64,** 1–12 (1960).

203. Wheeler, H. Small Antennas. *IEEE Transactions on Antennas and Propagation* **24,** 462–469 (1975).

204. Rozanov, K. N. Ultimate thickness to bandwidth ratio of radar absorbers. *IEEE Transactions on Antennas and Propagation* **48,** 1230–1234 (2000).

205. Gradoni, G. *et al.* Smart Radio Environments. *arXiv* **2111.08676** (2021).

206. Chaplain, G. J., Pajer, D., Ponti, J. M. D. & Craster, R. V. Delineating rainbow reflection and trapping with applications for energy harvesting. *New Journal of Physics* **22,** 063024 (2020).

207. Chen, Y., Kadic, M. & Wegener, M. Roton-like acoustical dispersion relations in 3D metamaterials. *Nature Communications* **12,** 3278 (2021).

208. Chaplain, G. J., Makwana, M. P. & Craster, R. V. Rayleigh–Bloch, topological edge and interface waves for structured elastic plates. *Wave Motion* **86,** 162–174 (2019).

209. Chaplain, G. J., Ponti, J. M. D., Aguzzi, G., Colombi, A. & Craster, R. V. Topological Rainbow Trapping for Elastic Energy Harvesting in Graded Su-Schrieffer-Heeger Systems. *Physical Review Applied* **14,** 054035 (2020).

210. Jose, K., Ferguson, N. & Bhaskar, A. Branched flows of flexural waves in non-uniform elastic plates. *Communications Physics* **5,** 152 (2022).

211. Torrent, D., Mayou, D. & Sánchez-Dehesa, J. Elastic analog of graphene: Dirac cones and edge states for flexural waves in thin plates. *Physical Review B* **87,** 115143 (2013).

212. Haslinger, S. G., Craster, R. V., Movchan, A. B., Movchan, N. V. & Jones, I. S. Dynamic interfacial trapping of flexural waves in structured plates. *Proceedings of the Royal Society A* **472,** 20150658 (2016).

213. Martí-Sabaté, M. & Torrent, D. Edge modes for flexural waves in quasi-periodic linear arrays of scatterers. *APL Materials* **9,** 081107 (2021).

214. Martí-Sabaté, M., Djafari-Rouhani, B. & Torrent, D. Bound states in the continuum in circular clusters of scatterers. *Physical Review Research* **5,** 013131 (2023).

215. Martí-Sabaté, M. & Torrent, D. Dipolar Localization of Waves in Twisted Phononic Crystal Plates. *Physical Review Applied* **15,** L011001 (2021).

216. El-Sayed, A.-L. & Hughes, S. Quasi-normal mode theory of elastic Purcell factors and Fano resonances in optomechanical beams. *Physical Review Research* **2,** 043290 (2020).

217. Laude, V. & Wang, Y.-F. Quasinormal mode representation of radiating resonators in open phononic systems. *arXiv* **2211.12823** (2022).

218. Pendry, J. B., Galiffi, E. & Huidobro, P. A. Gain mechanism in time-dependent media. *Optica* **8,** 636–637 (2021).

219. Horsley, S. A. R. & Pendry, J. B. Time varying gratings model Hawking radiation. *arXiv* **2302.04066** (2023).

220. Wen, X. *et al.* Unidirectional amplification with acoustic non-Hermitian space-time varying metamaterial. *Communications Physics* **5,** 18 (2022).

221. Cho, C., Wen, X., Park, N. & Li, J. Digitally virtualized atoms for acoustic metamaterials. *Nature Communications* **11,** 251 (2020).

222. Rooy, N. *'Differential Evolution from Scratch in Python'*, *https://nathanrooy.github.io/posts/2017-08-27/simple-differential-evolution-with-python/*

223. Burnett, D. S. *Finite Element Analysis: From Concepts to Applications* (Addison–Wesley, Massachusetts, 1987).

224. *The Finite Element Method https://www.comsol.com/multiphysics/finite-element-method, Accessed 14th Feb. 2023.*

225. Taflove, A. & Hagness, S. C. *Computational Electrodynamics: The Finite Difference Time Domain Method* (Artech House, Boston, 2006).

226. Johnson, S. G. Notes on Perfectly Matched Layers (PMLs). *arXiv:2108.05348* (2021).

227. Berenger, J.-P. A perfectly matched layer for the absorption of electromagnetic waves. *J. Comput. Phys.* **114,** 185–200 (1994).

228. Chew, W. C. & Weedon, W. H. A 3D perfectly matched medium from modified maxwell's equations with stretched coordinates. *Microw. Opt. Technol. Lett.* **7,** 599–604 (1994).

229. Yazdi, M. & Komjani, N. Polarizability Tensor Calculation Using Induced Charge and Current Distributions. *Progress In Electromagnetics Research M* **45,** 123–130 (2016).

230. Yazdi, M. & Komjani, N. Polarizability calculation of arbitrary individual scatterers, scatterers in arrays, and substrated scatterers. *J. Opt. Soc. Am. B* **33,** 491–500 (2016).